Acta Pharmacologica Sinica (2010) 31: 1–9
© 2010 CPS and SIMM All rights reserved 1671-4083/10 $32.00
www.nature.com/aps

Review

MicroRNAs: a novel class of potential therapeutic targets for cardiovascular diseases

Zhen-wei PAN, Yan-jie LU, Bao-feng YANG*

Department of Pharmacology (the State-Province Key Laboratories of Biomedicine-Pharmaceutics of China), Cardiovascular Research Institute, Harbin Medical University, Harbin 150086, China

Currently, cardiovascular diseases remain one of the leading causes of morbidity and mortality in the world, indicating the need for innovative therapies and diagnosis for heart disease. MicroRNAs (miRNAs) have recently emerged as one of the central players in regulating gene expression. Numerous studies have documented the implications of miRNAs in nearly every pathological process of the cardiovascular system, including cardiac arrhythmia, cardiac hypertrophy, heart failure, cardiac fibrosis, cardiac ischemia and vascular atherosclerosis. More surprisingly, forced expression or suppression of a single miRNA is enough to cause or alleviate the pathological alteration, underscoring the therapeutic potential of miRNAs in cardiovascular diseases. In this review we summarize the key miRNAs that can solely modulate the cardiovascular pathological process and discuss the mechanisms by which they exert their function and the perspective of these miRNAs as novel therapeutic targets and/or diagnostic markers. In addition, current approaches for manipulating the action of miRNAs will be introduced.

Keywords: microRNA; therapeutic target; cardiovascular disease

Acta Pharmacologica Sinica (2010) 31: 1–9; doi: 10.1038/aps.2009.175;

Introduction

MicroRNAs (miRNAs) are endogenous, conserved ~22-nucleotide non-coding RNAs that anneal to inexactly complementary sequences in the 3′-untranslated regions (3′UTR) of target mRNAs of protein-coding genes to cause mRNA cleavage or repression of the translational machinery for protein synthesis[1]. The first miRNA lin-4 was discovered in 1993, which regulates *C elegans* development by inhibiting the protein expression of lin-14 via binding to the 3′UTR of its mRNA[2]. In 2000, the second miRNA let-7 was identified as a 21-nucleotide small RNA that has a complementary sequence to the 3′UTR of lin-14 and participates in the regulation of *C elegans* development[3]. After that, a large number of miRNAs have been found and a series of research uncovered the functional role of miRNAs in diverse biological and pathophysiological processes[4, 5]. Among them, the involvement of miRNAs in the pathogenesis of cardiovascular diseases has recently been intensively investigated[6–8].

MiRNAs are initially transcribed as long RNA precursors called primary miRNAs that require the RNase III enzyme Drosha in the nucleus to trim them into precursor miRNAs. The latter, characterized by a stem loop or hairpin structure of 70–100 nt, is exported by the nuclear export factor exportin-5 to the cytoplasm where they are subsequently cropped to become mature miRNAs of 21–26 nt long by another RNase III enzyme Dicer[9–13]. Mature miRNAs can interact with Argonaute to form the RNA-induced silencing complex (RISC) and then guide the RISC to their target mRNAs, most favorably to the 3′UTR. In order for a miRNA to produce functional consequences, its 5′-end 2 to 8 nts must have exact base pairing to the target mRNA, the "seed" region, and partial complementarity with the rest of the sequence. An miRNA can either inhibit translation or induce degradation of its target mRNA, primarily depending upon the overall degree of complementarity of the binding site, number of binding sites, and the accessibility of the bindings sites (determined by free energy states). The greater the complementarity of the accessible binding sites, the more likely an miRNA degrades its targeted mRNA, and those miRNAs that display imperfect sequence complementarities with target mRNAs primarily result in translational inhibition[14–16]. MiRNAs are an abundant RNA species constituting >2% of the predicted human genes (>1000 genes), which regulates ~30% of protein–coding genes. Some miRNAs are expressed at >1000 copies per cell[17].

With the recent surge of research into miRNAs, this category of endogenous non-coding small ribonucleic acids

---

* To whom correspondence should be addressed.
E-mail yangbf@ems.hrbmu.edu.cn
Received 2009-07-19 Accepted 2009-11-12

has emerged as one of the central players of gene expression regulation. The research on miRNAs in relation to cardiovascular disease has become a most rapidly evolving field. The dysregulation of many individual miRNAs has been linked to the development and progression of cardiovascular disease. Forced expression or suppression of a single miRNA is enough to cause or alleviate the pathological change. The role of miRNAs in the pathogenesis of the heart and vessels points to a possibility of miRNAs as targets for treatment of cardiovascular disease. In this review, the aberrantly expressed miRNAs that underlie the development of cardiovascular diseases will be discussed. The therapeutic potential of miRNAs as new targets for cardiovascular diseases and strategies for manipulating miRNAs by influencing their expression, stability, and function will be introduced.

Therapeutic implications of miRNAs in cardiovascular diseases

miRNA and cardiac hypertrophy and heart failure

In response to stress (such as hemodynamic alterations associated with myocardial infarction, hypertension, aortic stenosis, valvular dysfunction, *etc*), the adult heart undergoes remodeling process and hypertrophic growth to adapt to altered workloads and to compensate for the impaired cardiac function. 'The remodeled heart frequently progresses into overt heart failure. Hypertrophic growth manifests enlargement of cardiomyocyte size and enhancement of protein synthesis through the activation of intracellular signaling pathways and transcriptional mediators in cardiac myocytes. The process is characterized by a reprogramming of cardiac gene expression and the activation of "fetal" cardiac genes[18]. In light of the role of miRNA in gene regulation, miRNAs may be involved in cardiac hypertrophy and heart failure. This concept was confirmed by a number of reports which demonstrated that dysregulation of a single miRNA is sufficient to induce this pathological alteration, pointing to miRNAs as potential novel therapeutic targets in cardiac hypertrophy and heart failure.

To date, 11 miRNAs have been experimentally established to determine this pathological process. These include miR-1, 133, 129, 18b, 195, 21, 23a, 23b, 24, 208, and 212. Of them, miR-1 and miR-133 are anti-hypertrophic, and miR-129, 18b, 195, 23a, 23b, 24, 208, and 212 are pro-hypertrophic. However, the role of miR-21 in cardiac hypertrophy is still controversial[19–28]. The first group of miRNAs regulating cardiac hypertrophy were identified in Olson's lab[20]. They described a typical signature pattern of miRNAs in cardiac tissue from mice in response to transverse aortic constriction (TAC) or expression of activated calcineurin, stimuli that induce pathological cardiac remodeling hypertrophic. They further showed that forced overexpression of individual stress-inducible miRNAs eg. miR-195, 23a, 23b, 24, or miR-195 alone induced hypertrophy in cultured cardiomyocytes. More interestingly, transgenic overexpression of miR-195 in mice was sufficient to induce pathological cardiac growth and heart failure as indicated by thinning of the left ventricular walls, increase in left ventricular diameter and deterioration in cardiac function. Olson's group then investigated the effect of miR-208[19], a cardiac-specific miRNA that is encoded by an intron of the α-MHC gene, on cardiac hypertrophy. They found that miR-208 is required for cardiomyocyte hypertrophy, fibrosis, and expression of β-MHC in response to stress and hypothyroidism. Mice homozygous for miR-208 deletion failed to undergo stress-induced cardiac remodeling, hypertrophic growth, and β-MHC upregulation, whereas transgenic expression of miR-208 was sufficient to induce β-MHC and hypertrophy. The thyroid hormone receptor associated protein 1 (THRAP1), a cofactor of the thyroid hormone receptor, was verified to be the target mRNA of miR-208. By repressing THRAP1, miR-208 regulates the expression of β-MHC and, thereby, the development of hypertrophy to stress. A recent study by Wang DZ *et al* confirmed the action of miR-208 by discovering that transgenic overexpression of miR-208a in the heart induced hypertrophic growth in mice, which resulted in pronounced repression of the miR-208 regulatory targets thyroid hormone–associated protein 1 and myostatin, 2 negative regulators of muscle growth and hypertrophy[29].

Sayed *et al*[24] explored the role of miR-1, a muscle-specific miRNA, in pressure-overload induced cardiac hypertrophy. They found that miR-1 was singularly downregulated as early as day 1, persisting through day 7, after TAC-induced hypertrophy in a mouse model. Moreover, the aberrant expressed miR-1 is a causative factor of hypertrophy. Overexpression of miR-1 carried by adenovirus vector prevented hypertrophic growth of neonatal cardiac myocytes by inhibiting its growth-related targets, including Ras guanosine-triphosphatase-activating protein, cyclin-dependent kinase 9, fibronectin, and Ras homolog enriched in brain. Consistently, Caré *et al*[28]confirmed the down-regulation of miR-1 in three different hypertrophic models, including transverse aortic arch–constricted mice, transgenic mice with selective cardiac overexpression of a constitutively active mutant of the Akt kinase, and exercised rats, and the inhibitory role of miR-1 on cardiac hypertrophy *in vitro*. miR-1 was also reported to negatively regulate the expression of hypertrophy-associated genes, Mef2a and Gata4, and attenuate cardiomyocyte hypertrophy in cultured neonatal rat cardiomyocytes and in the intact adult heart[25].

The antihypertrophic action of another muscle-specific miRNA, miR-133, was described in two studies. Caré *et al*[28] found that the expression of miR-133, which transcribed together with miR-1 as a bicistronic cluster, was decreased in the left ventricle of the above mentioned three hypertrophic models. *In vitro* overexpression of miR-133 inhibited cardiac hypertrophy. In contrast, suppression of miR-133 induced hypertrophy, which was more pronounced than that after stimulation with conventional inducers of hypertrophy. *In vivo* inhibition of miR-133 by a single infusion of a chemically modified antisense RNA oligonucleotide (termed 'antagomiR') targeted to miR-133 lead to one month miR-133 knockdown and caused marked and sustained cardiac hypertrophy. To elucidate the molecular mechanism underlying miR-133's control on cardiac hypertrophy, they identified specific targets of miR-133: RhoA, a guanosine diphosphate–guanosine triphosphate exchange protein regulating cardiac hypertrophy; Cdc42, a signal transduction kinase implicated in hypertrophy; and Nelf-A/WHSC2, a nuclear factor involved in cardiogenesis. Li PF's group found that miR-23a is a pro-hypertrophic miRNA, which is regulated by the transcription factor, nuclear factor of activated T cells (NFATc3). Under hypertrophic stimuli the expression of miR-23a was up-regulated, which leads to cardiac hypertrophy via targeting the muscle specific ring finger protein 1, an anti-hypertrophic protein. More excitingly, they demonstrated that knockdown of miR-23a using antagomir technique could significantly attenuate hypertrophy induced by isopropranolol, suggesting the potential of miR-23a as an anti-hypertrophic target[30]. Sucharov *et al* demonstrated that over-expression of miR-133b prevents changes in gene expression patterns mediated by β-adrenergic receptor stimulation[23].

Simultaneous overexpression of three fetal miRNAs upregulated in the failing heart (miR-21, miR-129, and miR-212) resulted in hypertrophic morphological changes of neonatal cardiomyocytes similar to that observed in the failing heart. Meanwhile, a number of both established (ANP, BNP, β-MHC, α-skeletal actin) and newly identified fetal genes (villin2, cspg2, phlda1, hsp90, RASA1, MEF2a, cradd, dtna) were reactivated or silenced by this modulation of the miRNA environment. Interestingly, overexpression of a single miRNA (miR-21, miR-129, or miR-212) had only minor effects, indicating that certain pathological changes may require an alteration of the miRNA environment[21]. Another study also confirmed the upregulation of miR-21 in hypertrophic heart and in cultured neonatal hypertrophic cardiomyocytes stimulated by angiotensin II or phenylephrine, and the antihypertrophic action of miR-21 was obtained by suppressing its aberrant expression via antisense-mediated depletion[27]. However, a contradictory result was also reported[22], namely that miR-21 produced antihypertrophic rather than prohypertrophic action.

miRNA and arrhythmia

Arrhythmias are electrical disturbances that can result in irregular heart beating, which is the leading cause of sudden cardiac death. Alterations of the three intrinsic properties of the heart, including impaired excitation conduction/propagation, enhanced automaticity, or abnormal repolarization lead to disturbed excitability, manifesting as arrhythmias. Cardiac ion channels are fundamental determinants of cardiac intrinsic properties. Malfunction of these ion channels either caused by mutations in the genes encoding the channel proteins or altered expression under proarrhythmic conditions, such as cardiac remodeling, ischemia etc, can predispose to arrhythmias. Conventional pharmacologic agents targeting ion channels remain the major therapeutic tools in treating cardiac arrhythmias. However, the limited efficacy and proarrhythmic potential of antiarrhythmic agents restricts their application. Recent findings that miRNAs regulate expression of cardiac ion channels strongly indicate a role of these miRNAs to influence arrhythmogenicity and a potential of these miRNAs being the new antiarrhythmic targets[31]. Life-threatening ischemic arrhythmias are common clinical complications in ischemic heart diseases. Our group found that the expression level of miR-1 in the myocardium of coronary artery disease patients was significantly increased. *In vivo* application of miR-1 into the myocardium induces arrhythmias in both healthy normal hearts and a rat model of myocardial infarction[31]. Knock down of miR-1 using its specific inhibitor antisense oligonucleotides (AMO) reversed these effects. GJA1/Cx43 and KCNJ2/Kir2.1 are the two targets of miR-1, which explains the arrhythmogenic action of miR-1, as decreased expression of Cx43 and Kir2.1 during cardiac ischemia underlies the occurrence of ischemic arrhythmia. These data indicated that myocardial infarction upregulates miR-1 expression via some unknown factors, which induces post-transcriptional repression of GJA1 and KCNJ2, resulting in conduction slowing that finally leading to ischemic arrhythmias[31]. This work was regarded as an exciting step in the dissection of new molecular signaling pathways for arrhythmias and sudden death[32]. Dmitry Terentyev *et al*[33] further confirmed the arrhythmogenic action of miR-1. They found that in the presence of isoproterenol, rhythmically paced, miR-1-overexpressing myocytes exhibited spontaneous arrhythmogenic oscillations of intracellular Ca^{2+}, events that occurred rarely in control myocytes under the same conditions. Protein phosphatase PP2A was validated as a new target of miR-1. Suppression of PP2A by miR-1 selectively leads to CaMKII-dependent hyperphosphorylation of RyR2, enhances RyR2 activity, and promotes arrhythmogenic SR Ca^{2+} release.

Atrial fibrillation is another most commonly encountered cardiac arrhythmia and is directly or indirectly responsible for considerable mortality and morbidity in cardiovascular disease patients. Elucidation of the molecular mechanisms underlying the development of atrial fibrillation may provide novel targets for future therapy. Our group found that miR-133 and miR-590 are involved in atrial structural remodeling, which is the major pathological basis for the development of atrial fibrillation[34]. In the atrium of nicotine treated dogs, TGF-β1 and TGF-β RII were upregulated at the protein level, while miR-133 and miR-590 were downregulated. TGF-β1 and TGF-βRII were verified as the targets of miR-133 and miR-590, respectively, as transfection of miR-133 or miR-590 into cultured atrial fibroblasts decreased levels of TGF-β1 and TGF-βRII and collagen content, which were abolished by the antisense oligonucleotides against miR-133 or miR-590[34]. This study indicates that interference with miRNAs using small silencing RNAs or antisense oligonucleotides has the potential to be developed as novel therapeutic approach to AF[35]. Interestingly, the cardiac specific miRNA miR-208a was demonstrated to participate in both cardiac conduction abnormality and the occurance of AF, as miR-208a transgenic mice manifested first-degree atrial-ventricular block, while miR-208a knockout mice developed AF, which strongly indicates the importance of maintaining the physiological balance of miRNA levels[29].

Pacemaker channels, which carry the nonselective cation currents, are critical in generating sinus rhythm and ectopic heart beats under various pathological settings such as cardiac hypertrophy. Luo *et al* showed that miR-1 and miR-133 also targeted pacemaker channels, HCN2 and HCN4, with HCN2 modulated by miR-1 and miR-133 and HCN4 by miR-1[36]. Forced expression of miR-1/miR-133 by transfection prevented overexpression of HCN2/HCN4 in hypertrophic cardiomyocytes, indicating its antiarrhythmic capability. Rapid delayed rectifier K^+ current (I_{Kr}), encoded by human *ether-á-go-go*-related gene (HERG), and slow delayed rectifier K^+ current (I_{Ks}), encoded by KCNQ1 assembles with KCNE1, are two potassium currents responsible for the repolarization of cardiac myocytes and play a critical role in governing cardiac APD. Impairment of these repolarization current channels can cause substantial prolongation of APD or QT interval prolongation, which is associated with an increased risk of sudden cardiac death consequent to lethal ventricular arrhythmias. Xiao *et al* tested the involvement of miRNAs underlying the discrepancy expression of ERG channels in a rabbit diabetic model. They found that repression of ERG by miR-133 in diabetic hearts likely underlies the differential changes of ERG protein and transcript, thereby causing depression of I_{Kr} and repolarization slowing, resulting in QT prolongation and arrhythmias[37]. In addition, they experimentally established that KCNQ1 and KCNE1 are targets of miR-133 and miR-1, respectively[38]. More importantly, they found that the distribution of miR-133 and miR-1 transcripts within the heart is also spatially heterogeneous with the patterns corresponding to the spatial distribution of KCNQ1 and KCNE1 proteins and I_{Ks}. Zhao *et al*[39] found that targeted deletion of the muscle-specific miRNA, miR-1-2, lead to abnormal propagation of cardiac electrical activity, manifested as slower heart rate, a shortened PR interval, and a broadened QRS complex, indicative of bundle branch block. They further validated the miR-1-2 targets, including the cardiac transcription factor, Irx5, which represses KCND2, a potassium channel subunit (Kv4.2) responsible for transient outward K^+ current (I_{to}). Clearly, the multi-target effects of muscle-specific miR-1 and miR-133 on ion channels supports a central role of miRNA for fine tuning the regulation of cardiac electrophysiology and the potential of them as novel therapeutic targets.

miRNA and cardiac fibrosis

Cardiac fibrosis, a process of excessive extracellular matrix (ECM) protein accumulation, also called ECM remodeling, is an important feature of cardiac adaptation to numerous pathological stimuli, such as hypertension and cardiac infarction. This process alters mechanical stiffness and electric properties of the heart and contributes to diastolic dysfunction, cardiomyocyte loss, arrhythmias, and the progression to heart failure. Alleviation of ECM remodeling was considered a reasonable strategy to improve cardiac function and prevent heart failure associated with cardiac infarction and hypertension. Interestingly, several miRNAs including miR-133, miR-21, miR-29 and miR-30 have been demonstrated to participate in the regulation of ECM remodeling. Olson's group[40] found that the miR-29 family of miRNAs, which consists of three members expressed from two bicistronic miRNA clusters (miR-29b-1 is co-expressed with miR-29a, and miR-29b-2 is co-expressed with miR-29c), are downregulated in the region of the heart adjacent to the infarct in chronic cardiac infarction rats. *In vivo* knockdown of cardiac miR-29b by tail vein injection of cholesterol-modified oligonucleotides (antagomiR miR-29b) modestly increased collagen expression in the heart, whereas over-expression of miR-29 in fibroblasts reduced collagen expression, indicating the potential role of miR-29 as a negative regulator of collagen expression. A large number of mRNAs that encode proteins involved in fibrosis, including multiple collagens, fibrillins, and elastin were found to be targets of miR-29.

The role of miR-21 in the process of fibrosis has been investigated in-depth[41, 42]. miR-21 was reported to be progressively upregulated in cardiac fibroblasts during cardiac ischemia/reperfusion[42] or the later stages of heart failure[41]. Upregulation of miR-21 in cardiac fibroblasts results in inhibition of SPRY1 protein expression, augmentation of ERK–MAP kinase activity, which in turn enhances cardiac fibroblast survival and thereby the interstitial fibrosis and cardiac remodeling that is characteristic of the failing heart[41]. More importantly, blocking of endogenous miR-21 by antagomiR-21, which is a chemically modified antisense oligonucleotide specific for miR-21, in pressure overload mice reduced genes encoding collagens and extracellular matrix molecules that are highly upregulated during cardiac fibrosis, and significantly attenuated the increased interstitial fibrosis, cardiomyocyte size and heart weight. This finding may provide a new remedy for the treatment of fibrosis.

Different from miR-29 and miR-21, another two miRNAs, miR-133 and miR-30c, are down regulated during ventricular hypertrophy[43]. Overexpression of miR-133 or miR-30c in cultured fibroblasts decreased the production of collagens by suppressing connective tissue growth factor (CTGF), which is a powerful inducer of ECM synthesis and contributes to myocardial remodeling[43].

miRNA and cardiac ischemic disease

Ischemic/reperfusion injury is one of the most common cardiovascular diseases that requires intensive research to fully elucidate the underlying mechanisms and improve the therapeutic outcomes. Oxidative stress and apoptosis are the key pathological processes that medicate ischemic/reperfusion injury. Induction of neovascularization and ischemic preconditioning has been established as effective cardioprotective strategies. Increasing evidence indicates that miRNAs, such as miR-1/106, miR-133, miR-21, miR-320, miR-199a and miR-92a, are also implicated in ischemic cardiac disease. We have recently shown that miR-1 level is markedly elevated in ischemic myocardium where apoptotic cell death plays an important role in the detrimental changes of the diseased heart[31]. Coincidently, another study from our laboratories revealed a novel aspect of cellular functions of the muscle-specific miRNAs miR-1 and miR-133, *ie* regulation of apoptosis and survival in cardiomyocytes. A unique feature of this regulation is the opposing actions with miR-1 being pro-apoptotic and miR-133 being anti-apoptotic, suggesting a possible role of relative miR-1 and miR-133 levels in regulating the cell fate. Post-transcriptional repression of heat shock protein 60 and heat shock protein 70 by miR-1 and of caspase 9 by miR-133 is probably one of the mechanisms underlying their regulation of apoptosis versus survival[44]. Our results therefore suggest that the ischemic elevation of miR-1 level may contribute to the enhanced apoptotic cell death in myocardial infarction, in addition to the enhanced arrhythmogenicity. This conception was proven by two studies from other researchers. Yu *et al*[45] reported that miR-1 is a key mediator of glucose induced apoptosis[46] and suppression of insulin-like growth factor-1 expression represents a new mechanism underlying its proapoptotic action. Furthermore, we found that miR-1 also participates in the regulation of beta-blocker produced cardioprotection[47]. Administration of propranolol reversed the up-regulation of miR-1 nearly back to the control level during ischemia, which then lead to relieving of myocardial injury by restoring the membrane depolarization and cardiac conduction slowing, and rescuing the expression of inward rectifying K^+ channel subunit Kir2.1 and gap junction channel connexin 43 (Figure 1).

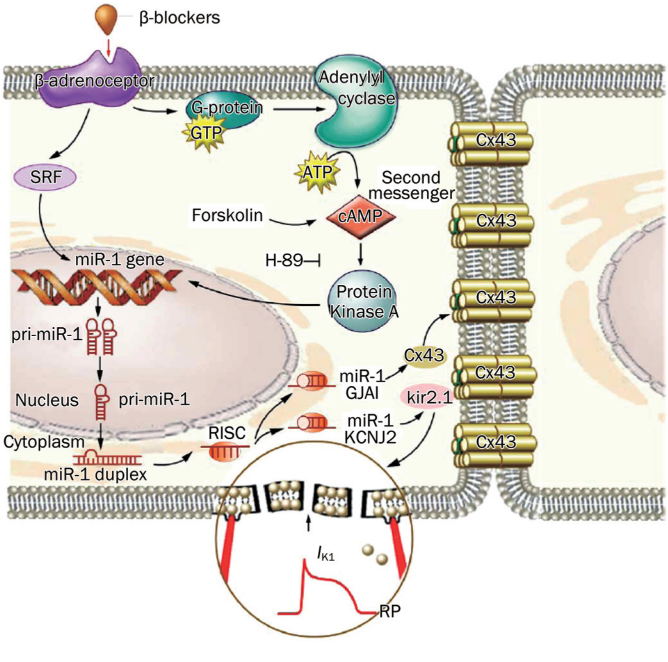

Figure 1. Summary of beta-adrenergic blocker produced protective effects against ischemic arrhythmias and cardiac injury[47]. Beta-blockers reduced miR-1 level via inhibiting beta-adrenoceptor-cAMP-PKA pathway and a transcriptional factor-serum response factor (SRF), which led to up-regulated expression of Cx43 formed gap junctions and inward rectifier potassium channels (I_{K1}).

Another miRNA, miR-21, was found to prevent cell damage subjected to H_2O_2, which mimics the pathological condition of high levels of reactive oxygen species (ROS) that act as an important inducer of cardiac cell injury[48]. Consistently, another study proved that miR-21 demonstrated a significant increase in mice heart subjected to cytoprotective heat-shock (HS). Moreover, overexpression of chemically synthesized miR-21 reduced infarct size which was associated with the inhibition of pro-apoptotic genes and increase in anti-apoptotic genes, whereas a miR-21 inhibitor abolished this effect[49]. In a mouse model of myocardial infarction, systemic administration of an antagomiR designed to inhibit miR-92a resulted in enhanced blood vessel growth and functional recovery of damaged tissue[50]. miR-92a appears to target mRNAs corresponding to several pro-angiogenic proteins, including the integrin subunit alpha5[50]. Ren *et al*[51] demonstrated that miR-320 is involved in the regulation of ischemia/reperfusion (I/R)-induced cardiac injury and dysfunction via antithetical regulation of Hsp20. Transgenic overexpression of miR-320 increased apoptosis and infarction size in the hearts on I/R, whereas in vivo treatment with antagomir-320 reduced infarction size relative to the administration of mutant antagomir-320 and saline controls. These studies not only elucidated the complex molecular mechanisms of cardiac injury in a new level, but also presented valuable therapeutic targets in the setting of ischemic disease.

miRNA and vascular disease

Aberrant proliferation of vascular smooth muscle cells (VSMCs) and the formation of neointimal lesion is a key pathological process of a variety of proliferative vascular diseases, such as atherosclerosis, coronary heart diseases, post-angioplasty restenosis and transplantation arteriopathy[52]. Recently, Zhang's group demonstrated the regulative role of miRNAs including miR-21, miR-221, and miR-222 in the process of aberrant VSMCs proliferation[53, 54]. They found that miR-21, miR-221, and miR-222 were significantly upregulated in carotid arteries after angioplasty. Depletion of the aberrantly overexpressed miR-21, miR-221, or miR-222, via antisense-mediated knockdown, has a significantly negative effect on neointimal lesion formation in rat artery after angioplasty, while forced overexpression of these miRNAs promotes VSMCs proliferation. They further confirmed that PTEN and Bcl-2, two important signal molecules associated with VSMC growth and apoptosis, are the targets of miR-21, through which miR-21 exerts its function[53]. They then elucidated that p27(Kip1) and p57(Kip2) are related to miR-221– and miR-222–mediated effect on VSMC proliferation, as in the VSMCs deficient of these genes the inhibitory effect of miR-221 and miR-222 on VSMC proliferation is decreased[54]. These results indicate that miRNAs are important regulators in the development of proliferative vascular diseases and the potential therapeutic targets in vascular diseases.

MiRNAs based therapeutic strategies

The recent studies on the role of miRNAs in cardiovascular diseases imply: (1) miRNAs are key regulators of a variety of cardiovascular diseases, including hypertrophy, heart failure, cardiac injury, arrhythmia and asthersclerosis etc; (2) Down- or up-regulation of one particular miRNA is enough to cause the pathogenesis of specific cardiovascular disease, which can be reversed by correcting the aberrant expressed miRNA, indicating the potential of miRNAs as pharmacological targets. Therefore, approaches to manipulate either positively or negatively the expression of miRNAs can be taken for therapeutic purposes. For those miRNAs that are downregulated under disease states, forced miRNA re-expression strategy is used to recover miRNA expression, whereas for those miRNAs upregulated, anti-miRNA strategy is employed to suppress their expression.

miRNA re-expression strategy

To recover the decreased miRNA levels in cardiovascular diseases and thus prevent the pathological process, the exogenous miRNAs either synthesized artificially or constructed in virus vectors have been often used in previous studies to achieve optimistic outcomes[24, 41]. Generally, these miRNAs are double-stranded and have the same sequence as endogenous miRNAs.

However, as one miRNA can target hundreds of mRNAs, the inhibitory action of a particular miRNA can be nonspecific and the off-target effect by an exogenous miRNA seems inevitable. In order to circumvent the problem of non-gene specificity of miRNA actions, a technology named miRNA Mimic technology was developed, which utilizes synthetic, non-natural nucleic acids that can bind to the unique sequence of target mRNAs in a gene-specific manner and elicits post-transcriptional regulatory effects as a miRNA does[55]. A miRNA mimic must be complementary to, only to, the 3’UTR of the target gene to elicit miRNA action, that is repressing the target gene at the post-transcriptional level with minimal effects on the mRNA level. Meanwhile, the 3’UTR of the target gene must contain a unique sequence distinct from other genes to elicit gene-specific action. This technique was successfully verified by applying it to cardiac pacemaker genes HCN2 and HCN4[55]. After identifying a stretch of sequence in the 3’UTR unique to the HCN2 (or HCN4) gene that is expectedly long enough for miRNA action, a 22-nt miRNA mimic complementary to the HCN2 (or HCN4) sequence was designed, which has eight nucleotides (nucleotides 2–8) at the 5′ end, and seven nucleotides at the 3’end. These miRNA mimics substantially repressed HCN channel protein expression, with concomitant depression of pacemaker activities and reduction of heart rate but with minimal effects on their mRNA levels. The results demonstrated a promise of utilizing the technology for gene-specific repression of expression at the protein level based on the principle of miRNA actions.

Anti-miRNA strategy

For those miRNAs that are aberrantly upregulated and play a causal role in disease states, the anti-miRNA techniques that suppress their expression should be employed. Inhibiting of miRNAs expression can be achieved by using antisense inhibitor oligonucleotides (AMO) technique. AMOs are artificially designed oligonucleotides fully complementary to their target miRNAs, which act to breakdown the targeted miRNAs with unknown mechanisms. AMOs are a necessary tool for studying miRNAs and have also been proposed as potential therapeutic agents[56, 57]. The function of a series of AMOs has been investigated in cardiovascular diseases, and demonstrated favorable therapeutic results[28, 31, 36]. The application of AMOs, to some extent, possesses similar characteristics to that of gene therapy.

Delivery method is a key obstacle that must be overcome before AMOs can be used clinically. To increase the tissue uptake of AMOs, cholesterol moieties that facilitate cell penetration can be attached to AMOs to form “antagomiRs”, which can strongly inhibit the expression of target miRNAs after *in vivo* application[58]. More strikingly, the studies have validated the therapeutic effects of antagomiR in cardiac hypertrophy[28] and infarction[40, 41, 50] by intravenous bolus injection, indicating its promising clinical application perspective.

As one miRNA may act on multiple targets, its inhibitor AMO can also influence the expression of a large number of proteins leading to non-gene-specific action and “off-target” effects. To tackle this problem, a technique termed miRNA-masking antisense oligodeoxynucleotides (miR-Mask) was developed[55], which was validated by testing its application to the cardiac pacemaker channel encoding genes HCN2 and HCN4. One of the major advantages of this technology is that it offers a gene-specific miRNA-interfering strategy. A miR-Mask is designed to be exactly antisense to the binding site for a given miRNA in the target mRNA, which can form duplex with the target mRNA. In this way, the miR-Mask acts as a target protector masking the binding site to stop the action of that miRNA. A recent study[59] confirmed the efficiency of this technology in which the authors investigated the role of zebrafish miR-430 in regulating expression of TGF-Nodal agonist squint and antagonist lefty, the key regulators of mesendoderm induction and left-right axis formation. They designed target protector morpholinos complementary to miRNA binding sites in target mRNAs in order to disrupt the interaction of specific miRNA-mRNA pairs. Protection of squint or lefty mRNAs from miR-430 resulted in enhanced or reduced Nodal signaling, respectively[59].

Another innovative approach termed “miRNA sponges” was invented by Ebert *et al*[60]. The idea behind it is to produce a single piece of RNAs containing multiple, tandem-binding sites for a miRNA seed family of interest, in order to target all members of that miRNA seed family, taking advantage of the fact that the interaction between miRNA and target is nucleated by and largely dependent on base pairing in the seed region (positions 2–8 of the miRNA). The authors constructed sponges by inserting tandemly arrayed miRNA binding sites into the 3'UTR of a reporter gene encoding destabilized green fluorescent protein driven by the cytomegalovirus promoter, which can yield abundant expression of the competitive inhibitor transcripts. Binding sites for a particular miRNA seed family were perfectly complementary in the seed region with a bulge at positions 9–12 to prevent RNA-interference-type cleavage and degradation of the sponge RNA. When vectors encoding these miRNA sponges are transiently transfected into cultured cells, they depress miRNA targets as strongly as the conventional AMOs. The major advancement of this technique over the AMO technique is that it can better inhibit functional classes of miRNAs than do AMOs that are designed to block single miRNA sequences.

It has become clear that a particular condition may be associated with multiple miRNAs, *eg* miR-29 and miR-21 in cardiac fibrosis and a given gene may be regulated by multiple miRNAs. Thus, simultaneously targeting multiple miRNAs relevant to a particular condition may offer an improved approach than targeting a single miRNA. To investigate this possibility, we developed an innovative strategy, the multiple-target AMO (MT-AMO) technology, which confers a single AMO fragment the capability of targeting multiple miRNAs[61]. We have validated the technique with two separate MTg-AMOs: anti-miR-21/anti-miR-155/anti-miR-17-5p and antimiR-1/anti-miR-133[61]. The MTg-AMO targeting miR-21, miR-155 and miR-17-5p produced a greater inhibitory effect on cancer cell growth, compared with the regular single-target AMOs. Moreover, while using the regular single-target AMOs excluded HCN2 as a target gene for either miR-1 or miR-133, the MTg-AMO approach is able to reveal HCN2 as the target for both miR-1 and miR-133[61].

Perspectives and limitations

miRNAs are a group of key regulators that modulate the development of various diseases, including cardiovascular diseases. Some individual miRNAs can dictate the pathogenesis of a specific disease, such as cardiac hypertrophy, arrhythmias, ischemia and atherosclerosis, *etc*. Moreover, manipulating the expression of the disease-causing miRNAs can prevent the disease progression, strongly indicating the therapeutic potential of miRNAs. Furthermore, several miRNA manipulation techniques have been created to accomplish “gain-of-function” or “loss-of-function” management on miRNA expression. The constructs designed based on these techniques have all demonstrated their efficacy in treating cardiovascular disease, which makes miRNAs step closer to clinical therapeutic application. Thus, it is not surprising that miRNAs have been continually attracting attention of researchers from nearly every areas of life sciences, which will inevitably impel the progress in miRNA biology and therapy. Additionally, miRNAs have also demonstrated their potential as diagnostic and prognostic markers[62]. Recent evidence supports the use of specific miRNA signatures to predict clinical outcomes of relevant conditions[62]. Our pervious work has validated miR-1 as a proarrhythmic miRNA in ischemic heart disease[31]. In a recent study, we found that the serum miR-1 level is closely linked to the severity of cardiac infarction and the occurrence of lethal arrhythmias in coronary artery disease patients (unpublished data), which represents a new diagnostic marker.

However, we have merely made a first step towards the application of miRNA-interfering technologies. We still face many unanswered questions and unsolved problems. First, as a particular disease condition may be associated with multiple miRNAs, and a given gene may be regulated by multiple miRNAs. Thus, interactions between miRNAs may have impact on the protein expression of the target genes and may complicate the potential role of miRNA as therapeutic targets in cardiovascular disease. We should further validate the specificity of the established miRNA targets before application. Second, the detailed molecular mechanism under which miRNAs regulate cardiovascular diseases still requires further eludicitation. Third, the biggest obstable on the way to miRNA-based clinical therapy is how to efficiently deliver miRNA mimics and inhibitors to the target organs. Not until we will have had rational answers to these questions after rigorous fundamental and clinical studies, will we have better ideas about miRNAs as targets for the development of therapeutic agents for cardiovascular disease.

Acknowledgements

This work was supported by the National Basic Research Program of China (973 Program; 2007CB512000/2007CB512006) awarded to Prof Bao-feng YANG.

References

1 Lai EC. Micro RNAs are complementary to 3'UTR sequence motifs that mediate negative post-transcriptional regulation. Nat Genet 2002; 30: 363−4.
2 Wightman B, Ha I, Ruvkun G. Posttranscriptional regulation of the heterochronic gene lin-14 by lin-4 mediates temporal pattern formation in *C elegans*. Cell 1993; 75: 855−62.
3 Pasquinelli AE, Reinhart BJ, Slack F, Martindale MQ, Kuroda MI, Maller B, *et al*. Conservation of the sequence and temporal expression of let-7 heterochronic regulatory RNA. Nature 2000; 408: 86−9.
4 Chua JH, Armugam A, Jeyaseelan K. MicroRNAs: biogenesis, function and applications. Curr Opin Mol Ther 2009; 11: 189−99.
5 Li M, Marin-Muller C, Bharadwaj U, Chow KH, Yao Q, Chen C. MicroRNAs: control and loss of control in human physiology and disease. World J Surg 2009; 33: 667−84.
6 Wang Z, Luo X, Lu Y, Yang B. miRNAs at the heart of the matter. J Mol Med 2008; 86: 771−83.
7 Latronico MV, Catalucci D, Condorelli G. Emerging role of microRNAs in cardiovascular biology. Circ Res 2007; 101: 1225−36.
8 Latronico MV, Condorelli G. MicroRNAs and cardiac pathology. Nat Rev Cardiol 2009; 6: 419−29.
9 Lee Y, Jeon K, Lee JT, Kim S, Kim VN. MicroRNA maturation: stepwise processing and subcellular localization. EMBO J 2002; 21: 4663−70.
10 Lee Y, Kim M, Han J, Yeom KH, Lee S, Baek SH, *et al*. MicroRNA genes are transcribed by RNA polymerase II. EMBO J 2004; 23: 4051−60.
11 Kim VN. MicroRNA precursors in motion: exportin-5 mediates their nuclear export. Trends Cell Biol 2004; 14: 156−9.
12 Peters L, Meister G. Argonaute proteins: mediators of RNA silencing. Mol Cell 2007; 26: 611−23.
13 Liu J, Valencia-Sanchez MA, Hannon GJ, Parker R. MicroRNA-dependent localization of targeted mRNAs to mammalian P-bodies. Nat Cell Biol 2005; 7: 719−23.
14 Brennecke J, Stark A, Russell RB, Cohen SM. Principles of microRNA-target recognition. PLoS Biol 2005; 3: e85.
15 Nilsen TW. Mechanisms of microRNA-mediated gene regulation in animal cells. Trends Genet 2007; 23: 243-9.

16 Lewis BP, Shih IH, Jones-Rhoades MW, Bartel DP, Burge CB. Prediction of mammalian microRNA targets. Cell 2003; 115: 787−98.

17 Miranda KC, Huynh T, Tay Y, Ang YS, Tam WL, Thomson AM, *et al*. A pattern-based method for the identification of MicroRNA binding sites and their corresponding heteroduplexes. Cell 2006; 126: 1203−17.

18 McKinsey TA, Olson EN. Toward transcriptional therapies for the failing heart: chemical screens to modulate genes. J Clin Invest 2005; 115: 538−46.

19 van Rooij E, Sutherland LB, Qi X, Richardson JA, Hill J, Olson EN. Control of stress-dependent cardiac growth and gene expression by a microRNA. Science 2007; 316: 575−9.

20 van Rooij E, Sutherland LB, Liu N, Williams AH, McAnally J, Gerard RD, *et al*. A signature pattern of stress-responsive microRNAs that can evoke cardiac hypertrophy and heart failure. Proc Natl Acad Sci USA 2006; 103: 18255−60.

21 Thum T, Galuppo P, Wolf C, Fiedler J, Kneitz S, van Laake LW, *et al*. MicroRNAs in the human heart: a clue to fetal gene reprogramming in heart failure. Circulation 2007; 116: 258−67.

22 Tatsuguchi M, Seok HY, Callis TE, Thomson JM, Chen JF, Newman M, *et al*. Expression of microRNAs is dynamically regulated during cardiomyocyte hypertrophy. J Mol Cell Cardiol 2007; 42: 1137−41.

23 Sucharov C, Bristow MR, Port JD. miRNA expression in the failing human heart: functional correlates. J Mol Cell Cardiol 2008; 45: 185−92.

24 Sayed D, Hong C, Chen IY, Lypowy J, Abdellatif M. MicroRNAs play an essential role in the development of cardiac hypertrophy. Circ Res 2007; 100: 416−24.

25 Ikeda S, He A, Kong SW, Lu J, Bejar R, Bodyak N, *et al*. MicroRNA-1 negatively regulates expression of the hypertrophy-associated calmodulin and Mef2a genes. Mol Cell Biol 2009; 29: 2193−204.

26 da Costa Martins PA, Bourajjaj M, Gladka M, Kortland M, van Oort RJ, Pinto YM, *et al*. Conditional dicer gene deletion in the postnatal myocardium provokes spontaneous cardiac remodeling. Circulation 2008; 118: 1567−76.

27 Cheng Y, Ji R, Yue J, Yang J, Liu X, Chen H, *et al*. MicroRNAs are aberrantly expressed in hypertrophic heart: do they play a role in cardiac hypertrophy? Am J Pathol 2007; 170: 1831−40.

28 Care A, Catalucci D, Felicetti F, Bonci D, Addario A, Gallo P, *et al*. MicroRNA-133 controls cardiac hypertrophy. Nat Med 2007; 13: 613−8.

29 Callis TE, Pandya K, Seok HY, Tang RH, Tatsuguchi M, Huang ZP, *et al*. MicroRNA-208a is a regulator of cardiac hypertrophy and conduction in mice. J Clin Invest 2009; 119: 2772−86.

30 Lin Z, Murtaza I, Wang K, Jiao J, Gao J, Li PF. miR-23a functions downstream of NFATc3 to regulate cardiac hypertrophy. Proc Natl Acad Sci USA 2009; 106: 12103–8.

31 Yang B, Lin H, Xiao J, Lu Y, Luo X, Li B, *et al*. The muscle-specific microRNA miR-1 regulates cardiac arrhythmogenic potential by targeting GJA1 and KCNJ2. Nat Med 2007; 13: 486−91.

32 Anderson ME, Mohler PJ. MicroRNA may have macro effect on sudden death. Nat Med 2007; 13: 410–1.

33 Terentyev D, Belevych AE, Terentyeva R, Martin MM, Malana GE, Kuhn DE, *et al*. MiR-1 overexpression enhances Ca^{2+} release and promotes cardiac arrhythmogenesis by targeting PP2A regulatory subunit B56alpha and causing CaMKII-dependent hyperphosphorylation of RyR_2. Circ Res 2009; 104: 514−21.

34 Shan H, Zhang Y, Lu Y, Pan Z, Cai B, Wang N, *et al*. Downregulation of miR-133 and miR-590 contributes to nicotine-induced atrial remodelling in canines. Cardiovasc Res 2009; 83: 465−72.

35 Goette A. Nicotine, atrial fibrosis, and atrial fibrillation: do microRNAs help to clear the smoke? Cardiovasc Res 2009; 83: 421−22.

36 Luo X, Lin H, Pan Z, Xiao J, Zhang Y, Lu Y, *et al*. Down-regulation of miR-1/miR-133 contributes to re-expression of pacemaker channel genes HCN2 and HCN4 in hypertrophic heart. J Biol Chem 2008; 283: 20045−52.

37 Xiao J, Luo X, Lin H, Zhang Y, Lu Y, Wang N, *et al*. MicroRNA miR-133 represses HERG K^+ channel expression contributing to QT prolongation in diabetic hearts. J Biol Chem 2007; 282: 12363−7.

38 Luo X, Xiao J, Lin H, Li B, Lu Y, Yang B, *et al*. Transcriptional activation by stimulating protein 1 and post-transcriptional repression by muscle-specific microRNAs of IKs-encoding genes and potential implications in regional heterogeneity of their expressions. J Cell Physiol 2007; 212: 358−67.

39 Zhao Y, Ransom JF, Li A, Vedantham V, von Drehle M, Muth AN, *et al*. Dysregulation of cardiogenesis, cardiac conduction, and cell cycle in mice lacking miRNA-1-2. Cell 2007; 129: 303−17.

40 van Rooij E, Sutherland LB, Thatcher JE, DiMaio JM, Naseem RH, Marshall WS, *et al*. Dysregulation of microRNAs after myocardial infarction reveals a role of miR-29 in cardiac fibrosis. Proc Natl Acad Sci USA 2008; 105: 13027−32.

41 Thum T, Gross C, Fiedler J, Fischer T, Kissler S, Bussen M, *et al*. MicroRNA-21 contributes to myocardial disease by stimulating MAP kinase signalling in fibroblasts. Nature 2008; 456: 980−4.

42 Roy S, Khanna S, Hussain SR, Biswas S, Azad A, Rink C, *et al*. MicroRNA expression in response to murine myocardial infarction: miR-21 regulates fibroblast metalloprotease-2 via phosphatase and tensin homologue. Cardiovasc Res 2009; 82: 21−9.

43 Duisters RF, Tijsen AJ, Schroen B, Leenders JJ, Lentink V, van der Made I, *et al*. miR-133 and miR-30 regulate connective tissue growth factor: implications for a role of microRNAs in myocardial matrix remodeling. Circ Res 2009; 104: 170−8, 6p following 178.

44 Xu C, Lu Y, Pan Z, Chu W, Luo X, Lin H, *et al*. The muscle-specific microRNAs miR-1 and miR-133 produce opposing effects on apoptosis by targeting HSP60, HSP70 and caspase-9 in cardiomyocytes. J Cell Sci 2007; 120: 3045−52.

45 Shan ZX, Lin QX, Fu YH, Deng CY, Zhou ZL, Zhu JN, *et al*. Upregulated expression of miR-1/miR-206 in a rat model of myocardial infarction. Biochem Biophys Res Commun 2009; 381: 597−601.

46 Yu XY, Song YH, Geng YJ, Lin QX, Shan ZX, Lin SG, *et al*. Glucose induces apoptosis of cardiomyocytes via microRNA-1 and IGF-1. Biochem Biophys Res Commun 2008; 376: 548−52.

47 Lu Y, Zhang Y, Shan H, Pan Z, Li X, Li B, *et al*. MicroRNA-1 downregulation by propranolol in a rat model of myocardial infarction: a new mechanism for ischemic cardioprotection. Cardiovasc Res 2009; 84: 434–41.

48 Cheng Y, Liu X, Zhang S, Lin Y, Yang J, Zhang C. MicroRNA-21 protects against the H_2O_2-induced injury on cardiac myocytes via its target gene PDCD4. J Mol Cell Cardiol 2009; 47: 5−14.

49 Yin C, Wang X, Kukreja RC. Endogenous microRNAs induced by heat-shock reduce myocardial infarction following ischemia-reperfusion in mice. FEBS Lett 2008; 582: 4137−42.

50 Bonauer A, Carmona G, Iwasaki M, Mione M, Koyanagi M, Fischer A, *et al*. MicroRNA-92a controls angiogenesis and functional recovery of ischemic tissues in mice. Science 2009; 324: 1710−3.

51 Ren XP, Wu J, Wang X, Sartor MA, Qian J, Jones K, *et al*. MicroRNA-320 is involved in the regulation of cardiac ischemia/reperfusion injury by targeting heat-shock protein 20. Circulation 2009; 119: 2357−66.

52 Zhang C. MicroRNAs: role in cardiovascular biology and disease. Clin Sci (Lond) 2008; 114: 699−706.

53 Ji R, Cheng Y, Yue J, Yang J, Liu X, Chen H, *et al*. MicroRNA expression signature and antisense-mediated depletion reveal an essential role of MicroRNA in vascular neointimal lesion formation. Circ Res 2007;

100: 1579−88.

54 Liu X, Cheng Y, Zhang S, Lin Y, Yang J, Zhang C. A necessary role of miR-221 and miR-222 in vascular smooth muscle cell proliferation and neointimal hyperplasia. Circ Res 2009; 104: 476−87.

55 Xiao J, Yang B, Lin H, Lu Y, Luo X, Wang Z. Novel approaches for gene-specific interference via manipulating actions of microRNAs: examination on the pacemaker channel genes HCN2 and HCN4. J Cell Physiol 2007; 212: 285−92.

56 Chan JA, Krichevsky AM, Kosik KS. MicroRNA-21 is an antiapoptotic factor in human glioblastoma cells. Cancer Res 2005; 65: 6029−33.

57 Cheng AM, Byrom MW, Shelton J, Ford LP. Antisense inhibition of human miRNAs and indications for an involvement of miRNA in cell growth and apoptosis. Nucleic Acids Res 2005; 33: 1290−7.

58 Krutzfeldt J, Rajewsky N, Braich R, Rajeev KG, Tuschl T, Manoharan M, *et al*. Silencing of microRNAs *in vivo* with 'antagomirs'. Nature 2005; 438: 685−9.

59 Choi WY, Giraldez AJ, Schier AF. Target protectors reveal dampening and balancing of Nodal agonist and antagonist by miR-430. Science 2007; 318: 271–4.

60 Ebert MS, Neilson JR, Sharp PA. MicroRNA sponges: competitive inhibitors of small RNAs in mammalian cells. Nat Methods 2007; 4: 721−6.

61 Lu Y, Xiao J, Lin H, Bai Y, Luo X, Wang Z, *et al*. A single anti-microRNA antisense oligodeoxyribonucleotide (AMO) targeting multiple microRNAs offers an improved approach for microRNA interference. Nucleic Acids Res 2009; 37: e24.

62 Vandenboom Ii TG, Li Y, Philip PA, Sarkar FH. MicroRNA and cancer: tiny molecules with major implications. Curr Genomics 2008; 9: 97−109.

npg
Acta Pharmacologica Sinica (2010) 31: 10–18
© 2010 CPS and SIMM All rights reserved 1671-4083/10 $32.00
www.nature.com/aps

Original Article

Krüppel-like factor (KLF) 5 mediates cyclin D1 expression and cell proliferation via interaction with c-Jun in Ang II-induced VSMCs

Yu LIU, Jin-kun WEN, Li-hua DONG, Bin ZHENG, Mei HAN*

Department of Biochemistry and Molecular Biology, Institute of Basic Medicine, Hebei Medical University, Shijiazhuang 050017, China

Aim: To elucidate how krüppel-like factor (KLF5) activates cyclin D1 expression in Ang II-induced vascular smooth muscle cells (VSMC) proliferation.
Methods: An adenoviral vector containing the full-length cDNA of KLF5 and a recombinant plasmid expressing c-Jun were constructed. MTT assay and flow cytometric analysis were used to determine the effect of Ang II on cell growth. The luciferase assay and chromatin immunoprecipitation were used to detect the relationship between KLF5 and c-Jun in transactivation of cyclin D1 gene expression.
Results: Ang II upregulated the expression of KLF5 with concurrent acceleration of the cell cycle progression in VSMCs. Ang II induced KLF5 activation via the ERK and p38 MAPK pathways triggered by AT-1 receptor. High DNA binding activity and functional interaction of KLF5 and c-Jun were found in Ang II-induced VSMCs. Cotransfection of KLF5 and c-Jun expression vectors significantly increased cyclin D1 promoter activity.
Conclusion: KLF5 is a downstream signal of the ERK 1/2 and p38 MAPK pathways, and activates the transcription of cyclin D1 gene via functional interaction with c-Jun in Ang II-induced VSMC proliferation.

Keywords: Krüppel-like factor 5; cyclin D1; angiotensin II; proliferation; vascular smooth muscle cells

Acta Pharmacologica Sinica (2010) 31: 10–18; doi: 10.1038/aps.2009.185; published online 28 December 2009

Introduction

Multiple lines of experimental and clinical evidence indicate that angiotensin II (Ang II) not only induces hypertension, but also directly contributes to pathophysiological vascular thickening and atherosclerosis in humans[1]. A large number of studies of the functions of Ang II *in vitro* and *in vivo* have indicated that Ang II activates multiple intracellular signaling cascades, such as those mediated by mitogen-activated protein kinase (MAPK), and regulates various transcription factors, and causes cell growth in vascular smooth muscle cells (VSMCs)[1–3]. A growing body of evidence shows that Ang II type 1 (AT-1) receptor but not AT-2 is involved in the signal transduction underlying Ang II-induced VSMC growth[1], such as activation of JNK[4] and p38[5]. However, little is known about the role of these signal cascades in Ang II-induced proliferative response.

Krüppel-like factor 5 (KLF5), a member of the Sp/KLF family of zinc finger factors, is a key regulator of cardiovascular remodeling[6]. One mechanism by which KLF5 accomplishes its proliferative effect is to transcriptionally activate several cell cycle-promoting genes, including cyclin D1, cyclin B1, and Cdc2[7–9]. Our recent study has demonstrated the interaction of KLF5 and c-Jun in Ang II-induced suppression of p21 expression[10]. In view of involvement of KLF5 and cyclin D1 in VSMC proliferation, we hypothesize that KLF5 might be required for Ang II-mediated expression of cyclin D1 and cell proliferation in VSMC.

In this study, we report that KLF5 plays a crucial role in Ang II-induced cyclin D1 expression and proliferation of VSMCs. We show that Ang II induces KLF5 expression and activation via ERK and p38 MAPK pathways. A functional interaction was found between KLF5 and c-Jun, which enhanced the transactivating activity of the both proteins, and consequently led to a synergistic increase in the expression of cyclin D1 gene. These results indicate that KLF5 is a downstream target of the ERK 1/2 and p38 MAPK pathways and enhances the transcriptional ability of cyclin D1 gene to promote proliferation in Ang II-induced VSMCs.

---

* To whom correspondence should be addressed.
E-mail hanmei@hebmu.edu.cn
Received 2009-06-30 Accepted 2009-11-20

Materials and methods

Construction of recombinant plasmids and adenoviral vectors

The pGL3-CD1-Luc luciferase reporter plasmid containing the cyclin D1 promoter (from -1745 to +134) was a generous gift from Dr Richard G PESTELL (Northwestern University Medical School, Chicago, IL). Full-length mouse KLF5 cDNA was cloned into pEGFP-N1 and pAd/CMV/V5-DEST Gateway Vector (Invitrogen, Carlsbad, CA) according to the manufacturer's protocol to obtain the pEGFP-KLF5 and Ad-KLF5 constructs, respectively. To construct the c-Jun expression plasmid, c-Jun cDNA was obtained from the pBIISK(–)-Jun plasmid via *EcoR* I digestion and then inserted into the pcDNA3.1 vector and sequenced. All clones were verified by sequencing (data not shown).

Cell culture and treatment

VSMCs were isolated from the thoracic aorta of 90–110 g male Sprague-Dawley rats as described previously[11]. VSMCs and the COS-7 cell line were grown in low glucose DMEM (Dulbecco's modified Eagle's medium) (Invitrogen), supplemented with 10% FBS (fetal bovine serum) under 5% CO_2 at 37 °C. VSMCs grown to 70% confluence were serum deprived for 24 h, then treated with 10^{-7} mol/L Ang II following pretreatment with or without valsartan (antagonist of AT-1 receptor) and PD123319 (antagonist of AT-2 receptor) (Sigma)[3, 12] in DMEM containing 2% FBS for the indicated time periods.

Transfection and infection

The cultured VSMCs grown to 60% confluence were serum deprived for 24 h and then transfected with rat KLF5-specific siRNA (5'-AACCCGGAUCUGGAGAAGCGA-3') or nonspecific NS-siRNA (5'-GCGCGCUUUGUAGGAUUCG-3')[13] using the Lipofectamine 2000 reagent (Invitrogen), according to the manufacturer's protocol. Twenty hours after transfection, the VSMCs were treated with Ang II (10^{-7} mol/L) or vehicle for 24 h. Alternatively, VSMCs were infected with Ad-KLF5 or empty Ad for 48 h and then treated with Ang II. Cells were then collected for assays, which are described below.

MTT assay

After treatment, the viability of VSMCs cultured in 96-well plates was measured using MTT (3-[4,5-dimehyl-2-thiazolyl]-2, 5-diphenyl-2H-tetrazolium bromide). In brief, after cells were collected and incubated in medium containing 2 mg/mL MTT reagent (Sigma Chemical Co) at 37 °C for 4 h, the formazan crystals converted from tetrazolium salts by viable cells were dissolved in DMSO (200 μL/well) and the absorbance was measured at 570 nm using a microplate reader to reflect cell viability. The experiment was repeated three times.

Cell number assay

Cell count experiments were performed as described previously[14]. Briefly, a suspension of VSMCs (0.5×10^5 cells/mL) was prepared and treated with or without Ang II (10^{-7} mol/L) for different time periods. Cells were counted in a hemocytometer using a light microscope.

Flow cytometric analysis

Cells were plated in 100-mm dishes at a density of 3×10^6 per dish. The medium was removed and pooled with trypsinized adherent cells. Cells were washed and resuspended in cold PBS at a density of $(1–3)\times10^6$ cells/mL, and then 500 μL of propidium iodide (PI) buffer (0.1 mg/mL PI in PBS) and 500 μL of RNase A (2 mg/mL) were added, respectively. After 30 min incubation at room temperature in the dark, cells were filtered through a nylon mesh filter and subjected to flow cytometry.

RNA isolation and reverse transcription (RT)-PCR

Total RNA was isolated from VSMCs using the TRIzol reagent, according to the manufacturer's instructions (Invitrogen, Carlsbad, CA). Reverse transcription was performed with the Superscript First Strand Synthesis System for RT-PCR (Invitrogen, Carlsbad, CA). The cDNA was then used as a template for PCR using specific primers for cyclin D1 (forward, 5'-ACCAATCTCCTCAACGACC-3'; reverse, 5'-TTGTTCTCATCCGCCTCT-3') and β-actin (forward, 5'-CAGGGTGTGATGGTGGG-3'; reverse, 5'-GGAAGAGGATGCGGCAG-3'). The amplified products were separated on a 2% agarose gel containing ethidium bromide, and the band intensities were quantified using the Image J software provided by the NIH.

Western blot and immunoprecipitation

Lysates from VSMCs were prepared with lysis buffer (1% Triton X-100, 150 mmol/L NaCl, 10 mmol/L Tris-HCl, pH 7.4, 1 mmol/L EDTA, 1 mmol/L EGTA, pH 8.0, 0.2 mmol/L Na_3VO_4, 0.2 mmol/L phenylmethylsulfonyl fluoride and 0.5% NP-40). Equal amounts of protein (60~100 μg) were separated via 8% SDS-PAGE and transferred to a PVDF membrane. Membranes were blocked with 5% BSA for 2 h at room temperature and then incubated with anti-KLF5 (1:400), anti-cyclin D1 (1:300), anti-PCNA (1:400), anti-SM22α (1:400) (Santa Cruz), anti-AT-1 (1:400), anti-ERK (1:400), anti-phospho-ERK (1:400), anti-JNK (1:200), anti-phospho-JNK (1:200), anti-p38 MAPK (1:400), anti-phospho-p38 MAPK (1:400) or anti-β-actin (1:1000) antibodies (Cell Signaling) overnight, and then with the HRP-conjugated secondary antibody (1:10 000) for 2 h. Bands were detected using the enhanced chemiluminescence (ECL) detection system. The experiments were repeated three times. Immunoprecipitation was performed as described previously[15]. Briefly, the cell extract was first pre-cleared with protein A-agarose. The supernatant was incubated with 1–2 μg of anti-phospho-Ser or anti-KLF5 antibodies and subsequently incubated with protein A-agarose overnight at 4 °C. Protein A-agarose-antigen-antibody complexes were then analyzed via Western blot as described above. The experiments were repeated at least three times.

Chromatin immunoprecipitation (ChIP) assay

VSMCs were treated with Ang II (10^{-7} mol/L) for 1 h and fixed with 1% formaldehyde. ChIP assays were then performed using 2 μg of anti-KLF5 and anti-c-Jun antibodies (Santa Cruz) as described previously[16]. An aliquot of the cell lysate was used to isolate total DNA. PCR amplification of the immunoprecipitated DNA was performed using the following primers: KLF5, 5′-CACCTTATCGGCTCACACAT-3′ and 5′-GAGACACGATAGGCTCTTTG-3′ (-868~-1094); 5′-GGATAAACCGGTCACTGTAA-3′ and 5′-CCAGACGAGCCCTAAGTTTT-3′ (-538~-801); 5′-CGCTCTTTCCCAGCTTAGA-3′ and 5′-CAACTTCAACAAAACTCCCCT-3′ (-10~-245); AP-1, 5′-CGCTCTTTCCCAGCTTAGA-3′ and 5′-CAACTTCAACAAAACTCCCCT-3′ (-10~-245).

Luciferase assay

COS-7 cells were grown to 70% confluence and then transfected in triplicate with pGL3-CD1-luc, pEGFP-KLF5, pcDNA3.1-c-Jun or pGL3-Basic, along with pRL-TK in the absence of serum medium. Twenty-four hours after transfection, cells were treated with Ang II (10^{-7} mol/L) for 24 h. Cell lysates were harvested and then the luciferase activity was measured with the Dual-Luciferase® Reporter Assay System (Promega, Madison, WI) according to the manufacturer's manual. The relative luciferase activities compared with the luciferase activities of pRL-TK were presented as means±SEM.

Statistical analysis

The experiments were repeated three times with similar results. The data shown are derived from replicated measurements obtained from a single VSMC culture. Data are presented as means±SEM. Statistical analyses were carried out with the SPSS 11.5 statistical software package (Chicago, IL). The primary statistical test used was the one-way ANOVA. $P<0.05$ was considered statistically significant.

Results

Ang II promotes cell cycle progression to stimulate growth of VSMCs

Ang II functions as a growth factor in VSMCs[17]. Thus, we tested the effects of Ang II on VSMC growth. The results from MTT, cell number and flow cytometric analyses, were used to indirectly and directly determine cell viability, were expected to reflect the regulation of cell growth by Ang II. The results of the MTT and cell number assays showed that Ang II treatment caused a concentration-dependent stimulation of VSMC growth at 10^{-8} mol/L and higher. Significant stimulation was observed from the dose of 10^{-7} mol/L Ang II (Figure 1A, 1B). These results indicate that Ang II exerts a growth-stimulating effect on VSMCs. Furthermore, the proliferative effect of Ang II was verified by evaluating the fate of Ang II-treated VSMCs with regard to cell cycle progression. Cells were synchronized via 24-h serum starvation and then induced by treatment with Ang II to re-enter the cell cycle. Flow cytometric analysis was performed after propidium iodide staining. After 24 h of treatment, Ang II significantly reduced the proportion of cells in the G_0/G_1-phase, and increased the proportion of S-phase cells in a dose-dependent fashion (10^{-8}–10^{-6} mol/L; Figure 1C). The level of proliferating cell nuclear antigen (PCNA), a marker of cell growth, paralleled the number of cells that re-entered the cell cycle, while the level of SM22α (a marker of differentiated VSMCs) inversely correlated with this number (Figure 1D). These results suggest that Ang II promotes cell cycle progression to stimulate growth of VSMCs.

KLF5 is involved in Ang II-induced cyclin D1 expression and VSMC proliferation

Cyclin D1 is a growth sensor that is induced by growth factors and mitogens to accelerate G_1 progression[18]. To investigate the observed G_1-phase progression after Ang II treatment, we first examined the effect of Ang II on cyclin D1 expression. In VSMCs, the amounts of cyclin D1 protein detected via Western blot analysis gradually increased with increasing doses of Ang II (Figure 2A). To determine the mechanism of cyclin D1 induction, total RNA was isolated from VSMCs, and RT-PCR was performed. Ang II (10^{-7} mol/L) induced the expression of cyclin D1 at the mRNA level in a time-dependent manner, with a maximum of a 4-fold increase at 12 h, and maintenance at this level at least for 24 h, with concurrent changes in the level of cyclin D1 protein expression (Figure 2).

KLF5 has previously been shown to increase cell growth and cell cycle progression in NIH3T3 cells by accelerating both the G_1/S transition and entry into mitosis[8, 9]. To investigate whether KLF5 is involved in Ang II-induced cyclin D1 expression and cell proliferation, the level of KLF5 protein in VSMCs was detected via Western blot analysis following Ang II treatment. As shown in Figure 2B, Ang II increased KLF5 protein levels in a dose-dependent manner, which correlated with Ang II-induced cell proliferation and cyclin D1 expression. The level of KLF5 protein began to increase at 3 h after Ang II treatment, peaked at a maximum of 4-fold at 12 h, and declined thereafter, consistant with cyclin D1 expression profiles.

To confirm the role of KLF5 in Ang II-induced cyclin D1 expression and cell proliferation, VSMCs were infected with Ad-KLF5 to overexpress KLF5 or with KLF5-specific siRNA to knockdown endogenous KLF5 expression (Figure 2C). Overexpression of KLF5 increased endogenous cyclin D1 protein levels (Figure 2C). As shown in Figure 2D, in response to Ang II, the level of KLF5 protein was significantly attenuated in VSMCs transfected with KLF5-specific siRNA as compared to cells transfected with non-specific siRNA (NS-siRNA). Similarly, KLF5-specific siRNA abolished Ang II–induced cyclin D1 protein expression. However, these changes were not observed in the cells treated with NS-siRNA. MTT and flow cytometric analysis showed that KLF5 overexpression resulted in increased proliferation, and a reduction in the proportion of cells in the G_0/G_1-phase, compared with empty vector controls. In addition, knockdown of KLF5 expression dramatically reduced cell growth and the number of S-phase cells, even after Ang II treatment (Figure 2E, F), indicating that KLF5 is critical for Ang II-mediated VSMC proliferation. Taken together, KLF5 is required for both Ang II-induced cyclin D1 expression and VSMC proliferation.

Ang II induces KLF5 activation via the ERK 1/2 and p38 MAPK pathways

Protein phosphorylation plays a major role in modulating the

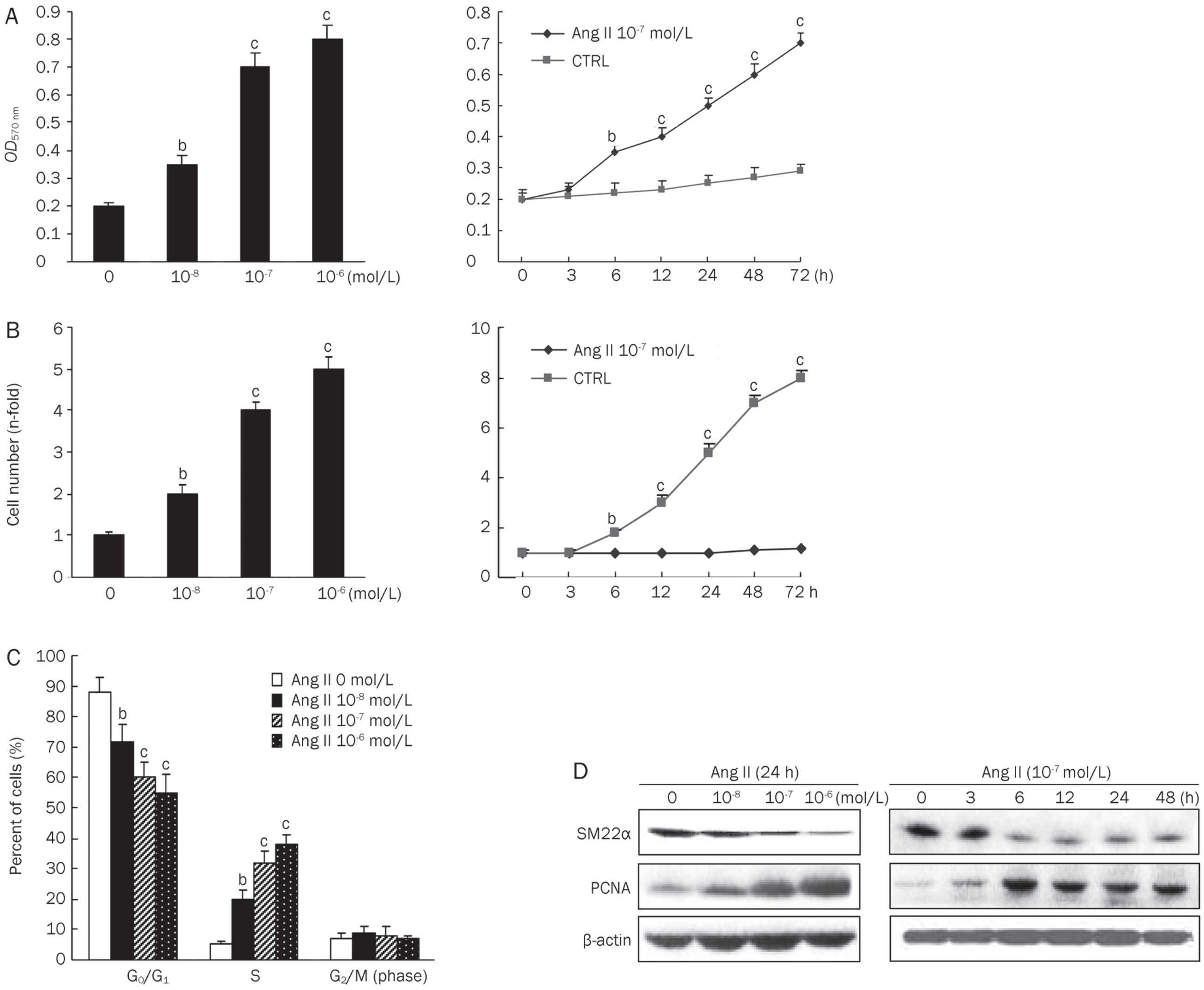

Figure 1. Ang II promotes cell cycle progression to stimulate growth of VSMCs. (A and B) VSMC proliferation induced by Ang II was tested using MTT (A) or cell number (B) assays. ${}^{b}P<0.05$, ${}^{c}P<0.01$ *vs* PBS control. (C) Cell cycle of VSMCs was tested by flow cytometric analysis. ${}^{b}P<0.05$, ${}^{c}P<0.01$ *vs* PBS control. (D) Expression of PCNA and SM22α in VSMCs was detected by Western blotting. β-actin was used as an internal control.

activity of transcription factors[19]. As Ang II induced both KLF5 and cyclin D1 expression in same profile manner, KLF5-mediated cyclin D1 expression may result from KLF5 activation but not its expression. For this, the phosphorylation status of KLF5 was tested via cross-immunoprecipitation using anti-phospho-Ser and anti-KLF5 antibodies. As shown in Figure 3A, Ang II effectively increased the level of phosphorylated KLF5, and effect that was significant at 0.5 h and peaked at 1 h. In contrast, Ang II treatment had little influence on total KLF5 protein levels. Ang II regulates cell growth through ERK 1/2, which is a key mediator of growth[20]. ERK 1/2 mediates the transmission of signals elicited by extracellular stimuli acting on plasma membrane proteins to the nucleus by phosphorylating and activating a variety of transcription factors. KLF5 has been shown to be phosphorylated by ERK 1/2[9]. To determine whether ERK 1/2 is involved in KLF5 phosphorylation in VSMCs stimulated by Ang II, the phosphorylation of three MAPKs (ERK 1/2, JNK, and p38 MAPK) in response to Ang II treatment was analyzed via Western blot, using specific anti-phospho-kinase antibodies. After treatment of VSMCs with Ang II, phosphorylated ERK 1/2 and phosphorylated p38 MAPK increased and reached a maximum at 15 min, and then decreased gradually within 30 min after treatment, while phosphorylated JNK levels did not change (Figure 3B). Importantly, blockade of ERK activity with PD98059 and p38 MAPK using SB203580 depressed both Ang II–induced KLF5 phosphorylation and cyclin D1 protein expression (Figure 3C), indicating that either ERK 1/2 or p38 MAPK are involved in Ang II-induced KLF5 activation. To address the role of either AT-1 or AT-2 receptors in Ang II-induced KLF5 phosphorylation and cell proliferation, VSMCs were pretreated by AT-1 antagonist valsartan and AT-2 antagonist PD123319, respectively, and then stimulated by Ang II. The KLF5 phosphorylation induced by Ang II was abolished in valsartan-pretreated

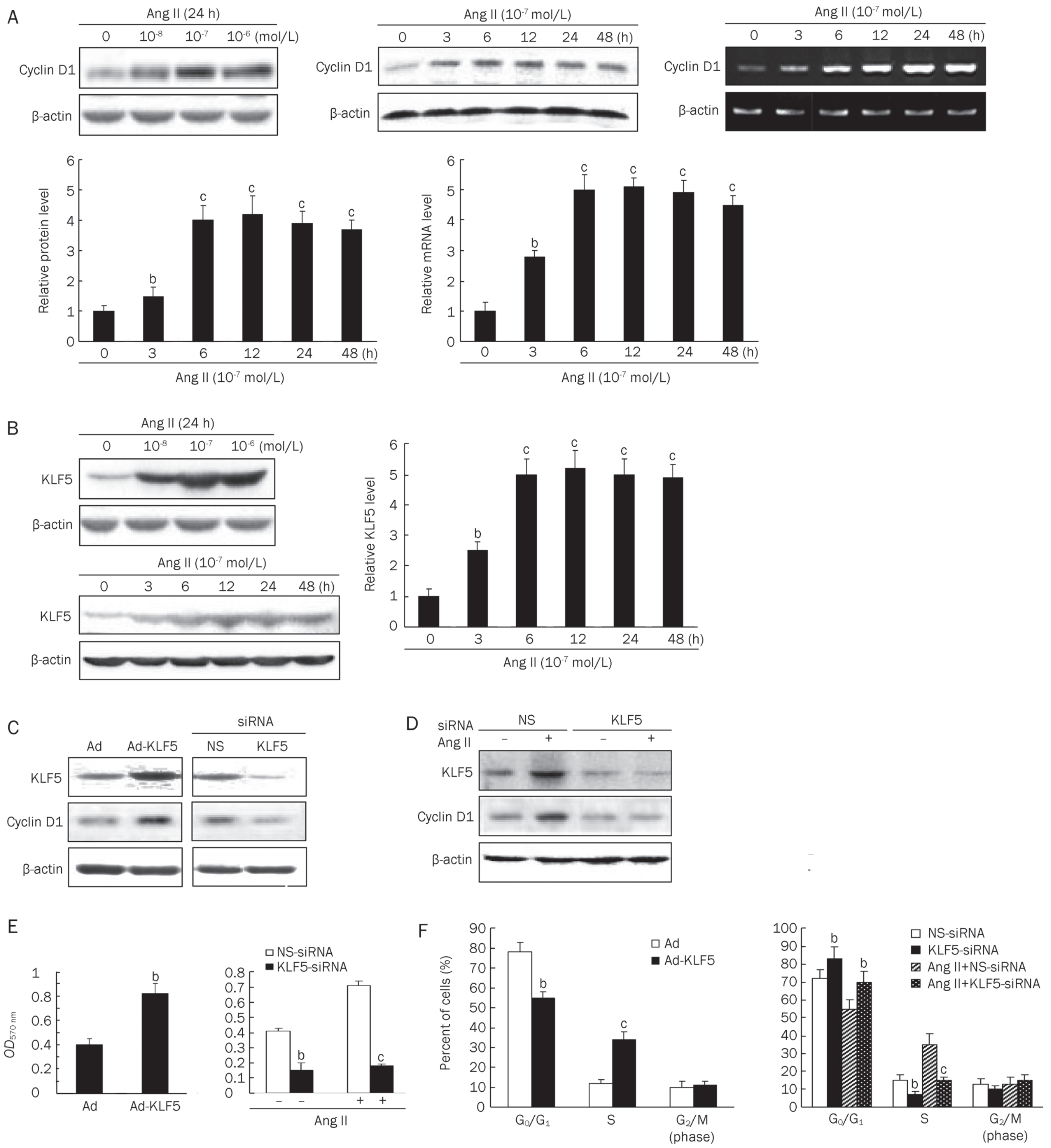

Figure 2. KLF5 is involved in Ang II-induced cyclin D1 expression and VSMC proliferation. (A) cyclin D1 expression induced by Ang II was detected by Western blotting (left and middle) and RT-PCR analysis (right), respectively. The graphs represent the relative level of the protein and mRNA of four independent experiments. $^{b}P<0.05$, $^{c}P<0.01$ *vs* PBS control. (B) KLF5 protein was detected by Western blotting. β-actin was used as an internal control. The graphs represent the relative level of KLF5 protein of four independent experiments. $^{b}P<0.05$, $^{c}P<0.01$ *vs* PBS control. (C and D) Expression of KLF5 and cyclin D1 was detected by Western blotting. β-actin was used as an internal control. (E and F) Cell proliferation of VSMCs was analyzed by MTT assay (E) and flow cytometry (F). $^{b}P<0.05$, $^{c}P<0.01$ *vs* Ad or NS-siRNA.

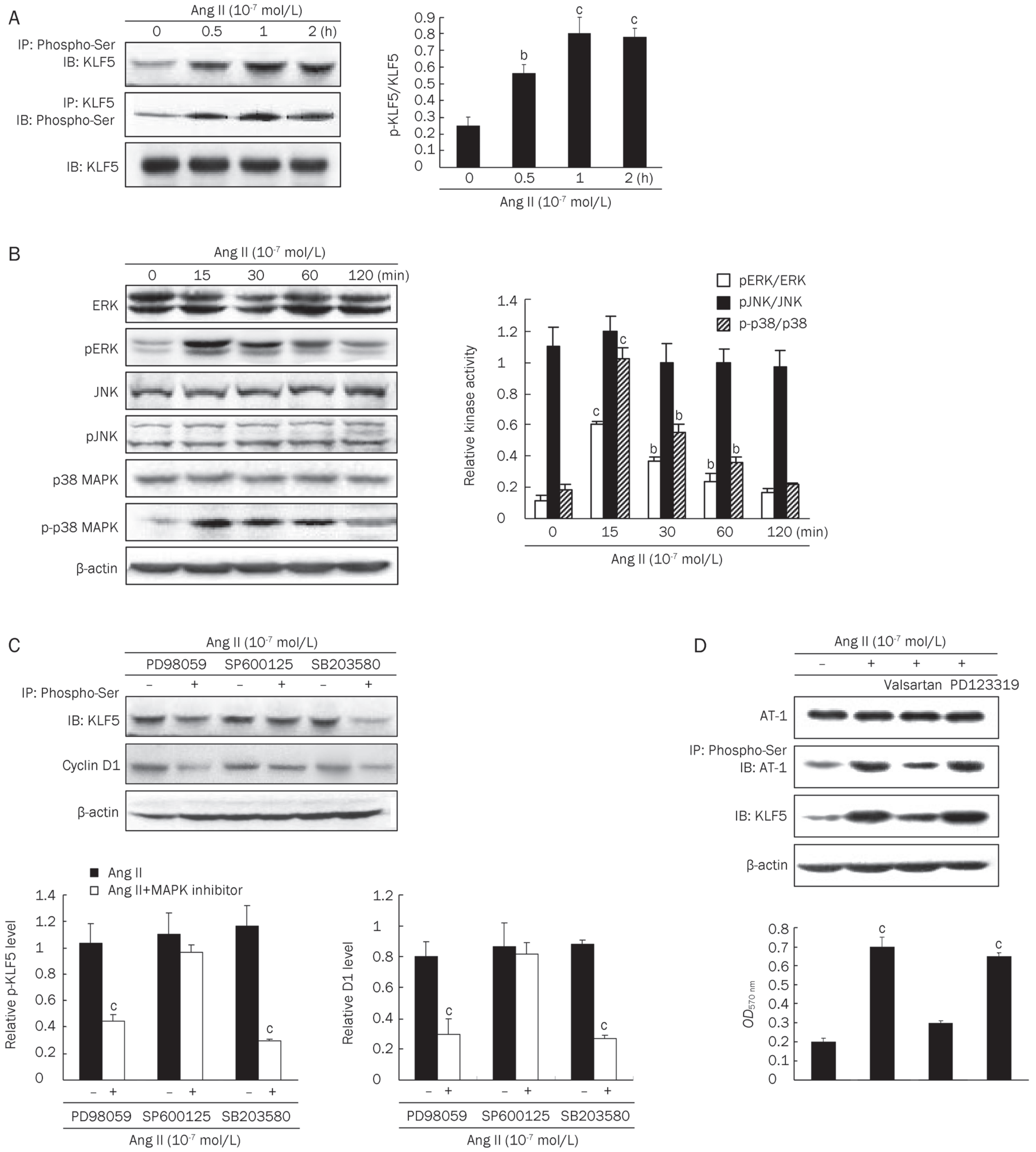

Figure 3. Ang II induces KLF5 activation via the ERK 1/2 and p38 MAPK pathways. (A) Phosphorylated KLF5 was immunoprecipitated with anti-phospho-Ser and then analyzed by Western blotting. The graphs represent the relative level of p-KLF5 of four independent experiments. $^{b}P<0.05$, $^{c}P<0.01$ *vs* 0 h. (B) Phosphorylation of ERK, JNK and p38 MAPK in VSMCs was analyzed by Western blotting. The graphs represent the relative activity of these kinases of four independent experiments. $^{b}P<0.05$, $^{c}P<0.01$ *vs* 0 min. (C) KLF5 phosphorylation and cyclin D1 expression were analyzed by immunoprecipitation and Western blotting, respectively. β-actin was used as an internal control. The graphs represent the relative level of p-KLF5 and cyclin D1 protein of four independent experiments. $^{c}P<0.01$ *vs* no inhibitors. (D) The expression and phosphorylation of KLF5 and AT-1 were analyzed by immunoprecipitation and Western blotting, respectively. β-actin was used as an internal control. VSMC proliferation was tested using MTT. $^{c}P<0.01$ *vs* control.

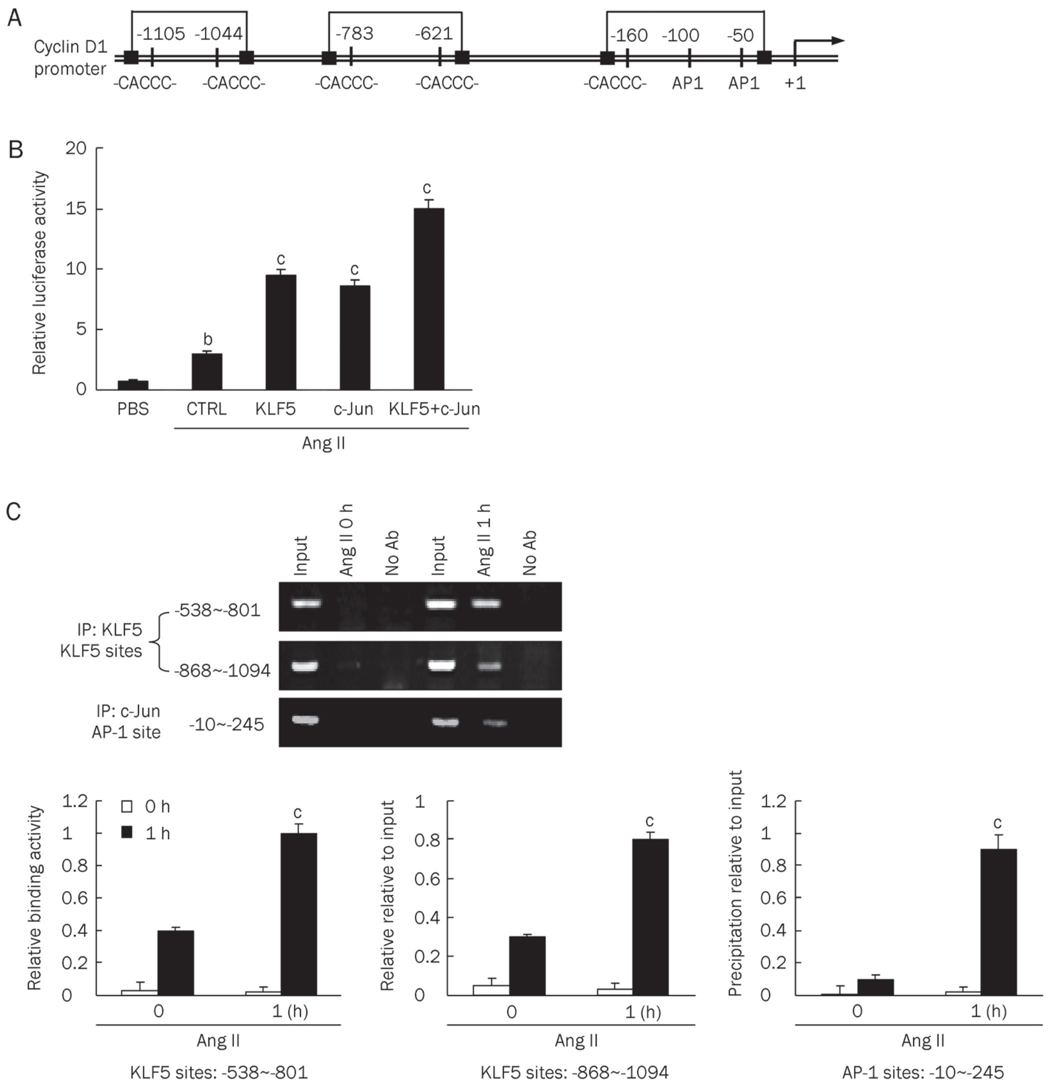

Figure 4. KLF5 mediates Ang II-induced cyclin D1 expression via interaction with AP-1. (A) Schematic representation of the KLF5 and AP-1 binding sites in the cyclin D1 promoter regions. (B) COS-7 cell lysates co-transfected using pGL3-CD1-Luc with expression vectors expressing KLF5 and/or c-Jun were subjected to luciferase activity assays. The graphs are expressed as the relative luciferase activity (*n*=3). $^{b}P<0.05$, $^{c}P<0.01$ *vs* empty vector control. (C) The chromatin fragments were immunoprecipitated (IP) with anti-KLF5 or anti-c-Jun antibodies, and then the cyclin D1 promoter regions containing KLF5 (-538~-801 and -868~-1094) or AP-1 (-10~-245) binding sequences were amplified by PCR. The graphs represent the relative binding activity of KLF5 or AP-1 to DNA elements of four independent experiments. $^{c}P<0.01$ *vs* 0 h.

cells with decrease in cell proliferation (Figure 3D), suggesting that AT-1 receptor triggers the mechanism by which KLF5 mediates Ang II-induced VSMC proliferation.

KLF5 mediates Ang II-induced cyclin D1 expression via its functional interaction with AP-1

To study the involvement of the KLF5 in cyclin D1 gene activation, a cyclin D1 promoter fragment spanning positions -1745 to +134 was analyzed via sequence comparison. These data showed that the cyclin D1 promoter contains multiple KLF5 and AP-1 regulatory elements that may be involved in the transcriptional regulation of gene expression (Figure 4A). To further characterize this, the pGL3-CD1-Luc construct containing the cyclin D1 promoter (from -1745 to +134) was transfected into COS-7 cells and the promoter activity was assayed following Ang II treatment. Ang II increased cyclin D1 promoter activity significantly over the level observed in the untreated cells, and cotransfection of KLF5 with the c-Jun expression vectors significantly increased cyclin D1 promoter activity 5-fold over that seen with the reporter alone following Ang II treatment (Figure 4B). Further, the ability of KLF5 to bind to the promoter of cyclin D1 gene was assessed via a ChIP assay. As shown in Figure 4C, Ang II significantly increased KLF5 and c-Jun binding to the cyclin D1 promoter. The two distal KLF5 binding elements of the cyclin D1 gene promoter were amplified by PCR in the immunoprecipitates pulled down by the anti-KLF5 antibody. However, a DNA fragment containing two AP-1 binding sites and one proximal KLF5 element (-10~-245) was amplified only in pellets immunoprecipitated using anti-c-Jun, but not anti-KLF5 antibody (Figure 4C). These observations were consistent with the results of the reporter gene assay, suggesting that there is a functional interaction between KLF5 and c-Jun in transactivating expression of cyclin D1 gene.

Discussion

The major purpose of the present study was to examine the action mechanism of KLF5 during Ang II-induced cyclin D1 expression and VSMC proliferation. We demonstrated the direct effect of Ang II on the induction of cyclin D1 expression and the stimulation of VSMC growth. We also showed that Ang II increased the activity of KLF5 by inducing both its expression and phosphorylation via the ERK 1/2 and p38 MAPK pathways activated by AT-1. Evidence for a functional interaction between KLF5 and c-Jun was provided by ChIP and the reporter gene assays. After Ang II treatment or KLF5 and c-Jun overexpression, there is a increased activity of cyclin D1 promoter, with increased binding ability of KLF5 and AP-1 on cyclin D1 promoter. Our results support a physiological role for Ang II as a positive regulator of KLF5.

It has been demonstrated that the molecular and cellular actions of Ang II in cardiovascular are almost exclusively mediated by AT-1 receptor and AT-1 regulate cell growth through the ERK 1/2 pathway[21] which is required for mediating Ang II-induced proliferation in rat aortic SMCs[22]. In the present study, we also showed that AT-1 receptor mediated Ang II-induced KLF5 activation and cell proliferation by ERK 1/2 signaling pathway.

The role of KLF5 in the vasculature is first suggested when it is isolated as a transcription factor that binds the promoter of the embryonic smooth muscle myosin heavy chain SMemb gene[23]. In vascular tissues, KLF5 is abundantly expressed in embryonic SMCs and is downregulated with vascular development, but notably, it is reinduced in proliferating neointimal SMCs in response to vascular injury[24]. The previous study has shown that KLF5 and c-Jun cooperatively inhibit p21 expression in Ang II-stimulated VSMCs**[10]**, indicating the mechanism by which KLF5 promotes cell proliferation. Recently, KLF5 has been demonstrated direct binding to the promoter and up-regulated gene expression of cyclin D1 in cardiovascular cells[25]. Meanwhile, our findings also indicate a novel mechanism by which KLF5 mediates Ang II-induced cyclin D1 expression and proliferation of VSMCs via functional interaction with c-Jun.

The activity of KLF5 is regulated by a variety of transcriptional regulators and nuclear receptors through phosphorylation and/or acetylation[19, 26, 27]. Ang II has been shown to activate the ERK 1/2 pathway[21]. Moreover, KLF5 is activated via an ERK 1/2-dependent mechanism under certain conditions[28]. We show that Ang II induces both KLF5 and cyclin D1 expression in same profile manner, and cyclin D1 protein expression depends on KLF5 phosphorylation via ERK and p38 MAPK signaling pathway, suggesting that KLF5-mediated cyclin D1 expression may result from KLF5 activation but not its expression.

In summary, KLF5, as a target of Ang II-mediated signaling, plays an important role in the expression of cyclin D1 and the proliferation of VSMCs. The AT-1 receptor mediates the activation of KLF5 via ERK 1/2 and p38 MAPK pathways in Ang II-induced VSMCs. KLF5 activates the transcription of cyclin D1 gene via functional interaction with c-Jun in Ang II-induced VSMC proliferation.

Acknowledgements

This work was supported by the National Natural Science Foundation of China (N<u>o</u> 30670845 and 30770787), the “973” Program of China (N<u>o</u> 2008CB517402) and the Hebei Province Natural Science Foundation (N<u>o</u> C2006000814 and C2005000722).

Author contribution

Mei HAN and Jin-kun WEN designed research and revised the manuscript; Yu LIU performed research and analyzed data; Li-hua DONG and Bin ZHENG performed research.

References

1 Kim S, Iwao H. Molecular and cellular mechanisms of angiotensin II-mediated cardiovascular and renal diseases. Pharmacol Rev 2000; 52: 11–34.

2 Eguchi S, Dempsey PJ, Frank GD, Motley ED, Inagami T. Activation of MAPKs by angiotensin II in vascular smooth muscle cells. Metalloprotease-dependent EGF receptor activation is required for activation of ERK and p38 MAPK but not for JNK. J Biol Chem 2001; 276: 7957–62.

3 Gao D, Niu X, Ning N, Hao G. Regulation of angiotensin II-induced krüppel-like factor 5 expression in vascular smooth muscle cells. Biol Pharm Bull 2006; 29: 2004–8.

4 Schmitz U, Ishida T, Ishida M, Surapisitchat J, Hasham MI, Pelech S, *et al*. Angiotensin II stimulates p21-activated kinase in vascular smooth muscle cells: role in activation of JNK. Circ Res 1998; 82: 1272–8.

5 Kusuhara M, Takahashi E, Peterson TE, Abe J, Ishida M, Han J, *et al*. p38 Kinase is a negative regulator of angiotensin II signal transduction in vascular smooth muscle cells: effects on Na^+/H^+ exchange and ERK1/2. Circ Res 1998; 83: 824–31.

6 Suzuki T, Muto S, Miyamoto S, Aizawa K, Horikoshi M, Nagai R. Functional interaction of the DNA-binding transcription factor Sp1 through its DNA-binding domain with the histone chaperone TAF-I. J Biol Chem 2003; 278: 28758–64.

7 Bateman NW, Tan D, Pestell RG, Black JD, Black AR. Intestinal tumor progression is associated with altered function of KLF5. J Biol Chem 2004; 279: 12093–101.

8 Nandan MO, Chanchevalap S, Dalton WB, Yang VW. Kruppel-like factor 5 promotes mitosis by activating the cyclin B1/Cdc2 complex during oncogenic Ras-mediated transformation. FEBS Lett 2005; 579: 4757–62.

9 Nandan MO, Yoon HS, Zhao W, Ouko LA, Chanchevalap S, Yang VW. Krüppel-like factor 5 mediates the transforming activity of oncogenic H-Ras. Oncogene 2004; 23: 3404–13.

10 He M, Han M, Zheng B, Shu YN, Wen JK. Angiotensin II stimulates KLF5 phosphorylation and its interaction with c-Jun leading to

suppression of p21 expression in vascular smooth muscle cells. J Biochem 2009; 146: 683–91

11 Han M, Wen JK, Zheng B, Cheng Y, Zhang C. Serum deprivation results in redifferentiation of human umbilical vascular smooth muscle cells. Am J Physiol Cell Physiol 2006; 291: C50–8.

12 Li AY, Han M, Zheng B, Wen JK. Roscovitine inhibits ERK1/2 activation induced by angiotensin II in vascular smooth muscle cells. FEBS Lett 2008; 582: 243–8.

13 Chanchevalap S, Nandan MO, McConnell BB, Charrier L, Merlin D, Katz JP, *et al*. Kruppel-like factor 5 is an important mediator for lipopolysaccharide-induced proinflammatory response in intestinal epithelial cells. Nucleic Acids Res 2006; 34: 1216–23.

14 Xiao F, Puddefoot JR, Barker S, Vinson GP. Mechanism for aldosterone potentiation of angiotensin II-stimulated rat arterial smooth muscle cell proliferation. Hypertension 2004; 44: 340–5.

15 Li JJ, Han M, Wen JK, Li AY. Osteopontin stimulates vascular smooth muscle cell migration by inducing FAK phosphorylation and ILK dephosphorylation. Biochem Biophys Res Commun 2007; 356: 13–9.

16 Wang C, Han M, Zhao XM, Wen JK. Kruppel-like factor 4 is required for the expression of vascular smooth muscle cell differentiation marker genes induced by all-trans retinoic acid. J Biochem 2008; 144: 313–21.

17 Weiss D, Sorescu D, Taylor WR. Angiotensin II and atherosclerosis. Am J Cardiol 2001; 87: 25C–32C.

18 Knudsen KE, Diehl JA, Haiman CA, Knudsen ES. Cyclin D1: polymorphism, aberrant splicing and cancer risk. Oncogene 2006; 25: 1620–8.

19 Zhang Z, Teng CT. Phosphorylation of Kruppel-like factor 5 (KLF5/IKLF) at the CBP interaction region enhances its transactivation function. Nucleic Acids Res 2003; 31: 2196–208.

20 Kyaw M, Yoshizumi M, Tsuchiya K, Kirima K, Tamaki T. Antioxidants inhibit JNK and p38 MAPK activation but not ERK 1/2 activation by angiotensin II in rat aortic smooth muscle cells. Hypertens Res 2001; 24: 251–61.

21 Gervais M, Dugourd C, Muller L, Ardidie C, Canton B, Loviconi L, *et al*. Akt down-regulates ERK1/2 nuclear localization and angiotensin II-induced cell proliferation through PEA-15. Mol Biol Cell 2006; 17: 3940–51.

22 Dugourd C, Gervais M, Corvol P, Monnot C. Akt is a major downstream target of PI3-kinase involved in angiotensin II-induced proliferation. Hypertension 2003; 41: 882–90.

23 Watanabe N, Kurabayashi M, Shimomura Y, Kawai-Kowase K, Hoshino Y, Manabe I, *et al*. BTEB2, a Kruppel-like transcription factor, regulates expression of the SMemb/Nonmuscle myosin heavy chain B (SMemb/NMHC-B) gene. Circ Res 1999; 85: 182–91.

24 Suzuki T, Aizawa K, Matsumura T, Nagai R. Vascular implications of the Kruppel-like family of transcription factors. Arterioscler Thromb Vasc Biol 2005; 25: 1135–41.

25 Suzuki T, Sawaki D, Aizawa K, Munemasa Y, Matsumura T, Ishida J, *et al*. Kruppel-like factor 5 shows proliferation-specific roles in vascular remodeling, direct stimulation of cell growth, and inhibition of apoptosis. J Biol Chem 2009; 284: 9549–57.

26 Miyamoto S, Suzuki T, Muto S, Aizawa K, Kimura A, Mizuno Y, *et al*. Positive and negative regulation of the cardiovascular transcription factor KLF5 by p300 and the oncogenic regulator SET through interaction and acetylation on the DNA-binding domain. Mol Cell Biol 2003; 23: 8528–41.

27 Matsumura T, Suzuki T, Aizawa K, Munemasa Y, Muto S, Horikoshi M, *et al*. The deacetylase HDAC1 negatively regulates the cardiovascular transcription factor Kruppel-like factor 5 through direct interaction. J Biol Chem 2005; 280: 12123–9.

28 Zhang H, Bialkowska A, Rusovici R, Chanchevalap S, Shim H, Katz JP, *et al*. Lysophosphatidic acid facilitates proliferation of colon cancer cells via induction of Kruppel-like factor 5. J Biol Chem 2007; 282: 15541–9.

Acta Pharmacologica Sinica (2010) 31: 19–26
© 2010 CPS and SIMM All rights reserved 1671-4083/10 $32.00
www.nature.com/aps

Original Article

Reduction in extracellular Ca^{2+} attenuates endothelium-dependent relaxation more than nitroprusside-induced relaxation

Shigehiro HAYASHI*, R Kelly HESTER

Department of Medical Pharmacology and Toxicology, and Microcirculation Research Institute, College of Medicine, Texas A&M University, College Station, Texas 77843–1114, USA

Aim: To quantitatively assess the effect of lowering external Ca^{2+} ($[Ca^{2+}]_o$) on both endothelium-dependent and -independent relaxations in rabbit aorta.
Methods: Isometric contractions and relaxations of isolated aortae were recorded. When assessing the effect of reduced $[Ca^{2+}]_o$ on relaxations, the normal $[Ca^{2+}]_o$ solution was substituted with one of the reduced $[Ca^{2+}]_o$ solutions for one aorta, while a paired aorta was replenished with normal $[Ca^{2+}]_o$ solution.
Results: The extent of acetylcholine (ACh)-induced relaxation, which is dependent on an intact endothelium, is time-dependent, and inversely related to $[Ca^{2+}]_o$ in a range of 0.02−2 mmol/L. ACh-induced relaxations were not significantly altered by the magnitude of the precontraction induced by $PGF_{2\alpha}$. Nitroprusside-induced relaxations, which are independent of the endothelium, are also attenuated by reduced $[Ca^{2+}]_o$. Relaxant responses to ACh were significantly more susceptible to reduced $[Ca^{2+}]_o$ than nitroprusside-induced relaxations. A maximally effective relaxing concentration of D600, an *L*-type Ca channel blocker methoxyverapamil, (10^{-5} mol/L) attenuated ACh-induced relaxations, whereas nitroprusside-induced relaxations were unaffected by D600.
Conclusion: Thus, endothelium-dependent relaxation is more dependent on $[Ca^{2+}]_o$ than endothelium-independent relaxation, and it seems likely that $[Ca^{2+}]_o$ plays an important role not only in contractile processes, but also in relaxant processes as well.

Keywords: calcium; relaxation; vascular smooth muscle; aorta; endothelium; nitroprusside; D600

Acta Pharmacologica Sinica (2010) 31: 19–26; doi: 10.1038/aps.2009.164; published online 16 Nov 2009

Introduction

Extracellular Ca^{2+} ($[Ca^{2+}]_o$) is required for full contractile responses of vascular smooth muscle[1, 2], and this Ca^{2+} dependence varies depending upon specific stimulants and blood vessels[3–6]. In contrast to a large number of investigations concerned with delineating the relationship between Ca^{2+} and the excitation/contraction coupling processes in vascular smooth muscle, it has not been clearly elucidated what general role $[Ca^{2+}]_o$ might play in relaxant responses.

There is clear evidence that some vasodilators such as acetylcholine (ACh) cause relaxation by liberating an endothelium-derived relaxing factor (EDRF)[7], nitric oxide (NO) which was identified later[8, 9]. On the other hand, other vasodilators such as nitroprusside, are generally regarded as endothelium-independent, and have direct inhibitory effects on vascular smooth muscle[10, 11]. It has been recently demonstrated that the presence of extracellular Ca^{2+} is required for release of EDRF[11–14]. In these studies, Ca^{2+}-free conditions abolished endothelium-dependent relaxation, whereas different. Ca^{2+} entry blockers had varied effects on similar endothelium-dependent relaxations. The use of Ca^{2+}-free solutions frequently employed in these types of studies usually results in a noticeably diminished tension response which is generally required for quantitative analyses of relaxations, and this may have made it difficult to quantitatively assess the role of $[Ca^{2+}]_o$ in relaxation processes. Thus, the present study was undertaken to quantitatively assess the effect of reducing $[Ca^{2+}]_o$ in a concentration-dependent fashion on both endothelium-dependent and -independent relaxations in rabbit aorta.

Materials and methods

Isolated aortae

New Zealand white rabbits of either sex were anesthetized with 50 mg/kg (iv) of sodium pentobarbital, and then sacri-

---

* To whom correspondence should be addressed. Faculty of Pharmaceutical Sciences, Ohu University, 31-1 Tomitacho-Misumido Koriyama 963-8611, Japan
E-mail s-hayashi@pha.ohu-u.ac.jp
Received 2009-08-20 Accepted 2009-10-10

ficed by exsanguination from the common carotid arteries. Rabbits used in this study were 10−12 weeks old with a mean body weight of 1.86±0.03 kg (*n*=60). Thoracic aortae were quickly removed, isolated and cleaned, and cut into opened aortic rings 3 mm wide similar to the method of Carrier *et al*[15]. Tissues were fixed vertically between stainless steel clips in a tissue bath containing 20 mL nutrient solution, aerated with 95% O_2+5% CO_2, and maintained at 36−37 °C. The clip anchoring the upper end of the strip was connected to the lever of a force-displacement transducer (Grass FT 03). Using previously described procedures for passive force-active force relationships[16], near optimum resting tension at which actively developed contractions were maximized in rabbit aortae was found to include a broad range (2.0−6.0 g) of passive forces (Authors, unpublished data). A resting force of 2.0 g was placed on each tissue to be consistent with previous studies[17].

Procedures of aortic contraction/relaxation experiment in the bath

Constituents of the nutrient solution (normal Ca^{2+}) were as follows (mmol/L): NaCl, 142; KCl, 5.4; $CaCl_2$, 2.0; $NaHCO_3$, 18.0; and dextrose, 11.0. The modified solutions of reduced $[Ca^{2+}]_o$ contained the following concentrations of $CaCl_2$ instead of 2.0 mmol/L: 1.0 mmol/L (1/2); 0.5 mmol/L (1/4); 0.2 mmol/L (1/10) ; 0.06 mmol/L (3/100); and 0.02 mmol/L (1/100). The pH of continuously aerated solutions at 37 °C was 7.35−7.45. Osmotic adjustment was not made when KCl was increased up to 80 mmol/L. Before specific experimental protocols were initiated, preparations were allowed to equilibrate for 60-90 min in the bathing medium, during which time the solution was replaced every 10 to 15 min.

Isometric contractions and relaxations were recorded on an inkwriting oscillograph (Gould 2600S). Concentration-effect relationships were obtained by adding drugs directly to the bathing medium in a cumulative fashion. For studies on relaxant responses to ACh and nitroprusside, preparations were initially contracted with $PGF_{2\alpha}$ (4×10^{-7}−10^{-6} mol/L). At the end of each series of experiments, papaverine (10^{-4} mol/L) plus nitroprusside (10^{-4} mol/L) was added to obtain the maximum relaxation. In experiments conducted in reduced $[Ca^{2+}]_o$, 2 mmol/L $CaCl_2$ was added with papaverine plus nitroprusside. Some aortae were dragged slowly for one min with intimal surface down[7] over a sheet of sandpaper (3M, #320) wetted with nutrient solution to remove the endothelium. Abolition of relaxant responses to ACh was used to verify functional damage of endothelial cells in these intimal-rubbed preparations.

Substitution with reduced $[Ca^{2+}]_o$ solutions

When assessing the effect of reduced $[Ca^{2+}]_o$ on relaxations, the normal Ca^{2+} solution was substituted with one of the reduced $[Ca^{2+}]_o$ solutions for one aorta, while a paired aorta was replenished with normal Ca^{2+} solution. Before substitution, modified solutions were maintained at 37 °C and continuously aerated. In every experiment, it was confirmed that substitution with normal Ca^{2+} solution did not appreciably alter resting tension. A substitution of normal Ca^{2+} solution with a low Ca was carefully made, since somewhat mechanical agitation of strip with change in the nutrient solution may alter aortic tension and/or endothelial activity as well as potential activation of some ion channels. However, no osmolarity adjustment was posed for Ca^{2+} within a small range of 2 mmol/L. KCl was added in a concentration of 80 mmol/L without osmorality adjustment, but this procedure and response was made at first in every aortic strip for checking the reactivity, suggesting a separate experiment from the low Ca study.

In experiments utilizing a 1/100 $[Ca^{2+}]_o$ solution, responses to ACh were examined 30 min, 60 min, or 120 min after the substitution. $PGF_{2\alpha}$ was added 15 min before the ACh-test relaxation to attain and maintain precontraction in 30 min studies and 15−30 min prior in 60 or 120 min studies. In all other studies using solutions with varied $[Ca^{2+}]_o$ or added D600, aortae were exposed to either procedure for 120 min, including exposure to $PGF_{2\alpha}$ for 15−30 min, prior to ACh- or nitroprusside-induced relaxations. Results are expressed as mean±SEM. Statistical analyses were made using Student's unpaired *t*-test.

Drugs

Drugs used were acetylcholine chloride (Sigma, St Louis, MO), sodium nitroprusside (Sigma), prostaglandin $F_{2\alpha}$-tromethamine (Upjohn, Kalamazoo, MI), methoxyverapamil (D600, Knoll AG, Ludwigshafen, West Germany) and histamine dihydrochloride (Sigma).

Results

Effect of reduced $[Ca^{2+}]_o$ on ACh-induced relaxations

ACh elicited a relaxation of $PGF_{2\alpha}$ -precontracted aortae that was readily abolished in endothelial rubbed preparations. The maximum relaxation due to 10^{-6} mol/L ACh was 68%±6% (*n*=8) of the papaverine plus nitroprusside-induced relaxation in aortae with intact endothelium, but -35±8% (*n*=8) (contraction) in aortae with damaged endothelium. Reducing $[Ca^{2+}]_o$ to 0.02 mmol/L attenuated the ACh-induced relaxation in endothelium intact aortae. Significant attenuation occurred 30 min after the initial substitution with this reduced $[Ca^{2+}]_o$ solution, reaching a maximum within 2 h (Figure 1). Thus in the following experiments concerned with defining the effects of various reductions in $[Ca^{2+}]_o$ on relaxation, a 2 h exposure to the reduced $[Ca^{2+}]_o$ solution was used. ACh-induced relaxation was attenuated by reducing $[Ca^{2+}]_o$ from 2 to 0.2–0.02 mmol/L. The degree of attenuation was inversely related to $[Ca^{2+}]_o$, where reducing $[Ca^{2+}]_o$ to 0.02 mmol/L essentially eliminated any ACh-induced relaxation (Figure 2). In a few experiments Ca^{2+} was added after the maximum ACh-induced relaxation without the concomitant addition of nitroprusside plus papaverine, and further relaxation ensued.

When the level of precontraction was raised or lowered by increasing or decreasing the concentration of $PGF_{2\alpha}$ rather than reducing $[Ca^{2+}]_o$, ACh-induced relaxation, expressed as a percent of the maximal papaverine plus nitroprusside-induced

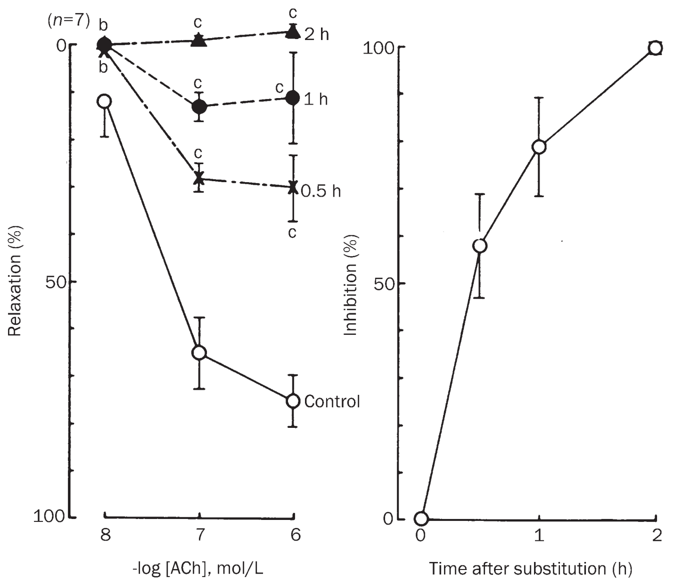

Figure 1. Inhibition of ACh-induced relaxation by reduced $[Ca^{2+}]_o$ as a function of the duration of exposure to reduced $[Ca^{2+}]_o$. Preparations in normal Ca^{2+} or reduced $[Ca^{2+}]_o$ (0.02 mmol/L) solutions were precontracted with $PGF_{2\alpha}$ before adding ACh; contractions were 1825±233 mg (normal Ca^{2+}) , 1284±386 mg (30 min), 1250±439 mg (60 min), and 1384±347 mg (120 min). Relaxant responses to ACh were expressed as a % of the papaverine plus nitroprusside-induced relaxation attained at the end of each experiment; relaxations were 2067±256 mg (control), 1368±400 mg (30 min), 1343±483 mg (60 min), and 1434±348 mg (120 min). $^bP<0.05$, $^cP<0.01$ *vs* control.

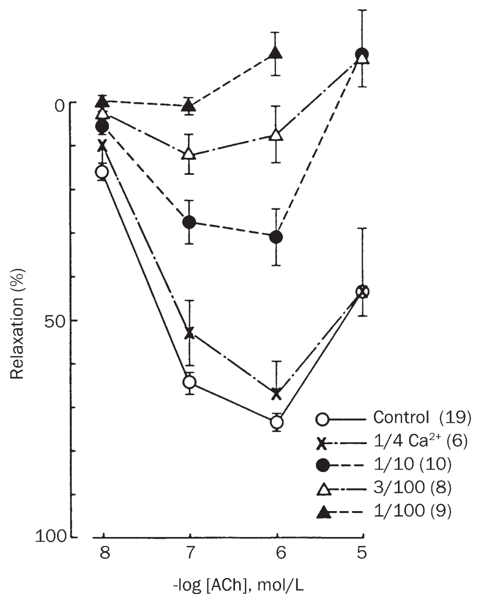

Figure 2. Effects of reduced $[Ca^{2+}]_o$ on relaxant responses to ACh in preparations precontracted with $PGF_{2\alpha}$. Contractions were 1541±128 mg (normal Ca^{2+}) , 1211±365 mg (1/4), 978±180 mg (1/10), 1341±361 mg (3/100), and 1249±178 mg (1/100). Papaverine plus nitroprusside-induced relaxation at the end of each experiment was taken as 100%; 1825±154 mg (normal Ca^{2+}), 1400±356 mg (1/4), 1208±232 mg (1/10), 1582±347 mg (3/100), and 1331±188 mg (1/100).

relaxation, did not differ (Figure 3). Also, if the level of tension in reduced $[Ca^{2+}]_o$ was increased to approximate the same level as precontraction levels in normal Ca^{2+} by increasing the concentration of $PGF_{2\alpha}$ accordingly, ACh-induced relaxatlon was still similarly depressed by reducing $[Ca^{2+}]_o$ (data not shown).

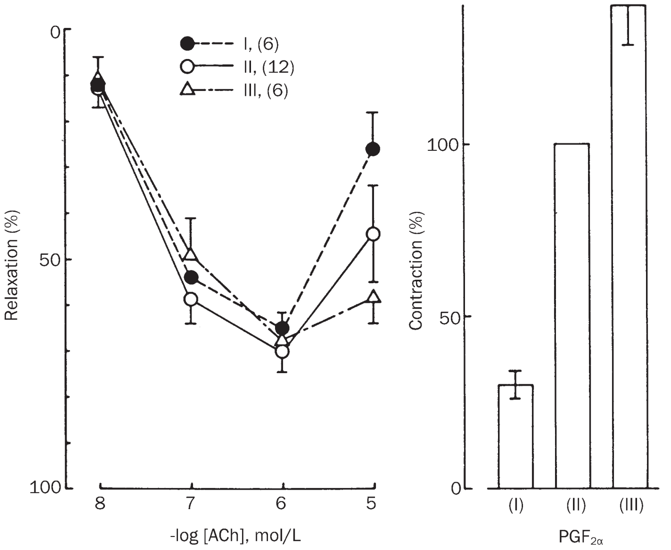

Figure 3. Effects of varying the initial level of tone by altering the concentration of $PGF_{2\alpha}$ on ACh-induced relaxations in a normal Ca^{2+} solution. Preparations were precontracted with 10^{-7} mol/L (I), 7×10^{-7} mol/L (II) or 10^{-5} mol/L (III) $PGF_{2\alpha}$; relative contractions shown at right in which contraction to concentration II was taken as 100%: 563±149 mg (I), 1792±194 mg (II), and 2258±155 mg (III).

When precontraction was induced by histamine (1×10^{-6}–3×10^{-6} mol/L) instead of $PGF_{2\alpha}$, reducing $[Ca^{2+}]_o$ to 0.02 mmol/L also attenuated the maximum ACh-induced relaxation; 72%±4% of papaverine plus nitroprusside-induced relaxation in normal Ca^{2+} and 8%±8% in reduced $[Ca^{2+}]_o$ (*n*=4).

Effects of reduced $[Ca^{2+}]_o$ on nitroprusside-induced relaxations

Reducing the $[Ca^{2+}]_o$ also attenuated relaxant responses to nitroprusside (Figure 4), which is not affected by endothelial damage (Figure 5, left). However, the attenuation was not apparent until $[Ca^{2+}]_o$ was reduced to 0.06 mmol/L. Even in aortae without intact endothelium, reducing $[Ca^{2+}]_o$ to 0.02 mmol/L depressed the nitroprusside-induced relaxation (Figure 5, right). Attenuation of the nitroprusside-induced relaxation by reducing $[Ca^{2+}]_o$ to 0.02 mmol/L was also observed in aortae precontracted with histamine (1×10^{-6}–3×10^{-6} mol/L); maximum response to nitroprusside was 95%±1% in normal Ca^{2+} and 4%±1% in reduced $[Ca^{2+}]_o$.

Inhibitory effects of reduced $[Ca^{2+}]_o$ on relaxant responses to nitroprusside were also compared to the inhibitory effects on ACh-induced responses (Figure 6). In terms of maximum responses, inhibition of nitroprusside-induced relaxations in a reduced $[Ca^{2+}]_o$ solution was significantly less than that of

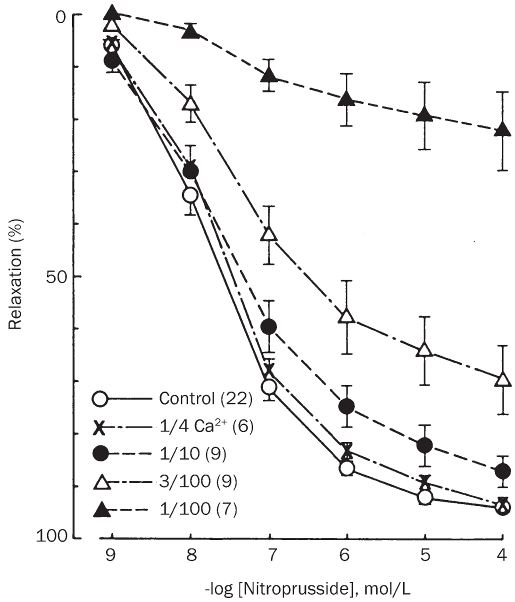

Figure 4. Effects of reduced $[Ca^{2+}]_o$ on relaxant responses to nitroprusside in $PGF_{2\alpha}$-precontracted aortae. Precontractions were 1784±172 mg (normal Ca^{2+}), 1842±392 mg (1/4), 1048±300 mg (1/10), 664±179 mg (3/100), and 1157±207 mg (1/100). Papaverine-induced relaxations at the end of each experiment were taken as 100%: 1979±198 mg (normal Ca^{2+}), 2108±446 mg (1/4), 1214±318 mg (1/10), 794±175 mg (3/100), and 1271±243 mg (1/100).

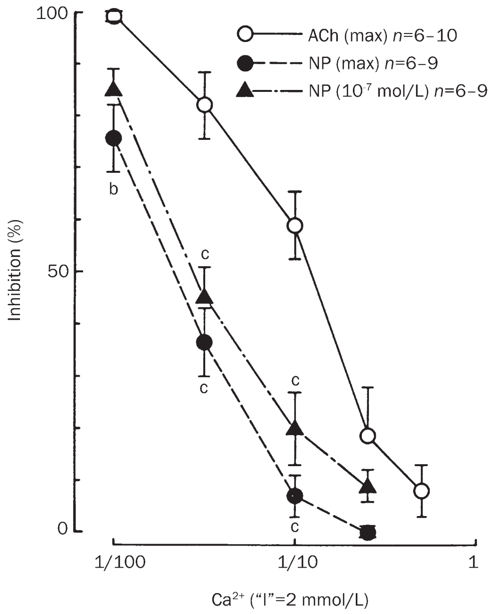

Figure 6. Inhibitory effects of reduced $[Ca^{2+}]_o$ on ACh-induced relaxations compared with similar effects on nitroprusside-induced relaxations. Comparisons were made based on data noted in Figure 2 and 4. The ordinate is expressed as inhibition (%) which represents the percent that maximum relaxant responses to ACh or nitroprusside in a reduced $[Ca^{2+}]_o$ solution were to the maximum papaverine plus nitroprusside-induced relaxations divided by the same relationship in normal Ca^{2+} solution. Control maximum responses to ACh and nitroprusside were 73%±2% and 94%±1%, respectively, of papaverine plus nitroprusside-induced relaxations. Responses to 10^{-7} mol/L nitroprusside (closed triangles) were compared in normal and reduced $[Ca^{2+}]_o$ solutions; relaxations in control were 71%±2% of the papaverine plus nitroprusside-induced relaxation. Significantly $^bP<0.05$, $^cP<0.01$ *vs* values of ACh (max).

ACh-induced relaxations. Furthermore, the relaxant response to 10^{-7} mol/L nitroprusside, which caused a similar degree of relaxation as the maximum effective concentration of ACh (71% *vs* 73%, respectively), was less attenuated by reduced $[Ca^{2+}]_o$ than the ACh-induced relaxation.

Effects of Mg^{2+} and reduced $[Ca^{2+}]_o$ on relaxant responses to ACh and nitroprusside

Mg^{2+} (0.6 mmol/L) did not significantly affect the ACh-induced relaxation in normal Ca^{2+} ; responses to ACh at concentrations of 10^{-7} and 10^{-6} mol/L were 63%±5% and 74%±5%; respectively, in the presence of Mg^{2+}, and 63%±5%

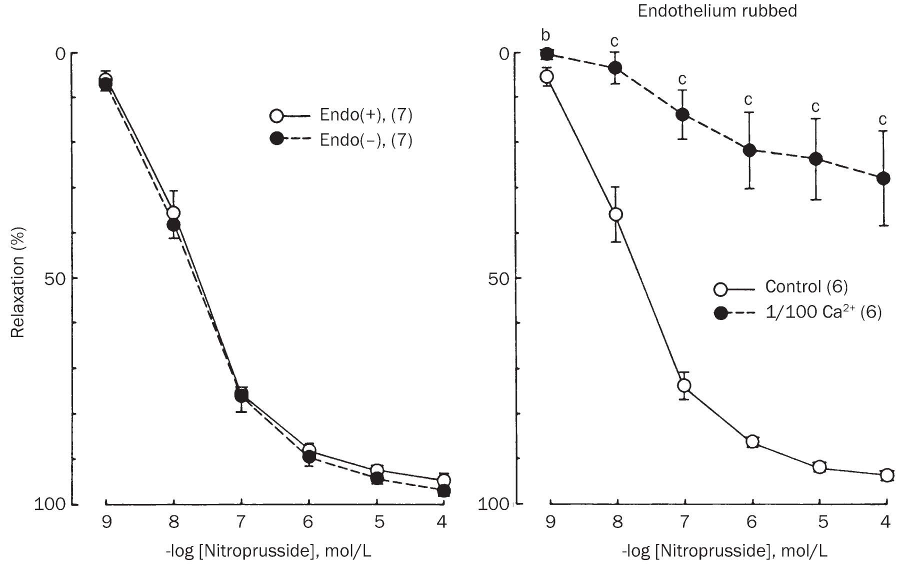

Figure 5. Relaxant responses to nitroprusside in aortae with and without intact endothelium (left), and the effect of reducing $[Ca^{2+}]_o$ to 0.02 mmol/L on relaxations in aortae without endothelium (right). Precontractions were 1547±285 mg and 2213±335 mg in aortae with (+) and without (–) endothelium (Endo), respectively, and 1833±223 mg (normal Ca^{2+}) and 1230±317 mg (1/100 without endothelium) (right). Papaverine-induced relaxations after nitroprusside were taken as 100%: 1737±292 mg (Endo+), 2477±369 mg (Endo–), and 2104±241 mg (normal Ca^{2+}), and 1332±331 mg (1/100) without endothelium (right). $^bP<0.05$, $^cP<0.01$ *vs* control.

and 72%±4% in the absence (*n*=9). Mg^{2+} also did not prevent the inhibitory effects of reducing $[Ca^{2+}]_o$ to 0.02 mmol/L on ACh-induced relaxations; maximum responses to ACh were 73%±4% in normal Ca^{2+} in the absence of Mg, and 14%±4% in reduced $[Ca^{2+}]_o$ (0.02 mmol/L) plus Mg^{2+} (*n*=8) ($P<0.001$). Additionally, Mg^{2+} did not prevent the inhibitory effects of reduced $[Ca^{2+}]_o$ on nitroprusside-induced relaxations; maximum responses to nitroprusside were 93%±2% in normal Ca^{2+} in the absence of Mg, and 41%±19% in the reduced $[Ca^{2+}]_o$ (0.02 mmol/L) plus Mg^{2+} (*n*=5) ($P<0.05$).

Effects of reduced $[Ca^{2+}]_o$ on contractile responses and resting tension

Reducing $[Ca^{2+}]_o$ to 0.02 mmol/L for 2 h suppressed contractile responses to either $PGF_{2\alpha}$ or KCl (Figure 7). Additionally, reducing $[Ca^{2+}]_o$ to 0.02 mmol/L for 2 h resulted in a small, but appreciable and slow developing contraction of 255±74 mg, while tissue remaining in a normal Ca^{2+} solution for the same time period lost 63±28 mg (*n*=20) ($P<0.001$).

Effects of D600 on ACh- and nitroprusside-induced relaxations

Addition of D600 to preparations precontracred with KCl (15 mmol/L) produced a concentration-dependent relaxation, reaching a maximum at 10^{-5} mol/L D600; which is 91%±2% of the papaverine plus nitroprusside-induced relaxation (*n*=7). Prior treatment with D600 (10^{-5} mol/L) for 120 min attenuated relaxant responses to ACh to a smaller extent than in normal $[Ca^{2+}]_o$ (Figure 8). In contrast, nitroprusside-induced relax-

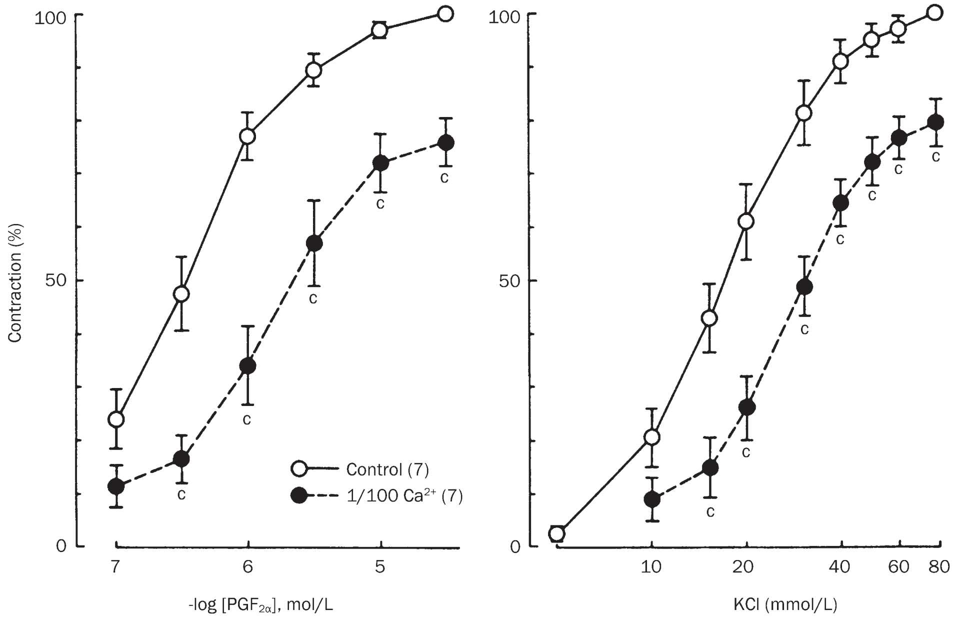

Figure 7. Effect of reducing $[Ca^{2+}]_o$ to 0.02 mmol/L on contractile responses to $PGF_{2\alpha}$ and KCl. Maximum contractions of control and Ca^{2+} deficient preparations in the presence of 2 mmol/L Ca^{2+} were taken as 100%. In the latter, Ca^{2+} was readmitted at the end of each experiment. They were 2579±289 mg (control, left), 3093±453 mg (1/100, left), 3514±204 mg (control, right) and 3986±290 mg (1/100, right). $^cP<0.01$ *vs* control.

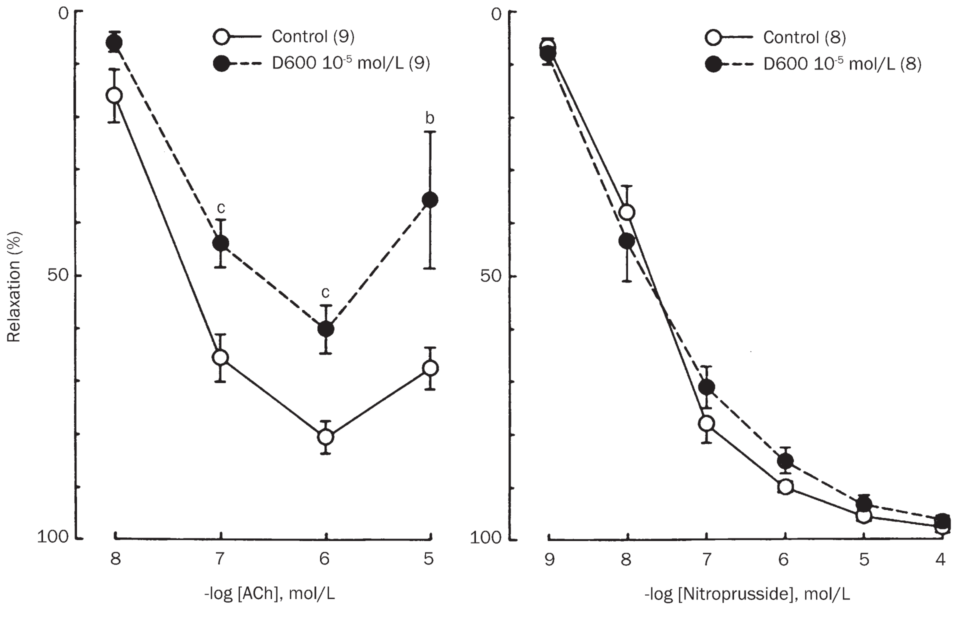

Figure 8. Effect of D600 on relaxant responses to ACh and nitroprusside. Preparations with or without prior D600 (10^{-5} mol/L) were precontracted with $PGF_{2\alpha}$ prior to relaxants; contractions were 1771±218 mg (control, left), 1191±291 mg (D600, left), 1583±219 mg (control, right), and 680±237 mg (D600, right). The papaverine plus nitroprusside-induced relaxation was taken as 100%. Relaxations were 1999±238 mg, 1409±321 mg, 1939±286 mg, and 1016±232 mg, respectively. $^bP<0.05$, $^cP<0.01$ *vs* control.

ations were not affected by prior D600.

Discussion

The current study clearly illustrates in a quantitative manner, the concentration-dependent effects of lowering $[Ca^{2+}]_o$ on ACh-induced relaxations in rabbit aorta, emphasizing the importance of extracellular Ca^{2+} in ACh-mediated release of EDRF and/or its subsequent action on the smooth muscle. This is an agreement with previous studies that noted a marked reduction in, or elimination of endothelium-dependent relaxation in both rabbit[14] and rat aorta[11–13] when these tissues were exposed to solutions from which Ca^{2+} had been omitted. All of these supports the original proposal by Furchgott and co-workers[7] that Ca^{2+} plays a critical role in endothelium-dependent relaxations. In addition, this study has demonstrated the obvious importance of Ca^{2+} also in endothelium-independent relaxations, since nitroprusside-induced relaxations are depressed by reducing $[Ca^{2+}]_o$.

Since the level of precontraction generated by $PGF_{2\alpha}$ was depressed by reduced $[Ca^{2+}]_o$, the lowered state of contraction could be responsible for depression of subsequent relaxation. However, ACh-induced relaxations were not different in a normal Ca^{2+} solution when the magnitude of the maintained contraction was varied by utilizing different concentrations of $PGF_{2\alpha}$ (Figure 3). Inhibition by reduced $[Ca^{2+}]_o$ of ACh-induced relaxation was still observed, when the depressed precontraction was similarly increased. Thus, a lower magnitude of contraction is unlikely to account for the depressed relaxant responses to these vasodilators noted when $[Ca^{2+}]_o$ is reduced. Furthermore, both ACh- and nitroprusside-induced relaxations in aortae precontracted with histamine instead of $PGF_{2\alpha}$ were also attenuated by a reduction in $[Ca^{2+}]_o$, illustrating that attenuation of relaxant responses in reduced $[Ca^{2+}]_o$ is not unique for $PGF_{2\alpha}$-induced contractions.

Since membrane Ca^{2+} controls its own entry into smooth muscle[18], an increased conductance to Ca^{2+} following a reduction in $[Ca^{2+}]_o$ may effectively increase cytoplasmic Ca^{2+} levels, resulting in functional antagonism of relaxant responses. Furthermore, membrane potential may be altered by reduced $[Ca^{2+}]_o$[19], and Casteels *et al*[20] have demonstrated in rabbit mesenteric artery that a reduction in $[Ca^{2+}]_o$ from 2.5 mmol/L to 0.16 mmol/L results in a progressive decrease in resting membrane potential. In the present study, in fact, a small but appreciable contraction was observed following 2 h exposure to a reduced. $[Ca^{2+}]_o$ solution that may be attributed to this proposed membrane depolarization and increased permeability to Ca^{2+}.

Webb and Bohr[21] suggested that high concentrations of Ca^{2+} (>4 mmol/L) stimulate the Na^+-K^+ ATPase, resulting in relaxation in rat tail artery. Thus in opposition to raising $[Ca^{2+}]_o$, lowering $[Ca^{2+}]_o$ might depress the Na^+–K^+ ATPase. Conditions that inhibit the Na^+–K^+ ATPase in smooth muscle, *eg* K^+-deficient solutions or cardiac glycosides, cause contraction through direct excitatory actions on the smooth muscle membrane[22–24], and can physiologically antagonize both ACh-[25] and nitroprusside-induced relaxations[10]. Nitroprusside stimulates guanylate cyclase and increases cGMP, which has been suggested to result in activation of the Na^+–K^+ ATPase[10]. However, neither nitroprusside-induced increases in the levels of cGMP nor concurrent effects on Na^+–K^+ ATPase appear to be dependent on $[Ca^{2+}]_o$[10, 26]. In addition, lowering $[Ca^{2+}]_o$ also depresses relaxant response to isoproterenol (Authors, unpublished observations), which is apparently mediated through an increase in cellular cAMP level[27]. Therefore, the depressant actions of reduced $[Ca^{2+}]_o$ are not unique for relaxants that concomitantly increase the levels of cGMP (ACh and nitroprusside). On the other hand, since both increases in cGMP[28] and cAMP[29] may stimulate Ca^{2+} ATPase-mediated extrusion mechanisms in vascular smooth muscle, an effect of reduced $[Ca^{2+}]_o$ on this system cannot be ruled out.

It has been recently shown that dichlorobenzamil, a proposed inhibitor of Ca influx via the Na^+-Ca^{2+} exchange system depressed endothelium-dependent relaxations but did not affect nitroprusside-induced relaxations[11]. Thus, the Na^+-Ca^{2+} exchange system would not be contributing to the general attenuation of these two relaxant responses that occurs in reduced $[Ca^{2+}]_o$ solutions.

Since there was an initial absence of Mg^{2+} in control and reduced $[Ca^{2+}]_o$ solutions, the Mg^{2+} deficiency could contribute to increased tone. It has been shown that acute Mg^{2+} deficiency can contribute to increased tone and reactivity to vasoconstrictors in coronary arteries[30]. However, the lack of Mg^{2+} in the present study is not likely to contribute to the actions of reduced $[Ca^{2+}]_o$, since the presence of Mg^{2+} neither modified the ACh-induced relaxation in a normal Ca^{2+} solution nor prevented the attenuating effects of reduced $[Ca^{2+}]_o$.

Sex related differences in cardiovascular function[31] are raised particularly for variation of existing hormonal status in female, while no specific comparison was made in this study. Greater endothelial responses to ACh in small femoral arteries of female mice than male mice are attributable to endothelium-derived hyperpolarizing factor (EDHF) in female[32]. It is of interest whether endothelial susceptibility to low Ca is linked to EDHF in female.

ACh at a high concentration of 10^{-5} mol/L elicited a contraction after the preceded relaxant responses. A contractile effect of ACh without relaxation effect occurs in newborn baboon cerebral artery[33]. The aorta may have excitatory muscarinic receptors that are different from M1 and M2 receptor binding sites as suggested in porcine coronary arteries[34]. As Vanhoutte and his colleagues proposed, it is conceivable that endothelium-derived contracting factor (EDCF) is attributable to the ACh-induced contraction, via endothelial cyclooxigenase-1, which stimulates thromboxane A_2 on vascular smooth muscle[35]. It remains to clarify whether change in the contracting factor is involved in the low Ca^{2+} effect on the relaxing factor.

Quantitative analyses clearly reveal that reduced $[Ca^{2+}]_o$ resulted in greater inhibition of ACh-induced relaxation than nitroprusside-induced (Figure 6). Likewise nitroprusside-induced relaxations were unaffected by D600, whereas relaxations to ACh were attenuated. Thus, it is apparent that endothelium-dependent relaxation is more dependent on $[Ca^{2+}]_o$. The greater inhibition of ACh-induced relaxations than nitroprusside-induced ones is probably directly related to the dual sites apparently affected by reduced $[Ca^{2+}]_o$: (1) obvious requirement of the endothelium for Ca^{2+} in production and/or release of EDRF resulting in less EDRF for a given stimulus and less relaxation, and (2) an apparent requirement of vascular smooth muscle for a critical amount of extracellular Ca^{2+} for full expression of the direct action of EDRF, as well as other vasodilators on smooth muscle. Thus, endothelium-dependent relaxation is more dependent on $[Ca^{2+}]_o$ than on endothelium-independent relaxatlon, and it seems likely that $[Ca^{2+}]_o$ plays an important role in vascular smooth muscle responsiveness not only to vasoconstrictors, but also to vascular relaxants as well.

Acknowledgements

This work was supported by NHLBI grant NHL 26L2I. Methoxyverapamil (D600) was generously supplied by Knoll AG, Ludwigshafen, West Germany. The authors would like to thank Mrs Beth BECKER for her technical assistance and Mrs Patty SAMPSON for her kind assistance in preparation of the manuscript.

Author contribution

Shigehiro HAYASHI designed research, performed research, wrote the paper; R Kelly HESTER designed research, contributed reagents/tools, wrote the paper.

References

1 Bohr DF. Vascular smooth muscle updated. Circ Res 1973; 32: 665–72.
2 Johansson B, Somlyo AP. Electrophysiology and Excitation-contraction coupling. In: Bohr DF, Somlyo AP, and Sparks HV Jr, editors. Handbook of physiology, Sect 2, Vol II, Vascular Smooth Muscle, Bethesda, Maryland, USA: Am Physiol Soc; 1980. p 301–323.
3 Hayashi S, Toda N. Inhibition by Cd^{2+}, verapamil and papaverine of Ca^{2+}-induced contraction in isolated cerebral and peripheral arteries of the dog. Br J Pharmacol 1977; 60: 35–43.
4 Hester RK, Weiss GB, Fry WJ. Effects of norepinephrine, dopamine and potassium on tension and 45Ca fluxes in canine and rabbit renal arteries. J Pharmacol Exp Ther 1978; 207: 364–71.
5 Hester RK, Weiss GB. Comparison of the degree of dependence of canine renal arteries and veins on high and low affinity calcium for responses to norepinephrine and potassium. J Pharmacol Exp Ther 1981; 216: 239–46.
6 Ratz PH, Flaim SF. Species and blood vessel specificity in the use of calcium for contraction. In: Flaim SF and Zelis R, editors. Calcium Blockers. Baltimore, USA: Urban and Schwarzenberg; 1982. p 77–98.
7 Furchgott RF. Role of endothelium in responses of vascular smooth muscle. Circ Res 1983; 53: 557–73.
8 Ignarro LJ, Buga GM, Wood KS, Byrns RE, Chaudhuri G. Endothelium-derived relaxing factor produced and released from artery and vein is nitric oxide. Proc Natl Acad Sci USA 1987; 84: 9265–9.
9 Palmer RM, Ferrige AG, Moncada S. Nitric oxide release accounts for the biological activity of endothelium-derived relaxing factor. Nature 1987; 327: 524–6.
10 Rapoport RM, Schwartz K, Murad F. Effect of sodium-potassium pump inhibitors and membrane-depolarizing agents on sodium nitroprusside-induced relaxation and cyclic guanosine monophosphate accumulation in rat aorta. Circ Res 1985; 57: 164–70.
11 Winquist RJ, Bunting PB, Schofield TL. Blockade of endothelium-dependent relaxation by the amiloride analog dichlorobenzamil: Possible role of Na^+/Ca^{2+} exchange in the release of endothelium-derived relaxant factor. J Pharmacol Exp Ther 1985; 235: 644–50.
12 Miller RC, Schoeffter P, Stoclet JC. Insensitivity of calcium-dependent endothelial stimulation in rat isolated aorta to the calcium entry blocker, flunarizine. Br J Pharmacol 1985; 85: 481–7.
13 Long CJ, Stone TW. The release of endothelium-derived relaxant factor is calcium dependent. Blood Vessels 1985; 22: 205–8.
14 Singer HA, Peach MJ. Calcium- and endothelial-mediated vascular smooth muscle relaxation in rabbit aorta. Hypertension 1982; 4: 19–25.
15 Carrier O Jr, Wedell EK, Barron KW. Specific α-adrenergic receptor desensitization in vascular smooth muscle. Blood Vessels 1978; 15: 247–58.
16 Hayashi S, Park MK, Kuehl TJ. Relaxant and contractile responses to prostaglandins in premature, newborn and adult baboon cerebral arteries. J Pharmacol Exp Ther 1985; 233: 628–35.
17 Hester RK. The effect of 2-nicotinamidoethyl nitrate on agonist-sensitive Ca^{2+} release and Ca^{2+} entry in rabbit aorta. J Pharmacol Exp Ther 1985; 233; 100–11.
18 Somlyo AP, Somlyo AV. Vascular smooth muscle. I. Normal structure, pathology, biochemistry, and biophysics. Pharmacol Rev 1968; 20: 197–272.
19 Shanes AM. Electrochemical aspects of physiological and pharmacological action in excitable cells. I. The resting cell and its alteration by extrinsic factors. Pharmacol Rev 1958; 10: 59–164.
20 Casteels R, Kitamura K, Kuriyama H, Suzuki H. The membrane properties of the smooth muscle cells of the rabbit main pulmonary artery. J Physiol 1977; 271: 41–61.
21 Webb RC, Bohr DF. Mechanism of membrane stabilization by calcium in vascular smooth muscle. Am J Physiol 1978; 235: C227–32.
22 Belardinelli L, Harder D, Sperelakis N, Rubio RM. Berne RM. Cardiac glycoside stimulation of inward Ca^{2+} current in vascular smooth muscle of canine coronary artery. J Pharmacol Exp Ther 1979; 209: 62–6.
23 Haddy FJ. Potassium effects on contraction in arterial smooth muscle mediated by Na^+, K^+-ATPase. Fed Proc 1983; 42: 239–45.
24 Hayashi S, Park MK. Neurogenic and myogenic contractile responses of dog mesenteric arteries to reduced K^+ concentration and their interaction with ouabain. J Pharmacol Exp Ther 1984; 230: 527–33.
25 De Mey JG, Vanhoutte PM. Interaction between Na^+, K^+ exchanges and the direct inhibitory effect of acetylcholine on canine femoral arteries. Circ Res 1980; 46: 826–36.
26 Schultz KD, Schultz K, Schultz G. Sodium nitroprusside and other smooth muscle relaxants increase cyclic GMP levels in rat ductus deferens. Nature 1977; 265: 750–1.
27 Andersson R, Lundholm L, Mohme-Lundholm E, Nilsson K. Role of cyclic AMP and Ca^{2+} in metabolic and mechanical events in smooth muscle. Adv Cyclic Nucleotide Res 1972; 1: 213–29.
28 Popescu LM, Panoiu C, Hinescu M, Nutu O. The mechanism of cGMP-induced relaxation in vascular smooth muscle. Eur J Pharmacol 1985; 107: 393–4.
29 Bulbring E, den Hertog A. The action of isoprenaline on the smooth muscle of the guinea-pig taenia coli. J Physiol 1980; 304: 277–96.
30 Turlapaty, PDMV, Altura BM. Magnesium deficiency produces spasms of coronary arteries: Relationship to etiology of sudden death

ischemic heart disease. Science 1980; 208: 198−200.

31 Kauser K, Rubanyi GM. Gender difference in endothelial dysfunction in the aorta of spontaneously hypertensive rats. Hypertension 1995; 25 (4 Pt 1): 517−23.

32 Luksha L, Poston L, Gustafsson JA, Hultenby K, Kublickiene K. The oestrogen receptor beta contributes to sex related differences in endothelial function of murine small arteries via EDHF. J Physiol 2006; 577(Pt-3): 945−5.

33 Hayashi S, Park MK and Kuehl TJ. Higher sensitivity of cerebral arteries isolated from premature and newborn baboons to adrenergic and cholinergic stimulation. Life Sci 1984; 35: 253−60.

34 Rinner I, Doods HN, van Charldorp KJ, Davidesko D, van Zwieten PA. Binding of muscarine receptor antagonists to pig coronary smooth muscle. Naunyn-Schmiedeberg's Arch Pharmacol 1988; 337: 146−50.

35 Gluais P, Lonchampt M, Morrow JD, Vanhoutte PM, Feletou M. Acetylcholine-induced endothelium-dependent contractions in the SHR aorta: the Janus face of prostacyclin. Br J Pharmacol 2005; 146: 834−45.

Acta Pharmacologica Sinica (2010) 31: 27–34
© 2010 CPS and SIMM All rights reserved 1671-4083/10 $32.00
www.nature.com/aps

Original Article

Antifibrotic effects of ZK_{14}, a novel nitric oxide-donating biphenyldicarboxylate derivative, on rat HSC-T6 cells and CCl_4-induced hepatic fibrosis

Li DAI[1], Hui JI[1, *], Xiang-wen KONG[2], Yi-hua ZHANG[2, *]

[1]Department of Pharmacology, China Pharmaceutical University, Nanjing 210009, China; [2]Center of Drug Discovery, China Pharmaceutical University, Nanjing 210009, China

Aim: To study the pharmacologic effect of ZK_{14}, a novel nitric oxide-donating biphenyldicarboxylate (DDB) derivative, on HSC-T6 cells and on CCl_4-induced hepatic fibrosis.
Methods: Inhibition of HSC-T6 cell growth by ZK_{14} was evaluated by MTT assay. The effect of ZK_{14} on the percentage of HSC-T6 cells undergoing apoptosis was measured using Annexin-V/PI double-staining and TUNEL assay. Mitochondrial membrane potential (MMP) and caspase activities were tested. Hepatic fibrosis was induced in Sprague-Dawley rats by intraperitoneal injection with 14% CCl_4. Rats with hepatic fibrosis were randomly divided into four groups: model control, ZK_{14} (20 mg/kg), ZK_{14} (10 mg/kg) and DDB (5 mg/kg). Levels of aspartate aminotransferase (AST), alanine aminotransferase (ALT), hyaluronic acid (HA), type III collagen (PCIII), and nitric oxide (NO) were assessed, and liver samples were stained with hematoxylin-eosin. The NO level in cells treated with ZK_{14} *in vitro* was also measured.
Results: The effect of ZK_{14} on HSC-T6 cell apoptosis was concentration- and time-dependent, with up to 50% of cells becoming apoptotic when exposed to 100 μmol/L ZK_{14} for 18 h. ZK_{14} treatment resulted in mitochondrial membrane depolarization and activation of caspases 3 and 9. At a dose of 20 mg/kg, ZK_{14} significantly decreased serum transaminase (AST, ALT) activities and fibrotic index (HA, PCIII) levels and significantly inhibited fibrogenesis.
Conclusion: These data indicate that ZK_{14}, a novel NO-donating DDB derivative, promotes HSC-T6 apoptosis *in vitro* through a signaling mechanism involving mitochondria and caspase activation and it inhibits CCl_4-induced hepatic fibrosis *in vivo*. The results suggest that ZK_{14} has potential therapeutic value in the treatment of hepatic fibrosis.

Keywords: nitric oxide; apoptosis; hepatic fibrosis; HSC-T6; CCl_4; biphenyldicarboxylate; ZK_{14}

Acta Pharmacologica Sinica (2010) 31: 27–34; doi: 10.1038/aps.2009.170; published online 7 December 2009

Introduction

Hepatic fibrosis is a dynamic process resulting from chronic liver injury of diverse etiology (viral, toxic, metabolic, autoimmune) and eventually leads to cirrhosis[1]. During such chronic injury, the perisinusoidal retinoid-storing quiescent hepatic stellate cells (HSCs) transform into retinoid-free proliferating myofibroblast-like cells, which give rise to subpopulations of stellate cells with discrete cytoskeletal and phenotypic profiles and thereby promote a net increase in extracellular matrix[2].

Attention is increasingly focused on the mechanism by which liver fibrosis regresses, and in particular on the fate of activated stellate cells as fibrosis recedes[3]. Liver tissue can undergo regression of fibrosis after withdrawal of the damaging stimulus[4], even at advanced stages of cirrhosis[5]. Gliotoxin, a fungal toxin, can provoke selective apoptosis in HSCs in culture and *in vivo*, leading to reduced fibrosis[6, 7]. However, the clinical usefulness of apoptosis-inducing drugs is limited due to the lack of cell specificity and the risk of severe adverse effects[8, 9]. Thus, although selective induction of apoptosis in HSCs is desirable, it is also important to find drugs that can prevent severe adverse effects such as further loss of liver function during progression of disease.

Biphenyldicarboxylate (DDB), a traditional therapeutic in the treatment of hepatic disease, is an intermediate in the synthesis of schizandrin. It can reduce the activity of glutamic-pyruvic transaminase in serum, is targeted to the liver and can protect injured hepatocytes and increase liver detoxifying function[10, 11]. DDB showed a better hepatoprotective effect than ursodesoxycholic acid and it has been suggested

---

* To whom correspondence should be addressed.
E-mail huijicpu@163.com and zyhtgd@sohu.com
Received 2009-03-17 Accepted 2009-11-02

that it might prove of benefit in the therapy of chronic liver disease[12, 13].

With these considerations in mind, we conjugated DDB to the nitric oxide (NO) donor furoxan, using amino acids as spacers in compound synthesis. We hypothesized that NO-releasing derivatives of DDB might have dual functions, inducing apoptosis in HSC-T6 cells by means of releasing NO and causing protection in hepatocytes by DDB.

Pharmacological analysis of 55 NO-donating DDB derivatives revealed that 4,4′-dimethoxy-5,6,5′,6′-dimethylenedioxy-2-methoxycarbonyl-2′-{*N*-[alanine 2-(3-phenylsulfonyl-1,2,5-oxadiazole-2-oxide-4-) oxyethoxyethyl ester]} carbamoyl biphenyl (ZK_{14}, Figure 1) had the strongest apoptosis-inducing activities *in vitro*[14]. It was therefore selected as the target compound. This study investigates the biological activity and mechanism of action of ZK_{14} in HSC-T6 cells *in vitro* and also evaluates the activity of ZK_{14} in CCl_4-induced male hepatofibrotic rats *in vivo*.

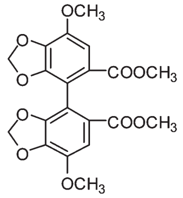

DDB

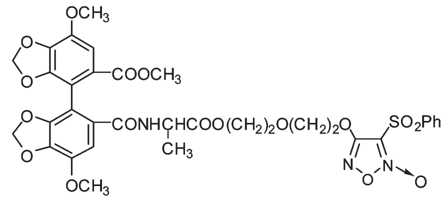

ZK_{14}

Figure 1. Chemical structure of DDB and ZK_{14}.

Materials and methods

Reagents

ZK_{14}, DDB and furoxan monomer (furoxan) were gifts of Prof Yi-hua ZHANG[4]. ZK_{14} was obtained in good yield (98%) and confirmed by ^1H NMR spectra[14]. It was dissolved in dimethyl sulfoxide (DMSO) at a final concentration of 100 mmol/L and stored at -20 ºC. At use, it was freshly diluted with phosphate-buffered saline containing 0.1% DMSO. For each experiment, controls were treated with an identical amount of DMSO.

Cell culture

The HSC-T6 cell line was obtained from Prof SL FRIEDMAN (Liver Disease Research Center of San Francisco General Hospital, CA, USA). HSC-T6 cells were routinely cultured in DMEM (Gibco, USA) supplemented with 10% heat-inactivated fetal bovine serum, 100 IU/mL penicillin and 100 μg/mL streptomycin. Cultures were maintained in a humidified atmosphere of 95% air and 5% CO_2 at 37 ºC; 0.25% trypsin was used for cell passage. The human liver cell line L-02 (Nanjing KeyGen, China) was cultured in RPMI-1640 medium (Gibco, USA).

Viability tests and *in vitro* screening of compounds

HSC-T6 cells were cultured at a density of 5×10^4 cells/mL in 100 μL culture medium in 96-well microplates. After 6, 12, and 18 h of treatment with different doses of various compounds, the culture medium was removed and 20 μL MTT [3-(4,5-dimethylthiazol-2-yl)-2, 5-diphenyl tetrazolium bromide, 5 mg/mL) (MTT, Sigma, USA) was added. Four hours later, the supernatant was discarded and 100 μL DMSO was added to each well. The mixture was shaken and *OD* values were measured at 570 nm using a Universal Microplate Reader (EL800, BIO-TEK Instruments Inc). The extent of inhibition of HSC-T6 proliferation and the IC_{50} of 55 compounds were calculated using the results of the MTT assay; primary screening and evaluation were also performed.

Annexin-V/PI double-staining assay

After treatment with 50 μmol/L ZK_{14} for 12 h, cells were washed and resuspended in PBS. Apoptotic cells were identified using the Annexin V-FITC Apoptosis Detection kit (BD, USA) according to the manufacturer's instructions; early apoptotic cells were labeled with Annexin-V^+/PI^-.

Terminal deoxynucleotidyl transferase-mediated digoxigenin-11-dUTP nick end labeling (TUNEL) assay

After treatment with ZK_{14}, HSC-T6 cells were collected and 50−100 μL of cell suspension was spread onto glass slides. Air-dried samples were fixed with freshly prepared fixation solution for 1 h at 15−25 °C; the slides were then washed with phosphate buffered saline (PBS), incubated with blocking solution for 10 min at 15−25 °C, washed with PBS, incubated in permeabilization solution for 2 min on ice (2−8 °C) and rinsed twice with PBS. The area around the samples was dried and 50 μL TUNEL reaction mixture from the TUNEL Apoptosis Detection Kit (Nanjing KeyGen, China) was added to each sample.

Assessment of mitochondrial membrane potential (MMP)

Pretreated HSC-T6 cells were collected and suspended in 1 mL of complete medium containing 10 μg/mL JC-1 (5,5′,6,6′-tetrachloro-1,1′,3,3′-tetraethylbenzimidazolylcarbocyanineiodide), a fluorescent dye (purchased from Nanjing KeyGen, China), for 30 min at 37 °C. To assess the mitochondrial potential transition, 10 000 cells/sample stained by JC-1 were observed using fluorescence microscopy (Leica, Germane) and flow cytometry.

Colorimetric assay for caspase activities

HSC-T6 cells treated with ZK_{14} were collected and caspase activity of effectors of caspase 3 and 9 was determined using the Caspase Colorimetric Assay Kit (Nanjing KeyGen, China).

Animals and treatments

Male Sprague-Dawley rats weighing 150−180 g were obtained from the animal facility of Nanjing Military Hospital (SCXK2003-0004). All animals were housed in conventional cages under controlled conditions of temperature (23±3 ºC) and relative humidity (50%±20%), with light illumination for 12 h/day. The animals were allowed access to food and tap water *ad libitum* throughout the acclimatization and experimental periods. All experimental protocols described in this study were in accordance with the NIH Guide for the Care and Use of Laboratory Animals, NIH publication No̲ 85–23, 1985.

Following acclimatization for one week after arrival, forty-eight rats were randomly divided into two groups, a normal control group (*n*=6) and an administration group (*n*=42). Animals in the administration group were given drinking water containing phenobarbital sodium (350 mg/L)[15] and were injected intraperitoneally with 0.025 mL CCl_4 (1:6 with olive oil) three times weekly. Rats in the normal control group were injected with the same volume of vehicle. After six weeks, four rats were dead including two that did not tolerate modeling and two that were sacrificed to confirm successful modeling. The remaining thirty-eight rats with successful modeling were randomly divided into a model control group, a ZK_{14} high dose group (20 mg/kg), a ZK_{14} low dose group (10 mg/kg) and a DDB (5 mg/kg) group. All compounds were suspended with 0.5% sodium carboxymethylcellulose and intragastrically administered. To maintain etiology stimulation, CCl_4 was injected once a week during drug administration. After four weeks, blood was collected from all rats by bleeding from the ophthalmic artery and vein. Serum samples were prepared by centrifugation and stored at -70 ºC. Liver tissue specimens were fixed in neutral formalin and embedded in paraffin.

Serum activities of AST and ALT were assayed by standard enzymatic methods, HA and PCIII concentrations were measured with radioimmunoassay (RIA) using a commercial kit (Navy Medical Institute, Shanghai, China). Liver tissue samples were fixed in 40 g/L paraformaldehyde and embedded in paraffin. Hematoxylin and eosin (HE) staining was performed according to standard procedures by the pathology department of Southeast University. The semi-quantitative method used for scoring severity of fibrosis has been previously described[16]. Slides were scored independently by two pathologists with no knowledge of liver sources. The degree of fibrosis was expressed as the mean of ten different fields in each slide.

Measurement of nitrite/nitrate levels *in vitro* and *in vivo*

Because of its active chemical properties, NO was metabolized to NO_2^- and NO_3^- in the culture medium, and NO_2^- was transformed to NO_3^-. NO_3^- was deoxidized to NO_2^- by nitrate reductase in the NO assay kit (JianCheng, Nanjing, China), and the concentration of total NO_2^-, representing the level of NO released from ZK_{14}, was measured by optical density (*OD*) assay. A solution of ZK_{14} (20 µL) in DMSO was added to phosphate buffer (pH 7.4). The final concentration of the compound was 1 µmol/L. After different times of incubation at 37 °C, the *OD* at 540 nm, which represented NO level released from ZK_{14} *in vitro*, was measured. The serum NO level in hepatic fibrosis rats, representing NO released from $ZK_{14,}$ was also assessed.

Statistical analysis

Quantitative data were presented as mean±SD and compared using the Student's *t*-test. The rank-sum test was used for histopathological fibrosis scores. *P*<0.05 was considered statistically significant.

Results

NO donor ZK_{14} inhibited HSC-T6 proliferation

HSC-T6 cells were exposed to different compounds *in vitro* and proliferation of the cells was assessed using the MTT method. Several compounds showed inhibitory effects on HSC-T6 cells; ZK_{14}, which had the lowest IC_{50} (half-maximal inhibitory concentration) (17.83 µmol/L; data not shown) was selected as the target compound.

NO donor ZK_{14} induced HSC-T6 apoptosis

HSC-T6 cells were exposed to NO donor ZK_{14} at different concentrations and for different amounts of time and apoptosis was quantitated via TUNEL and Annexin-V/PI double-staining assays (Figure 2A, 2B). The apoptosis was both concentration- and time-dependent, with up to 70% of the cells becoming apoptotic when exposed to 100 µmol/L ZK_{14} for 18 h (Figure 2C). In all subsequent experiments, the dose of ZK_{14} (50 µmol/L) consistently resulted in an apoptosis rate of about 40% on 18 h exposure (Figure 2C, 2D). ZK_{14} of 1 µmol/L generated a concentration of 0.06 µmol/L of nitrite in 350 min, as measured by nitric reduction assay.

Since NO is a highly reactive free radical, we sought to test whether induction of apoptosis by an NO donor could result in injury to normal liver tissue cells. When exposed to 50 µmol/L ZK_{14}, the apoptotic rate of L-02 cells was relatively low (17%) compared with that of HSC-T6 (Figure 2E). Exposure to ZK_{14} resulted in a higher rate of apoptosis (45%) than exposure to either furoxan (28%) or DDB (9%); these experiments also revealed a synergistic effect of furoxan and DDB on apoptosis induction in HSC-T6 cells (Figure 2F).

NO donor ZK_{14}-mediated apoptosis is related to mitochondrial dysfunction and caspase activation

It has been shown that integrity of mitochondria plays an important role in programmed cell death and that disruption of MMP enhances apoptosis[17]. To probe the mechanism by which NO donor ZK_{14} induced HSC-T6 apoptosis, HSC-T6 cells were treated with ZK_{14} (50 µmol/L) for 12 h and stained with JC-1, a potential-sensitive fluorescent dye. When apoptosis was induced in cells, the mitochondrial membrane was depolarized and JC-1 was released from mitochondria to cytoplasts that gave off weak red and green fluorescence. In normal cells, JC-1 bound to the inner membrane of mitochon-

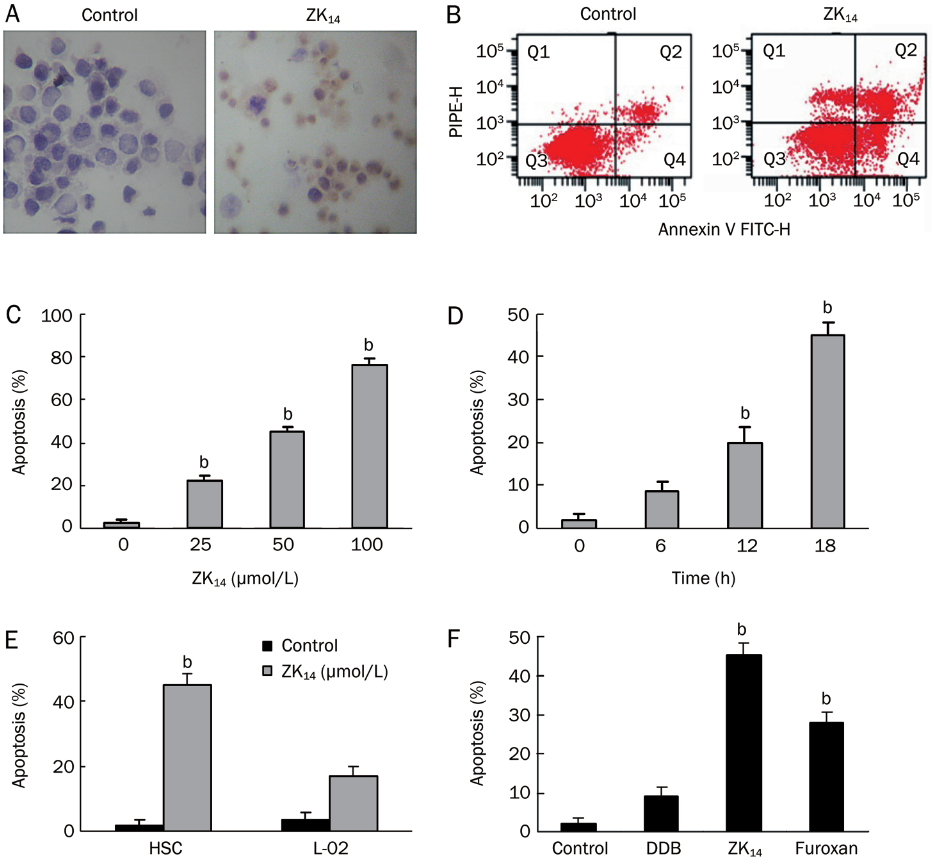

Figure 2. Effect of ZK$_{14}$ on HSC-T6 cells *in vitro*. (A) TUNEL assay of DNA integrity. HSC-T6 cells were pretreated with 50 μmol/L ZK$_{14}$ for 12 h. 3′-OH DNA ends were stained dark brown with DAB. (B) Flow cytometry of apoptosis. HSC-T6 cells displayed increased Annexin-V positivity after exposure to ZK$_{14}$ 50 μmol/L for 12 h. (C) Concentration-dependent apoptosis. HSC-T6 cells were exposed to increasing concentrations of ZK$_{14}$ (0–100 μmol/L) for 18 h. Apoptosis was quantitated by flow cytometry. (D) Time-dependent apoptosis. HSC-T6 cells were exposed to ZK$_{14}$ 50 μmol/L for increasing times. Apoptosis was quantitated by flow cytometry. (E) Apoptosis of HSC-T6 cells and hepatocytes L-02 exposed to ZK$_{14}$ 50 μmol/L for 18 h. (F) HSC-T6 cells were exposed to 50 μmol/L ZK$_{14}$, furoxan, and DDB. *n*=3. Mean±SD. $^{b}P<0.05$ *vs* control.

dria and gave off bright red fluorescence as polymers. FCM analysis showed that the percentage of normal cells labeled by JC-1 was 96.2% (Figure 3A). However, in apoptotic cells, due to depolarization of MMP, JC-1 was released from mitochondria to cytoplasts and decomposed to monomers; as a result, the percentage of cells labeled by JC-1 decreased to 59.7% (Figure 3B). The decreased number of cells labeled by JC-1 in the ZK$_{14}$-treated group indicated loss of MMP.

Caspases (cysteinyl aspartate proteinases) play a major role in apoptosis. Caspase 9 is an upstream molecule, while cas-

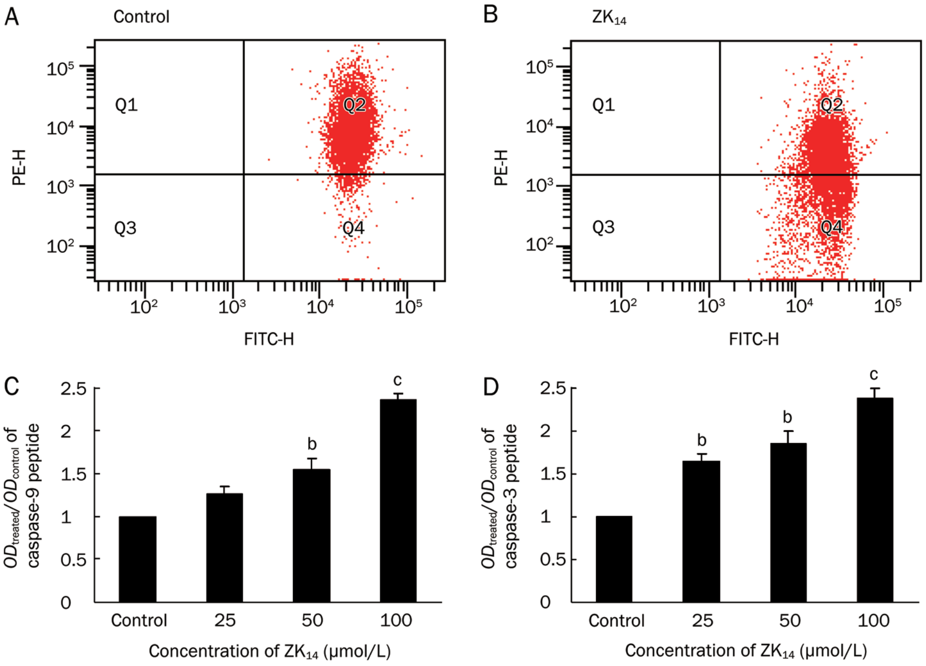

Figure 3. (A, B) Normal HSC-T6 cell percentage labeled with JC-1 in the inner membrane of mitochondria was 96.2%, and decreased to 59.7% when treated with 50 μmol/L ZK$_{14}$ for 18 h. The decreased cells labeled with JC-1 revealed the loss of MMP and subsequently with the apoptosis of HSC-T6 cells. (C, D) Caspase 9 and 3 activity was measured and represented by ratios of $OD_{\text{treated}}/OD_{\text{control}}$ after exposure to ZK$_{14}$ for 18 h. After treated with 25, 50, and 100 μmol/L of ZK$_{14}$ for 12 h, caspase 9 activity increased to 1.26, 1.55, and 2.36, and caspase-3 activity increased to 1.64, 1.85 and 2.38. *n*=3. Mean±SD. $^{b}P<0.05$, $^{c}P<0.01$ *vs* control.

pase 3 is the key executive molecule in the cascade reaction, coupling caspase-specific peptides to chromophoric groups. After treatment with ZK_{14} (0, 25, 50, or 100 μmol/L) for 12 h, the activity of caspase 9 increased from 1 to 1.26, 1.55, and 2.36, respectively (Figure 3C), and the activity of caspase 3 increased to 1.64, 1.85, and 2.38 (Figure 3D). This result shows that the apoptosis induced in HSC-T6 cells was related to enhanced activity of caspases 3 and 9.

NO donor ZK_{14} ameliorated liver injury and fibrosis in CCl_4-induced rats

Table 1 shows levels of liver enzymes and fibrosis markers in CCl_4-treated male rats. Serum levels of ALT and AST are sensitive markers of hepatocyte function. Serum levels of HA and PCIII are surrogate markers of liver fibrogenesis. Compared with normal rats, the model control rats had obvious liver inflammation and formed hepatic pseudolobules due to collagen deposition; these animals also exhibited higher levels of serum ALT, AST, HA, and PCIII (Table 1 and Figure 4). These results show that hepatic fibrosis was successfully induced in rats. ZK_{14} (20 mg/kg) and DDB (5 mg/kg) significantly decreased elevated serum ALT and AST levels, while ZK_{14} (10 mg/kg) had no obvious effect. ZK_{14} (20 mg/kg) caused a significant decrease in serum levels of HA and PCIII, while DDB (5 mg/kg) and ZK_{14} (10 mg/kg) did not have significant effects (Table 1).

On hepatic histological examination, it could be seen that high dose of ZK_{14} (20 mg/kg) significantly inhibited the production of collagen fibers in the livers of rats (Table 2). As shown in Figure 4, the structure of liver tissues was normal in the normal group (Figure 4A). In tissues of the hepatic fibrosis model group, shown in Figure 4B, fibrous septa encircled the hepatic lobule, hepatic pseudolobules were formed, and severe centrilobular fibrosis and fatty changes were also observed. There was mild collagen proliferation. In animals of the model group that received high dose of ZK_{14}, the structure of the hepatic lobules was renewed (Figure 4C). There was no obvious amelioration either in the low dose ZK_{14} group or in the DDB group (Figure 4D, 4E); in these animals, significant fatty change and pseudolobule were observed.

ZK_{14} released NO effectively *in vitro* and *in vivo*

As Figure 5 shows, NO could be stably released from ZK_{14} *in vitro*. The content of NO reached a maximum value of about 0.06 μmol/L and maintained stable levels over the subsequent 350 min. As shown in Table 1, serum NO level increased significantly in ZK_{14} (20 mg/kg) and ZK_{14} (10 mg/kg) groups compared with the normal group, while NO levels in the model and DDB groups did not change.

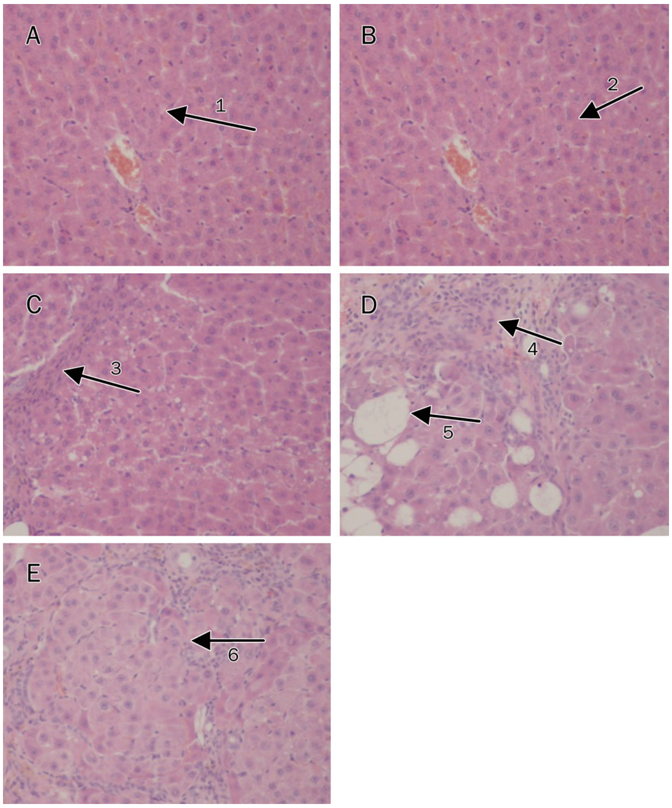

Figure 4. The photomicrographs of liver section taken from rats. (A) Normal group, saline injection only, normal hepatic lobule (arrow 1). (B) Model group, CCl_4 (0.025 mL) injection only, obvious hepatic pseudolobule (arrow 2). (C) ZK_{14} high dose group, CCl_4+ZK_{14} (20 mg/kg), centrilobular fibrosis (arrow 3). (D) ZK_{14} low dose group, CCl_4+ZK_{14} (10 mg/kg), centrilobular fibrosis (arrow 4) and fatty degeneration (arrow 5). (E) DDB group, CCl_4+DDB (5 mg/kg), hepatic pseudolobule (arrow 6). HE stain, ×200.

Discussion

The pharmacological effects of compound ZK_{14}, a novel nitric oxide-donating DDB derivative, were examined *in vitro* and

Table 1. Effects of ZK_{14} on serum ALT, AST, HA, PCIII, and NO level in hepatic fibrosis rats induced by CCl_4. Mean±SD. $^bP<0.05$, $^cP<0.01$ *vs* normal. $^eP<0.05$, $^fP<0.01$ *vs* model.

Groups	Dose (mg/kg)	*n*	ALT (U/L)	AST (U/L)	HA (ng/mL)	PCIII (ng/mL)	NO (μg/L)
Normal	/	6	22.73±3.5	113.35±11.35	248.19±37.53	7.85±2.15	50.69±15.37
Model	/	8	$50.12±12.56^b$	$222.83±25.36^b$	$1017.45±52.84^c$	$35.36±9.70^c$	42.34±14.21
ZK_{14}	20	10	$35.74±7.05^e$	$145.19±34.77^e$	$422.27±56.23^f$	$20.93±6.73^f$	$154.84±29.49^c$
ZK_{14}	10	10	47.16±25.72	208.41±32.45	957.62±52.01	39.88±8.45	$96.67±20.45^b$
DDB	5	10	$27.47±30.37^e$	$136.79±30.43^e$	967.46±66.32	32.72±8.78	46.88±12.20

Table 2. Effects of ZK_{14} on the pathologic grading of hepatic fibrosis rats induced by CCl_4. $P<0.01$, compared with normal group. $P<0.05$, compared with model group.

Groups	Dose (mg/kg)	*n*	Pathologic grading of hepatic fibrosis 0	I	II	III	IV	*P*
Normal	/	6	10	0	0	0	0	–
Model	/	8	0	0	3	4	3	<0.01
ZK_{14}	20	10	0	1	6	3	0	<0.05
ZK_{14}	10	10	0	1	2	5	2	–
DDB	5	10	0		3	6	2	–

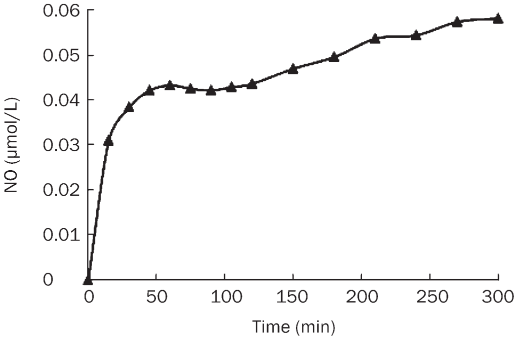

Figure 5. NO releasing from ZK_{14} *in vitro*. ZK_{14} was dissolved in DMSO and reached the concentration of 1 μmol/L. The maximum releasing content of NO was about 0.06 μmol/L, and maintained stable levels in subsequent 350 min.

in vivo. Our studies showed significant apoptosis-inducing activity of ZK_{14} in HSC-T6 *in vitro*, as reflected by decreased MMP and increased caspase-3 and 9 activities. Furthermore, high doses of ZK_{14} (20 mg/kg) showed anti-fibrotic as well as hepatocyte-protective activity in CCl_4-induced male hepatofibrotic rats.

NO is a highly reactive free radical capable of mediating a multitude of reactions; it is produced by the catalytic reaction of L-lysine via nitric oxide synthases or generated from synthetic NO-releasing compounds such as furoxan, nitrate, diazeniumdiolate and others. Compound ZK_{14}, which we synthesized with the NO donor furoxan, could release NO stably *in vitro* in 350 min. Furthermore, serum NO level increased remarkably in animals treated with high or low doses of ZK_{14}. These results show that NO can be released from ZK_{14} both *in vitro* and *in vivo*, and demonstrate that ZK_{14} is an efficacious NO donor.

NO generated from endothelial NO synthase (eNOS) in turn exerts paracrine effects on adjacent HSCs, culminating in the inhibition of vasoconstriction, proliferation, and migration[18–20]. Recent studies suggest that NO promotes HSC apoptosis through a signaling mechanism that involves mitochondria and that occurs independently of caspase activation[21].

Our study *in vitro* showed that the apoptosis induced by NO donor ZK_{14} was both concentration- and time-dependent. When exposed to ZK_{14} (50 μmol/L), the apoptotic rate in HSC-T6 cells was about 40%, while that in L-02 cells was moderately low (17%). This shows that apoptosis induced by ZK_{14} is not cell-specific, and that to improve cell-selectivity, synthesis of a different compound is needed.

NO can pass through cell membranes due to its water-soluble and lipid-soluble properties; inside cells, it acts on target molecules and induces apoptosis[22–24] in various cells and tissues. NO can directly induce cytochrome *c* release through MMP loss, and released cytochrome *c* can activate the caspase-dependent apoptotic signaling cascade[25]. NO-induced apoptosis occurs by two separate pathways: caspase-dependent and caspase-independent. The caspase-dependent pathway can be either intrinsic or extrinsic in nature. The intrinsic pathway is stimulated by apoptotic stimuli, including radiation and the 2–5A/RNase L/RNase L inhibitor (RNI), leading to the loss of MMP and release of cytochrome *c* into the cytosol. Along with ATP, apoptotic protease activating factor-1 (Apaf-1) and procaspase-9, cytochrome *c* directs the activation of the initiator caspase 9 followed by the processing of procaspase-3 and its activation. Thus, apoptosis occurs downstream of active caspase 3.

When treated with ZK_{14}, the MMP of HSC-T6 cells decreased and the activities of caspase 3 and 9 increased. This result shows that the mechanism of apoptosis induced by ZK_{14} in HSC-T6 is related to the intrinsic caspase-dependent pathway. It is likely that when NO was released from ZK_{14}, MMP decreased and cytochrome *c* activated caspase 9 and subsequently caspase-3, which initiated apoptosis in HSC-T6 cells.

Serum levels of HA and PCIII are surrogate markers of liver fibrogenesis. Significant amelioration in serum markers of liver fibrogenesis and in hepatic histological pathology occurred in the ZK_{14} high-dose group (20 mg/kg), while no significant effects were observed in the DDB group (5 mg/kg) or the ZK_{14} low-dose group (10 mg/kg). This result suggests that apoptosis induced by NO generated from ZK_{14} resulted in subsequent elimination of activated HSCs and extracellular matrix, with collagen fibers being destroyed and absorbed and the structure of the hepatic lobules renewed.

Serum levels of ALT and AST are sensitive markers of hepatocyte function. We observed significant decreases in serum ALT and AST levels in the ZK_{14} high dose group (20 mg/kg) and in the DDB group (5 mg/kg), with no obvious effect in the ZK_{14} low dose group (10 mg/kg). This suggests a protective effect of ZK_{14} on liver function in hepatic fibrosis due to mother nucleus DDB.

As a synthetic commercial hepatoprotectant, DDB has been widely used to treat chronic viral hepatitis B patients in China for more than 20 years. Oral administration of DDB significantly prevented the occurrence of erythromycin-induced liver damage[26]. DDB directly inhibited IFN-alpha signaling-mediated replication of HBV in infected hepatocytes[27]. DDB could exert its biochemical effects through enhancement of antioxidant enzyme activities and reduction of glutathione levels as well as by decreasing lipid peroxides[28, 29]. DDB might inhibit inflammatory responses in association with reduction of NF-kappa B activation through prevention of I-kappa B alpha degradation and subsequent TNF-alpha production[30].

By contrast, apoptosis induced by ZK_{14} in HSC-T6 cells *in vitro* was attributed to NO; DDB treatment did not induce apoptosis effectively (Figure 2F). We considered that by virtue of its anti-inflammatory and anti-immune properties, DDB would exert its role of protecting liver and reducing enzyme levels *in vivo* rather *in vitro*. In animal experiments, high-dose of ZK_{14} and DDB exhibited preferable liver protection, while ZK_{14} did not exert its protecting effects against apoptosis of L-02 cells *in vitro*.

Depending on its concentration, NO can have pro- or anti-apoptotic properties. High NO concentrations promote apoptosis in most cases, whereas low NO concentrations can result in resistance to apoptosis[24]. There was no significant reduction in liver fibrosis in the ZK_{14} low-dose group (10 mg/kg). This might be because a low NO concentration released in this group was insufficient to induce apoptosis, and instead inversely induced proliferation of HSC and caused aggravation of liver fibrosis.

In conclusion, we performed a primary screening and evaluation of ZK_{14} as a novel NO donor compound and found it was effective both *in vitro* and *in vivo*. ZK_{14} promoted apoptosis in HSC-T6 cells by releasing NO and activating a signaling mechanism that involved mitochondrial dysfunction and caspase activation. Furthermore, ZK_{14} could alleviate the syndrome of hepatic fibrosis *in vivo*, and protect liver function by DDB. These results demonstrate that ZK_{14}, a novel nitric oxide-donating DDB derivative, has effective antifibrotic activity both *in vitro* and *in vivo*. We hope our experiments will provide novel support for the use of apoptosis induction for active HSC in therapy of hepatic fibrosis.

Acknowledgements

This work was supported in part by the Research Fund for the Doctoral Program of Higher Education (No 20070316007).

Author contribution

Hui JI and Li DAI designed research; Li DAI performed research, analyzed data and wrote the paper; Yi-hua ZHANG and Xiang-wen KONG contributed key compounds.

References

1 Yao HW, Li J, Chen JQ, Xu SY. Inhibitory effect of leflunomide on hepatic fibrosis induced by CCl_4 in rats. Acta Pharmacol Sin 2004; 25: 915–20.

2 Friedman SL. Liver fibrosis – from bench to bedside. J Hepatol 2003; 38: S38–S53.

3 Iredale JP, Benyon RC, Pickering J, McCullen M, Northrop M, Pawley S, *et al*. Mechanisms of spontaneous resolution of rat liver fibrosis: hepatic stellate cell apoptosis and reduced hepatic expression of metalloproteinase inhibitors. J Clin Invest 1998; 102: 538–49.

4 Issa R, Zhou X, Constandinou CM, Fallowfield J, Millward-Sadler H, Gaca MDA, *et al*. Spontaneous recovery from micronodular cirrhosis: evidence for incomplete resolution associated with matrix cross-linking. Gastroenterology 2004; 126: 1795–808.

5 Friedman SL. Hepatic fibrosis-overview. Toxicology 2008; 3: 120–9.

6 Dekel R, Zvibel I, Brill S, Brazovsky E, Halpern Z, Oren R. Gliotoxin ameliorates development of fibrosis and cirrhosis in a thioacetamide rat model. Dig Dis Sci 2003; 48: 1642–7.

7 Wright MC, Issa R, Smart DE, Trim N, Murray GI, Primrose JN, *et al*. Gliotoxin stimulates the apoptosis of human and rat hepatic stellate cells and enhances the resolution of liver fibrosis in rats. Gastroenterology 2001; 121: 685–98.

8 Beljaars L, Meijer DK, Poelstra K. Targeting hepatic stellate cells for cell-specific treatment of liver fibrosis. Front Biosci 2002; 7: e214–22.

9 Hagens WI, Olinga P, Meijer DK, Groothuis GM, Beljaars L, Poelstra K. Gliotoxin non-selectively induces apoptosis in fibrotic and normal livers. Liver Int 2006; 26: 232–9.

10 Fu TB, Liu GT. A research on protective effect of biphenyl dimethyl dicaboxylate on injured hepatocytes. Nat Med J China 1990; 7: 201–4.

11 Wang MR, Jia KM. A study on protective effect of biphenyl dimethyl dicaboxylate (BOD) on ultrastructure of human fetal hepatocytes injured by CCl_4. Med J Chin People's Liberation Army 1990; 15: 436–8.

12 Abdel-Hameid NA. Protective role of dimethyl diphenyl bicarboxylate (DDB) against erythromycin induced hepatotoxicity in male rats. Toxicol *In Vitro* 2007; 21: 618–25.

13 Abdel-Salam OM, Sleem AA, Morsy FA. Effects of biphenyldimethyl-dicarboxylate administration alone or combined with silymarin in the CCl_4 model of liver fibrosis in rats. ScientificWorldJournal 2007; 7: 1242–55.

14 Kong XW, Zhang YH, Dai L, Ji H. Synthesis and biological evaluation of nitric oxide-releasing sixalkoxyl biphenyl derivatives as anticancer agents. Chin Chem Lett 2008, 19: 149–52.

15 McLean EK, McLean AE, Sutton PM. Instant cirrhosis. An improved method for producing cirrhosis of the liver in rats by simultaneous administration of carbon tetrachloride and phenobarbitone. Br J Exp Pathol 1969, 50: 502–6.

16 Wang H, Wei W, Wang NP, Wu CY, Yan SX, Yue L, *et al*. Effects of total glucosides of peony on immunological hepatic fibrosis in rats. World J Gastroenterol 2005; 11: 2124–9.

17 Qiao AM, Ikejima T, Tashiro S, Onodera S, Zhang WG, Wu YL. Involvement of mitochondria and caspase pathways in N-demethyl-clarithromycin-induced apoptosis in human cervical cancer HeLa cell. Acta Pharmacol Sin 2006; 27: 1622–9.

18 Perri RE, Langer DA, Chatterjee S, Gibbons SJ, Gadgil J, Cao S, *et al*. Defects in cGMP-PKG pathway contribute to impaired NO-dependent responses in hepatic stellate cells upon activation. Am J Physiol Gastrointest Liver Physiol 2006; 290: G535–G542.

19 Failli P, De FR, Caligiuri A, Gentilini A, Romanelli RG, Marra F, *et al*. Nitrovasodilators inhibit platelet-derived growth factor-induced proliferation and migration of activated human hepatic stellate cells. Gastroenterology 2000; 119: 479–92.

20 Lee JS, Decker N, Chatterjee S, Yao J, Friedman S, Shah V. Mechanisms of nitric oxide interplay with Rho GTPase family members in modulation of actin membrane dynamics in pericytes and fibroblasts. Am J Pathol 2005; 166: 1861–70.

21 Langer DA, Das A, Semela D, Kang-Decker N, Hendrickson H, Bronk SF. Nitric oxide promotes caspase-independent hepatic stellate cell apoptosis through the generation of reactive oxygen species. Hepatology 2008; 47: 1983–93

22 Wang YF, Tian H, Tang CS, Jin HF, Du JB. Nitric oxide modulates hypoxic pulmonary smooth muscle cell proliferation and apoptosis by regulating carbon monoxide pathway. Acta Pharmacol Sin 2007; 28:

28–35.
23 Vieira H, Kroemer G. Mitochondria as targets of apoptosis regulation by nitric oxide. IUBMB Life 2003; 55: 613–6.
24 Rishi L, Dhiman R, Raje M, Majumdar S. Nitric oxide induces apoptosis in cutaneous T cell lymphoma (HuT-78) by downregulating constitutive NF-κB. Biochim Biophys Acta 2007; 1770: 1230–9.
25 Bonavida B, Khineche S, Huerta-Yepez S, Garbán H. Therapeutic potential of nitric oxide in cancer. Drug Resist Updat 2006; 9: 157–73.
26 Abdel-Hameid NA. Protective role of dimethyl diphenyl bicarboxylate (DDB) against erythromycin induced hepatotoxicity in male rats. Ai Zheng 2006; 25: 1464–9.
27 Joo SS, Won TJ, Kim MJ, Hwang KW, Lee do I. Interferon signal transduction of biphenyl dimethyl dicarboxylate/amantadine and anti-HBV activity in HepG2 2.2.15. J Biochem Mol Biol 2005; 38: 300–6.
28 El-Beshbishy HA. The effect of dimethyl dimethoxy biphenyl dicarboxylate (DDB) against tamoxifen-induced liver injury in rats: DDB use is curative or protective. East Mediterr Health J 2002; 8: 95–104.
29 el-Sawy SA, el-Shafey AM, el-Bahrawy HA. Effect of dimethyl diphenyl bicarboxylate on normal and chemically-injured liver. Yao Xue Xue Bao 2001; 36: 493–7.
30 Kim SG, Kim HJ, Choi SH, Ryu JY. Inhibition of lipopolysaccharide-induced I-kappaB degradation and tumor necrosis factor-alpha expression by dimethyl-4,4′-dimethoxy-5,6,5′,6′-dimethylene dioxybiphenyl-2,2′-dicarboxylate (DDB): minor role in hepatic detoxifying enzyme expression. Mol Cell Biochem 2000; 205: 111–4.

Acta Pharmacologica Sinica (2010) 31: 35–42
© 2010 CPS and SIMM All rights reserved 1671-4083/10 $32.00
www.nature.com/aps

Original Article

Atorvastatin improves insulin sensitivity in mice with obesity induced by monosodium glutamate

Ning ZHANG, Yi HUAN, Hui HUANG, Guang-ming SONG, Su-juan SUN, Zhu-fang SHEN*

Institute of Materia Medica, Chinese Academy of Medical Science & Peking Union Medical College, Beijing 100050, China

Aim: To examine the mechanisms underlying the effects of atorvastatin on glucose and lipid metabolism.
Methods: Mice with insulin resistance and obesity induced by monosodium glutamate (MSG) were used. Atorvastatin (80 $mg\cdot kg^{-1}\cdot d^{-1}$) or vehicle control treatment was given orally once a day for 30 days. Plasma levels of total cholesterol, triglycerides, low-density lipoprotein cholesterol (LDL-C), high-density lipoprotein cholesterol (HDL-C), and free fatty acids were monitored. Serum insulin and glucose concentrations were used to calculate the insulin resistance index and insulin sensitivity index using a homeostasis model. Body length, waistline circumference, intraperitoneal adipose tissue mass, and total body mass were measured. Semi-quantitative RT-PCR and Western analysis were used to determine the expression of inflammatory factors and proteins involved in inflammation signaling pathways.
Results: Atorvastatin improved insulin sensitivity, ameliorated glucose tolerance, and decreased plasma levels of total cholesterol, triglycerides, LDL-C, HDL-C and free fatty acids. Semi-quantitative RT-PCR and Western analysis revealed increased expression of interleukin 6 (IL-6) and tumor necrosis factor α (TNF-α) in serum and adipose tissue in MSG obese mice. Atorvastatin treatment decreased expression of IL-6, TNF-α, nuclear factor κB (NF-κB) and I-kappa-B (IκB) kinase-β, but increased the expression of IκB, in adipose tissue.
Conclusion: Atorvastatin is a potential candidate for the prevention and therapy of diseases associated with insulin resistance such as type 2 diabetes mellitus and cardiovascular disease. One possible mechanism underlying the effects of atorvastatin on glucose and lipid metabolism may be to ameliorate a state of chronic inflammation.

Keywords: atorvastatin; insulin resistance; HMG-CoA reductase inhibitor; monosodium glutamate; obesity

Acta Pharmacologica Sinica (2010) 31: 35–42; doi: 10.1038/aps.2009.176; published online 21 December 2009

Introduction

Obesity is frequently associated with metabolic syndrome, a disease state that includes glucose intolerance, insulin resistance, hypertension, hypertriglyceridemia, low level of high-density lipoprotein cholesterol (HDL-C), and type 2 diabetes mellitus (T2DM)[1]. Low-grade inflammation is associated with insulin resistance and precedes the onset of T2DM in obese individuals[2]. Adipose tissue is an important endocrine organ that regulates the insulin sensitivity of other peripheral insulin target tissues[3]. Excess adipose tissue, especially in the visceral compartment, results in excess secretion of peptide hormones and cytokines, which leads to whole-body insulin resistance and predisposes to T2DM[4].

Tumor necrosis factor α (TNF-α), interleukin 6 (IL-6), and monocyte chemotactic protein 1 (MCP-1) are some of the inflammatory signaling molecules that may contribute to insulin resistance. TNF-α may enhance Ser^{307} phosphorylation of insulin receptor substrate 1 (IRS-1) proteins or other downstream effectors of the insulin signaling cascade that play negative regulatory roles in insulin action. Serine phosphorylation impairs insulin-stimulated tyrosine phosphorylation of IRS proteins, uncouples insulin signal transduction, and has been implicated in the development of insulin resistance[5–7].

Previously, Hong[8] implicated the signaling pathway of the transcription factor, nuclear factor κB (NF-κB), in the induction of insulin resistance. I-kappa-B (IκB) kinase (IKK) plays an important role in this pathway. IKKs, together with their upstream activating kinases, mediate signaling to NF-κB from a diverse array of stimuli, including TNF-α. TNF-α activates IKKs, which can in turn phosphorylate IκBs (the inhibitors of NF-κB) and activate NF-κB. Increased NF-κB activity upregulates multiple inflammatory factors that aggravate insulin resistance[9].

Statins, the inhibitors of 3-hydroxy-3-methyl glutaryl coenzyme A reductase (HMG-CoA) appear to have a number of potentially beneficial effects[10], some of which are indepen-

---

* To whom correspondence should be addressed.
E-mail shenzhf@imm.ac.cn
Received 2009-08-03 Accepted 2009-11-12

dent of their cholesterol-lowering effect. Some effects include improved endothelial function, anti-thrombotic and anti-proliferative effects, stabilization of atherosclerotic plaque, anti-cancer and anti-oxidant effects, and anti-inflammation. Regarding anti-inflammatory activity, statins may down-regulate activation of NF-κB in human endothelial and vascular smooth muscle cells[11]. By reducing the activity of this stimulator of IKK signaling, the anti-inflammatory consequences of statins may have benefits in insulin resistance. Therefore, we investigated the effects of atorvastatin, an HMG-CoA reductase inhibitor, on insulin resistance, glucose concentration, and lipid levels in an insulin-resistant mouse model of obesity.

Materials and methods

Reagents

Atorvastatin was obtained from Aifeimu Chemical Co (Zhejiang, China). Monosodium glutamate (MSG) was obtained from Huaboyuan Technologic Development Center (Beijing). RNA_{in} protection liquid was from Applygen Technologies (Beijing). TRIzol reagent, random hexamer primers, and Superscript II reverse transcriptase were obtained from Invitrogen (Carlsbad, CA). Primary antibodies for NF-κB p65 and IκB-α were from Santa Cruz Biotechnology, Inc (Santa Cruz, CA). All other regents used in this paper were from Sigma Aldrich (St Louis, MO).

Animals and experimental protocol

Pregnant ICR mice were purchased from the Experimental Animal Center, Chinese Academy of Medical Sciences (Beijing), and cared for in accordance with the standards for laboratory animals established by the People's Republic of China (GB14925-2001). Monosodium glutamate (MSG) was subcutaneously injected in neonatal mice at 4 g/kg body weight once daily for 7 consecutive days after birth to induce obesity. Only mice with impaired insulin tolerance were used in this study[12]. Female and 6 months mice were divided into two groups (n=8 mice each) for treatment with vehicle (water) or atorvastatin (80 mg/kg), by oral administration. Treatment was given orally for 30 consecutive days, and mice underwent an insulin tolerance test (ITT) and oral glucose tolerance test (OGTT) and monitoring for plasma levels of cholesterol and triglycerides. On the last day of the experiment, mice were sacrificed by decapitatation. Plasma was collected for measurement of LDL-C, HDL-C, IL-6, and TNF-α. Body length, whole body mass, intraperitoneal adipose mass and waistline circumference were measured. The waistline index (waistline to body length) was calculated. Samples of plasma and adipose tissue were stored at -70 °C. Intraperitoneal adipose tissue was stored in an RNA protection liquid, RNA_{in}, at -70 °C for later semi-quantitative RT-PCR analysis. Eight female ICR mice were used as normal non-obese controls.

Oral glucose tolerance test (OGTT) and insulin tolerance test (ITT)

After 10 days of oral atorvastatin treatment, obese mice were fasted 2 h before the OGGT. Two hours after atorvastatin (80 mg/kg) or vehicle (water) treatment, initial blood samples were drawn. Then, glucose (2 g/kg) was administered orally. Subsequent blood samples were taken at 0, 30, 60, and 120 min. The ITT was preceded by 20 days of atorvastatin or vehicle treatment. Fasted mice were given 0.4 U of insulin intraperitoneally, and then blood samples were taken at 0, 40, and 90 min. Plasma glucose concentrations were measured by the glucose oxidase method. The areas under the curve (AUC) from blood glucose recordings were calculated.

Biochemical analysis

Plasma levels of total cholesterol, triglycerides, LDL-C, HDL-C, and free fatty acids (FFAs) were determined by enzymatic colorimetric methods with commercial kits (Biosino Bio-Technology and Science Inc, Beijing). Plasma insulin (PI) was measured with a radioimmunoassay kit (Chinese Institute of Atomic Energy, Beijing). Adipose tissue samples were homogenized in ice-cold PBS buffer containing 10 mmol/L sodium fluoride, 10 μg/mL leupeptin, and 10 μg/mL aprotinin and centrifuged at 14000×g for 15 min and the supernatants were collected for assay. The concentrations of TNF-α and IL-6 in plasma and adipose tissue were measured with a radioimmunoassay kit (North TZ-Biotech, Beijing).

Insulin resistance and insulin sensitivity index calculations

The homeostasis model assessment was used to calculate the insulin resistance (HOMA-IR) index and insulin sensitivity index (ISI) using the values of fasting plasma glucose (FPG) and PI as follows: ISI=1/(FPG×PI)×1000, with FPG expressed as mg/dL and PI as mU/L; HOMA-IR=FPG×PI/22.5, with FPG expressed as mmol/L and PI as mU/L.

RNA preparation and semi-quantitative RT-PCR

Total RNA was isolated from mouse adipose tissue with TRIzol reagent (Invitrogen, Carlsbad, CA). First-strand cDNA was synthesized from 5 μg of total RNA with random hexamer primers and Superscript II reverse transcriptase (Invitrogen). The reaction mixture was amplified with primers specific for inflammatory factors and proteins (Table 1) in a total volume of 20 μL. Linearity of the PCR amplification was tested with amplification cycles between 32 and 40. The PCR products were analyzed on a 2% agarose gel, and the intensity of the corresponding bands was determined using a Kodak image station 440CF and 1D image analysis software (Eastman Kodak; Rochester, NY). mRNA expression of the genes was normalized to that of GAPDH[13].

Adipose tissue homogenization and Western analysis

Adipose tissue samples were homogenized in ice-cold buffer containing 50 mmol/L HEPES (pH 7.6), 150 mmol/L sodium chloride, 20 mmol/L beta-glycerophosphate, 10 mmol/L sodium fluoride, 2 mmol/L EDTA, 10% glycerol, 1 mmol/L magnesium chloride, 1 mmol/L calcium chloride, 10 μg/mL leupeptin, and 10 μg/mL aprotinin. Tissue homogenates were clarified by centrifugation at 14000×g for 15 min, and protein concentrations in the supernatant were determined with a

Table 1. Primers used for RT-PCR of inflammatory factors and proteins in monosodium glutamate (MSG)-induced obese mice with insulin resistance.

Target gene	Forward primer	Reverse primer
GAPDH	5′-AGGTCGGTGTGAACGGATTTG-3′	5′-TGTAGACCATGTAGTTGAGGTCA-3′
NF-κB p65	5′-AGGCTTCTGGGCCTTATGTG-3′	5′-TGCTTCTCTCGCCAGGAATAC-3′
IκB-α	5′-TGAAGGACGAGGAGTACGAGC-3′	5′-TTCGTGGATGATTGCCAAGTG-3′
IKK-β	5′-ACAGCCAGGAGATGGTACG-3′	5′-CAGGGTGACTGAGTCGAGAC-3′
TNF-α	5′-CCCTCACACTCAGATCATCTTCT-3′	5′-GCTACGACGTGGGCTACAG-3′
IL-6	5′-TAGTCCTTCCTACCCCAATTTCC-3′	5′-TTGGTCCTTAGCCACTCCTTC-3′

Bradford assay. Proteins in the supernatants of the tissue homogenates were resolved by SDS-PAGE and transferred to PVDF membrane. Bound proteins were blocked with 1% nonfat dry milk in Tris-buffered saline with 0.1% Tween 20, and probed with specific primary antibodies (NF-κB p65 and IκB-α from Santa Cruz). The membranes were washed with Tris-buffered saline with 0.5% Tween 20, then incubated with horseradish peroxidase-conjugated secondary antibody (Promega Corp, Madison, WI). Proteins were visualized by chemiluminescence reactions, and the intensity of the corresponding bands was analyzed with a Kodak image station 440CF and 1D image analysis software (Eastman Kodak). The expression of proteins was normalized to that of GAPDH[14].

Statistical analysis

Results are presented as means±SEM. Statistical significance of differences was assessed by ANOVA, followed by the *t*-test. $P<0.05$ was considered statistically significant. All analyses were performed using SPSS version 13.0.

Results

Insulin tolerance

Plasma glucose levels after insulin injection were significantly lower in the obese mice treated with atorvastatin (80 mg/kg) than those in the vehicle-treated control obese mice at all times tested. As shown in Figure 1B the mean AUC for glucose was significantly reduced after atorvastatin treatment, compared to the control treatment ($n=8$, $P<0.01$, Figure 1).

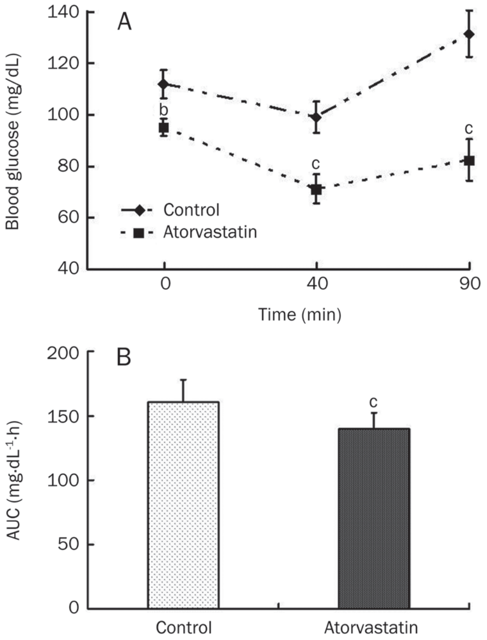

Figure 1. Effect of atorvastatin on insulin tolerance in MSG-induced obese mice with insulin resistance. (A) Mean blood glucose; (B) Mean area under the curve (AUC) by insulin tolerance test (ITT). Obese mice were challenged with oral glucose as described in the materials and methods, and blood glucose measured at the indicated times by tail blood sampling. Obese mice ($n=8$ /per group) were treated and untreated with atorvastatin (80 $mg·kg^{-1}·d^{-1}$) for 20 d. Results show means±SEM. $^bP<0.05$, $^cP<0.01$ compared with groups untreated with atorvastatin.

Oral glucose tolerance

Compared to the control treatment, atorvastatin treatment produced lower blood glucose concentrations before and 30, 60 and 120 min after glucose loading (Figure 2A), and reduced the mean glucose AUC (Figure 2B).

Effect of atorvastatin on plasma lipid profile

On day 12, obese mice treated with atorvastatin showed significantly lower plasma levels of total cholesterol, LDL-C and HDL-C than the control obese mice ($P<0.01$). The atorvastatin treated mice also had markedly lower levels of triglycerides and FFAs ($P<0.05$, Table 2).

Characteristics of MSG-induced obese mice

The physical characteristics of the normal non-obese mice and the obese mice treated with either atorvastatin or vehicle control are shown in Table 3. Normal non-obese mice were lean and had a smaller waistline circumstance, body weight and smaller waistline index than MSG-induced obese mice treated with vehicle control ($P<0.01$). Vehicle control-treated obese mice had more intraperitoneal fat and a greater intraperitoneal fat index than did non-obese mice ($P<0.01$). Atorvastatin treatment had no effect on body weight, body length, waistline, or intraperitoneal fat weight and index as compared with vehicle control treatment in obese mice.

Effect of atorvastatin on inflammatory factors in plasma and adipose tissue

The concentrations of IL-6 and TNF- α in serum and adipose

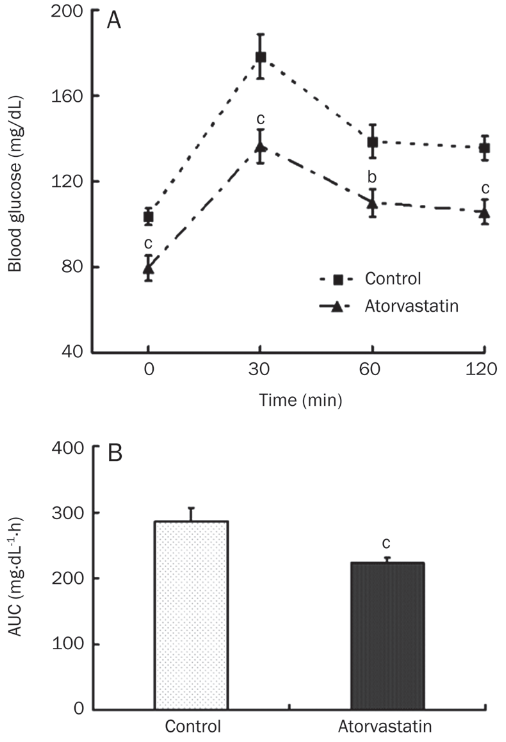

Figure 2. Effect of atorvastatin on glucose tolerance in MSG-induced obese mice with insulin resistance. (A) Mean blood glucose; (B) Mean area under the curve (AUC) by oral glucose tolerance test (OGTT). Mice (*n*=8/per group) were treated with atorvastatin (80 mg·kg^{-1}·d^{-1}) for 10 d. *n*=8. All data are represented by means±SEM. [b]*P*<0.05, [c]*P*<0.01 *vs* control group.

tissue are shown in Table 4. The serum concentration of IL-6 and TNF-α in vehicle control-treated obese mice was similar to that in normal non-obese mice. The atorvastatin-treated obese mice showed no difference in content from the vehicle-control treated obese mice. The adipose-tissue concentrations of IL-6 and TNF-α were significantly greater in vehicle-treated control obese mice than in normal non-obese mice (*n*=8, *P*<0.01). Thirty-day atrovastatin treatment produced significantly lower adipose-tissue concentrations of IL-6 and TNF-α compared to vehicle control treatment in the obese mice (*n*=8, *P*<0.05).

Homeostasis model assessment of insulin resistance (HOMA-IR) index and insulin sensitivity index (ISI)

The calculated values for the insulin resistance index and insulin sensitivity index are shown in Table 5. Fasting serum insulin levels were significant higher in vehicle treated control obese mice than in normal non-obese mice. The HOMA-IR index was also higher in vehicle treated control mice than in normal non-obese mice (*n*=8, *P*<0.001). The ISI for vehicle treated control mice was lower than that for normal non-obese mice (*n*=8, *P*<0.001). Atorvastatin treatment decreased the HOMA-IR index and increased the ISI compared to vehicle control treatment in obese mice (*P*<0.05, *P*<0.01, respectively) (Table 5).

Semi-quantitative RT-PCR analysis of inflammatory factors

A semi-quantitative analysis of the expression of factors involved in inflammation pathways are shown in Figure 3. The expression of TNF-α and IL-6 was higher in the vehicle-treated control obese mice than in normal non-obese mice (Figure 3B, 3C), and the expression of IκB was lower in vehicle treated obese controls than in normal non-obese mice (Figure 3E). Atorvastatin treatment decreased the expression of TNF-α, IL-6, NF-κB, and IKK-β (*P*<0.01, *P*=0.08, *P*<0.05, *P*<0.01, respectively) and enhanced of the expression of IκB

Table 2. Effect of atorvastatin on lipid metabolism in MSG-induced obese mice with insulin resistance. All data are represented by mean±SEM. Mice were treated with atorvastatin for 30 d. *n*=8 mice/group. [b]*P*<0.05, [c]*P*<0.01 *vs* control-treated obese mice.

Group	Triglycerides (mg/dL)	Total cholesterol (mg/dL)	LDL-C (mg/dL)	HDL-C (mg/dL)	Free fatty acids (μEq/L)
Control	79.9±5.1	103.9±7.8	16.7±1.0	77.7±6.4	415.7±15.9
Atorvastatin (80 mg/kg)	63.8±4.1[b]	59.3±5.4[c]	10.4±0.8[c]	37.5±2.9[c]	352.0±24.3[b]

LDL-C, low-density lipoprotein cholesterol; HDL-C, high-density lipoprotein cholesterol.

Table 3. Effect of atorvastatin on body characteristics of MSG-induced obese mice with insulin resistance. Data are mean±SEM. Mice were treated with atorvastatin for 30 d. *n*=8 mice/group. [b]*P*<0.05, [c]*P*<0.01 *vs* control obese mice.

Group	Body weight (g)	Body length (cm)	Waistline (cm)	Intraperitoneal fat (g)	Waistline index	Intraperitoneal fat index
Normal non-obese	30.7±2.4	10.1±0.3[b]	8.73±0.42[c]	0.600±0.100[c]	0.86±0.062[c]	0.02±0.003[c]
Control	63.0±7.5	10.9±0.5	13.24±0.77	6.650±1.753	1.21±0.090	10.54±2.416
Atorvastatin (80 mg/kg)	59.7±6.2	10.5±0.3	12.80±0.85	6.600±1.125	1.22±0.077	11.05±1.413

Waistline index=waistline circumference/body length. Intraperitoneal fat index is intraperitoneal fat/body weight.

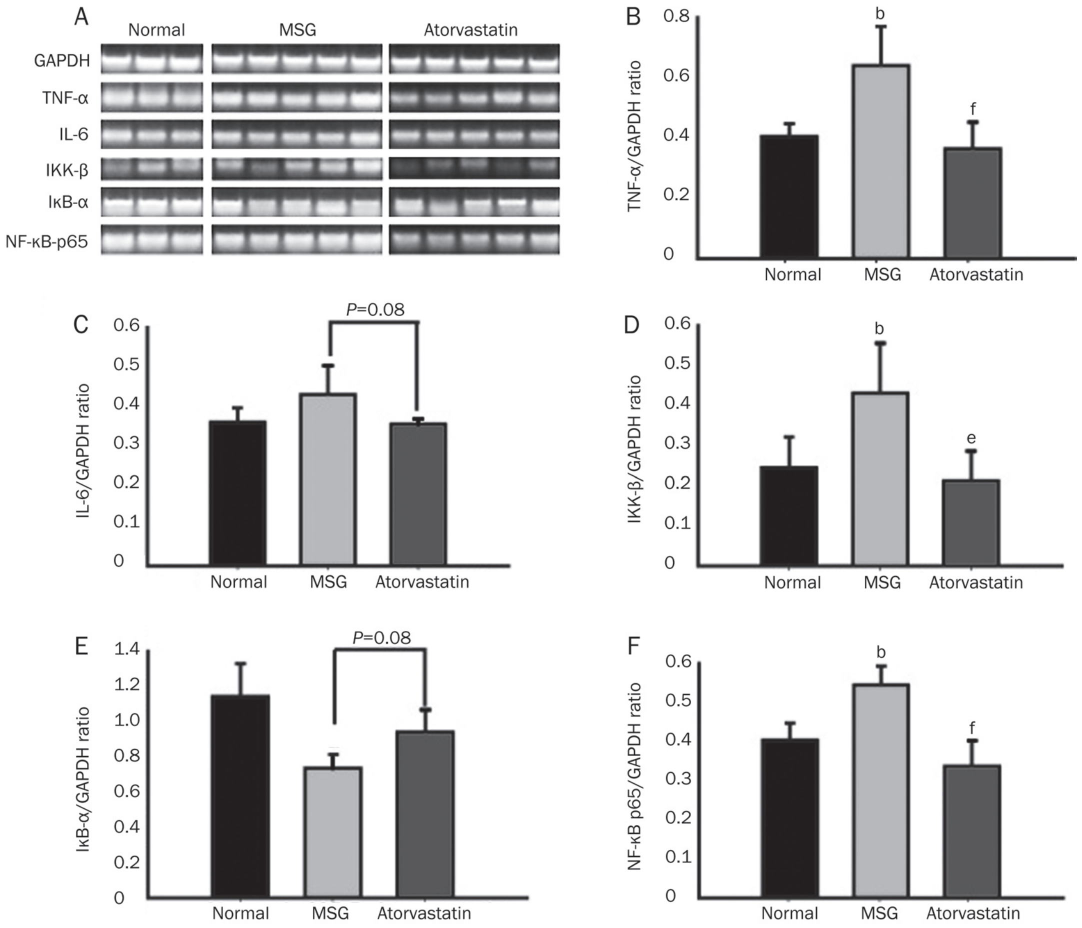

Figure 3. Effect of atorvastatin on inflammatory factors gene expressions at transcriptional levels in adipose tissue of MSG-induced obese mice with insulin resistance. Mice (*n*=5) were treated with atorvastatin (80 mg·kg^{-1}·d^{-1}) for 30 days. Non-obese mice (*n*=3) and vehicle control-treated obese mice (*n*=5) were normal and MSG respectively. (A) The products of semi-quantitative PCR were run on 2.0% agarose gels and stained with ethidium bromide. The expression level of each inflammatory factors mRNA was normalized to that of GAPDH shown in panel A. Atorvastatin inhibited the expression of TNF-α and IL-6 in the adipose tissue (B, C), meantime atorvastatin decreased the expression of IKK-β and NF-κB p65 (D, F). Futhermore, atorvastatin increased the IκB-α expression in adipose tissue (E). Values show means±SEM as ratio. $^{b}P<0.05$ *vs* normal non-obese mice; $^{e}P<0.05$, $^{f}P<0.01$ *vs* control-treated obese mice.

Table 4. Effect of atorvastatin on levels of TNF-α and IL-6 in MSG-induced obese mice with insulin resistance. Data are mean±SEM. Mice were treated with atorvastatin for 30 days. *n*=8 mice/group. $^{a}P>0.05$, $^{b}P<0.05$, $^{c}P<0.01$ *vs* control-treated obese mice.

Group	Serum IL-6 (ng/mL)	IL-6 in adipose tissue (ng/mg protein)	Serum TNF-α (ng/mL)	TNF-α in adipose tissue (ng/mg protein)
Normal non-obese	0.096±0.007	0.127±0.025^{c}	1.21±0.071	1.44±0.029^{c}
Control	0.091±0.007	0.341±0.039	1.19±0.039	3.79±0.062
Atorvastatin (80 mg/kg)	0.069±0.007^{a}	0.232±0.032^{b}	1.34±0.025	2.20±0.021^{b}

(*P*=0.08) compared to vehicle control treatment in obese mice (Figure 3).

Western blot analysis of NF-κB p65 and IκB-α

The level of NF-κB p65 and IκB-α proteins were analyzed by Western blot analysis, and the results shown in Figure 4. The protein level of NF-κB was higher in vehicle treated control obese mice than in normal non-obese mice. Atorvastatin treatment reduced the protein level of NF-κB in obese mice compared to vehicle-treated control mice (*P*<0.05, Figure 4A, 4B). The level of IκB-α protein was lower in vehicle treated controls than in normal non-obese mice, and atorvastatin treatment enhanced the protein expression of IκB-α in obese mice (*P*<0.05, Figure 4A, 4C).

Table 5. Effect of atorvastatin on homeostasis model assessment of insulin resistance (HOMA-IR) index and insulin sensitivity index (ISI) in MSG-induced obese mice with insulin resistance. Data are mean±SEM. Mice were treated with atorvastatin for 30 days. *n*=8 mice/group. $^{b}P<0.05$, $^{c}P<0.01$ vs control-treated obese mice.

Group	Fasting blood glucose (mg/dL)	Serum insulin (mIU/L)	ISI ($\times 10^{-4}$)	HOMA-IR
Normal non-obese	101.8±4.0^{c}	39.6±2.1^{c}	2.6±0.18^{c}	178.8±10.5^{c}
Control	135.6±6.1	177.3±34.2	0.6±0.11	1071.3±225.7
Atorvastatin (80 mg/kg)	116.8±4.8^{b}	85.0±10.4^{b}	1.2±0.20^{c}	429.0±55.5^{b}

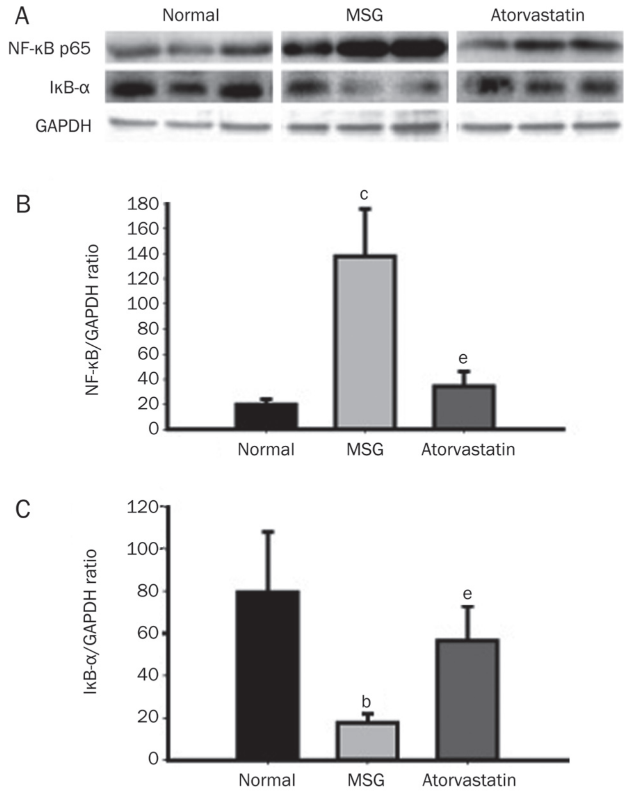

Figure 4. Effect of atorvastatin on the expression of NF-κB p65 and IκB-α at translational levels in adipose tissue of MSG-induced obese mice with insulin resistance. Mice were treated with atorvastatin (80 mg·kg^{-1}·d^{-1}) for 30 days. Normal: non-obese control mice; MSG: vehicle control-treated obese mice; Atorvastatin: atorvastatin-treated obese mice. The protein expressions of NF-κB p65, IκB-α, and GAPDH were analyzed by Western blot assay (A), the expressional levels of NF-κB p65, IκB-α, and GAPDH were normalized to that of GAPDH, respectively. Atorvastatin significantly reduced the expression of NF-κB p65 in adipose tissue compared to MSG group (B), but induced the expression of IκB-α (C). Values are means±SEM as ratio. $^{b}P<0.05$, $^{c}P<0.01$ *vs* normal mice; $^{e}P<0.05$ *vs* MSG mice.

Discussion

Insulin resistance is the critical pathological feature of type 2 diabetes mellitus, obesity, metabolic syndrome, and aging[15]. Although the precise pathogenesis of insulin resistance remains ill-defined, several factors have been proposed to have a role in this process, such as adipokines, defects in the insulin signaling pathway, mitochondrial dysfunction and inflammation[16, 17]. In the past few years it has been shown clearly that obesity, along with diabetes, is characterized by a state of chronic low-grade inflammation[18–20], implying that approaches designed to improve state of chronic low-grade inflammation should be useful in attenuating insulin resistance with obesity.

The effects of statins on insulin sensitivity had been reported in the past years, simvastatin and atorvastatin may improve insulin sensitivity in diabetic patients[21]; however, others have reported that simvastatin either did not change or worsened insulin sensitivity in diabetic patients[22, 23]. And there are no reports exist of their mechanism of action in insulin resistance, obesity animal models. We investigated the effect of atorvastatin on glucose metabolism and insulin resistance and the mechanism of action in MSG-induced obese mice, a model of T2DM with obesity, hyperinsulinemia, insulin resistance, hyperlipidemia and hyperglycemia[24]. Atorvastatin significantly inhibited the plasma glucose and decreased the plasma insulin level and the HOMA-IR index but increased the ISI in obese mice. These findings suggest that atorvastatin may improve insulin resistance in MSG-induced obese mice.

As mentioned before, mounting evidence indicates that adipose tissue is an important cytokines-secretory organ[25] and that adiposity contributes to a chronic state of systemic inflammation[26]. Actually, the molecular connection between obesity and inflammation was documented in 1993, after the demonstration of enhanced expression of TNF-α in adipose tissue of obese rodents, and more importantly, the amelioration of insulin sensitivity after neutralization of this multi-potent inflammatory cytokine. Inflammatory mediators derived from adipose tissue and increased in level in obesity include IL-6, IL-1β, and monocyte MCP-1[27, 28]. Further, growing evidence suggests that, similar to TNF-α, these and other inflammatory molecules negatively affect insulin sensitivity through activation of NF-κB, a transcription factor, which triggers the production of numerous inflammatory mediators such as TNF-α and IL-6. These factors can sustain and heighten inflammatory activation, thus leading to local and systemic insulin resistance[29]. In our study, atorvastatin significantly decreased the secretory level of TNF-α and IL-6 in adipose tissue. This finding suggests that atorvastatin may inhibit the generation of inflammatory factors, thereby improving insulin resistance in MSG-induced obese mice.

Furthermore, atorvastatin decreased the mRNA level of TNF-α and IL-6 but not significantly (*P*=0.08) in adipose tissue, which is consistent with the results of their secretory levels in adipose tissue. In addition, atorvastatin significantly decreased the expression of IKK-β and NF-κB and increased that the expression of the inhibitor of NF-κB, IκB-α. IKK-β is an important kinase that can affect insulin signaling through serine phosphorylation of IRS-1 and by phosphorylation of IκB-α, which leads to stimulation of the NF-κB pathway. IκB -α inhibits the transcriptional activity of NF-κB in the cytoplasm by preventing the nuclear translocation of NF-κB. In the nucleus, it dissociates NF-κB from DNA and transports it back to the cytoplasm[30]. To further support the mechanism of atorvastatin action through inflammatory factors, we analyzed the protein level of NF-κB and IκB-α and found that atorvastatin significantly reduced the level of NF-κB protein and increased protein levels of IκB-α. These findings support our hypothesis that atorvastatin inhibits the activity of IKK-β and NF-κB, and increases that of IκB-α, which inhibits the activity of NF-κB. Thus, atorvastatin reduced inflammatory factor activation and improved insulin resistance in MSG-induced obese mice.

Results from our study and that of others raise questions about the effects in humans being treated with approved doses of atorvastatin. We chose doses of atorvastatin comparable to those used for treatment of hypercholesterolemia in humans. The dose of 80 $mg \cdot kg^{-1} \cdot d^{-1}$ for mice is estimated to be slightly higher than the maximal approved dose for humans. Atorvastatin has a high LD_{50} (5000 mg/kg) in the mice[31] so the dose used was safe for the mice in our study. Atorvastatin can adversely affect liver function in some patients with liver dysfunction[32]. In our study, we also assayed AST and ALT levels in serum and found the liver function of MSG-induced obese mice with atorvastatin treatment had no difference from that of the treated control mice (data not shown). Interesting, we found a decrease in plasma HDL-cholesterol after atorvastatin treatment. This result seems to be conflicting with other reports about the role of increasing HDL with atorvastatin. However, compared to humans, mice and rats transport most of their serum cholesterol in the HDL-C fraction, not the LDL-C fraction[33]. In this mouse model, when atorvastatin decreased the plasma level of total cholesterol, the plasma level of HDL was decreased. However, we have used the mice with MSG-induced obesity as a model of obesity-associated insulin resistance for many years, and many characteristics of this animal model have a striking resemblance to human disease. The most important characteristic of such mice is abdominal obesity. A large amount of abdominal fat in MSG-induced obese mice with insulin resistance could be related to chronic inflammation, so MSG-induced obese mice are suitable for study of the effect of atorvastatin on improving insulin resistance to ameliorate the state of chronic inflammation and inhibit the activity of proteins in the inflammatory pathway.

In conclusion, atorvastatin treatment decreased lipid levels, improved glucose metabolism after glucose loading, and improved insulin resistance in MSG-induced obese mice. Possible mechanisms of the improved glucose metabolism with atorvastatin treatment may include ameliorating the state of chronic inflammation by inhibiting synthesis of inflammatory factors through inhibiting the expression of NF-κB and IKK-β, as well as increasing the expression of IκB-α in adipose tissue.

Acknowledgments

We thank Prof Ming-zhi XIE for her suggestions about this experimental design.

Author contribution

Ning ZHANG and Zhu-fang SHEN designed research; Ning ZHANG, Yi HUAN, Hui HUANG, Guang-ming SONG and Su-juan SUN performed research; Ning ZHANG analyzed data; Ning ZHANG and Zhu-fang SHEN wrote the paper.

References

1 Bosello O, Zamboni M. Visceral obesity and metabolic syndrome. Obes Rev 2000; 1: 47−56.
2 Christian H, Sophie S, Wolfgang R, Burkhard H, Heiko S, Horst W, *et al*. Low-grade inflammation, obesity, and insulin resistance in adolescents. J Clin Endocrinol Metab 2007; 92: 4569−74.
3 Koistinen HA, Forsgren M, Wallberg HH, Zierath JR. Insulin action on expression of novel adipose genes in healthy and type 2 diabetic subjects. Obes Res 2004; 12: 25−31.
4 Kahn BB, Flier JS. Obesity and insulin resistance. J Clin Invest 2000; 106: 473−81.
5 Paz K, Hemi R, LeRaith D, Karasik A, Elhanany E, Kanety H, *et al*. A molecular basis for insulin resistance: elevated serine/threonine phosphorylation of IRS-1 and IRS-2 inhibits their binding to the juxta membrane region of the insulin receptor and impairs their ability to undergo insulin-induced tyrosine phosphorylation. J Biol Chem 1997; 272: 29911−8.
6 Hotamisligil GS, Peraldi P, Budavari A, Ellis R, White MF, Spiegelman BM. IRS-1-mediated inhibition of insulin receptor tyrosine kinase activity in TNF-α and obesity induced insulin resistance. Science 1996; 271: 665−8.
7 Tanti JF, Grémeaux T, van Obberghen E, Le Marchand-Brustel Y. Serine/threonine phosphorylation of insulin receptor substrate 1 modulates insulin receptor signaling. J Biol Chem 1994; 269: 6051−7.
8 Hong R, Nir H, Todd RG, Luk VP, Harvey FL. Tumor necrosis factor-α suppresses adipocyte-specific genes and activates expression of preadipocyte genes in 3T3-L1 adipocytes: nuclear factor-kappaB activation by TNF-α is obligatory. Diabetes 2002; 51: 1319−36.
9 Prigent M, Barlat I, Langen H, Dargemont C. IκBα and IκBα/NF-κB complexes are retained in the cytoplasm through interaction with a novel partner, RasGAP SH3-binding protein 2. J Biol Chem 2000; 275: 36441−9.
10 Esther L, Mat D. HMG-CoA reductase inhibitors: lipid-lowering and beyond. Drug Discov Today Ther Strateg 2004; 1: 189−94.
11 Wolfgang D, Jozef D, Matthias F, Hannes FA, Severin PS, Mikko A, *et al*. HMG-CoA reductase inhibitors regulate inflammatory transcription factors in human endothelial and vascular smooth muscle cells. Arterioscler Thromb Vasc Biol 2003; 23: 58−63.
12 Macho L, Ficková M, Jezová, Zórad S. Late effects of postnatal administration of monosodium glutamate on insulin action in adult rats. Physiol Res 2000; 49: S79−85.

13 Tokushi K, Fumiaki I, Satoshi M, Koichi H. Gene expression of resistin in adipose tissue and mammary gland of lactating and non-lactating cows. J Endocrinol 2003; 178: R1−R5.

14 Shana S, Zhao BP, Yang JZ. Enhanced muscle by myostatin propeptide increases adipose tissue adiponectin, PPAR-α and PPAR- γ expressions. Biochem Biophys Res Commun 2008; 369: 767−73.

15 Newsholme P, Haber EP, Hirabara SM, Rebelato EL, Procopio J, Morgan D, *et al*. Diabetes associated cell stress and dysfunction: role of mitochondrial and non-mitochondrial ROS production and activity. J Physiol 2007; 583: 9–24.

16 Muoio DM, Newgard CB. Mechanisms of disease: molecular and metabolic mechanisms of insulin resistance and beta-cell failure in type 2 diabetes. Nat Rev Mol Cell Biol 2008; 9: 193–205.

17 Kim JA, Wei Y, Sowers JR. Role of mitochondrial dysfunction in insulin resistance. Circ Res 2008; 102: 401–14.

18 Engstrom G, Stavenow L, Hedblad B, Lind P, Eriksson KF, Janzon L, *et al*. Inflammation-sensitive plasma proteins, diabetes, and mortality and incidence of myocardial infarction and stroke: a population-based study. Diabetes 2003; 52: 442–7.

19 Festa A, D'Agostino R Jr, Williams K, Karter AJ, Mayer-Davis EJ, Tracy RP, *et al*. The relation of body fat mass and distribution to markers of chronic inflammation. Int J Obes Relat Metab Disord 2001; 25: 1407–15.

20 Yudkin JS, Stehouwer CD, Emeis JJ, Coppack SW. C-reactive protein in healthy subjects: associations with obesity, insulin resistance, and endothelial dysfunction: a potential role for cytokines originating from adipose tissue? Arterioscler Thromb Vasc Biol 1999; 19: 972–8.

21 Paolisso G, Barbagallo M, Petrella G, Ragno E, Barbieri M, Giordano M, *et al*. Effects of simvastatin and atorvastatin administration on insulin resistance and respiratory quotient in aged dyslipidemic non-insulin dependent diabetic patients. Atherosclerosis 2000; 150: 121−7.

22 Farrer M, Winocour PH, Evans K, Neil HA, Laker MF, Kesteven P, *et al*. Simvastatin in non-insulin-dependent diabetes mellitus: effect on serum lipids, lipoproteins and haemostatic measures. Diabetes Res Clin Pract 1994; 23: 111−9.

23 Ohrvall M, Lithell H, Johansson J, Vessby B. A comparison between the effects of gemfibrozil and simvastatin on insulin sensitivity in patients with non-insulin-dependent diabetes mellitus and hyperlipoproteinemia. Metabolism 1995; 44: 212−7.

24 Hirata AE, Andrade IS, Vaskevicius P, Dolnikoff MS. Monosodium glutamate (MSG)-obese rats develop glucose intolerance and insulin resistance to peripheral glucose uptake. Braz J Med Biol Res 1997; 30: 671−4.

25 Ahima RS, Flier JS. Adipose tissue as an endocrine organ. Trends Endocrinol Metab 2000; 11: 327–32.

26 Yudkin JS, Stehouwer CD, Emeis JJ, Coppack SW. C-reactive protein in healthy subjects: associations with obesity, insulin resistance, and endothelial dysfunction: a potential role for cytokines originating from adipose tissue? Arterioscler Thromb Vasc Biol 1999; 19: 972–8.

27 Kern PA, Ranganathan S, Li C, Wood L, Ranganathan G. Adipose tissue tumor necrosis factor and interleukin-6 expression in human obesity and insulin resistance. Am J Physiol Endocrinol Metab 2001; 280: E745−51.

28 Peter S, David JL. Monocyte chemoattractant protein 1 in obesity and insulin resistance. Proc Natl Acad Sci 2003; 100: 7265−70.

29 Tilg H, Moschen AR. Inflammatory mechanisms in the regulation of insulin resistance. Mol Med 2008; 14: 222−31.

30 Shoelson SE, Lee J, Yuan M. Inflammation and the IKKβ/IκB/NF-κB axis in obesity- and diet-induced insulin resistance. Int J Obes 2003; 27: 49−52.

31 Victor C, Melvin K, Charles R, Cheryl H, Jeffrey T. The genotoxicity profile of atorvastatin, a new drug in the treatment of hypercholesterolemia. Mutat Res 1995; 343: 95−107.

32 Clarke AT, Mills PR. Atorvastatin associated liver disease. Dig Liver Dis 2006; 38: 772−7.

33 Harris WS. n-3 Fatty acids and serum lipoproteins: animal studies. Am J Clin Nutr 1997; 65: 1611S−1616S.

Acta Pharmacologica Sinica (2010) 31: 43–50
© 2010 CPS and SIMM All rights reserved 1671-4083/10 $32.00
www.nature.com/aps

Original Article

PPARγ agonists inhibit TGF-β-PKA signaling in glomerulosclerosis

Rong ZOU[2,#], Gang XU[1,#], Xiao-cheng LIU[1], Min HAN[1], Jing-jing JIANG[1], Qian HUANG[1], Yong HE[1], Ying YAO[1,*]

[1]Department of Nephrology, Tongji Hospital, Tongji Medical College, Huazhong University of Science and Technology, Wuhan 430030, China; [2] Department of Nephrology, Wuhan Integrated TCM & Western Medicine Hospital, Tongji Medical College, Huazhong University of Science and Technology, Wuhan 430030, China

Aim: To study the probable mechanisms of the anti-glomerulosclerosis effects induced by peroxisome proliferator-activated receptor gamma (PPARγ) agonists in rat intraglomerular mesangial cells (MCs).
Methods: Cells were transfected with the pTAL-PPRE-tk-Luc$^+$ plasmid and then treated with different concentrations of PPARγ agonist, either troglitazone or telmisartan, for the indicated times. Promega luciferase assays were subsequently used for the detection of PPARγ activation. Protein expression levels were assessed by Western blot, and PepTag® assays were used for the non-radioactive detection of protein kinase A (PKA) activity. The deposition of α-smooth muscle actin (α-SMA) and p-cyclic AMP responsive element binding protein (pCREB) were analyzed by confocal laser scanning.
Results: Both troglitazone and telmisartan remarkably inhibit the PKA activation and pCREB expression that is stimulated by TGF-β. The PPARγ agonists also inhibited α-SMA and collagen IV protein expression by blocking PKA activation.
Conclusion: PPARγ ligands effectively suppress the activation of MCs and the accumulation of collagen IV stimulated by TGF-β *in vitro*. The renal protection provided by PPARγ agonists is partly mediated via their blockade of TGF-β/PKA signaling.

Keywords: PKA signal pathway; glomerulosclerosis; PPARγ; rat intraglomerular mesangial cells; troglitazone; telmisartan

Acta Pharmacologica Sinica (2010) 31: 43–50; doi: 10.1038/aps.2009.174; published online 28 December 2009

Introduction

Glomerulosclerosis, characterized by as a phenotype transition of mesangial cells and an increase in extracellular matrix formation[1, 2], is a final common pathway leading to the loss of renal function in a variety of underlying kidney diseases. Multiple injuries to the glomerulus stimulate the glomerular intrinsic cells to proliferate, secrete pro-inflammatory factors, undergo cell death or necrosis, and lay down extracellular matrix[3].

TGF-β, known as a pivotal driver of glomerulosclerosis and tubulointerstitial fibrosis, is a multifunctional cytokine that regulates cell proliferation, differentiation, and production of extracellular matrix proteins in a variety of cells including mesangial cells[4]. Many different cellular responses are elicited by TGF-β, and these are often cell-type specific[5]. The classic cellular response pathway involves Smad-mediated changes in target gene transcription, which have become well understood in the past few years. Other signaling pathways, including mitogen activated protein (MAP) kinases, PI3 kinases, and Rho-like GTPases, can modulate Smad-dependent or independent cellular responses[6, 7]. In particular, it has been proven that TGF-β also mediates protein kinase A (PKA) signal transduction *in vivo*[8]. After TGF-β combines with its receptor, the receptor phosphorylates PKA directly, with the formation of complexes between Smads and the regulatory subunits of PKA. Inhibition of the PKA signal pathway could block the matrix protein synthesis stimulated by TGF-β[9].

Multiple drugs with different pharmacological profiles are employed in the experiments on glomerulosclerosis, because it is one of the major pathological features of primary glomerular diseases. The more recently introduced drugs include the peroxisome proliferator-activated receptor (PPAR)γ agonists (thiazolidinediones or glitazones).

PPARγ, a nuclear receptor that regulates specific gene transcription[10] is involved in the regulation of lipid and glucose metabolism[11] , and inflammatory responses[12]. Through PPARγ activation, PPARγ agonists exert some beneficial effects on different renal diseases, such as anti-

---

[#] These two authors contributed equally to this article.
[*] To whom correspondence should be addressed.
E-mail yaoyingdd@hotmail.com
Received 2009-06-15 Accepted 2009-11-09

inflammatory effects[13], anti-fibrotic effects[14], and vascular protective effects[15], although the exact mechanism is not well understood[16]. Recently, it has been reported that the promoter activity and phosphorylation levels of cyclic AMP responsive element binding protein (CREB) could be inhibited by the activation of PPARγ, although it is still unclear what the exact regulation mechanism is and whether additional regulation exists at the level of CREB Ser133 phosphorylation. Because CREB phosphorylation is mainly modulated through PKA activation, similar modulation effects are also performed by the PPARγ agonist, raising the possibility that PPARγ activation might mediate the PKA signal pathway. These observations allow the speculation that a probable direct modulation on PKA signaling by PPARγ exists in the complex cellular signal networks. Therefore, the interaction between PPARγ and PKA signaling was examined. The probable mechanisms of anti-glomerulosclerosis effects mediated by PPARγ agonist in mesangial cells (MCs) were also investigated *in vivo*. On the other hand, telmisartan, a subclass of angiotensin receptor blockers (ARBs), has been reported to associate with PPARγ as a partial agonist[17]. Therefore, we chose both troglitazone and telmisartan as PPARγ ligands for these experiments.

Materials and methods

Reagents

Recombinant TGF-β_1 was purchased from R&D Systems (Minneapolis, MN). Telmisartan was obtained from Boehringer Ingelheim (Ingelheim, Germany). Troglitazone, a selective ligand for PPARγ, was kindly provided by Dr Ming HAN (Sankyo, Tokyo, Japan). Telmisartan and trogalitazone were dissolved in DMSO, with a final concentration of 0.05% in the culture medium. Polyclonal anti-PPARγ (sc-7196) and anti-collagen IV (sc-9301) were purchased from Santa Cruz Biotechnology (California, USA). Monoclonal antibodies against CRE binding protein (CREB, #9197) and phospho-CREB (#9198), which recognizes phosphorylated Ser133, were obtained from Cell Signaling Technology (Boston, USA). Monoclonal anti-alpha smooth muscle actin (α-SMA, ab32575) was obtained from Abcam (Cambridge, UK), and horseradish peroxidase (HRP)–conjugated anti-mouse, anti-rabbit immunoglobulin were obtained from Dako (Glostrup, Denmark). The ECL detection system was obtained from Pierce Biotechnology (Rockford, USA). GW9662, a specific PPARγ antagonist, was from Cayman chemical (Michigan, USA). H89, a selective inhibitor of PKA, was from Alexis Biochemicals (San Diego, USA).

Cell culture

Rat intraglomerular mesangial cells were cultured in Dulbecco's Modified Eagle's Medium (DMEM) supplemented with 10% fetal bovine serum (GIBCO, USA), at 37 °C in 95% air /5% CO_2. Throughout this study, cells from passages 5 to 15 were used. All treatments were done in a serum-free medium in confluent cells that had been cultured in medium without FBS for 24 h before stimulation.

Transient transfection and luciferase assay

To assess the PPARγ activation, MCs at 80% confluence were transiently transfected with 2.0 μg of luciferase reporter plasmids containing either three consensus PPARγ response elements (pTAL-3xPPRE-TK-Luc) or the corresponding empty vector (pTAL-Luc) (a kind gift from Dr Qiu-jun LÜ) along with a β-galactosidase vector (Promega) for 4 h using Lipofectamine (Invitrogen Life Technologies, USA). The PPREx3-Luc reporter plasmid was designed to contain PPRE sites (5′-GTCGACAGGGGACCAGGACAAAGGTCACGTTCGGGAGGTCAC-3′, three copies) attached to a luciferase vector (pTAL-Luc) as described[18]. After a 16-h recovery period in serum-free medium, cells were treated with trogalitazone or telmisartan. The transfections were done in triplicate and repeated at least three times to ensure the reproducibility of the results. Firefly luminescence and β-galactosidase values were measured in cell lysates according to the instructions of the manufacturer from Promega. PPRE activities were expressed as the ratio of relative light units to the β-galactosidase values. In all cases, the luciferase activity of the empty vectors was negligible. Results (mean±SD) were expressed as the fold increase in relative luciferase units, corrected to β-galactosidase, and compared with unstimulated cultures.

Western blotting

After being intervened with trogalitazone or telmisartan, washed cells (PBS, 4 °C) were harvested under non-denaturing conditions (4 °C/30 min) with lysis buffer (50 mmol/L Tris-HCl, pH 8.0, 150 mmol/L NaCl, 1% TritonX-100, 0.1% SDS, 1% NP-40, 0.5% deoxysodium cholate, 1 mmol/L EGTA, 0.5 mmol/L benzamidine, 1.5 mmol/L sodium fluoride, 30 μmol/L sodium vanadate, 10 μmol/L sodium pyrophosphate, 2 mmol/L PMSF, 10 μg/mL aprotinin, 10 μg/mL leupeptin). Proteins were separated by electrophoresis (10% sodium dodecyl sulfate-polyacrylamide gel) and electroblotted to a nitrocellulose membrane (Schleicher and Schuell, Keene, NH). The membranes were blocked with 5% nonfat dry milk in TBST (25 mmol/L Tris, 140 mmol/L NaCl, 3 mmol/L KCl, 0.05% Tween-20, pH 8.0, 37 °C, 1 h), and then were incubated with anti-PPARγ (1:200 dilution), anti-CREB (1:200 dilution), anti-pCREB (1:200 dilution), anti-α-SMA (1:200 dilution), and anti-collagen IV (1:100 dilution) antibodies at 4 °C overnight with continuous shaking in TBST containing 5% nonfat dry milk. Membranes were then washed with TBST (10 min×3 times) and were incubated with appropriate horseradish peroxidase-conjugated secondary antibodies (1:1000 dilution) at room temperature for 1 h. Appropriate bands were identified with ECL Chemiluminescence Reagent and were followed by exposure to X-ray film (X-OMAT, Kodak, USA). Subsequently, immune complexes were removed from the membrane (5% NaOH, 37 °C, 5 min). Then, the immune complexes were re-blocked with 5% non-fat milk (37 °C, 1 h). Protein was assessed by re-blotting with anti-actin antibody (1:200 dilution) and a horseradish peroxidase-conjugated anti-rabbit secondary antibody (1:1000 dilution). The bands were photographed using Chemilmager 5500 (Alpha Innotech, San Leandro, CA).

In vitro kinase assay for PKA activity

After treatment with TGF-β_1, trogalitazone, telmisartan, or H89 for the indicated time periods, the cells were washed with ice-cold PBS and were harvested on ice. Then, cells were suspended in 0.5 mL of cold PKA extraction buffer (25 mmol/L Tris-HCl, pH 7.4, 0.5 mmol/L EDTA, 0.5 mmol/L EGTA, 10 mmol/L β-mercaptoethanol, 1 μg/mL leupeptin, 1 μg/mL aprotinin) and homogenized using a cold homogenizer. The supernatant was mixed with other compositions after centrifuge (5 min, 4 °C, 14000 r/min). Subsequently, all reaction components were added on ice in a final volume of 25 μL of the following mixture: PKA Reaction 5×Buffer 5 μL, A1 Peptide (0.4 μg/μL) 5 μL, PKA Activator 5×Solution 5 μL, Peptide Protection Solution 1 μL, cAMP-Dependent Protein Kinase (2 μg/mL in PKA dilution buffer) 5 μL. The mixture was incubated for 30 min at room temperature. Then, the reaction was stopped by heating at 95 °C for 10 min, and the samples were loaded onto the agarose gel (0.8% agarose in 50 mmol/L Tris–HCl, pH 8.0) for electrophoresis. The phosphorylated peptide migrates towards the negative electrode (cathode) while the non-phosphorylated one migrates toward the positive electrode (anode). The negative control lacks PKA enzyme and contains only buffer, while only the positive control contains the PKA catalytic subunit (final concentration 16 U/mL) supplied with the kit. The intensity of the bands was quantified as above.

Confocal microscopy

Extracellular matrix accumulation and the p-CREB translocation into the nucleus were determined using confocal microscopy of monolayers stained with antibodies to collagen IV and p-CREB. The cells were plated in a chamber-slide for 24 h in regular medium and 24 h in serum-free medium. Accompanied with TGF-β_1 stimulation, treatments with trogalitazone, telmisartan, or H89 were applied for 24 h. This was followed by thorough washes with PBS. Then, the cells were fixed with 4% fresh paraformaldehyde at 4 °C for 30 min and were permeabilized in PBS containing 0.2% TritonX-100. To block the nonspecific reaction, the cells were incubated with 5% BSA in PBS for 60 min. Then, the cells were incubated with the specific primary antibodies against collagen IV at a dilution of 1:50 at 4 °C overnight. After washes, cells were incubated with FITC conjugated donkey anti-goat IgG (1:50) for 1 h in the dark at room temperature. Cells were double stained with PI (propidium iodide) to visualize the nuclei. Slides were washed three times with PBS and glass coverslips were applied after the addition of one drop of mounting media. Confocal microscopy was performed using a Zeiss confocal laser scanning microscope (Carl Zeiss, Inc, Thornwood, NY). Basal and apical membrane locations were determined visually in the Z-plane using light field microscopy. Two to three photomicrographs per monolayer at the basal and apical membranes were then scanned with an omnichrome laser filtered at 480 nm to detect FITC and 530 nm to detect PI.

Statistical analyses

Data were expressed as mean±SD. Difference of means was compared by one-way ANOVA and Student-Newman-Keuls *post hoc* test for the comparison of multiple means using SPSS 13.0 software. Statistical significance was defined as $P<0.05$.

Results

PPARγ ligands enhanced activity of PPARγ response elements (PPRE) in MCs

As shown in Figure 1, treatment with different concentrations of PPARγ agonist caused an effective activation of promoter plasmid. The differences of luciferase levels between the treatment group and the control group were statistically significant. Both troglitazone and telmisartan enhanced luciferase expression in a dose-dependent manner. Figure 1C shows the time course of the effects of 5 μmol/L trogalitazone or 10 μmol/L telmisartan on PPRE activities. The PPARγ activation was detected as early as 12 h after the start of incubation, and

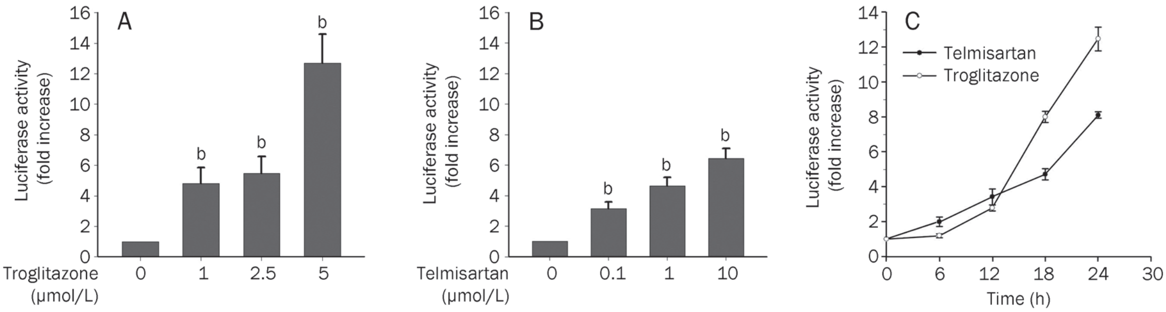

Figure 1. Both troglitazone and telmisartan activated PPARγ response elements (PPRE) effectively. MCs were transfected with 2.0 μg tk-PPREx3-Luc and 0.2 μg β-galactosidase vectors. After transfection, cells were treated with 1, 2.5, 5 μmol/L troglitazone (A) or 0.1, 1, and 10 μmol/L telmisartan (B) for 24 h. Meanwhile, transfected cells were treated with 5 μmol/L troglitazone or 10 μmol/L telmisartan for the indicated periods of time (C). Luciferase and β-galactosidase assays were performed at least three times, and the results were expressed as percentage of control considering the values in untreated samples as 100%. Luciferase activity represents data that have been normalized with β-galactosidase activity. The data represent the mean±SD of three independent experiments. $^bP<0.05$ *vs* the un-stimulated controls.

enhanced remarkably in 24 h after treatments. Both troglitazone and telmisartan enhanced luciferase expression in a time-dependent manner.

The suppression on PKA signaling induced by PPARγ agonists in normal MCs

To elucidate whether the influence on PKA pathway by PPARγ agonist existed in MCs, we measured the expression of major proteins of the PKA signal pathway. The inhibition of PKA activity was accelerated between 12 and 24 h after trogalitazone or telmisartan exposure and then performed moderately. Meanwhile, both troglitazone and telmisartan inhibited PKA activation in variety of concentrations (Figure 2). Because the CREB phosphorylation depends on the PKA activation, we extended our observations by measuring the pCREB expression levels in response to the PPARγ agonist. Accordingly, significant pCREB signals at Ser-133 were detected within 24 h of stimulation by troglitazone or telmisartan (Figure 3A). The pCREB expression was suppressed markedly after exposure to either troglitazone or telmisartan. The inhibition of pCREB stimulated by PPARγ agonist could be abolished by a specific PPARγ antagonist-GW9662 (Figure 3B). However, PPARγ agonist had little effect on the total CREB expression (Figure 3). These findings indicated that PPARγ activation could directly influence the activation of PKA/CREB signaling in normal mesangial cells.

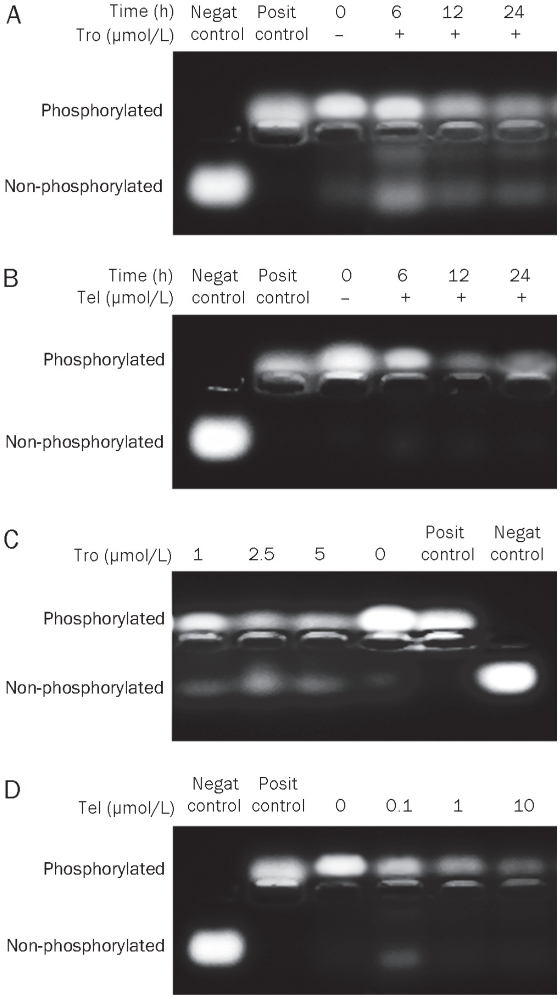

Figure 2. PPARγ agonists inhibited PKA signaling in normal MCs. (A) Time course 1. MCs were treated with troglitazone (Tro, 5 μmol/L) for the indicated time periods, and PKA activity was measured by PepTag® Non-Radioactive Protein Kinase Assays (promega) as described. Purified PKA catalytic subunit was used as a positive control (negative control contained only buffer), while all other samples contain cell lysates from treated and untreated cells. (B) Time course 2. Telmisartan (Tel, 10 μmol/L). PKA activity was estimated as in (A). (C) Dose response 1. MCs were treated with troglitazone (1, 2.5, and 5 μmol/L) for 24 h. (D) Dose response 2. Telmisartan (0, 0.1, 1, and 10 μmol/L, 24 h).

Inhibition of TGF-β_1-PKA signaling by PPARγ agonists

Because CREB cooperates with Smads to mediate TGF-β_1-induced glomerulosclerosis process, we tested whether the PKA signal pathway, under the influence of TGF-β_1, was suppressed by PPARγ agonist. In harmony with the former results, PPARγ agonist remarkably suppressed PKA activation induced by TGF-β_1 (Figure 4A). pCREB expression was also suppressed after PPARγ agonist treatments (Figure 4B), which was recovered by GW9662 (Figure 4B). We also examined the inhibition effects on PKA signaling performed by H89, a selective inhibitor of PKA. The mimic effects were also obtained after pre-incubation with 10 μmol/L H89 (Figure 4C, 4D). Similar results were also obtained by confocal microscopy assays. It is demonstrated that a visible expression of pCREB in TGF-β_1-treated MCs (Figure 4F) and noticeable suppression in PPARγ agonist-treated (Figure 4G) and H89-treated MCs compared with control (Figure 4E).

PPARγ agonists suppressed TGF-β1-induced MCs phenotype alteration

The induction of α-SMA is a hallmark for MCs phenotype alteration in glomerulosclerosis process. As shown in Figure 5, both troglitazone and telmisartan dramatically suppressed the α-SMA expression mediated by TGF-β1. The suppression effects performed by PPARγ agonists were abolished by GW9662 pre-incubation.

PPARγ agonists inhibit TGF-β1-mediated collagen IV expression

ECM accumulation is a dynamic process that results from the delicate balance between matrix synthesis and degradation. The collagen VI distribution, which was characterized as the important component of ECM[19], was shown by confocal microscopy. As shown in Figure 6, TGF-β1 ma rkedly induced collagen IV expression in the extracellular matrix. Either telmisartan or troglitazone significantly abolished collagen IV overproduction stimulated by TGF-β1 (Figure 6A). In harmony with immunoblotting, similar results were obtained when the MCs were stained with a specific antibody against collagen IV (Figure 6B−6F). The collagen IV over-expression induced by TGF-β_1 was notably reduced after both PPARγ agonists and H89 treatments.

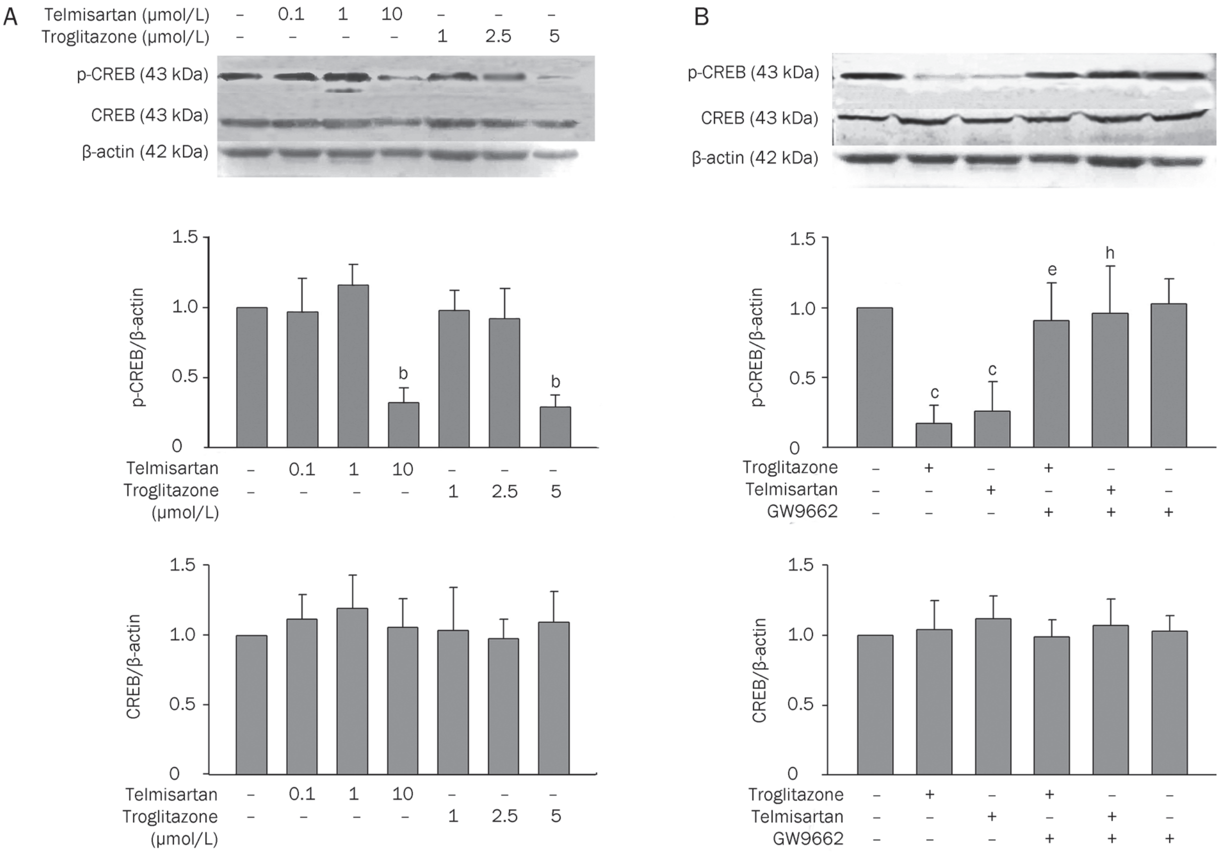

Figure 3. Both troglitazone and telmisartan inhibited the phosphorylation levels of cyclic AMP responsive element binding protein (CREB). Cells lysates were subjected to Western analysis with the pCREB and CREB antibody. β-actin was used as a loading control. (A) MCs were treated with troglitazone (0–5 μmol/L) or telmisartan (0–10 μmol/L) for 24 h. The expression levels of pCREB were represented as mean±SD. $^{b}P<0.05$ *vs* control (untreated cell), *n*=3. (B) MCs were treated with either troglitazone (5 μmol/L) or telmisartan (10 μmol/L) in the presence or absence of GW9662 (20 μmol/L). *n*=3. The data was represented as mean±SD. $^{c}P<0.01$ *vs* control (untreated cell). $^{e}P<0.05$ *vs* troglitazone group. $^{h}P<0.05$ vs telmisartan group.

Discussion

PPARγ is a ligand-activated transcription factor belonging to the nuclear hormone receptor superfamily. Like other nuclear receptors, PPARγ has a modular structure consisting of an agonist-dependent activation domain (AF-2), a DNA binding domain, and an agonist-independent activation domain (AF-1)[20] . Many of its biological effects are mediated by receptor regulation of target gene transcription in a ligand-dependent manner. It has been recognized increasingly that PPARγ agonists have protective effects on the progression of glomerulosclerosis[21, 22], possibly by a mechanism that is independent of insulin/glucose effects and associated with the regulation of glomerular cell proliferation, hypertrophy, and decreased PAI-1 and TGF-β expression[21]. Through a PPARγ-dependent manner, PPARγ agonists exert some beneficial effects on the kidney, although the molecular mechanism is not well understood.

In this paper, we demonstrated that both troglitazone and telmisartan suppressed PKA signal transduction in both dose-dependent and time-dependent manners in normal MCs. Pre-incubation with GW9662 abolished the suppression effects induced by both troglitazone and telmisartan, suggesting that the suppression effects were caused by PPARγ activation. It suggest that PPARγ agonists indeed influenced PKA signaling cascades in MCs by PPARγ dependent mechanisms.

The inactive holoenzyme PKA consists of two regulatory (R) and two catalytic subunits. Unlike many protein kinases whose activity is regulated by the transient addition of a phosphate to the activation loop, PKA is assembled as a fully active enzyme that is kept in its inactive state by inhibitory proteins[23]. There are two classes of inhibitors: the heat-stable protein kinase inhibitors (PKIs) and the regulatory subunit. PKI binds with high affinity to the free catalytic subunit, but, unlike the R subunit, it includes a nuclear export signal (NES) that mediates active nuclear export of the catalytic subunit. The NES at the C terminus of the PKI provides a mechanism for rapidly exporting the catalytic subunit from the nucleus[24]. Protein-protein interactions are important for many signaling processes. The research focused on PPARγ localizations disclosed the protein-protein interactions between PPARγ and MEKs in its nuclear translocation[25] . Indeed, several nuclear receptors were reported to interact with regulatory proteins via the AF2 domain of PPARγ, including glucocorticoid receptors, estrogen receptors, and NF-κB interactions with

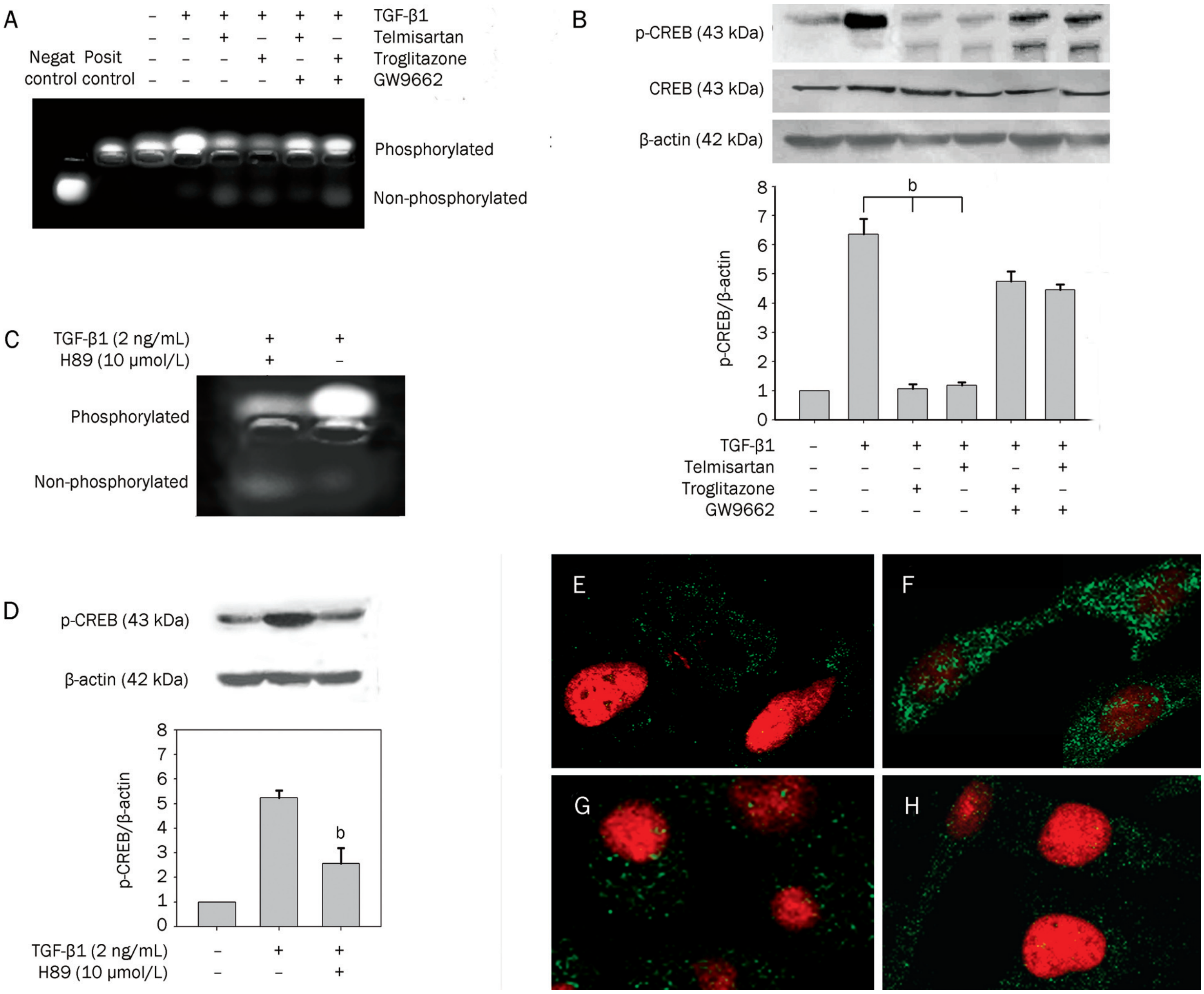

Figure 4. PPARγ agonists inhibited TGF-β1 /PKA signaling. (A and B) MCs were treated with troglitazone or telmisartan after exposure to TGF-β1, in the presence or absence of GW9662. PKA activation was measured in MC lysates as described (A). The expression levels of pCREB and total CREB were measured by Western blot (B). $^{b}P<0.05$, $n=3$. (C and D) MCs were pre-incubated with or without 10 μmol/L H89, then exposed to TGF-β1. PKA activation was measured (C). The expression levels of pCREB were measured by Western analysis (D). $^{b}P<0.05$ *vs* TGF-β1-treated cells. $n=3$. (E–H) Assess nuclear distribution of pCREB by confocal microscopy in TGF-β1-treated cells without or with PPARγ ligands. (E) normal group; (F) TGF-β1–treated group (2 ng/mL); (G) troglitazone (5 μmol/L) with TGF-β1; (H) telmisartan (10 μmol/L) with TGF-β1.

PPARγ[26]. How did PPARγ affect the PKA activities? One speculation is, through nuclear export processes of catalytic subunits, an interaction may exists in the protein complexes of the catalytic subunit and PKI caused by PPARγ. Whether the protein-protein interaction indeed exists between PPARγ and the catalytic subunit, and how it works, are questions that require further research.

As a multi-functional factor, TGF-β is a pivotal driver of glomerulosclerosis and tubulointerstitial fibrosis. The classical TGF-β/Smads pathway in the fibrotic process has been well illustrated[27]. In recent years, some signaling molecules other than Smads were found to be involved in TGF-β signaling. For example, p38 MAPK was previously recognized to play a critical role in the apoptosis of AML-12 cells induced by TGF-β[28]. Additionally, interactions between the TGF-β/Smads pathway components with the PKA/CREB signal pathway have been widely reported[8, 29, 30]. The phosphorylation of Smad3 and Smad4 by TGF-β have a direct protein-protein interaction with the regulatory subunit of PKA, leading to the release of the PKA catalytic subunit from the regulator subunit. When the PKA catalytic subunit translocates into the nucleus to phosphorylate its cellular substrate (CREB), the pCREB binds to conserved CREs in the promoters of many cAMP-responsive genes and regulates related gene transcription.

TGF-β/PKA signaling plays an important role in many aspects of physiologic and pathologic processes. For example, TGF-β induced apoptosis and Epithelial-to-Mesenchymal Transition (EMT) in AML-12 murine hepatocytes was associated with PKA activation[31]. Singh *et al* reported that laminin and fibronectin (Fn) expression induced by TGF-β1 could be down-regulated by PKA signaling blockage; however, the inhibition of PKC did not have significant effects on TGF-β1

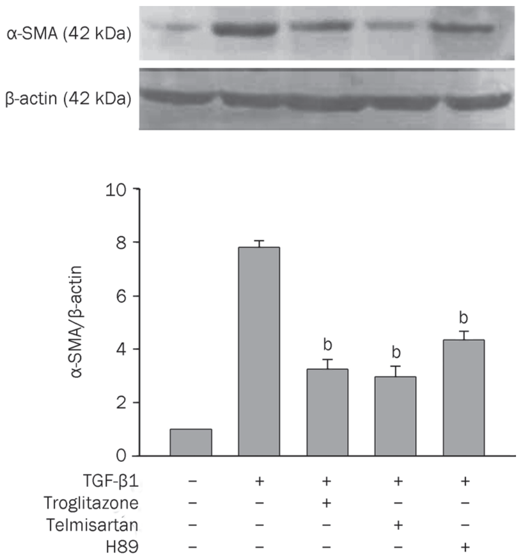

Figure 5. PPARγ ligands inhibit the activation of MCs mediated by TGF-β1. The expression of αSMA mediated by TGF-β1 was measured by Western blot. MCs were treated with troglitazone (5 μmol/L), telmisartan (10 μmol/L) or H89 (20 μmol/L) after exposure to TGF-β1. ${}^{b}P<0.05$ *vs* TGF-β1 treated group. $n=3$.

mediated laminin synthesis[32]. With these observations, it was also reported that the secretion of Fn was downregulated by PPARγ activation in lung carcinoma cells, which was mediated by antagonizing the transactivating activity of CREB binding to one CRE site in the Fn promoter[33]. These results indicate a potential involvement of PKA signaling in TGF-β mediated pro-glomerulosclerosis process.

In our study, we proved that PPARγ agonists remarkably suppressed the PKA signaling stimulated by TGF-β_1. The suppression effects were dependent on PPARγ activation. These results suggest that the suppression of PKA signaling cascades induced by PPARγ agonists not only in normal MCs, but also in TGF-β stimulated cells. Because of the tight interaction between TGF-β and the PKA/CREB pathway, which is important for the glomerulosclerosis process, these observations provided possibilities that PPARγ agonists might inhibit the TGF-β mediated glomerulosclerosis process through the suppression of the PKA pathway.

Furthermore, the inhibition of TGF-β/PKA signaling enacted by the PPARγ agonists efficiently blocked the αSMA expression and collagen IV accumulation. The results demonstrate that TGF-β1 itself could stimulate MCs to differentiate into myofibroblasts; and that treatment with PPARγ agonists, accompanied by TGF-β1-stimulated differentiation, could inhibit the differentiation of MCs. Moreover, the inhibition effects of both telmisartan and troglitazone were mediated by PPARγ activation.

In summary, PPARγ activation in MCs leads to beneficial effects for TGF-β-associated glomerulosclerosis. These renoprotective effects combine to suppress the activation of MCs and ECM accumulation. The relevant regulation mechanisms act through the suppression of PKA signaling, which is tightly associated with TGF-β. Our study thus suggests a novel inhibition of PKA signaling that is mediated by PPARγ activation, and explores the role of the reno-protective mechanisms induced by PPARγ agonists. This pathway will provide an additional therapeutic approach for the treatment of TGF-β-mediated glomerulosclerosis.

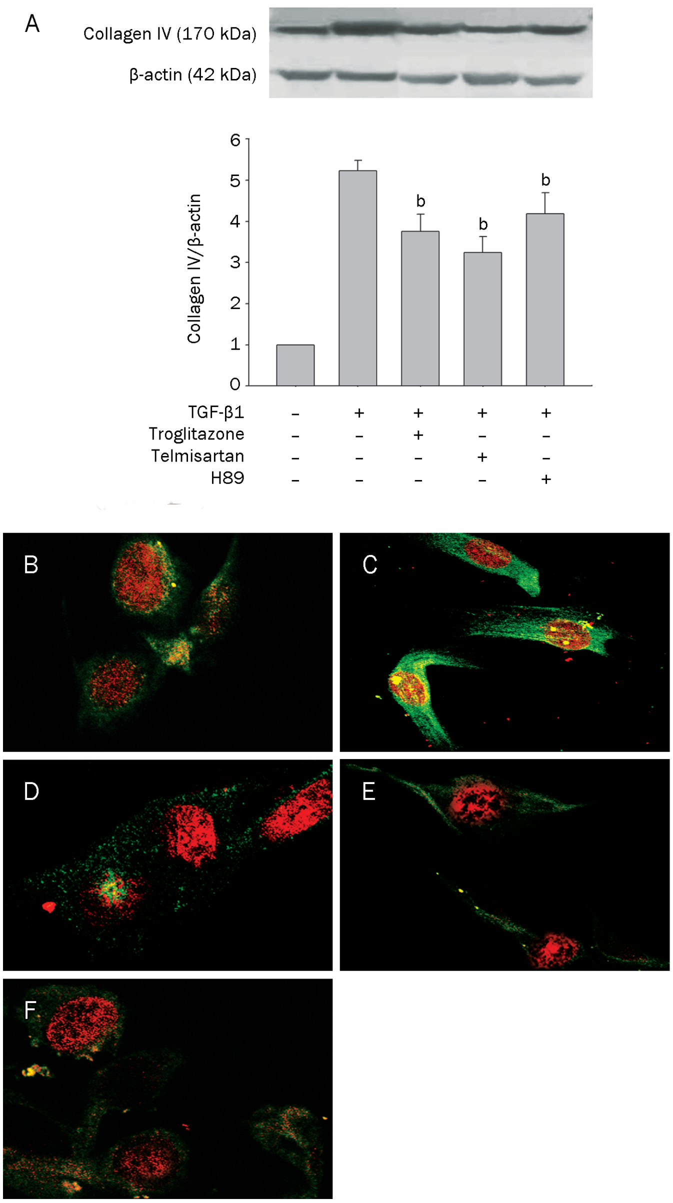

Figure 6. PPARγ agonists inhibited the collagen IV accumulation. (A) The expression levels of collagen IV were measured by Western blot. MCs were treated with troglitazone (5 μmol/L), telmisartan (10 μmol/L) or H89 (20 μmol/L) after exposure to TGF-β1. ${}^{b}P<0.05$ *vs* TGF-β1 treated group, $n=3$. (B–F) The localization of collagen IV in MCs was shown by confocal laser scanning microscopy. (B) Normal group; (C) TGF-β1-treated group (2 ng/mL); (D) Troglitazone (5 μmol/L) with TGF-β1; (E) Telmisartan (10 μmol/L) with TGF-β1; (F) H89 (20 μmol/L) with TGF-β1.

Acknowledgements

This project was supported by the National Natural Science Foundation of China (No 30672227; 30571950; 30600667; 30700895; 30628029; 30770913).

Author contribution

Ying YAO designed research; Rong ZOU performed research; Gang XU, Xiao-cheng LIU, Min HAN, Jing-jing JIANG, Qian HUANG, and Yong HE contributed new analytical tools and reagents; Rong ZOU and Ying YAO analyzed data; Rong ZOU wrote the paper.

References

1 Daskalakis N, Winn MP. Focal and segmental glomerulosclerosis. Cell Mol Life Sci 2006; 63: 2506–11.
2 Padiyar A, Sedor JR. Genetic and genomic approaches to glomerulosclerosis. Curr Mol Med 2005; 5: 497–507.
3 Cybulsky AV. Growth factor pathways in proliferative glomerulonephritis. Curr Opin Nephrol Hypertens 2000; 9: 217–23.
4 Chen S, Jim B, Ziyadeh FN. Diabetic nephropathy and transforming growth factor-beta: transforming our view of glomerulosclerosis and fibrosis build-up. Semin Nephrol 2003; 23: 532–43.
5 Massague J. How cells read TGF-beta signals. Nat Rev Mol Cell Biol 2000; 1: 169–78.
6 Li MO, Wan YY, Sanjabi S, Robertson AK, Flavell RA. Transforming growth factor-beta regulation of immune responses. Annu Rev Immunol 2006; 24: 99–146.
7 Prud'homme GJ. Pathobiology of transforming growth factor beta in cancer, fibrosis and immunologic disease, and therapeutic considerations. Lab Invest 2007; 87: 1077–91.
8 Zhang L, Duan CJ, Binkley C, Li G, Uhler MD, Logsdon CD, *et al*. A transforming growth factor beta-induced Smad3/Smad4 complex directly activates protein kinase A. Mol Cell Biol 2004; 24: 2169–80.
9 Singh LP, Green K, Alexander M, Bassly S, Crook ED. Hexosamines and TGF-beta1 use similar signaling pathways to mediate matrix protein synthesis in mesangial cells. Am J Physiol Renal Physiol 2004; 286: F409–16.
10 Libby P, Plutzky J. Inflammation in diabetes mellitus: role of peroxisome proliferator-activated receptor-alpha and peroxisome proliferator-activated receptor-gamma agonists. Am J Cardiol 2007; 99: 27–40.
11 Sharma AM, Staels B. Review: Peroxisome proliferator-activated receptor gamma and adipose tissue--understanding obesity-related changes in regulation of lipid and glucose metabolism. J Clin Endocrinol Metab 2007; 92: 386–95.
12 Spears M, McSharry C, Thomson NC. Peroxisome proliferator-activated receptor-gamma agonists as potential anti-inflammatory agents in asthma and chronic obstructive pulmonary disease. Clin Exp Allergy 2006; 36: 1494–504.
13 Guyton K, Bond R, Reilly C, Gilkeson G, Halushka P, Cook J. Differential effects of 15-deoxy-delta(12,14)-prostaglandin J2 and a peroxisome proliferator-activated receptor gamma agonist on macrophage activation. J Leukoc Biol 2001; 69: 631–8.
14 Zheng F, Fornoni A, Elliot SJ, Guan Y, Breyer MD, Striker LJ, *et al*. Upregulation of type I collagen by TGF-beta in mesangial cells is blocked by PPARgamma activation. Am J Physiol Renal Physiol 2002; 282: F639–48.
15 Tao L, Liu HR, Gao E, Teng ZP, Lopez BL, Christopher TA, *et al*. Antioxidative, antinitrative, and vasculoprotective effects of a peroxisome proliferator-activated receptor-gamma agonist in hypercholesterolemia. Circulation 2003; 108: 2805–11.
16 Iglesias P, Diez J J. Peroxisome proliferator-activated receptor gamma agonists in renal disease. Eur J Endocrinol 2006; 154: 613–21.
17 Forman BM, Tontonoz P, Chen J, Brun RP, Spiegelman BM, Evans RM. 15-Deoxy-delta 12, 14-prostaglandin J2 is a ligand for the adipocyte determination factor PPAR gamma. Cell 1995; 83: 803–12.
18 Auboeuf D, Rieusset J, Fajas L, Vallier P, Frering V, Riou JP, *et al*. Tissue distribution and quantification of the expression of mRNAs of peroxisome proliferator-activated receptors and liver X receptor-alpha in humans: no alteration in adipose tissue of obese and NIDDM patients. Diabetes 1997; 46: 1319–27.
19 Lennon AM, Ramaugé M, Dessouroux A, Pierre M. MAP kinase cascades are activated in astrocytes and preadipocytes by 15-deoxy-delta(12-14)-prostaglandin J(2) and the thiazolidinedione ciglitazone through peroxisome proliferator activator receptor gamma-independent mechanisms involving reactive oxygenated species. J Biol Chem 2002; 277: 29681–5.
20 Debril MB, Renaud JP, Fajas L, Auwerx J. The pleiotropic functions of peroxisome proliferator-activated receptor gamma. J Mol Med 2001; 79: 30–47.
21 Ma LJ, Marcantoni C, Linton MF, Fazio S, Fogo AB. Peroxisome proliferator-activated receptor-gamma agonist troglitazone protects against nondiabetic glomerulosclerosis in rats. Kidney Int 2001; 59: 1899–910.
22 Yang HC, Ma LJ, Ma J, Fogo AB. Peroxisome proliferator-activated receptor-gamma agonist is protective in podocyte injury-associated sclerosis. Kidney Int 2006; 69: 1756–64.
23 Tamaki H. Glucose-stimulated cAMP-protein kinase A pathway in yeast *Saccharomyces cerevisiae*. J Biosci Bioeng 2007; 104: 245–50.
24 Dalton GD, Dewey WL. Protein kinase inhibitor peptide (PKI): a family of endogenous neuropeptides that modulate neuronal cAMP-dependent protein kinase function. Neuropeptides 2006; 40: 23–34.
25 Burgermeister E, Chuderland D, Hanoch T, Meyer M, Liscovitch M, Seger R. Interaction with MEK causes nuclear export and downregulation of peroxisome proliferator-activated receptor gamma. Mol Cell Biol 2007; 27: 803–17.
26 Gao Z, He Q, Peng B, Chiao PJ, Ye J. Regulation of nuclear translocation of HDAC3 by IkappaBalpha is required for tumor necrosis factor inhibition of peroxisome proliferator-activated receptor gamma function. J Biol Chem 2006; 281: 4540–7.
27 Massague J, Seoane J, Wotton D. Smad transcription factors. Genes Dev 2005; 19: 2783–810.
28 Liao JH, Chen JS, Chai MQ, Zhao S, Song JG. The involvement of p38 MAPK in transforming growth factor beta1-induced apoptosis in murine hepatocytes. Cell Res 2001; 11: 89–94.
29 Zhang Y, Derynck R. Transcriptional regulation of the transforming growth factor-beta-inducible mouse germ line Ig alpha constant region gene by functional cooperation of Smad, CREB, and AML family members. J Biol Chem 2000; 275: 16979–85.
30 Liu G, Ding W, Neiman J, Mulder KM. Requirement of Smad3 and CREB-1 in mediating transforming growth factor-beta (TGF beta) induction of TGF beta 3 secretion. J Biol Chem 2006; 281: 29479–90.
31 Singh LP, Green K, Alexander M, Bassly S, Crook ED. Hexosamines and TGF-beta1 use similar signaling pathways to mediate matrix protein synthesis in mesangial cells. Am J Physiol Renal Physiol 2004; 286: F409–16.
32 Han S, Ritzenthaler JD, Rivera HN, Roman J. Peroxisome proliferator-activated receptor-gamma ligands suppress fibronectin gene expression in human lung carcinoma cells: involvement of both CRE and Sp1. Am J Physiol Lung Cell Mol Physiol 2005; 289: 419–28.
33 Shabb J B. Physiological substrates of cAMP-dependent protein kinase. Chem Rev 2001; 101: 2381–411.

Acta Pharmacologica Sinica (2010) 31: 51–65

www.nature.com/aps

Original Article

Effect of prototypical inducers on ligand activated nuclear receptor regulated drug disposition genes in rodent hepatic and intestinal cells

Philip MARTIN[1,*], Robert RILEY[2], Paul THOMPSON[3], Dominic WILLIAMS[1], David BACK[1], Andrew OWEN[1]

[1]Department of Pharmacology and Therapeutics, The University of Liverpool, Pembroke Place, Liverpool, L69 3GF, UK; [2]Department of Physical and Metabolic Science, AstraZeneca Charnwood, Leicestershire, LE11 5RH, UK; [3]School of Biomedical Sciences, The University of Ulster, Cromore Road, Coleraine, Co. Londondarry, BT52 1SA, UK

Aim: The aim of this study was to investigate the impact on expression of mRNA and protein by paradigm inducers/activators of nuclear receptors and their target genes in rat hepatic and intestinal cells. Furthermore, assess marked inter laboratory conflicting reports regarding species and tissue differences in expression to gain further insight and rationalise previously observed species differences between rodent and human based systems.
Methods: Quantitative real time-polymerase chain reaction (QRT-PCR) and immunoblots were used to assess messenger RNA (mRNA) and protein expression for CYP2B2, CYP3A1, CYP3A2, CYP3A9, ABCB1a, ABCB1b, ABCC1, ABCC2, pregnane X receptor (PXR), farnesoid X receptor (FXR) and constituitive androstane receptor (CAR) in rat hepatoma cell line H411E, intestinal cells, Iec-6, and rat primary hepatocytes, in response to exposure for 18 h with prototypical inducers.
Results: Dexamethasone (DEX) and pregnenolone 16α carbonitrile (PCN) significantly induced PXR, CYP3A9, ABCB1a and ABCB1b. However, when co-incubated, DEX appeared to restrict PCN-dependent induction. Chenodeoxycholic acid (CDCA) was the only ligand to induce FXR in all three cell types. Despite previously reported species differences between PCN and rifampicin (RIF), both compounds exhibited a similar profile of induction.
Conclusion: Data presented herein may explain some of the discrepancies previously reported with respect to species differences from different laboratories and have important implications for study design.

Keywords: nuclear receptors; hepatic cells; intestinal cells; prototypical inducers; rodents; dexamethasone; pregnenolone 16α carbonitrile; cytochrome P450; pregnane X receptor; constituitive androstane receptor

---

Acta Pharmacologica Sinica (2010) 31: 51-65; doi: 10.1038/aps.2009.187

Introduction

Constituitive androstane receptor (CAR), pregnane X receptor(PXR), and farnesoid X receptor (FXR) are key transcription factors regulating transcription of drug metabolising enzymes and transporters in response to prototypical inducers and activators such as PCN (rodent PXR), RIF (human PXR), PB (CAR) and CDCA (FXR). We have previously shown the impact of various prototypical inducers on expression of human isoforms of their genes[1]. The purpose of this study was to investigate the similarity and differences with rodent homologues using identical methodology.

Several important rodent homologues of human drug metabolising enzymes of CYP3A4/5 and CYP2B6 have been characterised in rodents: CYP3A1[2, 3], CYP3A2[4], CYP3A9[5] and CYP3A18[6, 7]. These CYPs are inducible by glucocorticoids such as DEX, antibiotics such as RIF and other steroids such as PCN[8–10]. In addition, CYP2B2 has been studied extensively[11–14] and is known to be induced by many structurally divergent compounds[15] incuding phenobarbital (PB).

PXR and CAR regulate overlapping sets of genes in a tissue specific fashion. In rodents, common activators of PXR and CAR upregulate ABCC2 in the liver via CAR, and in the intestine via PXR, while ABCB1a and ABCB1b are upregulated via PXR in the liver and intestine, with an additional effect via CAR in the intestine confined to ABCB1a[16]. A comparison of the PXR sequences from different mammalian species indicates that the PXR proteins share less than 80% amino acid identity in their ligand binding domains (LBD), while the DNA binding domain (DBD) is ~95% similar[17]. The species differences in these LBDs are believed to be responsible for the

---

[*] To whom correspondence should be addressed.
E-mail P.Martin@liverpool.ac.uk
Received 2009-07-20 Accepted 2009-12-01

selectivity in ligand binding, and thus the marked differences in the induction profiles between species[18].

FXR is a ligand-activated transcription factor regulating cholesterol and fatty acid metabolism and also functions as an endogenous sensor for bile acids[19–21]. The relative contribution of FXR to induction of disposition genes is still unclear. However, the observation that lithocholic acid (LCA) induces CYP3A in PXR-null mice and that FXR activates human CYP3A4 promoter *in vitro*, implies CYP3A gene expression may also be controlled by FXR[22, 23]. Furthermore, ABCC2 has also been shown to be a target of FXR[24, 25].

To date, analysis of gene expression and regulation of drug disposition genes utilise either immortalised or primary cell cultures. However, important differences have been reported between laboratories utilising the same strains of cells[26, 27]. The aim of this study was to investigate the impact of phenobarbital (PB:CAR), CDCA (FXR), PCN (rodent PXR) and RIF (human PXR) on mRNA and protein expression of ABCB1a, ABCB1b, ABCC1, ABCC2, CYP2B2, CYP3A1, CYP3A2, CYP3A9, PXR, CAR, and FXR in rat hepatic and intestinal cell lines (H411E and Iec-6) and rat primary hepatocytes.

Materials and methods

Cell culture

Rat hepatoma cell line H411E and rat intestinal cell line, Iec-6, were purchased from the American Tissue Culture Collection (ATCC, USA) and maintained in Dulbecco's modified Eagle's medium (DMEM; Sigma-Aldrich company, UK) supplemented with 10% fetal bovine serum (FBS; Bio-Whittaker, Europe). Cell lines were incubated at 37 °C and 5% CO_2 and subcultured every 4 days.

For isolation of fresh rat primary hepatocytes, rats were anaesthetised and the liver isolated and perfused for 10 min with wash buffer containing 10% *v/v* Hanks' balanced salt solution (HBSS; Sigma, UK), 0.138% *w/v* Hepes (Sigma, UK) and 0.5% *v/v* sodium hydrocarbonate (Sigma, UK) in deionised H_2O. The rat liver was further perfused for 6−10 min with 500 mL of pre-warmed (37ºC) digestion buffer containing wash buffer, 0.5% *v/v* calcium chloride, 250 mg Collagenase A (Sigma, UK) and 34 mg trypsin inhibitor (Sigma, UK). The digested rat liver was then placed into a petri dish containing 20 mg DNase and 200 mL wash buffer. The residual tissue was removed and the cells filtered through a 125 μm nylon blotting cloth and resuspended in DNase wash buffer and allowed to settle for 10 min, the supernatant was then removed and cells were washed and centrifuged at 50×*g* for 2 min and finally resuspended in wash buffer. Viability was determined based on Trypan blue exclusion[28, 29] and found to be 85%– 90% viable.

Assessment of protein binding

Equilibrium dialysis was used to determine protein binding of PB, CDCA, PCN, and RIF (all compounds purchased from Sigma, UK) within the culture supernatant. Briefly, Dianorm dialysis membranes (GmbH, Munich, Germany) with molecular weight cut-off (MWC) of 5000 were soaked for 1 h in DMEM (Sigma-Aldrich, UK). PB, CDCA, PCN, and RIF were then individually added to DMEM containing 10% FBS (H411E, Iec-6 and primary hepatocyte media) to a final concentration of 10 μmol/L. An aliquot (1 mL) was then dispensed into one side of the dialysis block divided by the pre-soaked membrane, the other side containing control (without additions) media. The dialysis block was then sealed and rotated in a water bath for 24 h at 37 °C. A 200 μL aliquot was subsequently removed from the control side of the dialysis block and placed in quench tubes containing 200 μL of ice-cold methanol. After centrifugation at 400×g for 20 min, the supernatant was transferred into 96-well plates and analysed using liquid chromatography/mass spectrophotometry (LC-MS/MS) (AstraZeneca in-house methodology).

Treatment of cell lines for induction

H411E and Iec-6 were seeded into Nunclon™ Surface 6 well plates (Nunc A/S, Denmark) at a density of 5×10^6 (per well) containing DMEM and FBS (10%). Initial experiments assessed the effect of DEX on expression of CYP3A9, ABCB1a, ABCB1b, and PXR and the inducibility of CYP3A9, ABCB1a, ABCB1b, and PXR by PCN in H411E and Iec-6 cells. After 24 hours the prototypical inducers, PB, CDCA, PCN, and RIF were added to give final concentrations of 0.01, 0.1, 1.0, 10, and 100 μmol/L. The control used was the test compound vehicle, methanol for RIF or Dimethyl sulfoxide (DMSO) (0.1% *v/v* for both vehicles) for PB, CDCA or PCN. Cells were incubated for a further 18 hours at 37 °C and 5% CO_2, total RNA isolated and cDNA constructed as described previously[30].

Treatment of rat primary hepatocytes for induction

Rat primary hepatocytes were seeded at a density of 1×10^6 per well into 10% FBS supplemented DMEM in Nunclon™ Surface 6 well plates (Nunc A/S, Denmark) and allowed to grow for 24 h prior to treatment. Test compounds, PB, CDCA, PCN and RIF were added to give a final concentration of 1.0 μmol/L and a time course was conducted. Cells were then incubated at 37 ºC and 5% CO_2 and sampled at 0, 2, 4, 6, and 18 hours. DMSO treated controls were used for PB, CDCA, PCN and methanol treated controls were used for RIF (0.1% *v/v* for both vehicles).

Toxicity

All test compounds were assayed for toxicity by 3-(4,5-dimethylthiazol-2-yl)-2,5-diphenyl-tetrazolium bromide (MTT) assay[31] for both cell lines at final concentrations of 0.01 to 100 μmol/L. These assays were performed at 18 h to assess cell death at the point of analysis. Toxicity of test compounds was also assessed after 5 days as toxic concentrations would not necessarily be evident after 18 hours.

Quantitative real-time PCR

For H411E, Iec-6 and rat primary hepatocytes, total RNA was isolated utilising Tri-reagent (Sigma, UK) and cDNA constructed as previously described[30]. Real-time PCR assays were developed for quantification relative to β-actin (housekeeping gene) for each transcript in each cell set (H411E, Iec-6, and primary hepatocytes). Formation of primer dimer was optimised and eliminated out of the reaction to ensure no false positive amplification data was incorporated as a result of non-specific intercalation of picogreen (Molecular Probes, Paisley, UK). Relative expression against housekeeping gene β-actin ($\Delta\Delta C_T$) of transcripts were performed in an Opticon2™ Fluorescence Detector (MJ Research, Bio-Rad, Hertfordshire, UK). Amplification was performed in a final reaction volume of 25 μL utilising pico green intercalating fluorescence dye. The reaction mixture consisted of, 2.5 μL 10×Taqman Buffer II, 0.5U Taq polymerase, 1.25 μmol/L $MgCl_2$ (Amplitaq Gold; Applied Biosystems, UK), 1.25 μmol/L dNTPs (Promega, UK), 20 ng cDNA, 0.5 μL pico green (final concentration 1:5000) and 0.03 μmol/L of forward and reverse primer, with the exception of constitutive androstane receptor and CYP3A9 which required 0.3 μmol/L (final concentration) and nuclease-free water was added to a final volume of 25 μL (Sigma-Aldrich, UK). Primer sequences and full assay conditions can be found on supplementary Table 1 and Table 2 respectively.

Immunoblotting

Western blotting analysis was performed in parallel with quantitative real time PCR using crude protein homogenates for CYPs, and for transporter proteins, crude membrane fractions which were purified as described previously[32]. In all cases, protein concentration was determined using the bicinchoninic acid assay (BCA)[33]. Samples were normalised to 5 μg/μL and stored at -80ºC prior to use. Western blotting of all proteins was performed using NuPage 4%−12% Bis-Tris Gels (Invitrogen, Paisley, UK). Blotting was conducted using nitrocellulose membranes and iBlot™ Gel Transfer System (Invitrogen, UK), as per manufacturer's instructions, and membranes were blocked in 10% non-fat-dried milk (NFDM) overnight at 4 ºC.

For CYP2B2, CYP3A1, CYP3A2, CYP3A9 (1:1000), mouse anti-rat CYP2B2 [sc-53242 (Santa Cruz Biotechnology, USA)], rabbit anti-rat CYP3A1 [AB1253 (Chemicon, USA)], rabbit anti-rat CYP3A2 [458223 (BD Gentest, USA)] and rabbit anti-rat CYP3A9 [AB1276 (Chemicon, USA)] were diluted in 0.1% T-TBS and 2% NFDM. For ABCB1a/b (1:4000), ABCC1 and ABCC2 (1:1000), mouse anti-rat ABCC2 [ab3373 (M2 III-6) (abcam, UK)], mouse anti rat ABCC1 [ab24102 (MRPm5) (abcam, UK)], goat anti rat P-gp [mdr(C-19) (Santa Cruz Biotechnology, USA)] were diluted in 0.05% T-TBS. β-actin loading control was used for all proteins (anti β-actin (1:5000) (Sigma, UK). All primary antibodies were incubated for 2 h at room temperature and all intermediate wash steps were performed with 0.05% T-TBS.

Horse radish peroxidise (HRP) conjugated secondary antibodies; STAR88P Donkey anti-sheep HRP conjugated (Serotec, USA), ab6701 Donkey anti-rabbit HRP conjugated (abcam, UK), P0449: rabbit anti-goat HRP conjugated (DakoCytomation, Denmark), sheep anti-mouse HRP conjugated (Amersham Biosciences, UK) were diluted 1:10000 and incubated for 1 hour at room temperature in 2% NFDM and 0.03% T-TBS. All subsequent washing steps were performed with 0.05% T-TBS, with the exception of ABCB1a/b which required 0.1% T-TBS.

Protein band visualisation was performed using enhanced chemiluminescence (ECL) technology (PerkinElmer, USA) and quantification was achieved using BioRad GS710 scanner and BioRad Quantity One™ densitometric analysis software (Bio-Rad, USA). Optical density and relative protein expression of bands was determined against β-actin loading controls. Background saturation of ECL treated nitrocellulose membranes was corrected by subtraction of measurements taken from random sections of membrane (n=4) and subtracted from protein band density.

Statistical and data analysis

All reported data are for 18 hour incubations. The minimum concentration at which induction was observed and maximum fold change (excluding toxic concentrations) versus control are presented throughout this manuscript. Caution was taken in interpretation from data generated with concentrations of test compound shown to be toxic at 5 days for H411E and Iec-6. Specifically, concentrations that produced toxicity after 5 days are illustrated in the figures as dashed lines and statistical analysis is only presented for data at which significant induction was observed below this threshold. Therefore robust EC_{50} and E_{max} estimates were compromised and thus not used. Normality was assessed using a Shapiro-Wilk statistical test. Differences in mRNA and protein expression were assessed using a paired *t*-test. Logarithmic and/or linear regression was used to determine the relationship between change in mRNA and protein in cell lines.

Results

Cell line characterisation

All CYPs were expressed at higher levels in liver tissue compared to intestine and primary hepatocytes (Figure 1A, 1B, and 1C), whereas transporters ABCB1a and ABCB1b were expressed at relatively higher levels in intestinal tissue compared to liver and primary hepatocytes (Figure 1D, 1E, and 1F). Lower basal levels of expression of nuclear receptors were found in the intestinal tissue compared to liver tissue and primary cells, specifically for PXR (Figure 1G, 1H, and 1I). Basal level of expression of transcripts were approximately 13 fold (NRs), 14 fold (transporters) and 6 fold (CYPs) higher in liver tissue compared to H411E and primary hepatocytes (Figure 1a, d and g respectively). 8 fold (NRs), 14 fold (transporters) and 4 fold (CYPs) higher in intestinal tissue compared Iec-6 and primary hepatocytes (Figure 1B, 1E, and 1H). Despite some minor oscillations in basal level of expression during passage, all transcripts were found to be stable from passage 5 to passage 21 after receipt from ATCC for both cell lines. However, for analysis, cell lines were only used between passage 11 and 13.

Toxicity

After 18 h, there was no significant toxicity observed for any

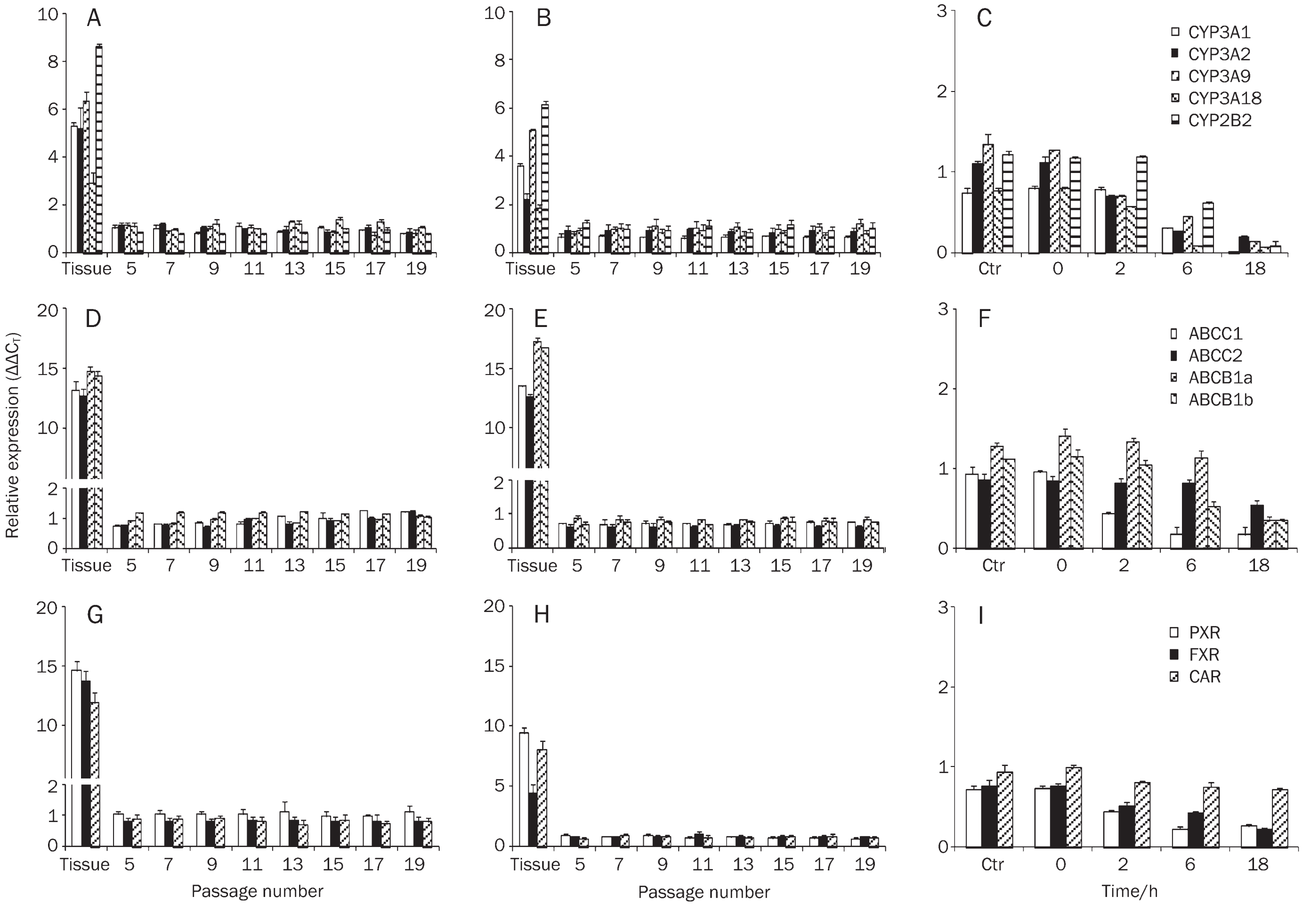

Figure 1. Basal level of expression and stability of CYPs, transporters (ABC) and nuclear hormone receptors in rodent liver versus rodent hepatic cell line H411E (A, D, and G) and rodent intestinal tissue versus rodent intestinal cell line Iec-6 (B, E, and H) during passage. Basal level of expression and stability of CYPs, transporters and nuclear hormone receptors in rat primary hepatocytes over time. Data are the mean±SD. *n*=4 experiments conducted in duplicate.

test compounds. However, after 5 days significant toxicity was detected for both H411E and Iec-6 (data not shown) implying that induction studies above certain concentrations may not be physiologically relevant *ie* for H411E, PB, PCN, CDCA, and RIF were all toxic at 100 μmol/L (P<0.0001). For Iec-6, CDCA, and PB were toxic at 10 μmol/L (P=0.0001 and P<0.0001 respectively) and PCN and RIF at 100 μmol/L (P=0.0027 and P<0.0001 P= 0.0027 respectively).

Protein binding

For DMEM containing 10% FBS, PB, PCN, RIF, and CDCA were determined as 98%, 97%, 98%, and 82% unbound respectively, indicating low levels of binding to FBS and a similar free drug concentration was present for incubations for all cell types.

Effects of DEX on CYP3A9, ABCB1a, ABCB1b, and PCN

DEX was a potent inducer of all transcripts in H411E (Figure 2A) and Iec-6 (Figure 2B). Concentration dependent induction was observed for all transcripts in both cell lines, with significant induction for ABCB1a and ABCB1b in H411E and ABCB1a, ABCB1b, and CYP3A9 in Iec-6 at 0.01 μmol/L. Significant induction of PXR was detected at 0.1 μmol/L DEX in both cell lines. With the exception of ABCB1a in H411E (10 μmol/L), all transcripts were maximally induced at 100 μmol/L DEX.

In H411E and Iec-6 cells, PCN significantly induced CYP3A9 mRNA (Figures 2C and 2D), ABCB1a (Figures 2E and 2F), ABCB1b (Figures 2G and 2H) and PXR (Figures 2I and 2J) when compared to DEX-free control. However, when DEX was included in the culture media no significant induction of ABCB1b in H411E (Figure 2G) or CYP3A9 in Iec-6 (Figure 2D) was observed compared to DEX-free control.

Induction of PXR, FXR, and CAR mRNA in H411E, Iec-6, and primary hepatocytes

A summary of the impact on all genes of interest by prototypical inducers in H411e, Iec-6, and rat primary hepatocytes can be found in Table 1. The impact of CDCA, PCN, PB, and RIF on PXR, FXR, and CAR mRNA expression in H411E, Iec-6, and primary hepatocytes are shown in Figure 3. CDCA significantly increased expression of PXR, FXR, and CAR in H411E

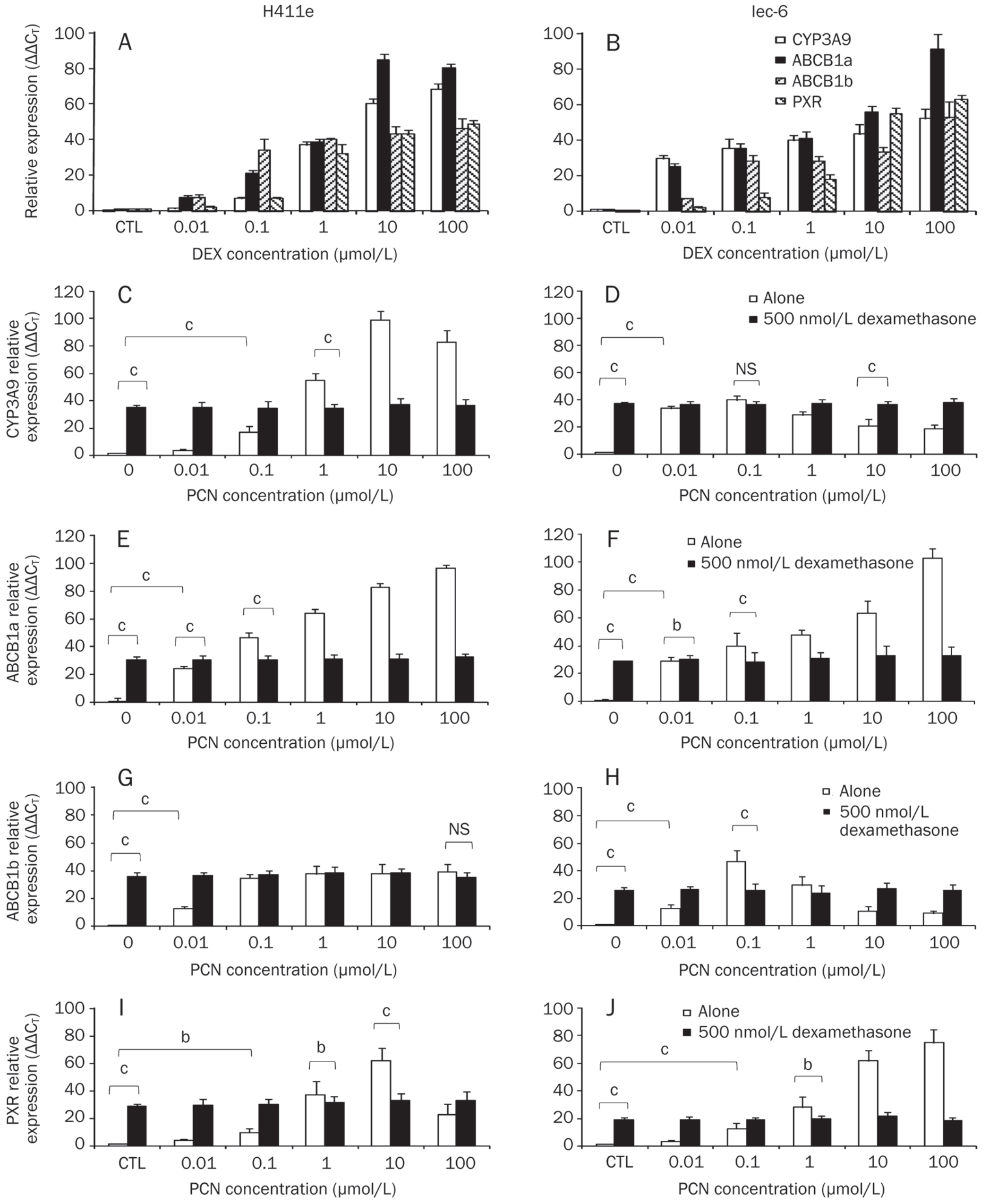

Figure 2. Implications of using dexamethasone (DEX) as a media supplement (A, B). Impact of dexamethasone (DEX) (0–100 μmol/L) on mRNA expression of CYP3A9, ABCB1a, ABCB1b, and pregnane X receptor (PXR) in H411E and Iec-6 (C–H). Impact of dexamethasone (DEX) (500 nmol/L) on inducibility of CYP3A9 (C, D), ABCB1a (E, F), ABCB1b (G, H) and pregnane X receptor (PXR) (I, J) by pregnenolone 16α-carbonitrile (PCN) in H411E and Iec-6 cells. Data are mean ±SD of four experiments conducted in duplicate. For clarity, not all statistical analyses are given: $^{b}P<0.05$, $^{c}P<0.01$. For each transcript, a significant increase in expression was observed at concentrations ≤1 μmol/L when cells were incubated with pregnenolone 16α-carbonitrile (PCN) alone, which would not have been observed when dexamethasone (DEX) was incorporated into the media.

(Figure 3A) and Iec-6 (Figure 3B), but only for FXR and CAR in primary hepatocytes (Figure 3C). PCN caused significant induction of PXR and CAR in H411E (Figure 3D), Iec-6 (Figure 3E) in primary hepatocytes (Figure 3F). However, there was no significant increase of FXR by PCN in any cells used. For PB, there was no significant increase in mRNA expression for FXR in H411E, Iec-6 or primary hepatocytes (Figures 3G, 3H, and 3I respectively). However, significant induction of PXR and CAR was observed for all three cell types. This effect by PB was more marked with respect to magnitude of fold change for CAR in Iec-6 cells (Figure 3H) compared to H411E and primary hepatocytes. RIF upregulated FXR, PXR, and CAR in H411E (Figure 3J), PXR and CAR in Iec-6 (Figure 3K) and primary hepatocytes (Figure 3L).

Induction of CYP2B2, CYP3A1, CYP3A2, and CYP3A9 mRNA in H411E, Iec-6, and primary hepatocytes

The effect of CDCA, PCN, PB, and RIF on mRNA expression of CYP2B2, CYP3A1, CYP3A2, and CYP3A9 can be seen in Figure 4. Statistical analysis is only given for the lowest concentration at which a significant induction was observed. CDCA significantly upregulated CYP2B2, CYP3A1, and CYP3A9 in H411E (Figure 4A), CYP2B2 and CYP3A1 in Iec-6 (Figure 4b) and CYP2B2, CYP3A1, CYP3A2, and CYP3A9 in primary hepatocytes (Figure 4C). For PCN, all CYPs were significantly increased at 0.1 μmol/L in H411E (Figure 4D), whereas in Iec-6 (Figure 4E), CYP3A1 and CYP3A9 were induced at 0.01 μmol/L, CYP2B2 at 0.1 μmol/L and CYP3A2 at 10 μmol/L PCN. In addition, all CYP transcripts were induced in pri-

Table 1. Summary of the impact of prototypical inducers (Chenodeoxycholiic acid; CDCA, Pregnane 16α-carbonitrile; PCN, Phenobarbital; PB and Rifampicin; RIF), on gene expression in H411e, Iec-6, and rat primary hepatocytes. For clarity, statistical analyses for cell lines H411e and Iec-6 are given only for the lowest concentration at which a significant difference was observed. For primary hepatocytes, the incubation time (in hours) when significant induction was detected: $^{b}P<0.05$, $^{c}P<0.01$.

	H411e Test compound (μmol/L)				Iec-6 Test compound (μmol/L)				Primary hepatocytes Test compound at 1 μmol/L (Incubation time in hours)			
Gene	CDCA	PCN	PB	RIF	CDCA	PCN	PB	RIF	CDCA	PCN	PB	RIF
CYP2B2	0.1^{c}	0.1^{c}	10^{b}	NS	1^{c}	0.1^{c}	NS	NS	2^{c}	2^{c}	2^{b}	NS
CYP3A1	10^{b}	0.1^{c}	10^{b}	1^{c}	0.1^{c}	0.01^{c}	1^{c}	0.1^{b}	2^{c}	2^{b}	2^{c}	2^{c}
CYP3A2	NS	0.1^{c}	10^{b}	1^{c}	NS	10^{c}	1^{b}	1^{c}	2^{c}	2^{c}	2^{c}	2^{c}
CYP3A9	0.1^{c}	0.1^{c}	10^{c}	0.01^{b}	NS	0.01^{c}	0.01^{c}	0.1^{c}	2^{c}	2^{c}	2^{c}	2^{c}
ABCC1	1^{c}	1^{c}	NS	1^{c}	1^{c}	1^{c}	NS	1^{b}	4^{b}	2^{c}	2^{b}	4^{b}
ABCC2	1^{b}	1^{c}	10^{c}	1^{c}	NS	NS	1^{b}	1^{c}	2^{c}	2^{b}	2^{b}	2^{b}
ABCB1a	0.01^{c}	0.01^{c}	0.01^{c}	0.01^{c}	0.01^{c}	0.01^{c}	0.01^{c}	0.01^{c}	2^{b}	2^{c}	2^{c}	4^{c}
ABCB1b	0.1^{c}	0.01^{c}	0.01^{c}	0.1^{c}	1^{c}	0.01^{c}	0.01^{c}	0.1^{c}	2^{c}	2^{b}	2^{c}	2^{c}
FXR	1^{c}	0.1^{c}	NS	1^{c}	0.1^{b}	NS	NS	NS	2^{c}	NS	NS	NS
PXR	10^{b}	NS	0.1^{c}	1^{c}	1^{b}	0.1^{b}	0.1^{b}	0.1^{c}	NS	2^{b}	2^{c}	2^{c}
CAR	1^{c}	1^{c}	10^{c}	1^{c}	1^{c}	0.1^{b}	0.1^{c}	0.1^{c}	2^{b}	4^{b}	2^{c}	2^{c}

mary hepatocytes (Figure 4F). With the notable exception of CYP2B2 in Iec-6 cells (Figure 4H), all CYPs were significantly induced in H411E cells (Figure 4G), Iec-6 cells (Figure 4H) and primary hepatocytes (Figure 4i) by PB. Finally, RIF had a potent effect on CYP3A1, CYP3A2, and CYP3A9 in all three cell types (Figure 4J, 4K, and 4L). This effect occurred at lower concentration in Iec-6 (Figure 4K), requiring only 0.1 μmol/L RIF to elicit a significant effect.

Induction of ABCB1a, ABCB1b, ABCC1, and ABCC2 mRNA in H411E, Iec-6, and primary hepatocytes

The impact of CDCA, PCN, PB, and RIF on the expression of rat transporters can be seen in Figure 5. With the exception of ABCC1 in Iec-6 cells (Figure 5B), CDCA significantly upregulated all transporters in all three cell types (Figures 5A, 5B, and 5C). PCN significantly induced all transporters in H411E and primary hepatocytes (Figure 5f). ABCB1a, ABCB1b, and ABCC1 were also significantly upregulated in Iec-6 (Figure 5E) when incubated with PCN. However, there was no significant induction of ABCC2 in Iec-6 below toxic concentrations (Figure 5E). For PB, there was a significant increase observed for mRNA expression of ABCB1a, ABCB1b, and ABCC2 in H411E (Figure 5G) and Iec-6 (Figure 5H) cells and all transporters in primary hepatocytes. However, PB did not elicit a significant effect on ABCC1 in H411E or Iec-6 below toxic concentrations. RIF had a potent effect on all four transporters in all three cell lines (Figure 5J, 5K, and 5L). However, this effect was more marked with respect to magnitude of fold change for transporters in H411E (Figure 5J), significantly for ABCB1a compared to ABCB1b, ABCC1, and ABCC2.

Induction of CYP2B2, CYP3A1, CYP3A2, CYP3A9, ABCB1a/b, ABCC1, and ABCC2 protein in H411E and Iec-6 cells

The effects of CDCA, PCN, PB, and RIF on protein expression of CYP2B2, CYP3A1, CYP3A2, ABCB1a/b, ABCC1, and ABCC2 in H411E and Iec-6 is shown in Figure 6. CDCA significantly upregulated CYP2B2, CYP3A1, ABCB1a/b, ABCC1, and ABCC2 in H411E and CYP2B2, CYP3A1, and ABCC2 in Iec-6 cells. With the exception of ABCC1 and ABCC2 in Iec-6, PCN significantly upregulated all proteins in both H411E and Iec-6. PB upregulated CYP2B2, CYP3A2, CYP3A9, ABCB1a/b, ABCC1, and ABCC2 in H411E cells and CYP3A9 and ABCB1a/b in Iec-6. RIF increased protein expression of CYP3A1, CYP3A2, ABCC1, and ABCC2 in H411E cells and CYP3A2, CYP3A9, ABCB1a/b, and ABCC2 in Iec-6.

Relationship between mRNA and protein expression

The relationship between mRNA induction and protein expression for H411e and Iec-6 can be seen in Figure 7 and Figure 8 respectively. In order to assess the relationship between mRNA induction and protein expression, 1μmol/L mRNA data for each transcript were plotted against the corresponding protein data. Correlations for ABCB1a and ABCB1b were collated as no primary antibodies were available to differentiate the individual proteins. In H411E, a significant logarithmic correlation was observed for mRNA and protein for CYP2B2, CYP3A1, CYP3A2, ABCB1a/b, ABCC1, and ABCC2. For Iec-6 cells, significant logarithmic relationships were observed for CYP2B2, CYP3A2, CYP3A9, ABCB1a/b, and ABCC2. Interestingly, the relationship between mRNA and protein expression was linear for CYP3A1.

Discussion

There are clear limitations associated with the use of rodent systems when extrapolating to human. For example, species differences often make it difficult to extrapolate rodent observations directly[34–36] and conventional reporter based assays demonstrate that species differences are apparent for

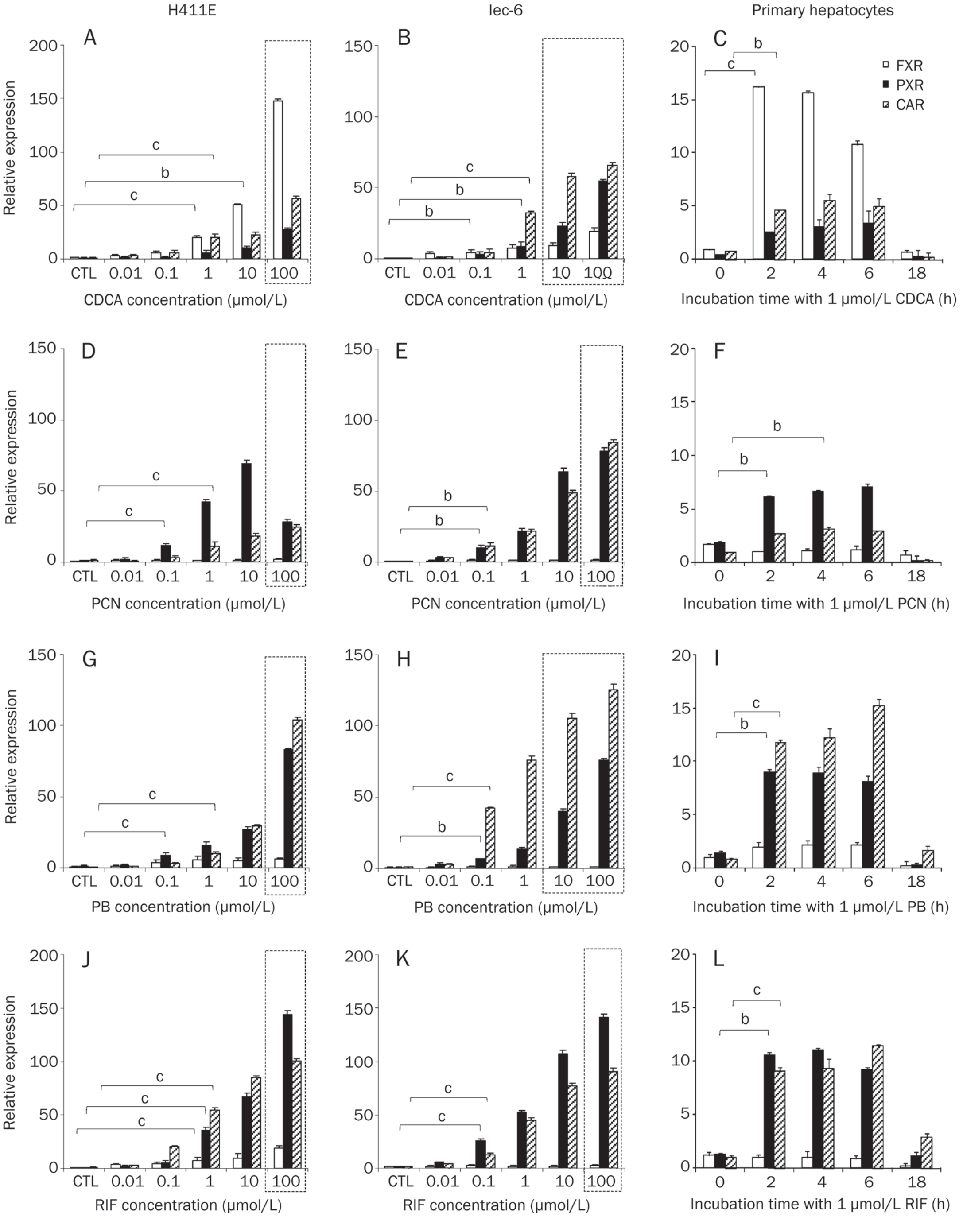

Figure 3. Impact of typical activators on nuclear receptors. Effect of chenodeoxycholic acid (CDCA) (A–C), pregnenolone 16α-carbonitrile (PCN) (D–F), phenobarbital (PB) (G–I) and rifampicin (RIF) (J–l) in H411E, Iec-6 and primary hepatocytes. Data are mean±SD of four experiments conducted in duplicate. In cell lines, concentration dependency was investigated, whereas, in primary cells, time dependency was assessed at 1 μmol/L of each compound. Dotted lines indicate concentrations at which toxicity was observed following 5-day incubations with drug. For clarity, statistical analyses are given only for the lowest concentration at which a significant difference was observed: $^{b}P<0.05$, $^{c}P<0.01$.

some ligands for PXR[37]. Importantly, PCN has been shown to activate rodent PXR but not human and the converse true for RIF[17]. However, other studies have reported that RIF treatment of rat hepatocytes increases CYP3A protein and PCN induces CYP3A mRNA in 50% of human cultures[38] and has also been shown to activate PXR in some human systems[39].

Cell lines have been reported to express decreased levels of certain transporters and CYP isoforms compared to primary cells[40, 41]. Previously, we have reported instability and variability of expression of some CYPs, transporters and nuclear receptors in the human hepatic (HepG2) and intestinal (Caco-2) cells over time[1]. Therefore, we conducted an initial

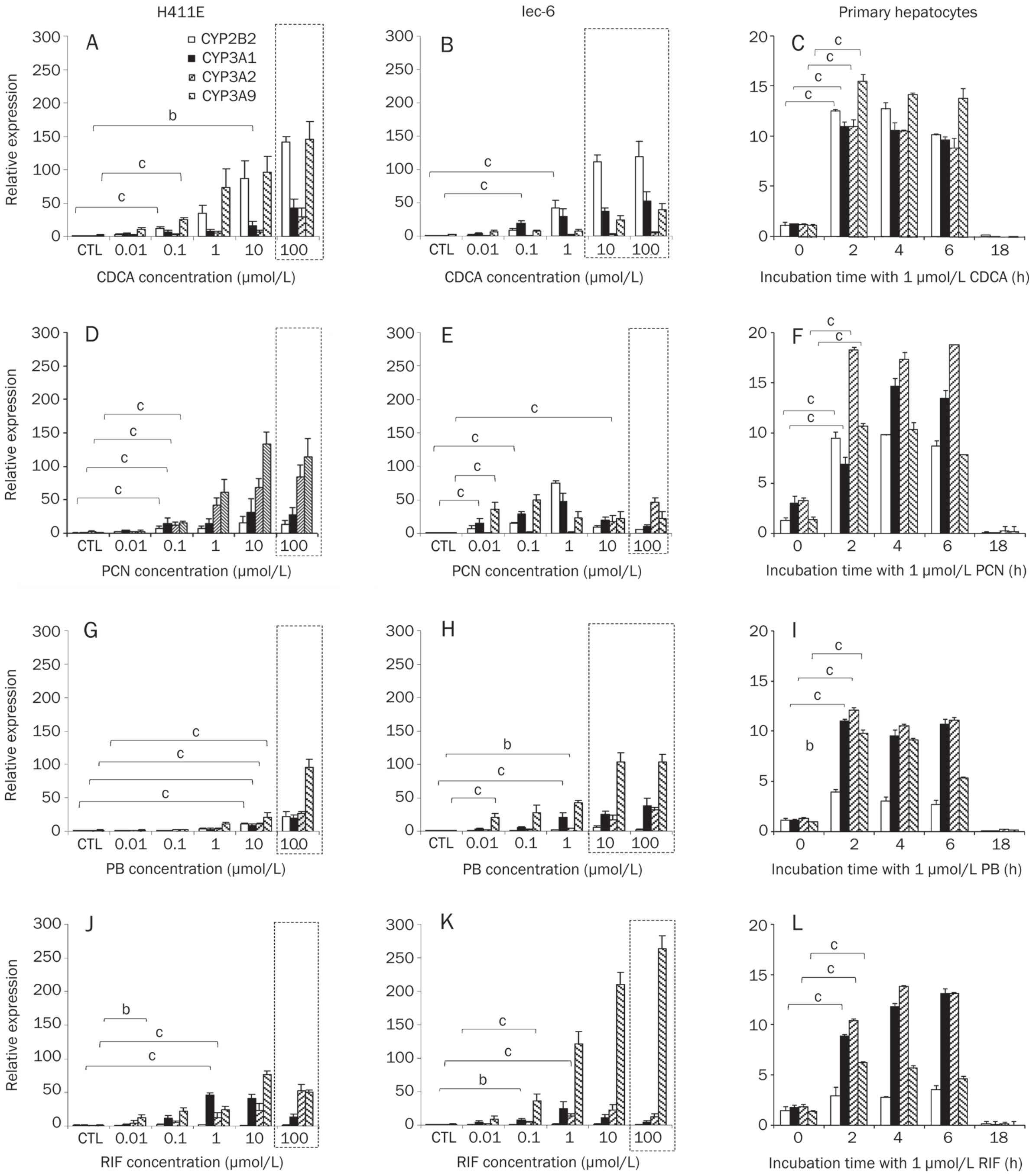

Figure 4. Impact of typical activators on CYP isoforms. Effect of chenodeoxycholic acid (CDCA) (A–C), pregnenolone 16α-carbonitrile (PCN) (D–F), phenobarbital (PB) (G–I) and rifampicin (RIF) (J–I) in H411E, Iec-6 and primary hepatocytes. Data are mean±SD of four experiments conducted in duplicate. In cell lines, concentration dependency was investigated, whereas, in primary cells, time dependency was assessed at 1 μmol/L of each compound. Dotted lines indicate concentrations at which toxicity was observed following 5-day incubations with drug. For clarity, statistical analyses are given only for the lowest concentration at which a significant difference was observed: $^{b}P<0.05$, $^{c}P<0.01$.

screen of the studied transcripts in H411E and Iec-6 in order to assess basal levels of expression and stability of transcripts. However, unlike HepG2 and Caco-2, all CYPs, transporters and nuclear receptors were found to be stable in the rodent cell lines used here.

Isolated primary hepatocytes can be used in suspension or they can be cultured[42–44]. In suspension they exhibit metabolic activity for a period of 4 to 6 h[45], thus remaining useful for the study of drug metabolism or toxicity[46]. However, gene expression changes taking place in primary hepatocyte cultures over time (0−18 h) in the absence of treatment were assessed and were consistent with previous studies involving

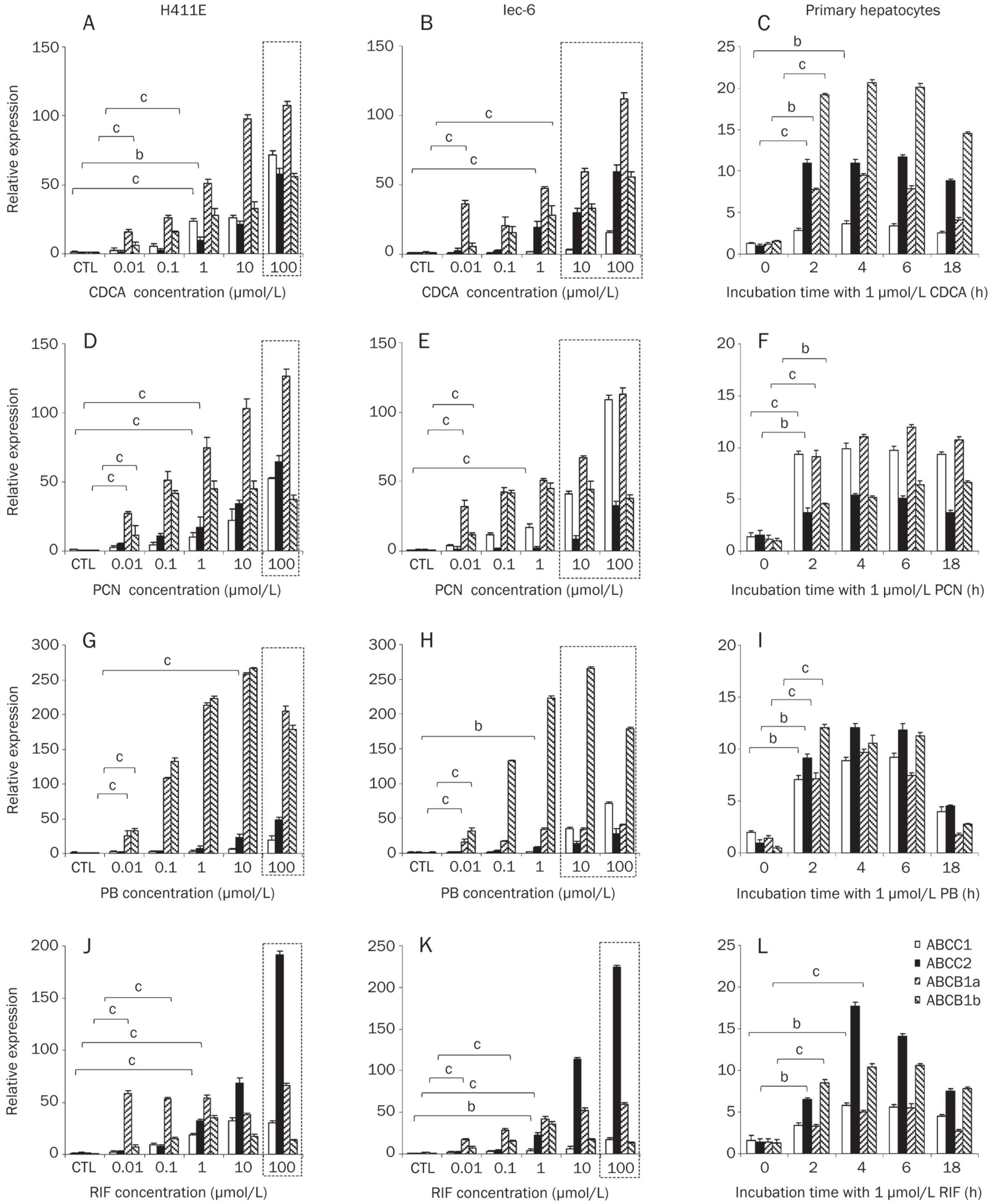

Figure 5. Impact of typical activators on transporters. Effect of chenodeoxycholic acid (CDCA) (A–C), pregnenolone 16α-carbonitrile (PCN) (D–F), phenobarbital (PB) (G–I) and rifampicin (RIF) (J–I) in H411E, Iec-6 and primary hepatocytes. Data are mean±SD of four experiments conducted in duplicate. In cell lines, concentration dependency was investigated, whereas, in primary cells, time dependency was assessed at 1 μmol/L of each compound. Dotted lines indicate concentrations at which toxicity was observed following 5-day incubations with drug. For clarity, statistical analyses are given only for the lowest concentration at which a significant difference was observed: $^bP<0.05$, $^cP<0.01$.

hepatocytes in pure cultures[47, 48].

The glucocorticoid DEX, is a widely used component in culture media and has been reported to exert a protective role on cell survival, prolonging cell viability, inhibiting the development of an apoptotic morphology, and stabilising expression of procaspase-3 in both human and rat hepatocytes[49]. However, DEX is a known inducer of the human PXR target gene *CYP3A4* and has also been shown to affect p-glycoprotein

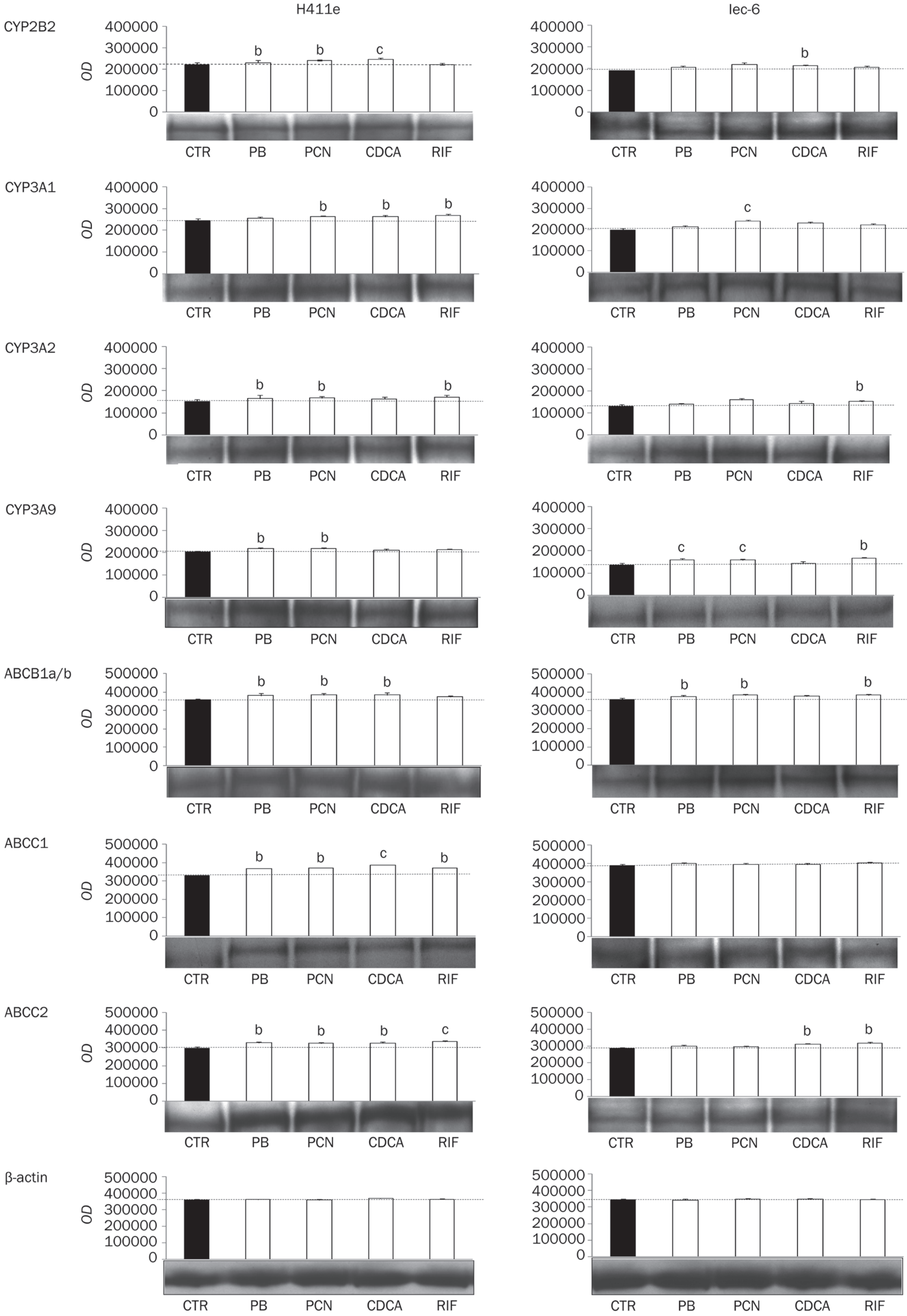

Figure 6. Effect of chenodeoxycholic acid (CDCA), pregnenolone 16α-carbonitrile (PCN), phenobarbital (PB) and rifampicin (RIF) on protein expression of CYP2B2, CYP3A1, CYP3A2, CYP3A9, ABCB1a/b, ABCC1, and ABCC2 in H411E and Iec-6. Results for β-actin are also given to illustrate equal loading. A representative western blot as well as the mean±SD optical densitometric results from four experiments conducted in duplicate are shown. $^{b}P<0.05$, $^{c}P<0.01$.

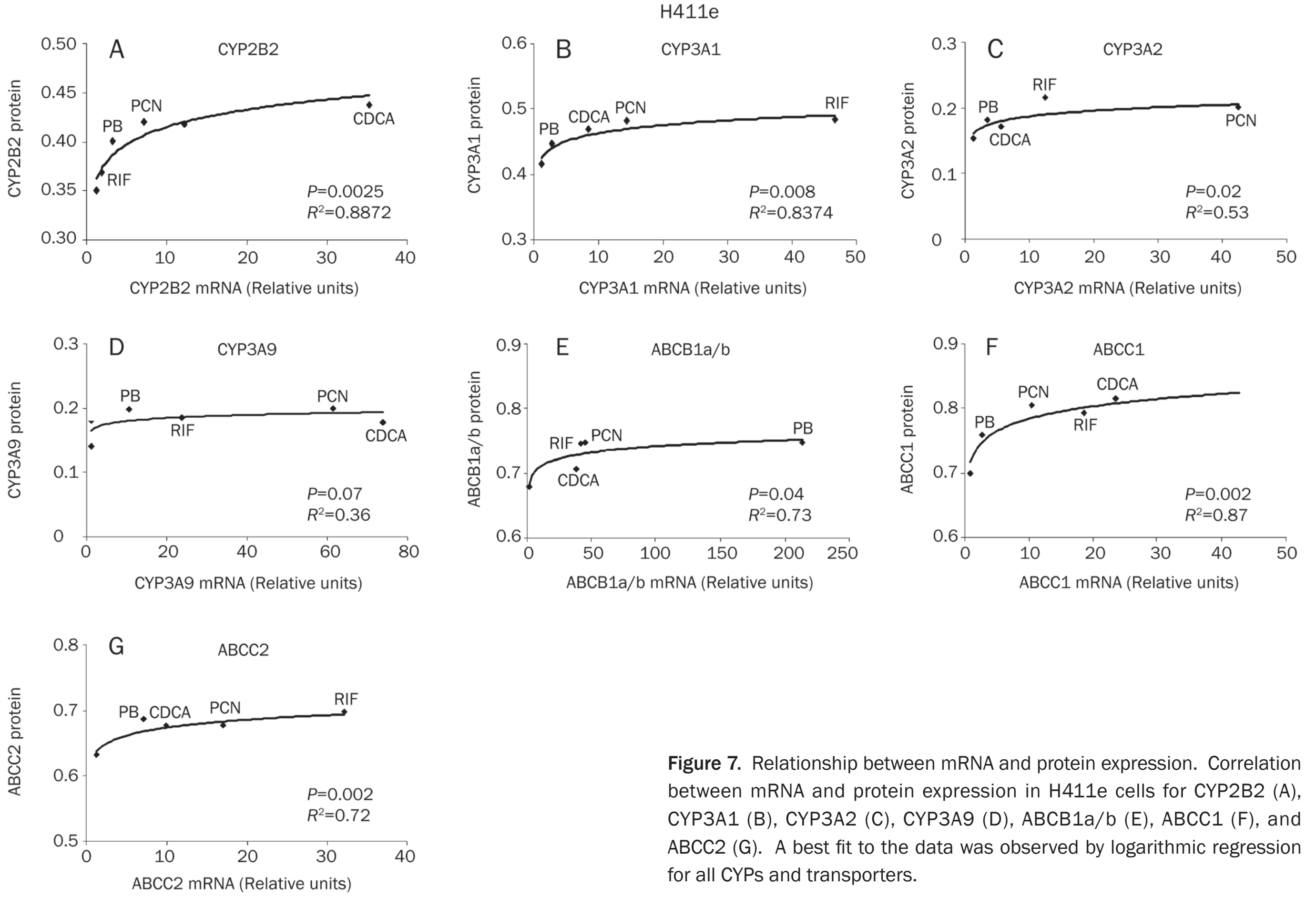

Figure 7. Relationship between mRNA and protein expression. Correlation between mRNA and protein expression in H411e cells for CYP2B2 (A), CYP3A1 (B), CYP3A2 (C), CYP3A9 (D), ABCB1a/b (E), ABCC1 (F), and ABCC2 (G). A best fit to the data was observed by logarithmic regression for all CYPs and transporters.

(P-gp) activity[50] and expression in primary rat hepatocytes[51]. In addition, DEX is believed to be a prerequisite for PCN inducible genes in rodent hepatocytes[52]. Previously we have shown that PCN upregulates expression of human CYP3A4, ABCB1 and PXR mRNA and inclusion of DEX as a media supplement resulted in a loss of ability to detect induction by PCN in human cells[1]. Generally, data presented herein show DEX had a similar effect in rat cells, where DEX significantly upregulated CYP3A9, ABCB1a, ABCB1b, and PXR. This is in broad agreement with similar observations in rat liver slices[53]. Furthermore, these data indicate a maximal response to PCN. Therefore, the addition of DEX increases the relative baseline but, as the maximum is fixed, a reduction in the potential effect is observed. This may allow competition in order to enable the biological system to prevent over-activation. Interestingly, a previous study indicated that the effects of DEX and PCN on rodent PXR target gene *CYP3A1* were partially dependent upon the order these compounds were administered[54].

The mechanisms controlling this PCN/DEX response currently remain unclear. However, previously it has been shown that sub-micromolar concentrations of PCN activate rodent PXR[55] but antagonise the glucocorticoid receptor (GR). Furthermore, activation of GR by DEX increases PXR expression and increases CYP3A1, whereas PCN activates PXR directly[54]. In addition, the proposed existence of a cascade of signal transmission: *GR-[PXR/CAR]*-metabolising enzymes-transporters[56] may explain the xenobiotic-mediated induction of CYP2B and CYP3A by prototypical activators of PXR and CAR in the presence of DEX[57–60]. Importantly, this cascade would imply processes affecting the transcriptional activity of GR would subsequently affect the expression of PXR, CAR and FXR, and thus the expression of their target genes[57]. Therefore, it is not possible to assume that the induction reported here is necessarily due to discrete activation of individual nuclear receptors. However, the issues involving the DEX effect, coupled with attempts to facilitate comparisons with our human data[1] led us not to include it as a supplement in subsequent experiments.

Significant induction of mRNA and protein of many transcripts in cell lines H411E and Iec-6 and primary hepatocytes in response to the nuclear receptor ligands were observed. Interestingly, for some of the genes investigated, a change in mRNA was observed with no corresponding change in protein and *vice-versa*. For example, mRNA was induced with no increase in protein for CYP3A9 by CDCA in H411e and CYP3A1 by PB in Iec-6, whereas increases in protein for ABCC1 by PB in H411e and ABCC2 by CDCA in Iec-6 with no corresponding increase in mRNA. However, recent work util-

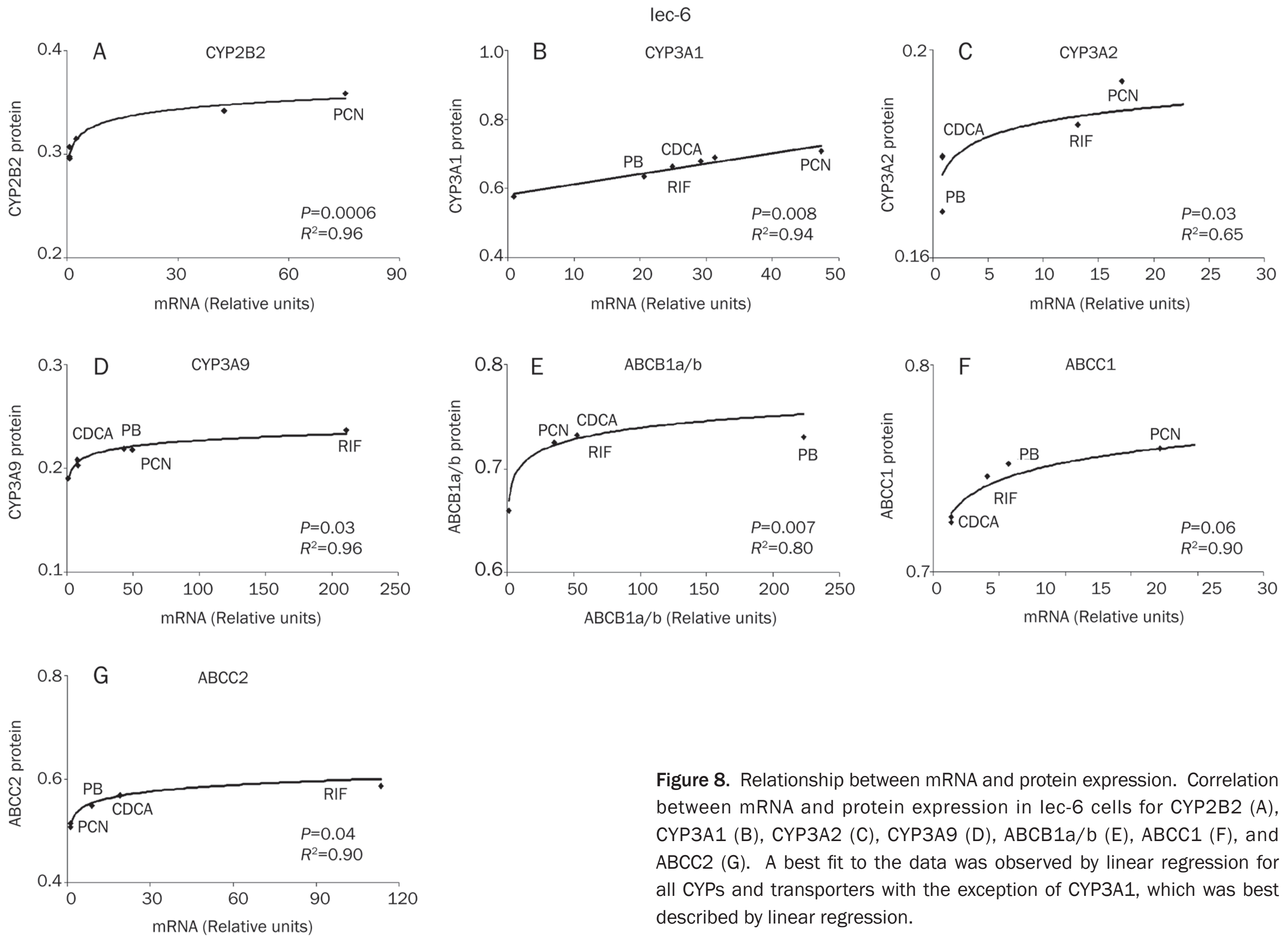

Figure 8. Relationship between mRNA and protein expression. Correlation between mRNA and protein expression in Iec-6 cells for CYP2B2 (A), CYP3A1 (B), CYP3A2 (C), CYP3A9 (D), ABCB1a/b (E), ABCC1 (F), and ABCC2 (G). A best fit to the data was observed by linear regression for all CYPs and transporters with the exception of CYP3A1, which was best described by linear regression.

ising microarray analysis has indicated that total mRNA levels do not always reflect protein levels[61]. For example, a study by Ideker *et al*, 2001, calculated an overall Pearson correlation coefficient between mRNA and protein expression of 0.61, although no change in protein expression was observed for almost 80% of genes reported as having a significant change in mRNA, indicating that a complex relationship exists between mRNA and protein expression. This work supporting data from a previous study[62] where they observed a poor correlation between mRNA and protein for all but the most abundant proteins examined. Some similarities and important differences were seen in the profiles of induction in H411E versus Iec-6 cells. However, our data are in broad agreement with previous studies conducted in rat cells incubated with PB[63, 64], PCN[65, 66], and RIF [38]. Where differences were observed, it is unclear whether this is due to inherent differences associated with specific tissue type (hepatic or intestinal) or whether they are due partly to the dedifferentiation process that occurs when generating and passaging continuously dividing cell systems. Specifically, because drug metabolism is a hallmark of highly differentiated, nondividing hepatocytes[67].

For rat primary hepatocytes, our study conflicts with previous studies which indicated that RIF had no effect on rat PXR[17]. However, these investigators included DEX as a culture supplement and our observations that rat CYP3As are inducible by RIF is in agreement with another study[68]. Taken together these observations reinforce the probability that culturing conditions, including commonly used culture supplements i.e. antibiotics, FBS concentration, and DEX, play a major role in the variability of results between laboratories.

Several interesting observations have emerged from this study. Of note, all compounds were potent inducers of ABCB1a and ABCB1b, ABCC1 and ABCC2. Importantly, CDCA and RIF were more potent with respect to magnitude of fold change and drug concentration for ABCB1a compared to ABCB1b, generally requiring the lowest concentration (0.01 μmol/L) to elicit a significant effect. This response is consistent with observations by[69], who reported preferential induction of ABCB1a versus ABCB1b. While it is difficult to directly link specific regulation of ABCB1a and ABCB1b to PXR and CAR and thus their relative contribution, from data presented herein. However, PCN and PB were more potent inducers of PXR than CAR in H411E and primary hepatocytes than for CAR in Iec-6 intestinal cells. Indeed, these observations are similar to a previous study[16] where they noted CAR had an additional effect on ABCB1a. Also of note, ABCC2 mRNA levels were found to be markedly increased in primary rat hepatocytes exposed to all test compounds. In addition, a previous study also observed that ABCC2 was up-regulated at higher concentrations of PB than that needed for induction of rat *CYP2B* and *CYP3A* genes[70]. This confirms the PB-mediated up-regulation of ABCC2[71] and suggests that ABCC2 and CYPs are differentially regulated in response to PB.

CDCA had a potent effect on transporters, including ABCC2, in this study. Interestingly, it has also been reported that activation of FXR by CDCA is dependent upon the species examined, with CDCA having both an increased potency and magnitude of induction through human FXR than rodent FXR[72]. This is in partial agreement with this study and our previous observations[1] where we found the effect of CDCA on FXR more potent for HepG2 than for H411E and a higher magnitude of induction for Caco-2 than for Iec-6. Furthermore, in both studies, human and rodent, we observed that CDCA was the only compound to significantly induce FXR mRNA.

Conclusion

In summary, induction of key transcriptional regulators PXR, CAR, and FXR by paradigm nuclear receptor ligands PB, PCN, RIF and CDCA in rat hepatic (H411E) and intestinal (Iec-6) cell lines and primary hepatocytes has been shown. In addition, a consequence of their induction is a corresponding induction of their target genes. Importantly, purported species specific PXR activators RIF (human PXR) and PCN (rodent PXR) showed comparable induction profiles of PXR and PXR target genes in all cells in the absence of DEX. Therefore, although species differences in activation of nuclear receptors are clearly evident, a similar spectrum of induction of target genes occurs in human and rat cells.

Acknowledgements

This work was funded by AstraZeneca Charnwood.

Author contribution

Philip MARTIN designed and performed all research experiments, collated all data and wrote the manuscript; Dominic WILLIAMS isolated fresh rat primary hepatocytes; Robert RILEY assisted with protein binding experiments and review of manuscript. Paul THOMPSON assisted with immunoblots and review of manuscript. David BACK assisted with writing and reviewing manuscript. Andrew OWEN performed statistical analysis for the relationship between mRNA and protein and writing manuscript.

References

1 Martin P, Riley R, Back DJ, Owen A. Comparison of the induction profile for drug disposition proteins by typical nuclear receptor activators in human hepatic and intestinal cells. Br J Pharmacol 2008; 153: 805–19.
2 Kirita S, Matsubara T. cDNA cloning and characterization of a novel member of steroid-induced cytochrome P450 3A in rats. Arch Biochem Biophys 1993; 307: 253–8.
3 Komori M, Oda Y. A major glucocorticoid-inducible P450 in rat liver is not P450 3A1. J Biochem 1994; 116: 114–20.
4 Gonzalez FJ, Song BJ, Hardwick JP. Pregnenolone 16 alpha-carbonitrile-inducible P-450 gene family: gene conversion and differential regulation. Mol Cell Biol 1986; 6: 2969–76.
5 Xue L, Zgoda VG, Arison B, Almira Correia M. Structure-function relationships of rat liver CYP3A9 to its human liver orthologs: site-directed active site mutagenesis to a progesterone dihydroxylase. Arch Biochem Biophys 2003; 409: 113–26.
6 Strotkamp D, Roos PH, Hanstein WG. A novel CYP3 gene from female rats. Biochim Biophys Acta 1995; 1260: 341–4.
7 Nagata K, Murayama N, Miyata M, Shimada M, Urahashi A, Yamazoe Y, *et al.* Isolation and characterization of a new rat P450 (CYP3A18) cDNA encoding P450(6)beta-2 catalyzing testosterone 6 beta- and 16 alpha-hydroxylations. Pharmacogenetics 1996; 6: 103–11.
8 Deng Y, Bi HC, Zhao LZ, He F, Liu YQ, Yu JJ, *et al.* Induction of cytochrome P450s by terpene trilactones and flavonoids of the *Ginkgo biloba* extract EGb 761 in rats. Xenobiotica 2008; 38: 465–81.
9 Garcia MC, Ma D, Dicioccio AT, Cali J. The use of a high-throughput luminescent method to assess CYP3A enzyme induction in cultured rat hepatocytes. *In Vitro* Cell Dev Biol Anim 2008; 44: 129–34.
10 Hartley DP, Dai X, He YD, Carlini EJ, Wang B, Huskey SE, *et al.* Activators of the rat pregnane X receptor differentially modulate hepatic and intestinal gene expression. Mol Pharmacol 2004; 65: 1159–71.
11 Audet-Walsh E, Lachaud AA, Anderson A. The CYP2B2 5' flank contains a complex glucocorticoid response unit. Biochem Pharmacol 2008; 76: 1298–306.
12 Shinohara T, Taura K, Imamura T, Yamada H, Oguri K. Induction of rat hepatic cytochrome P450 2B subfamily by azidophenobarbital, as a possible photoaffinity probe for the putative phenobarbital receptor: comparative study with modified phenobarbitals with different functional groups. Drug Metab Dispos 1997; 25: 1442–6.
13 Stoltz C, Vachon MH, Trottier E, Dubois S, Paquet Y, Anderson A. The CYP2B2 phenobarbital response unit contains an accessory factor element and a putative glucocorticoid response element essential for conferring maximal phenobarbital responsiveness. J Biol Chem 1998; 273: 8528–36.
14 Roberge C, Beaudet MJ, Anderson A. GABA(A)/central benzodiazepine receptor and peripheral benzodiazepine receptor ligands as inducers of phenobarbital-inducible CYP2B and CYP3A. Biochem Pharmacol 2004; 68: 1383–9.
15 Waxman DJ, Azaroff L. Phenobarbital induction of cytochrome P-450 gene expression. Biochem J 1992; 281 (Pt 3): 577–92.
16 Maglich JM, Stoltz CM, Goodwin B, Hawkins-Brown D, Moore JT, Kliewer SA. Nuclear pregnane X receptor and constitutive androstane receptor regulate overlapping but distinct sets of genes involved in xenobiotic detoxification. Mol Pharmacol 2002; 62: 638–46.
17 Jones SA, Moore LB, Shenk JL, Wisely GB, Hamilton GA, McKee DD, *et al.* The pregnane X receptor: a promiscuous xenobiotic receptor that has diverged during evolution. Mol Endocrinol 2000; 14: 27–39.
18 Quattrochi LC, Guzelian PS. CYP3A regulation: from pharmacology to nuclear receptors. Drug Metab Dispos 2001; 29: 615–22.
19 Modica S, Moschetta A. Nuclear bile acid receptor FXR as pharmacological target: are we there yet? FEBS Lett 2006; 580: 5492–9.
20 Wang YD, Chen WD, Moore DD, Huang W. FXR: a metabolic regulator and cell protector. Cell Res 2008; 18: 1087–95.
21 Sonoda J, Pei L, Evans RM. Nuclear receptors: decoding metabolic disease. FEBS Lett 2008; 582: 2–9.

22 Xie W, Radominska-Pandya A, Shi Y, Simon CM, Nelson MC, Ong ES*, et al.* An essential role for nuclear receptors SXR/PXR in detoxification of cholestatic bile acids. Proc Natl Acad Sci USA 2001; 98: 3375−80.

23 Stedman CA, Liddle C, Coulter SA, Sonoda J, Alvarez JG, Moore DD*, et al.* Nuclear receptors constitutive androstane receptor and pregnane X receptor ameliorate cholestatic liver injury. Proc Natl Acad Sci USA 2005; 102: 2063−8.

24 Echchgadda I, Song CS, Roy AK, Chatterjee B. Dehydroepiandrosterone sulfotransferase is a target for transcriptional induction by the vitamin D receptor. Mol Pharmacol 2004; 65: 720−9.

25 Kast HR, Goodwin B, Tarr PT, Jones SA, Anisfeld AM, Stoltz CM*, et al.* Regulation of multidrug resistance-associated protein 2 (ABCC2) by the nuclear receptors pregnane X receptor, farnesoid X-activated receptor, and constitutive androstane receptor. J Biol Chem 2002; 277: 2908−15.

26 Sambruy Y, Ferruzza S, Ranaldi G, De Angelis I. Intestinal cell culture models: applications in toxicology and pharmacology. Cell Biol Toxicol 2001; 17: 301−17.

27 Lin JH. CYP induction-mediated drug interactions: *in vitro* assessment and clinical implications. Pharm Res 2006; 23: 1089−116.

28 Loretz LJ, Li AP, Flye MW, Wilson AG. Optimization of cryopreservation procedures for rat and human hepatocytes. Xenobiotica 1989; 19: 489−98.

29 Li AP, Lu C, Brent JA, Pham C, Fackett A, Ruegg CE*, et al.* Cryopreserved human hepatocytes: characterization of drug-metabolizing enzyme activities and applications in higher throughput screening assays for hepatotoxicity, metabolic stability, and drug-drug interaction potential. Chem Biol Interact 1999; 121: 17−35.

30 Owen A, Chandler B, Back DJ, Khoo SH. Expression of pregnane-X-receptor transcript in peripheral blood mononuclear cells and correlation with MDR1 mRNA. Antivir Ther 2004; 9: 819−21.

31 Mosmann T. Rapid colorimetric assay for cellular growth and survival: application to proliferation and cytotoxicity assays. J Immunol Methods 1983; 65: 55−63.

32 Marshak D. Strategies for protein purification and characterization: A laboratory course manual. Plainview (NY): Cold Spring Harbor Laboratory Press; 1996.

33 Stoscheck CM. Quantitation of protein. Methods Enzymol 1990; 182: 50−68.

34 Bogaards JJ, Bertrand M, Jackson P, Oudshoorn MJ, Weaver RJ, van Bladeren PJ*, et al.* Determining the best animal model for human cytochrome P450 activities: a comparison of mouse, rat, rabbit, dog, micropig, monkey and man. Xenobiotica 2000; 30: 1131−52.

35 Barton HA, Pastoor TP, Baetcke K, Chambers JE, Diliberto J, Doerrer NG*, et al.* The acquisition and application of absorption, distribution, metabolism, and excretion (ADME) data in agricultural chemical safety assessments. Crit Rev Toxicol 2006; 36: 9−35.

36 Muruganandan S, Sinal CJ. Mice as clinically relevant models for the study of cytochrome P450-dependent metabolism. Clin Pharmacol Ther 2008; 83: 818−28.

37 Poso A, Honkakoski P. Ligand recognition by drug-activated nuclear receptors PXR and CAR: structural, site-directed mutagenesis and molecular modeling studies. Mini Rev Med Chem 2006; 6: 937−47.

38 Kocarek TA, Schuetz EG, Strom SC, Fisher RA, Guzelian PS. Comparative analysis of cytochrome P4503A induction in primary cultures of rat, rabbit, and human hepatocytes. Drug Metab Dispos 1995; 23: 415−21.

39 El-Sankary W, Gibson GG, Ayrton A, Plant N. Use of a reporter gene assay to predict and rank the potency and efficacy of CYP3A4 inducers. Drug Metab Dispos 2001; 29: 1499−504.

40 Nakamura T, Sakaeda T, Ohmoto N, Tamura T, Aoyama N, Shirakawa T*, et al.* Real-time quantitative polymerase chain reaction for MDR1, MRP1, MRP2, and CYP3A-mRNA levels in Caco-2 cell lines, human duodenal enterocytes, normal colorectal tissues, and colorectal adenocarcinomas. Drug Metab Dispos 2002; 30: 4−6.

41 Wilkening S, Stahl F, Bader A. Comparison of primary human hepatocytes and hepatoma cell line Hepg2 with regard to their biotransformation properties. Drug Metab Dispos 2003; 31: 1035−42.

42 Waring JF, Ciurlionis R, Jolly RA, Heindel M, Gagne G, Fagerland JA*, et al.* Isolated human hepatocytes in culture display markedly different gene expression patterns depending on attachment status. Toxicol *In Vitro* 2003; 17: 693−701.

43 Houle R, Raoul J, Levesque JF, Pang KS, Nicoll-Griffith DA, Silva JM. Retention of transporter activities in cryopreserved, isolated rat hepatocytes. Drug Metab Dispos 2003; 31: 447−51.

44 Sosef MN, Baust JM, Sugimachi K, Fowler A, Tompkins RG, Toner M. Cryopreservation of isolated primary rat hepatocytes: enhanced survival and long-term hepatospecific function. Ann Surg 2005; 241: 125−33.

45 Cervenkova K, Belejova M, Vesely J, Chmela Z, Rypka M, Ulrichova J*, et al.* Cell suspensions, cell cultures, and tissue slices--important metabolic *in vitro* systems. Biomed Pap Med Fac Univ Palacky Olomouc Czech Repub 2001; 145: 57−60.

46 Morel F, Langouet S, Maheo K, Guillouzo A. The use of primary hepatocyte cultures for the evaluation of chemoprotective agents. Cell Biol Toxicol 1997; 13: 323−9.

47 Tuschl G, Mueller SO. Effects of cell culture conditions on primary rat hepatocytes-cell morphology and differential gene expression. Toxicology 2006; 218: 205−15.

48 Paine AJ. The maintenance of cytochrome P-450 in rat hepatocyte culture: some applications of liver cell cultures to the study of drug metabolism, toxicity and the induction of the P-450 system. Chem Biol Interact 1990; 74: 1−31.

49 Bailly-Maitre B, de Sousa G, Boulukos K, Gugenheim J, Rahmani R. Dexamethasone inhibits spontaneous apoptosis in primary cultures of human and rat hepatocytes via Bcl-2 and Bcl-x_L induction. Cell Death Differ 2001; 8: 279−88.

50 Chieli E, Santoni-Rugiu E, Cervelli F, Sabbatini A, Petrini M, Romiti N*, et al.* Differential modulation of P-glycoprotein expression by dexamethasone and 3-methylcholanthrene in rat hepatocyte primary cultures. Carcinogenesis 1994; 15: 335−41.

51 Fardel O, Lecureur V, Guillouzo A. Regulation by dexamethasone of P-glycoprotein expression in cultured rat hepatocytes. FEBS Lett 1993; 327: 189−93.

52 Haag M, Fautrel A, Guillouzo A, Frossard N, Pons F. Expression of cytochromes P450 3A in mouse lung: effects of dexamethasone and pregnenolone 16alpha-carbonitrile. Arch Toxicol 2003; 77: 145−9.

53 Meredith C, Scott MP, Renwick AB, Price RJ, Lake BG. Studies on the induction of rat hepatic CYP1A, CYP2B, CYP3A and CYP4A subfamily form mRNAs *in vivo* and *in vitro* using precision-cut rat liver slices. Xenobiotica 2003; 33: 511−27.

54 Hosoe TN, Inouye TY. Divergent modes of induction of rat hepatic and pulmonary CYP3A1 by dexamethasone and pregnenolone16alpha-carbonitrile. J Health Sci 2005; 51: 75−9.

55 Shah YM, Ma X, Morimura K, Kim I, Gonzalez FJ. Pregnane X receptor activation ameliorates DSS-induced inflammatory bowel disease via inhibition of NF-kappaB target gene expression. Am J Physiol Gastrointest Liver Physiol 2007; 292: G1114−22.

56 Pascussi JM, Gerbal-Chaloin S, Drocourt L, Assenat E, Larrey D, Pichard-Garcia L*, et al.* Cross-talk between xenobiotic detoxication and other signalling pathways: clinical and toxicological consequences.

Xenobiotica 2004; 34: 633−64.

57 Duret C, Daujat-Chavanieu M, Pascussi JM, Pichard-Garcia L, Balaguer P, Fabre JM*, et al.* Ketoconazole and miconazole are antagonists of the human glucocorticoid receptor: consequences on the expression and function of the constitutive androstane receptor and the pregnane X receptor. Mol Pharmacol 2006; 70: 329−39.

58 Kliewer SA, Moore JT, Wade L, Staudinger JL, Watson MA, Jones SA*, et al.* An orphan nuclear receptor activated by pregnanes defines a novel steroid signaling pathway. Cell 1998; 92: 73−82.

59 Blumberg B, Sabbagh W Jr, Juguilon H, Bolado J Jr, van Meter CM, Ong ES*, et al.* SXR, a novel steroid and xenobiotic-sensing nuclear receptor. Genes Dev 1998; 12: 3195−205.

60 Schuetz EG, Schmid W, Schutz G, Brimer C, Yasuda K, Kamataki T*, et al.* The glucocorticoid receptor is essential for induction of cytochrome P-4502B by steroids but not for drug or steroid induction of CYP3A or P-450 reductase in mouse liver. Drug Metab Dispos 2000; 28: 268−78.

61 Pierrat OA, Mikitova V, Bush MS, Browning KS, Doonan JH. Control of protein translation by phosphorylation of the mRNA 5′-cap-binding complex. Biochem Soc Trans 2007; 35 (Pt 6): 1634−7.

62 Gygi SP, Rochon Y, Franza BR, Aebersold R. Correlation between protein and mRNA abundance in yeast. Mol Cell Biol 1999; 19: 1720−30.

63 Ganem LG, Trottier E, Anderson A, Jefcoate CR. Phenobarbital induction of CYP2B1/2 in primary hepatocytes: endocrine regulation and evidence for a single pathway for multiple inducers. Toxicol Appl Pharmacol 1999; 155: 32−42.

64 Joannard F, Galisteo M, Corcos L, Guillouzo A, Lagadic-Gossmann D. Regulation of phenobarbital-induction of CYP2B and CYP3A genes in rat cultured hepatocytes: involvement of several serine/threonine protein kinases and phosphatases. Cell Biol Toxicol 2000; 16: 325−37.

65 Schuetz EG, Guzelian PS. Induction of cytochrome P-450 by glucocorticoids in rat liver. II. Evidence that glucocorticoids regulate induction of cytochrome P-450 by a nonclassical receptor mechanism. J Biol Chem 1984; 259: 2007−12.

66 Debri K, Boobis AR, Davies DS, Edwards RJ. Distribution and induction of CYP3A1 and CYP3A2 in rat liver and extrahepatic tissues. Biochem Pharmacol 1995; 50: 2047−56.

67 Meyer UA, Hoffmann K. Phenobarbital-mediated changes in gene expression in the liver. Drug Metab Rev 1999; 31: 365−73.

68 Swales K, Plant N, Ayrton A, Hood S, Gibson G. Relative receptor expression is a determinant in xenobiotic-mediated CYP3A induction in rat and human cells. Xenobiotica 2003; 33: 703−16.

69 Lothstein L, Hsu SI, Horwitz SB, Greenberger LM. Alternate overexpression of two P-glycoprotein [corrected] genes is associated with changes in multidrug resistance in a J774.2 cell line. J Biol Chem 1989; 264: 16054−8.

70 Courtois A, Payen L, Le Ferrec E, Scheffer GL, Trinquart Y, Guillouzo A*, et al.* Differential regulation of multidrug resistance-associated protein 2 (MRP2) and cytochromes P450 2B1/2 and 3A1/2 in phenobarbital-treated hepatocytes. Biochem Pharmacol 2002; 63: 333−41.

71 Wang H, Faucette S, Sueyoshi T, Moore R, Ferguson S, Negishi M*, et al.* A novel distal enhancer module regulated by pregnane X receptor/constitutive androstane receptor is essential for the maximal induction of CYP2B6 gene expression. J Biol Chem 2003; 278: 14146−52.

72 Cui J, Heard TS, Yu J, Lo JL, Huang L, Li Y*, et al.* The amino acid residues asparagine 354 and isoleucine 372 of human farnesoid X receptor confer the receptor with high sensitivity to chenodeoxycholate. J Biol Chem 2002; 277: 25963−9.

npg
Acta Pharmacologica Sinica (2010) 31: 66–72
© 2010 CPS and SIMM All rights reserved 1671-4083/10 $32.00
www.nature.com/aps

Original Article

Effect of betulinic acid on the regulation of Hiwi and cyclin B1 in human gastric adenocarcinoma AGS cells

Li-jing YANG[1,#], Yan CHEN[1,#], Qi MA[2], Jun FANG[1], Jing HE[1], Yi-quan CHENG[1], Qiu-ling WU[1,*]

[1]Institute of Hematology, Union Hospital, Tongji Medical College, Huazhong University of Science and Technology, Wuhan 430022, China; [2]Vascular Biology Institute, University of Miami, Miller School of Medicine, Miami, Florida 33136, USA

Aim: To investigate the effect of betulinic acid (BA) on the proliferation, apoptosis and cell cycle of gastric adenocarcinoma cell AGS *in vitro* and elucidate the underlying mechanisms.
Methods: The effect of BA on the proliferation of AGS cells was measured by using 3-(4,5-dimethyl-2-thiazolyl)-2,5-diphenyl-2*H*-tetrazolium (MTT) assay. Apoptosis was analyzed by using Annexin V-fluorescein isothiocyanate (FITC)/propidium iodide (PI) double-labeled flow cytometry (FCM) and Hoechst 33258 staining. The influence of BA on cell cycle of AGS cells was tested by PI staining. Both FCM and reverse transcription-PCR (RT-PCR) technologies were applied to detect the expression of Hiwi and Cyclin B1.
Results: BA exhibited significant cell proliferation inhibition, as well as its potency of inducing apoptosis in AGS cells *in vitro* in a time- and dose-dependent manner. The IC_{50} value for 24 h was 18.25 μg/mL (95% confidence interval: 15.16 to 27.31 μg/mL). Cells treated with BA showed increased cell population in G_2/M phase, with decreased S phase population. The expression of Hiwi and Cyclin B1 was down-regulated in BA-treated AGS cells in a dose-dependent manner.
Conclusion: BA exerted potent effect on growth inhibition, G_2/M cell cycle arrest and induction of apoptosis in AGS cells *in vitro*, possibly associated with the down-regulation of Hiwi and its downstream target Cyclin B1 expression. The potent antitumor capacity of BA suggested that it could be a promising new experimental anticancer agent in human gastric adenocarcinoma treatment.

Keywords: betulinic acid; gastric adenocarcinoma AGS cells; Hiwi; cyclin B1; cell cycle; apoptosis

Acta Pharmacologica Sinica (2010) 31: 66–72; doi: 10.1038/aps.2009.177; published online 28 December 2009

Introduction

Betulinic acid (BA), isolated from birch trees, is a natural pentacyclic triterpene which has demonstrated anti-HIV, anti-HBV and anti-malarial abilities[1–3]. In addition, BA is believed to play an important role in delaying or preventing carcinogenesis. It was proved to be able to kill melanoma cells via induction of apoptosis[4]. Many other cancer cell lines derived from a variety of different malignancies such as leukemia, prostate, ovarian, breast, lung, and colon cancers were also found to be sensitive to apoptosis induced by BA[5–7]. BA did not induce apoptosis in normal cells. And in animal studies, no adverse effect was observed at concentrations up to 100 mg/kg body weight[8]. However, whether BA can inhibit the proliferation of human gastric adenocarcinoma AGS cell remains unknown.

The cytotoxic mechanism of BA, which is linked to its alteration in cell apoptosis and cell cycle, is controversial. Treatment with BA resulted in up-regulation of the pro-apoptotic Bax in neuroblastoma, glioblastoma and melanoma cells, whereas anti-apoptotic Bcl-XS was found at elevated levels in BA-treated neuroblastoma cells[9-11]. An increase in Bcl-2 protein levels was reported in glioblastoma cells[10]. BA also triggered up regulation of Mcl-1, another anti-apoptotic Bcl-2 family protein, in melanoma cells, whereas no changes in Mcl-1 levels were detected in squamous cell carcinoma cells[11–13]. While BA was found to reduce the expression of p21 protein in melanoma cells, an increase of p21 protein was observed upon treatment with BA in glioblastoma cells[10, 14]. Therefore how BA-mediated cell cycle changes are linked to its antitumor activity remains to be addressed. Since bcl-X_L, p21, Cyclin D1, and Cdc2-Cyclin B complex expression modulated by BA are also regulated by Hiwi[15–17], it is very possible that BA exerts its antitumor effect through directly affecting a major target Hiwi and then indirectly impacting other factors.

The Piwi family comprises Hili, Hiwi1, Hiwi2 and Hiwi3 in humans, Mili, Miwi and Miwi2 in mice and Piwi, Aubergine

---

[#] The two authors contributed equally to this work.
[*] To whom correspondence should be addressed.
E-mail wuqiuling@medmail.com.cn
Received 2009-08-25 Accepted 2009-11-12

(Aub) and Ago3 in flies. This family is united via a common domain structure – PAZ and PIWI – and a common molecular mechanism: short, guide-strand-mediated target recognition and, in the majority of cases, a capacity for target slicing. Genetic and biochemical studies first linked Piwi proteins to signaling processes that affect cellular differentiation and development[18]. In addition, numerous groups have shown that Piwi proteins function as part of the RNAi machinery to mediate posttranscriptional gene, chromatin silencing and cell cycle regulation[17, 19]. Moreover, Piwi proteins are proved to serve as effector molecules that provide specificity in gene-silencing pathways[20]. Dicer processed micro-RNAs or small interfering RNAs (siRNA) bind Piwi proteins to form ribonucleoprotein complexes termed RNA induced silencing complexes (RISCs), which are thought to mediate mRNA degradation, translational repression, or chromatin silencing in a homology-dependent manner[20]. It has been estimated that Piwi protein-dependent RNAi controls the expression of more than 30% of genes in the human genome[20].

It has recently been observed that seminoma tumors are often associated with increased levels of Hiwi mRNA[21]. Coincidentally, Hiwi was first reported as a gene that is expressed in undifferentiated haematopoietic stem cells, but not in differentiated cells[22]. Likewise, the expression of the *D melanogaster* orthologue of Hiwi, Piwi, had previously been reported to promote mitosis in stem cells[18]. In addition, the chromosomal locus 12q24.33 that includes the Hiwi gene has been linked to testicular germ cell tumors[23]. Conversely, deletion of this region is associated with hypogonadism[24]. Together, these observations are consistent with a scenario in which overexpression of certain Piwi proteins is associated with increased mitosis in undifferentiated cells. So Hiwi plays a critical core role in the carcinogenesis and can be served as a new therapeutic target for human cancer. Mechanisms regulating Hiwi may provide novel opportunities for anti-tumour drug development.

In this study, we examined the efficiency of BA on gastric adenocarcinoma AGS cell proliferation and apoptosis, and explored its relationship with the regulation of Hiwi and Cyclin B1 gene expression. We demonstrated that BA down-regulated the expression of Hiwi and its downstream targets Cyclin B1 in AGS cells, accompanied by apoptosis induction, cell cycle arrest and proliferation inhibition.

Materials and methods

Reagents and cell cultures

BA ($C_{30}H_{48}O_3$, molecular weight 456.7), from the Alexis Co, (USA), was initially dissolved in 100% demethylsulfoxide (DMSO), stored at -20 ºC, and thawed before use. Dulbecco's modified Eagle's medium (DMEM) was from Gibco Co, (USA). Fetal bovine serum (FBS) was from Hangzhou Sijiqing Biological Engineering Materials Co, Ltd (China). 3-(4,5-Dimethyl-2-thiazolyl)-2,5-diphenyl-2*H*-tetrazolium (MTT), DMSO, propidium iodide (PI), Hoechst 33258, RNase A, and Ficoll-Hypaque were from Sigma Co, (USA). Annexin V-fluorescein isothiocyanate (FITC)/PI reagent Kit was from Nanjing KeyGen Biotech Co, Ltd (China). Trizol reagent kit was from Invitrogen Co (USA). Reverse transcription-PCR (RT-PCR) reagent kit was from TOYOBO Co (Japan). Primers were synthesized by Shanghai Sangon Biological Engineering Technology & Services Co, Ltd (China). Anti-Hiwi antibody was from Abcam Co (UK). Anti-Cyclin B1 antibody and FITC-labeled secondary antibody were from Santa Cruz Biotech Co (USA). Peripheral blood monouclear cells (PBMCs) were obtained by Ficoll-Hypaque density gradient centrifugation. AGS cells were a present from Department of Immunology, Tongji Medical College, Huazhong University of Science and Technology, Wuhan, China and cultured in DMEM supplemented with 10% FBS, 100 U/mL penicillin, 100 µg/mL streptomycin and placed in a humidified incubator with 95% air and 5% CO_2 at 37 ºC.

MTT assay

The effect of BA on proliferation of AGS cells was examined using a MTT assay. AGS cells were maintained in DMEM medium until mid-log phase and plated at a density of 1×10^4 cells per well in 96-well plate in triplicates. Cells were allowed to attach overnight, then incubated with various concentrations of BA for 24 h, 36 h and 48 h, respectively. PBMCs were plated at a density of 5000 cells per well in 96-well plate as control cells, followed by adding BA immediately. The final concentrations of BA were 9, 12, 15, 18 and 21 µg/mL, while the group dissolved with maximal DMSO concentration served as the control. After incubation, 20 µL MTT solution (5 mg/mL) was added and the cells were further incubated at 37 ºC for 4 h. The supernatant was discarded and 150 µL DMSO was added. The plate was gently shaken until the blue crystals were dissolved. Absorbance (*A*) at 570 nm wavelength was read using a 96-well multiscanner autoreader (Biotech Instruments, NY, USA). Relative cell proliferation was calculated with the following formula: cell proliferation inhibition of =[1-(*A* of experimental samples/*A* of the control)]×100%.

Annexin V-FITC/PI double-labeled flow cytometry

For detection of apoptotic cells treated with BA, the expression of Annexin V-FITC and exclusion of PI were detected by two-color flow cytometry (FCM). Cells incubated with different concentrations of BA (9, 12, 15 and 18 µg/mL) for 24 h were collected and washed with PBS, then resuspended in 100 µL binding buffer. Samples were incubated with 5 µL Annexin V-FITC in dark for 10 min at 4 ºC, then volume was adjusted to 500 µL with binding buffer. PI (5 µL) was added and samples were incubated for another 10 min at 4 ºC. Fluorescence was measured with a flow cytometer (Becton Dickinson, USA).

Hoechst 33258 staining

Nuclear fragmentation of AGS cells treated with 15 µg/mL BA was visualized by Hoechst 33258 staining. AGS cells were plated in 6-well plates at the density of 1×10^5 cells. After being allowed to attach overnight, cells were treated with 15 µg/mL BA for 24 h and collected by trypsin digestion method. Cells were fixed in 4% paraformaldehyde for 10 min at room temperature and re-suspended in 50 μL PBS before deposition on poly lysine-coated cover slips. After 30 min, the adhered cell were permeabilized with 0.1% Triton X-100 for 5 min at 4 °C and incubated with Hoechst 33258 for 30 min at room temperature. Cover slips were rinsed with PBS, mounted on slides with glycerol, and imaged with an Olympus BH-2 fluorescence microscope (Tokyo, Japan).

Cell cycle analysis

AGS cells treated with BA at various concentrations were collected, washed with PBS, and then suspended in 70% ethanol at 4 °C overnight. Cells were incubated with 20 μL 0.1% RNase A for 15 min at room temperature, and incubated with 50 μg/mL PI for 15 min. DNA content was examined by using FCM and the cell cycle analysis was performed using CellQuest software (Becton Dickinson, USA).

Detection of the expression of Hiwi and Cyclin B1 protein

AGS cells at 1×10^6 treated respectively with 0, 9, 12, 15 and 18 μg/mL BA for 24 h were collected, washed with PBS, and then fixed in 4% paraformaldehyde for 10 min at room temperature. Fixed cells were resuspended in PBS containing 1% heat-inactivated FBS and incubated for 1 h, then incubated with anti-Hiwi or anti-Cyclin B1 antibody (1:100) at 4 °C overnight. Cells were washed with PBS containing 1% heat-inactivated FBS and incubated with FITC-labeled secondary antibody (1:100) at 37 °C for 30 min. Samples were analyzed with a FACSort (Becton Dickinson, USA). In each test, 1×10^4 cells were collected and the mean fluorescence intensity represented the expression level of protein in the BA-treated AGS cells.

Reverse transcriptional RCR

2×10^5 AGS cells per well in 6-well plates were incubated with 0, 9, 12, 15, 18 and 21 μg/mL BA for 24 h, respectively. Cells were lysed with Trizol reagent and total RNA was extracted. cDNA was synthesized according to the manufacturer's instruction of TOYOBO kit. The primers were as follows: Hiwi (Genebank accession No AF104260.2), 5′-TCTGTTGTCAAGTAATCGGAAGG-3′, 5′-AGACTTTGAGCCCATCTACCAG-3′, the PCR products were 359 bp; Cyclin B1 (Genebank accession No NM_031966.2), 5′-GCCTATTTTGGTTGATACTGC-3′, 5′-ATCTGTCTGATTTGGTGCTTAGT-3′, the PCR products were 501 bp; β-actin (Genebank accession No NM_001101.3), 5′-CTGTCCCTGTATGCCTCTG-3′, 5′-ATGTCACGCACGATTTCC-3′, the PCR products were 218 bp. The following PCR conditions were used: 94 °C for 30 s; 94 °C for 30 s, 57 °C (Hiwi) or 53 °C (β-actin and Cyclin B1) for 30 s, 72 °C for 1 min, 30 cycles; 74 °C for 10 min; 4 °C for 30 min. After amplification, 5 μL aliquots of products were electrophoresed on 1.7% agarose gel. DNA bands were quantified using Smart View Bio-electrophoresis Image Analysis System. The ratio between Hiwi (or Cyclin B1) and β-actin band density represented the relative expression level of the target gene.

Statistical analysis

All experiments were repeated three times. All data were expressed as mean±SD and processed by SPSS 13.0 statistical software for Window. One-way ANOVA and Student-Newman-Keuls (SNK) test were applied for comparison between each group and $P<0.05$ was considered to be statistically significant.

Results

Effect of BA on proliferation of AGS cells

The cytotoxicity of BA to AGS cells at 0, 9, 12, 15, 18 and 21 μg/mL for various time was measured using MTT assay. AGS cells were treated with various concentrations BA for 0, 24, 36 and 48 h, respectively, which resulted in a significant decrease of cell viability of AGS cells in a dose- and time-dependent manner (Figure 1). The IC$_{50}$ of BA to AGS cells for 24, 36 and 48 h were 18.25 μg/mL (95% confidence interval: 15.16 to 27.31 μg/mL), 15.86 μg/mL (95% confidence interval: 12.18 to 21.17 μg/mL) and 12.99 μg/mL (95% confidence interval: 8.64 to 16.04 μg/mL), respectively. After being treated with 21 μg/mL BA for 24 h, AGS cells inhibition ratio was 63.2%±3.4%, while PBMCs inhibition ratio was 10.1%±2.8% ($P<0.05$).

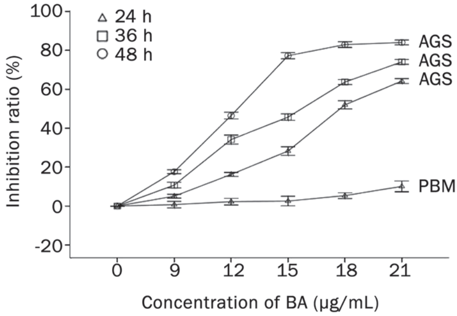

Figure 1. Inhibition of proliferation by BA in AGS cells. Cells were treated *in vitro* with various concentrations of BA (9, 12, 15, 18 and 21 μg/mL) for 24, 36 and 48 h, respectively, while PBMCs treated with BA for 24 h were served as control. Growth inhibition was detected by MTT assay and shown as an inhibition ratio. Data were mean±SD of three independent experiments.

Effect of BA on apoptosis of AGS cells

Apoptosis rate of AGS cells treated with various concentrations of BA (0, 9, 12, 15 and 18 μg/mL) for 24 h was analyzed by Annexin V-FITC/PI double-labeled flow cytometry. The degree of early apoptosis was quantitatively expressed as a percentage of the Annexin V-FITC-positive but PI-negative cells, while late apoptosis was quantitatively expressed as a percentage of the Annexin V-FITC-positive and PI-positive cells. The apoptosis rate was the sum of early apoptosis and late apoptosis. There was little binding of Annexin V-FITC in untreated and 9 μg/mL BA treated AGS cells (Figure 2). However, after treatment of cells with BA at 12, 15 and 18 μg/mL for 24 h, the apoptosis rate was 9.90%±0.44%, 29.13%±1.57%

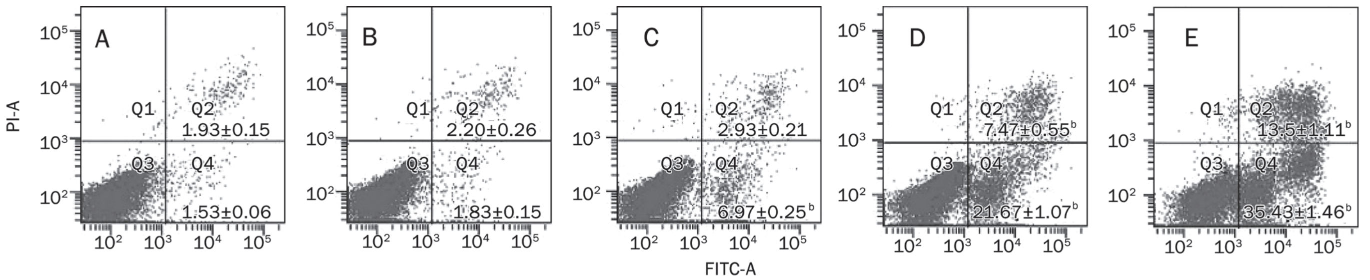

Figure 2. Effect of BA on apoptosis rate of AGS cells. Apoptosis ratio was detected with FCM using Annexin V-FITC/PI double staining. Q2 quadrant represented late apoptosis, while Q4 quadrant represented early apoptosis. (A) 0 μg/mL; (B) 9 μg/mL; (C) 12 μg/mL; (D) 15 μg/mL; (E) 18 μg/mL. The figures were representative of three separate experiments. $^{b}P<0.05$ vs control group.

and 48.96%±2.55%, respectively, which were statistically higher than the control 3.47%±0.21% (Figure 2). The nuclear fragmentation of AGS cells treated with 15 μg/mL BA for 24 h was stained by Hoechst 33258 (Figure 3). Apoptotic body containing nuclear fragments was found in BA-treated cells, the nuclear envelope appeared lytic and the cytoplasm shrunk. In contrast, the cells in the culture without BA showed normal cell nuclei morphology.

Cell cycle analysis

After incubation with BA, AGS cells were analyzed using FCM to analyze alterations in cell cycle distribution. DNA content distribution in AGS cells was changed after 24 h treatment with various concentrations of BA (0, 9, 12, 15, and 18 μg/mL) (Figure 4). As the dose of BA increased, the percentage of cells in G_2/M phase was increased with a concomitant sub-G_1 apoptotic peak, and that in S phase decreased in a dose-dependent manner. There were minimal changes in G_0/G_1 phase cell population. As compared with control sample, the ratio of apoptotic cells in BA-treated samples was higher. This sug-

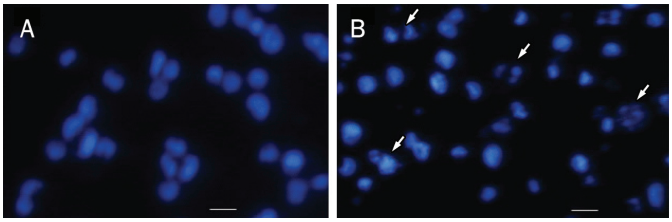

Figure 3. Effect of BA on apoptosis of AGS cells. Morphological changes of AGS cells treated with 15 μg/mL BA for 24 h which were stained with Hoechst33258 and detected using a fluorescence microscope. Fragmented or condensed nuclei indicative of apoptosis could be observed in the BA-treated groups as the arrows indicated (B), while the untreated cells showed normal cell nuclei morphology (A). White bars: 25 μm (Magnification×400).

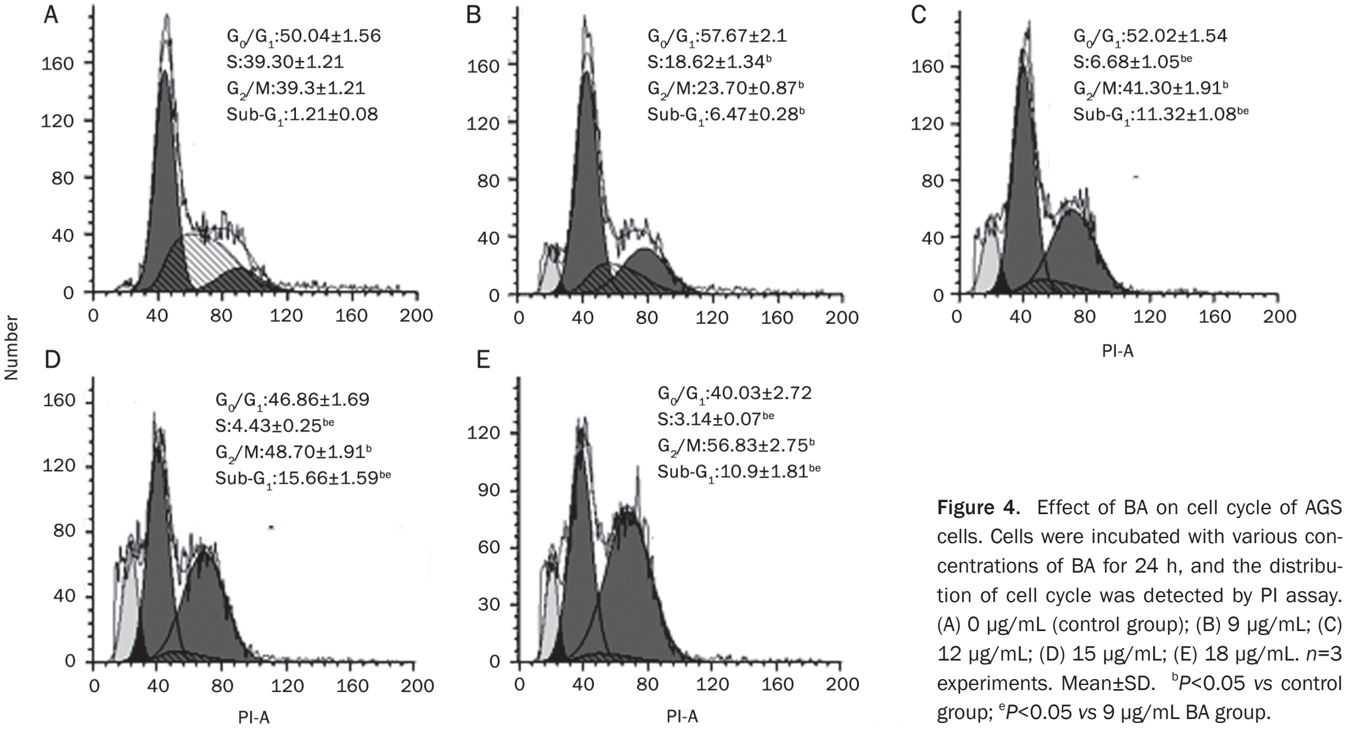

Figure 4. Effect of BA on cell cycle of AGS cells. Cells were incubated with various concentrations of BA for 24 h, and the distribution of cell cycle was detected by PI assay. (A) 0 μg/mL (control group); (B) 9 μg/mL; (C) 12 μg/mL; (D) 15 μg/mL; (E) 18 μg/mL. n=3 experiments. Mean±SD. $^{b}P<0.05$ *vs* control group; $^{e}P<0.05$ *vs* 9 μg/mL BA group.

gested that BA might inhibit cell proliferation by inducing cell G_2/M arrest, followed by apoptosis in AGS cells.

Expression of Hiwi and Cyclin B1 protein in AGS cells

Extensive investigations have implicated that the overexpression of Hiwi is known for tumor cell growth and survival response, which performs multiple functions ranging from posttranscriptional gene, chromatin silencing and cell cycle regulation. The present study and other findings have demonstrated that BA potently inhibited cell proliferation and induced apoptosis of AGS cells and many other cell lines. We therefore hypothesized that BA might be disrupting these cellular processes by primarily inhibiting the Hiwi gene. To test this hypothesis, we first examined whether constitutive deregulation of Hiwi existed in AGS cells. Since CyclinB1, which is under the control of Piwi protein, also plays a key role in tumorigenesis including gastric cancer, we further investigated whether BA could also inhibit Cyclin B1 activity in AGS cells. FCM was used to detect the expression of Hiwi and Cyclin B1 protein in AGS cells, and the mean fluorescence intensity represented the expression levels of Hiwi and Cyclin B1 protein. The wave crest representing the fluorescence intensity shifted left after AGS cells were treated with BA for 24 h (Figure 5A). In this experiment, the mean fluorescence intensity value of Hiwi protein in untreated group was 1405±21, while that in the groups treated with 9, 12, 15 and 18 µg/mL BA was down-regulated to 1159±17, 681±13, 645±10 and 621±8, respectively (Figure 5B). The Cyclin B1 protein expression in AGS cells was also down-regulated by BA. The mean fluorescence intensity of Cyclin B1 in the control group was 512±14, while that in the groups treated with 9, 12, 15 and 18 µg/mL BA was 447±13, 415±11, 384±8 and 351±9, respectively (Figure 5C). The results indicated that BA down-regulated the expression of Hiwi and Cyclin-B1 protein in a dose-dependent manner.

Detection of Hiwi and Cyclin B1 mRNA by RT-PCR

In order to identify whether the decrease of Hiwi and Cyclin B1 proteins was mediated at the transcriptional level by a decrease of Hiwi and Cyclin B1 mRNA expression, or at the post-translation level, we performed reversed transcriptase PCR (RT-PCR). Highest expression of Hiwi mRNA was detected in control group, with a mean value of 1.319±0.045 as compared with β-actin. After incubation with 9, 12, 15, 18 and 21 µg/mL BA for 24 h, Hiwi/β-actin ratio in AGS cells was decreased to 0.822±0.094, 0.674±0.065, 0.506±0.041, 0.272±0.023 and 0.209±0.027, respectively (Figure 6A, Figure 6C). The Cyclin B1 mRNA expression was also down-regulated. The expression level of Cyclin B1 mRNA in 9 µg/mL BA-treated group was not significantly different from that in the control (1.273±0.017 *vs* 1.304±0.021, $P>0.05$), but the differences in AGS cells treated with 12, 15, 18 and 21 µg/mL were statistically significant, with mean values of the Cyclin B1 mRNA expression being 1.124±0.022, 0.945±0.018, 0.875±0.028 and 0.501±0.027, respectively (Figure 6B, Figure 6D).

Discussion

BA is a natural pentacyclic triterpene isolated from birth trees. It is a very potent anticancer compound that is capable of killing a plethora of tumor cells. However, antitumor activity and action mechanism of BA still remains elusive. Our results indicated that BA possessed significant cytoxitity against AGS cells in a dose- and time-dependent manner, and IC_{50} for 24 h was 18.25 µg/mL (95% confidence interval: 15.16 to 27.31 µg/mL), well below the established tolerance level. BA also induced distinct G_2/M phase arrest and apoptosis in AGS cells, accompanied with typical apoptotic morphological changes. It have been revealed numerous pro-apoptosis and cell cycle proteins (eg, Cyclin B1, CyclinD1 and Bcl-x_L) were targeted by BA[15–17] . Because Bcl-x_L, Cyclin D1 and Cyclin B1

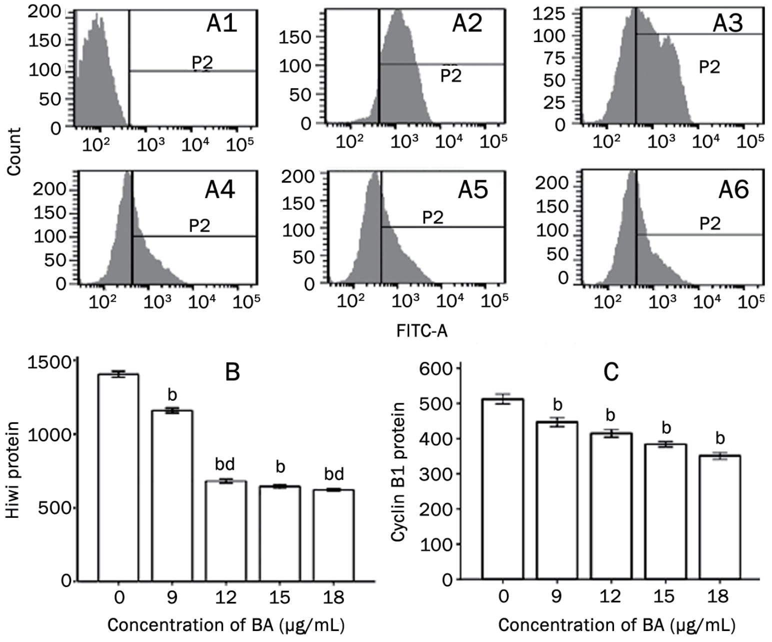

Figure 5. The expression of Hiwi and Cyclin B1 protein in the AGS cells treated with various concentrations of BA. Untreated cells served as controls. Mean fluorescence intensity represented the expression levels of Hiwi and Cyclin B1. Panel A: The graphs of flow cytometry of Hiwi protein in AGS cells treated with various concentration of BA. (A1) negative control; (A2) 0 µg/mL (control); (A3) 9 µg/mL; (A4) 12 µg/mL; (A5) 15 µg/mL; (A6) 18 µg/mL. Panel B: Mean fluorescence intensity of Hiwi protein in AGS cells. Panel C: Mean fluorescence intensity of Cyclin B1 protein. *n*=3 experiments. Mean±SD. $^bP<0.05$ *vs* control group; $^dP>0.05$ *vs* 15 µg/mL BA-treated group.

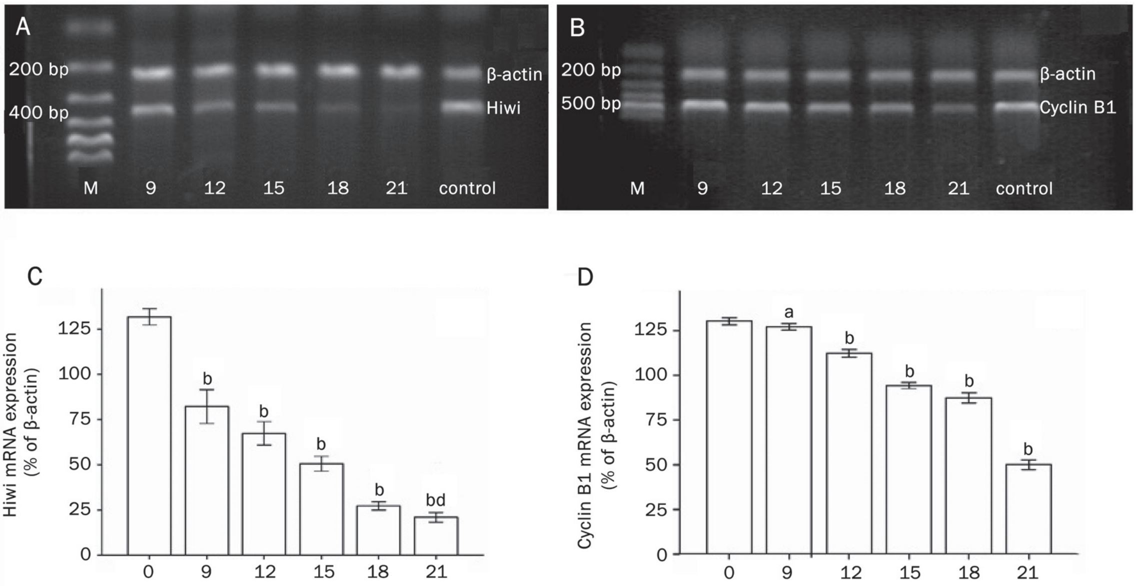

Figure 6. Effect of BA on mRNA expression of Hiwi (panel A) and Cyclin B1 (panel B) in AGS cells. M: marker, 9: 9 μg/mL, 12: 12 μg/mL, 15: 15 μg/mL, 18: 18 μg/mL, 21: 21 μg/mL, control: 0 μg/mL (control group). *n*=3 experiments. Mean±SD. $^{a}P>0.05$, $^{b}P<0.05$ *vs* control group; $^{d}P>0.05$ *vs* 18 μg/mL BA-treated group.

gene expression modulated by BA is regulated by Piwi protein, we investigated whether the anticarcinogenic effect of BA was mediated through modulation of Hiwi and Hiwi-regulated gene products. The significant decrease of the levels of both Hiwi mRNA and protein in AGS cells upon BA treatment strongly supported this hypothesis. BA also modulated Piwi-dependent gene products Cyclin B1 which are believed to be important for apoptosis and G_2/M arrest and serve as a common target for cancer drug development. It suggests that BA is an effective anti-gastric cancer reagent through the ability of inducing growth-arrest and apoptosis and cell cycle arrest via the downregulation of Hiwi.

Hiwi is human subfamily of Piwi family. PPD (PAZ Piwi domain) proteins form the core of RNA-induced silencing complexes (RISCs), which is required for gene silencing. Previous studies have shown that Piwi performs multiple functions ranging from epigenetic programming and repression of transposition to post transcriptional regulation[25, 26]. Moreover, it has recently become evident that PPD proteins and Dicer also function in siRNA-independent and dependant pathways that regulate cell cycle event[27]. High-level expression of Hiwi mRNA is related with high risk of tumor-related death in soft-tissue sarcomas patients[28]. It had been reported that Hiwi expression was higher in gastric cancers than in normal mucosa or in mucosa with atrophic gastritis or intestinal metaplasia, and the suppression of Hiwi by antisense or RNAi inhibited the growth of gastric cancer cells and induced cell cycle arrest in G_2/M phase[29]. These studies suggest that Hiwi might be an attractive target for future gastric cancer therapeutic drugs. Consistent with the above observation, we also found Hiwi was overexpressed in AGS cells. Moreover, this is the first report to suggest that BA could downregulate the levels of both Hiwi mRNA and protein, which inhibited growth, induced apoptosis and cell cycle arrest of AGS cells.

Overexpression of the Piwi in yeast resulted in cell cycle delay at the G_2/M boundary[17]. For example in *Drosophila*, altering the expression level of Piwi leads to changes in the proliferation rate of germline stem cells[18]. Furthermore, the Piwi signaling network exhibits cross talk with the Hedgehog signaling machinery[30], a developmental patterning system that influences the cell cycle through the actions of Patched1 on cyclin B1[31]. Piwi is required for regulated hyperphosphorylation of the cyclin-dependent kinase Cdc2[32], which controls the transition from the G_2 phase of the cell cycle to mitosis through binding with Cyclin B. Inhibitory phosphorylation of Cdc2 is required to prevent the onset of mitosis in situations where damaged or unreplicated DNA is present[33]. In our study, BA induced cell cycle arrest at G_2/M and simultaneously decreased the expression of Hiwi in AGS cells in a dose-dependent manner. We could infer that BA down-regulated Hiwi through inhibiting Cyclin B1. In agreement with this hypothesis, we found that BA treatment could strongly inhibit CyclinB1 concurrently with Hiwi.

Taken together, our results demonstrated that BA presented potent effect on growth inhibition, G_2/M cell cycle arrest and induction of apoptosis in AGS cells *in vitro* via down-regulating Hiwi and Cyclin B. Based on the outcome of this study, it is suggested that Hiwi might be a novel target for gastric cancer treatment and BA could be used as a potent agent for the management of gastric cancer. However, further studies are needed to establish a cause-and-effect relationship between Hiwi/Cyclin B pathway and BA effect. Furthermore, it will also be important to validate these findings in the *in vivo* animal models, which could better relate to human situations.

Acknowledgements

This work was supported by the National Natural Science Foundation of China (No 30500686).

Author contribution

Yan CHEN and Qiu-ling WU designed research; Li-jing YANG performed research; Jun FANG and Jing HE managed analytical tools and reagents; Li-jing YANG and Yi-quan CHENG analyzed data; Li-jing YANG and Qi MA wrote the paper.

References

1 Theo A, Masebe T, Suzuki Y, Kikuchi H, Wada S, Obi CL, *et al*. *Peltophorum africanum*, a traditional South African medicinal plant, contains an anti HIV-1 constituent, betulinic acid. Tohoku J Exp Med 2009; 217: 93–9.

2 Yao D, LI H, Gou Y, Zhang H, Zhou H, Liu Z, *et al*. Betulinic acid-mediated inhibitory effect on hepatitis B virus by suppression of manganese superoxide dismutase expression. FEBS J 2009; 279: 2599–614.

3 Ziegler HL, Franzyk H, Sairafianpour M, Tabatabai M, Tehrani MD, Bagherzadeh K, *et al*. Erythrocyte membrane modifying agents and the inhibition of *Plasmodium falciparum* growth: structure-activity relationships for betulinic acid analogues. Bioorg Med Chem 2004; 12: 119–27.

4 Pisha E, Chai H, Lee IS, Chagwedera TE, Farnsworth NR, Cordell GA, *et al*. Discovery of betulinic acid as a selective inhibitor of human melanoma that functions by induction of apoptosis. Nat Med 1995; 1: 1046–51.

5 Ehrhardt H, Fulda S, Fuhrer M, Debatin KM, Jeremias I. Betulinic acid-induced apoptosis in leukemia cells. Leukemia 2004; 18: 1406–12.

6 Kessler JH, Mullauer FB, de Roo GM, Medema JP. Broad *in vitro* efficacy of plant-derived betulinic acid against cell lines derived from the most prevalent human cancer types. Cancer Lett 2007; 251: 132–45.

7 Jung GR, Kim KJ, Choi CH, Lee TB, Han SI, Han HK, *et al*. Effect of betulinic acid on anticancer drug-resistant colon cancer cells. Basic Clin Pharmacol Toxicol 2007; 101: 277–85.

8 Zuco V, Supino R, Righetti SC, Cleris L, Marchesi E, Formelli F, *et al*. Selective cytotoxicity of betulinic acid on tumor cell lines, but not on normal cells. Cancer Lett 2002; 175: 17–25.

9 Fulda S, Friesen C, Los M, Scaffidi C, Mier W, Benedict M, *et al*. Betulinic acid triggers CD95 (APO-1/Fas)- and p53-independent apoptosis via activation of caspases in neuroectodermal tumors. Cancer Res 1997; 57: 4956–64.

10 Wick W, Grimmel C, Wagenknecht B, Dichgans J, Weller M. Betulinic acid-induced apoptosis in glioma cells: a sequential requirement for new protein synthesis, formation of reactive oxygen species, and caspase processing. J Pharmacol Exp Ther 1999; 289: 1306–12.

11 Selzer E, Pimentel E, Wacheck V, Schlegel W, Pehamberger H, Jansen B, *et al*. Effects of betulinic acid alone and in combination with irradiation in human melanoma cells. J Invest Dermatol 2000; 114: 935–40.

12 Selzer E, Thallinger C, Hoeller C, Oberkleiner P, Wacheck V, Pehamberger H, *et al*. Betulinic acid-induced Mcl-1 expression in human melanoma–mode of action and functional significance. Mol Med 2002; 8: 877–84.

13 Thurnher D, Turhani D, Pelzmann M, Wannemacher B, Knerer B, Formanek M, *et al*. Betulinic acid: a new cytotoxic compound against malignant head and neck cancer cells. Head Neck 2003; 25: 732–40.

14 Rieber M, Strasberg Rieber M. Induction of p53 without increase in p21$^{\mathrm{WAF1}}$ in betulinic acid-mediated cell death is preferential for human metastatic melanoma. DNA Cell Biol 1998; 17: 399–406.

15 Lee JH, Schütte D, Wulf G, Füzesi L, Radzun HJ, Schweyer S, *et al*. Stem-cell protein Piwil2 is widely expressed in tumors and inhibits apoptosis through activation of Stat3/Bcl-xl pathway. Hum Mol Genet 2006; 15: 201–11.

16 Morris KV, Santoso S, Turner AM, Pastori C, Hawkins PG. Bidirectional transcription directs both transcriptional gene activation and suppression in human cells. PLoS Genet 2008; 4: e1000258.

17 Stoica C, Carmichael JB, Parker H, Pare J, Hobman TC. Interactions between the RNA interference effector protein Ago1 and 14-3-3 proteins. J Biol Chem. 2006; 281: 37646–51.

18 Cox DN, Chao A, Lin H. Piwi encodes a nucleoplasmic factor whose activity modulates the number and division rate of germline stem cells. Development 2000; 127: 503–14.

19 Pal-Bhadra M, Bhadra U, Birchler JA. RNAi related mechanisms affect both transcriptional and posttranscriptional transgene silencing in *Drosophila*. Mol Cell 2002; 9: 315–27.

20 Hannon GJ. RNA interference. Nature 2002; 418: 244–51.

21 Qiao D, Zeeman AM, Deng W, Looijenga LH, Lin H. Molecular characterization of Hiwi, a human member of the piwi gene family whose overexpression is correlated to seminomas. Oncogene 2002; 21: 3988–99.

22 Sharma AK, Nelson MC, Brandt JE, Wessman M, Mahmud N, Weller KP, *et al*. Human CD34 (+) stem cells express the hiwi gene, a human homologue of the *Drosophila* gene piwi. Blood 2001; 97: 426–34.

23 Summersgill B, Osin P, Lu YJ, Huddart R, Shipley J. Chromosomal imbalances associated with carcinoma in situ and associated testicular germ cell tumours of adolescents and adults. Br J Cancer 2001; 85: 213–20.

24 Sathya P, Tomkins DJ, Freeman V, Paes B, Nowaczyk MJ. De novo deletion 12q: report of a patient with 12q24.31q24.33 deletion. Am J Med Genet 1999; 84, 116–9.

25 Deng W, Lin H. Miwi, a murine homolog of piwi, encodes a cytoplasmic protein essential for spermatogenesis. Dev Cell 2002; 2: 819–30.

26 Houwing S, Kamminga LM, Berezikov E, Cronembold D, Girard A, Elst H, *et al*. A role for Piwi and piRNAs in germ cell maintenance and transposon silencing in zebrafish. Cell 2007; 129: 69–82.

27 Carmichael JB, Provost P, Ekwall K, Hobman TC. Aago1 and dcr1, two core components of the RNA interference pathway, functionally diverge from rdp1 in regulating cell cycle events in *Schizosaccharomyces* pombe. Mol Biol Cell 2004; 15, 1425–35.

28 Taubert H, Greither T, Kaushal D, Bache M, Barter F, Kehlen A, *et al*. Expression of the stem cell self-renewal gene Hiwi and risk of tumour-related death in patients with soft-tissue sarcoma. Oncogene 2007; 26: 1098–100.

29 Liu X, Sun Y, Guo J, Ma H, LI J, Dong B, *et al*. Expression of Hiwi gene in human gastric cancer was associated with proliferation of cancer cells. Int J Cancer 2006; 118: 1922–9.

30 King FJ, Szakmary A, Cox DN, Lin H. Yb modulates the divisions of both germline and somatic stem cells through piwi- and hh-mediated mechanisms in the *Drosophila* ovary. Mol Cell 2001; 7: 497–508.

31 Roy S, Ingham PW. Hedgehogs tryst with the cell cycle. J Cell Sci 2002; 115: 4393–7.

32 Carmichael JB, Provost P, Ekwall K, Hobman TC. Ago1 and Dcr1, two core components of the RNA interference pathway, functionally diverge from rdp1 in regulating cell cycle events in *Schizosaccharomyces* pombe. Mol Biol Cell 2004; 15: 1425–35.

33 Rhind N, Russell P. Tyrosine phosphorylation of cdc2 is required for the replication checkpoint in *Schizosaccharomyces pombe*. Mol Cell Biol 1998; 18: 3782–7.

Acta Pharmacologica Sinica (2010) 31: 73–80
© 2010 CPS and SIMM All rights reserved 1671-4083/10 $32.00
www.nature.com/aps

Original Article

Aspirin inhibits proliferation of gemcitabine-resistant human pancreatic cancer cells and augments gemcitabine-induced cytotoxicity

Yan-qiu OU#, Wen bo ZHU#, Yan LI#, Peng-xin QIU, Yi-jun HUANG, Jun XIE, Song-min HE, Xiao-ke ZHENG, Tian-dong LENG, Dong XU, Guang-mei YAN*

Department of Pharmacology, Zhong-shan Medical College, Sun Yat-Sen University, Guangzhou 510089, China

Aim: To investigate whether aspirin is able to augment gemcitabine-induced cytotoxicity in human pancreatic cancer cells.
Methods: Two gemcitabine-insensitive human pancreatic cancer cell lines, PANC-1 and Capan-1, were used. Cells were treated with either aspirin or gemcitabine alone or both of them. Cell growth and apoptosis were determined by MTT assay, Annexin V or Hoechest 33258 staining. Cell cycle distribution was examined by flow cytometry. Western blot with specific phosphorylated protein antibodies was used to detect the activation of protein kinase. RT-PCR and Western blot were applied to assess the transcription and protein level for cyclin D1 and Bcl-2.
Results: Aspirin alone significantly inhibits the proliferation of PANC-1 cells by causing cell cycle arrest at G_1 phase. Aspirin potentiates the anti-survival effect of gemcitabine as well as its pro-apoptotic effect in PANC-1 cells, although aspirin per se does not trigger apoptosis. Aspirin inhibits GSK-3β activation and suppresses the expression of its downstream gene products (cyclin D1 and Bcl-2), which are implicated in proliferation, survival and chemoresistance of pancreatic cancer. The effects of aspirin on Capan-1, were similar to that on PANC-1.
Conclusion: Our results suggest that aspirin inhibits the proliferation of gemcitabine-resistant pancreatic cancer cells and augments the antisurvival effect of gemcitabine, probably by suppressing the activity of GSK-3β and its downstream gene products.

Keywords: aspirin; human pancreatic cancer; gemcitabine; apoptosis; GSK-3β; cyclin D1; Bcl-2

Acta Pharmacologica Sinica (2010) 31: 73–80; doi: 10.1038/aps.2009.172; published online 7 December 2009

Introduction

Pancreatic cancer remains a fatal disease with a 5-year survival rate less than 5%[1]. Besides surgery and radiation, chemotherapy regimens often fail to improve the outcome of pancreatic cancer patients. Currently, gemcitabine (difluorodeoxycytidine) appears to be the best chemotherapeutic agent in the treatment of advanced pancreatic cancer[2]. However, even with this drug, the objective tumor response rate is less than 10%, and the impact of the drug on survival is minor[3]. Moreover, gemcitabine is associated with drug resistance and highly toxic for tumor cells as well as normal cells[2, 4]. Thus, there is a need for novel strategies involving less toxic agents that can sensitize pancreatic cancer cells to chemotherapy.

The transcription factor nuclear factor-κB (NF-κB) plays a major role in promoting gemcitabine resistance[2], because NF-κB mediates transcription of a serial of proliferation and antiapoptosis genes, such as *cyclin D1* and *Bcl-2*. Recent evidence indicates that glycogen synthase kinase-3β (GSK-3β) positively regulates NF-κB-mediated gene transcription and cell survival[5, 6]. It is reported that pancreatic cancer cells contain a pool of active GSK-3β and that pharmacologic inhibition of GSK-3β kinase activity using small molecule inhibitors or genetic depletion of GSK-3β by RNA interference influences NF-κB-mediated gene (such as *cyclin D1*, *Bcl-2*) transcription, leading to decreased cancer cell proliferation and survival. Together, this evidence suggests GSK-3β as a potential therapeutic target in the treatment of pancreatic cancer. Therefore, agents that block GSK-3β activation could reduce chemoresistance to gemcitabine and perhaps be used in combination with gemcitabine as a novel therapeutic regimen for pancreatic cancer.

Aspirin (acetylsalicylic acid, ASA), the traditional non-steroid anti-inflammatory drug (NSAID), is one such agent

---

# These authors contributed equally to this work.
* To whom correspondence should be addressed.
E-mail ygm@mail.sysu.edu.cn
Received 2009-07-10 Accepted 2009-11-04

that is nontoxic to humans, which has become one of the most commonly utilized therapeutic drugs all over the world since its introduction into modern medicine in 1897[7]. Dihlmann[8] suggested that ASA was able to induce phosphorylation/inactivation of GSK-3β in several colon cancer cell lines. Nevertheless, the effect of ASA on GSK-3β activity in pancreatic cancer cells is never, to our knowledge, investigated before. In addition, although previous studies report that ASA is capable of suppressing pancreatic cancers growth *in vitro* and *in vivo*[9], the exact function and the underlying mechanism of ASA on pancreatic cancer remain to be further explored.

Thus, the goal of this study was to investigate the impact of ASA on the growth of human pancreatic cancer cells. Additionally, we investigate whether ASA can potentiate the gemcitabine-induced cytotoxicity in pancreatic cancer cells *in vitro*.

Materials and methods

Cell culture and drug treatment

Human pancreatic cancer cell line PANC-1, Capan-1 were obtained from Shanghai Cell Bank and maintained in DMEM (Invitrogen, Grand Island, NY) supplemented with 10% fetal bovine serum (FBS, Invitrogen), 100×10^3 U/L penicillin, and 100×10^3 U/L streptomycin in 5% CO_2 at 37 °C. Human pancreatic cancer cell line PANC-1, Capan-1 were chosen as *in vitro* model, because they are considered relatively resistant to many chemotherapeutic regimens[10]. ASA (Sigma, St Louis, Mo) was dissolved in DMSO (Sigma) and diluted with DMEM medium to a final concentration of 1% DMSO. The pH value of the ASA-containing medium was adjusted to 7.2 with 2.8% $NaHCO_3$ (Shanghai Sangon Biological Engineering Technology & Services Co, Ltd, China). Vehicle was treated with an equivalent volume of 10% FBS-medium with 1% DMSO. Gemcitabine (difluorodeoxycytidine, Lilly, Bad Homburg, Germany) was stored at 4 °C and dissolved in PBS on the day of use.

Cell growth and survival assays

All assays were carried out in quintuple of three separate experiments. Cell growth was tested by 3-(4,5-dimethylthiazol-2-yl)-2,5-diphenyl-tetrazolium bromide (MTT, Sigma) assay. Apoptosis was evaluated with Annexin V–fluoroisothiocyanate apoptosis detection kit according to the instruction of the manufacturer (Sigma) and analyzed with use of a EPICS ALTRA flow cytometer (Beckman Coulter, Fullerton, CA) and CellQuest software as previously described[11]. Apoptosis was observed by Hoechst 33258 staining as described[12]. Apoptotic cells were characterized by morphological alteration as condensed nuclei and cell shrinkage. Necrosis was assayed using the CytoTox96 non-radioactive cytotoxicity assay kit (Promega, Madison, WI), which quantifies cell death and cell lysis, based on the measurement of lactate dehydrogenase (LDH) activity released from the cytosol of damaged cells into the supernatant.

Cell cycle analysis

Cell cycle was assessed as previously described[13] with minor modifications. Briefly, cells were plated in parallel in 35-mm^2 culture plates at a concentration of 8×10^5 cells per plate. After 24 h of serum starve, cells were exposed to 10% FBS-medium with/without 4 mmol/L ASA for various durations and then were harvested by trypsinization, washed in cool PBS twice and fixed in 75% ethanol overnight in 4 °C. After that, cells were incubated in solution with DNA-binding dye propidium iodide (PI, 50 g/L), RNase (4×10^3 kU/L), NaF (0.3 g/L) and sodium citrate (1 g/L) for 30 min at 37 °C in the dark. Finally, red fluorescence from 488 mm laser-excited PI in every cells was analyzed by EPICS ALTRA flow cytometer (Beckman Coulter, Fullerton, CA) using a peak fluorescence gate to discriminate aggregates. The percentage of cells in G_0/G_1, S and G_2/M was determined from DNA content histograms by Multicycle for windows (Phoenix Flow Systems, San Diego, CA).

Preparation of nuclear extracts

PANC-1 cells were incubated with different concentrations of ASA for 24 h, followed by preparation of nuclear extracts using nuclear extract kit (Pierce, IL) according to the manufacturer's instructions. In brief, about 3×10^6 cells per sample were washed with ice-cold PBS/phosphate inhibitors, scraped, and collected by centrifugation at 500×*g* for 5 min. The pellets were suspended in 500 μL of hypotonic buffer, incubated on ice for 15 min and centrifuged at 14000×*g* for 30 s at 4 °C. The supernatant (cytosolic extract) was removed and the pellet (nuclear fraction) was suspended in 50 μL of complete lysis buffer and incubated on ice for 30 min with frequent mixing. Finally the suspension was centrifuged at 14000×*g* for 10 min at 4 °C and the supernatant (nuclear extract) was subjected to Western blot analysis.

Western blot analysis

Western blot was performed as previously described[13]. The following antibodies were used: antibody against PCNA (1:15000, Cell Signaling Technology, Beverly, MA), GAPDH, cyclin D1, Bcl-2, GSK-3β, phosphor-GSK-3β-Ser9, Akt, phosphor-Akt-Ser473 (1:1000, Cell Signaling Technology), phosphor-PP2A-Tyr307 (1:1000, Santa Cruz Biotechnology, Santa Cruz, CA), PP2A (1:1000, Millipore, Billerica, MA), β-actin (1:1000, Thermo Scientific IHC, Fremont, CA) and C23 (also as designated nucleolin, 1:1000, Santa Cruz Biotechnology).

Reverse transcription-polymerase chain reaction (RT-PCR)

Total RNA was isolated with TRIzol reagent (Gibco-BRL) according to the manufacturer's instructions. Complementary DNA was synthesized from 1 μg of total RNA by reverse transcription using the Superscript^{TM} II reverse transcriptase kit (Gibco-BRL). Sequence of the PCR primers: GAPDH: 5′-CCACCCATGGCAAATTCCATGGCA-3′ (sense primer), 5′-TCTAGACGGCAGGTCAGGTCCACC-3′ (antisense primer). Cyclin D1: 5′-GTCACACTTGATCACTCTGG-3′ (sense primer), 5′-TGGCCATGAACTACCTGGA-3′ (antisense primer). Bcl-2: 5′-GTGGAGGAGCTCTTCAGGGA-3′(sense primer), 5′-CGGTGCTTGGCAATTAGTGG-3′ (antisense primer). The PCR conditions contained an initial cDNA synthesis reaction at 42 °C for 1 h, followed by a denaturation step for 5 min at 94 °C and 22 cycles: 30 s at 94 °C, 30 s at 50 °C and 30 s at 72 °C. After the last cycle a final extension was performed at 72 °C for 10 min.

Statistics

Data are presented as mean±SEM for three separate experiments. $P<0.05$ was considered significant using Student's *t* test.

Results

ASA inhibits the growth of PANC-1 cells *in vitro*

Initially, we determined the effect of ASA on the growth of PANC-1 cells using MTT assay. As the growth curve shown, ASA treatment attenuates the growth rate of PANC-1 cells time- and dose-dependently (Figure 1). Compared with the untreated cells, 4 mmol/L ASA is sufficient to inhibit the cell growth by about 40% ($P<0.01$) at 24 h, and the inhibitory effect of ASA becomes more significant at 72 h. Clearly, ASA alone is able to slow down the growth of PANC-1 cells.

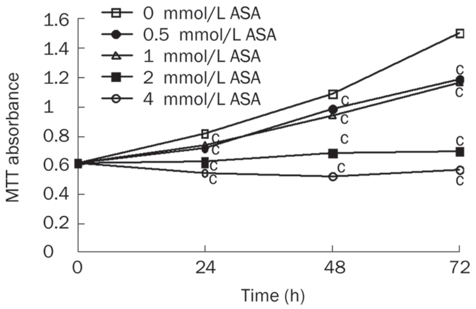

Figure 1. ASA inhibits growth of PANC-1 cells. Cells were treated with various concentrations of ASA and cell growth was determined using the MTT assay at 24, 48, and 72 h. Results represent the mean absorbance at 570 nm of three different experiments with quintuple wells. SEM bars are not included for clarity. $^{c}P<0.01$ compared with untreated cells at all time points.

ASA decreases proliferation instead of inducing apoptosis or necrosis in PANC-1 cells

The reduction in growth of PANC-1 cells in response to ASA could be explained either by increased cell death or by reduced cell proliferation. Thus, the level of proliferating cell nuclear antigen (PCNA), an established index for proliferation cells, was firstly assessed to determine cell proliferation in PANC-1 cells[14]. Western blot analysis clearly shows that PCNA protein expression undergoes a down-regulation change in a time-dependent manner after exposure to ASA (Figure 2A). Secondly, Anexin V, Hoechst staining and LDH examination were used to investigate whether treatment of ASA causes apoptosis or necrosis. There was no increase of Anexin V positive cells after ASA treatment during 24 h to 72 h (Figure 2B). Meanwhile, Apoptotic bodies are not observed in either

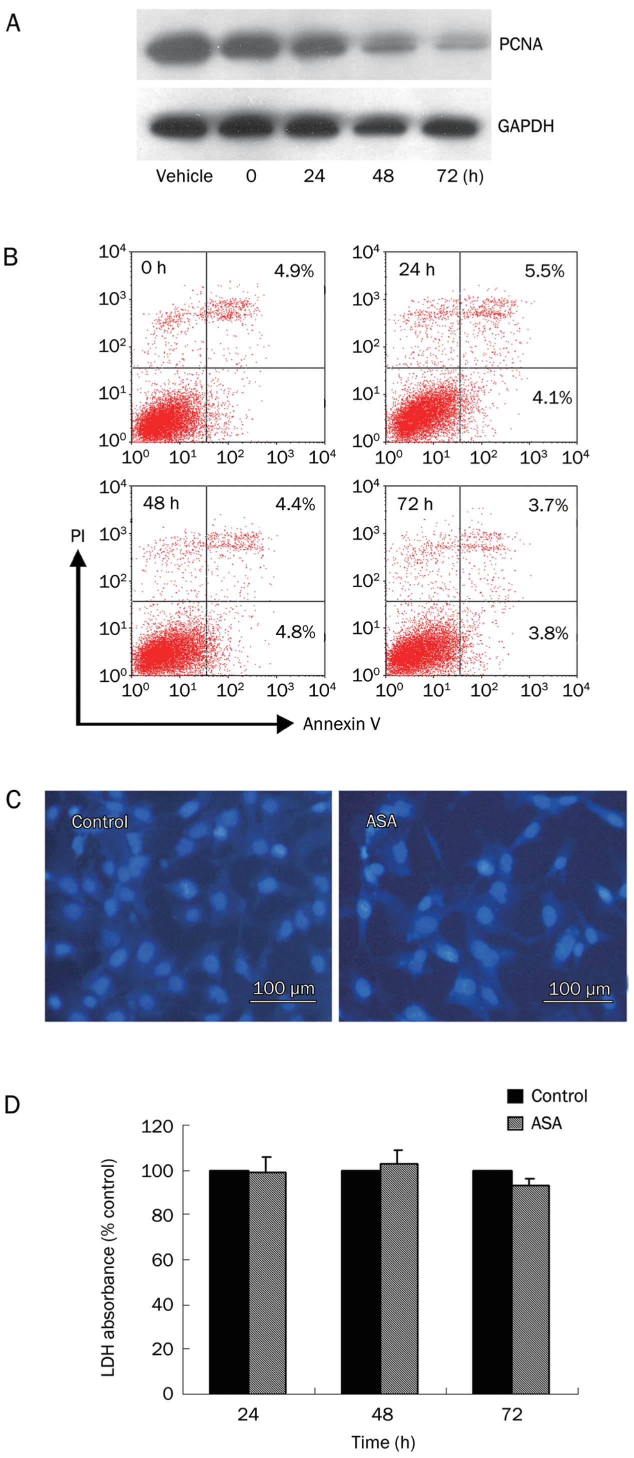

Figure 2. Effect of ASA on PANC-1 cells proliferation, apoptosis and necrosis. (A) PANC-1 cells were treated with 4 mmol/L ASA for various time and cell lysates were subjected to Western blot using anti-PCNA and anti-GAPDH antibodies. (B) AnnexinV/propidium iodide double staining for apoptosis assay. (C) Fluorescent staining of nuclei by Hoechst 33258 in PANC-1 cells treated with or without 4 mmol/L ASA for 24 h. (D) PANC-1 cells were incubated with 4 mmol/L ASA for the indicated time and cultured medium was collected for LDH release assay. Results represent the mean of three different experiments with quintuple wells.

ASA-treated or untreated cells (Figure 2C). And there is not any statistically significant difference in the mean LDH absorbance between ASA-treated and untreated cells during the time course of 24 h to 72 h (Figure 2D). Hence, cytotoxicity is not contributing to the reduction in cell growth. Therefore, we strongly believe that the inhibitory effect of ASA on PANC-1 growth is based on the reduction of proliferation instead of induction of cell death.

ASA causes cell cycle arrest at G_1 phase and decreases S phase fraction in PANC-1 cells

To determine the mechanism involved in the reduction of cell proliferation, we analyzed the cell cycle distributions of PANC-1 cells treated by ASA. ASA hampers the cell cycle progression by arresting up to three quarters of cancer cells at G_1 phase, and by decreasing S phase fraction by about 40% in 24 h compared with the control (Figure 3). Additionally, no subdiploid (sub-G_0/G_1) peak in DNA content histograms is obtained by flow cytometry, which further supports the findings mentioned above that no apoptosis is induced by ASA.

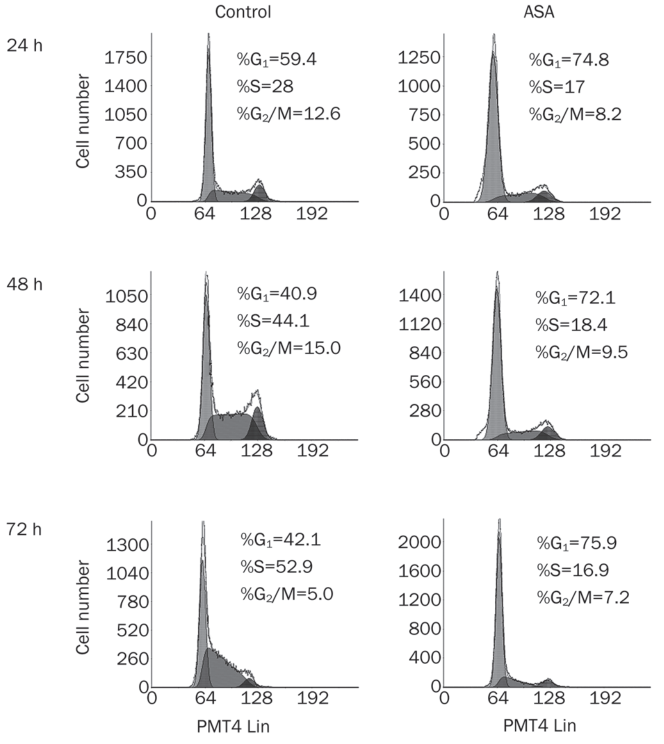

Figure 3. Cell cycle distributions in ASA-treated PANC-1 cells. PANC-1 cells were treated with or without 4 mmol/L ASA for various time and cell cycle analysis was performed using the fluorescent cytometry.

ASA augments the effect of gemcitabine on cell survival and induction of apoptosis in PANC-1 cells

To determine the effect of ASA on gemcitabine-induced cytotoxicity, PANC-1 cells were treated with gemcitabine in the presence of ASA. Only minor reduction of cell survival was observed with the treatment of gemcitabine alone at the dose of 0.2 μmol/L to 20 μmol/L in 24 h (Figure 4A). Obviously, human pancreatic PANC-1 cells are not sensitive to gemcitabine treatment, which is consistent with the previous report[10]. However, ASA significantly promotes gemcitabine-induced cytotoxicity, which is dependent upon concentrations of ASA and gemcitabine ($P<0.05$). Similar results were observed with Hoechst staining. Data from Hoechst assays (Figure 4B) show that ASA pronouncedly increased the apoptotic effect of gemcitabine, whereas gemcitabine alone, has minimal apoptotic effect on the PANC-1 cells.

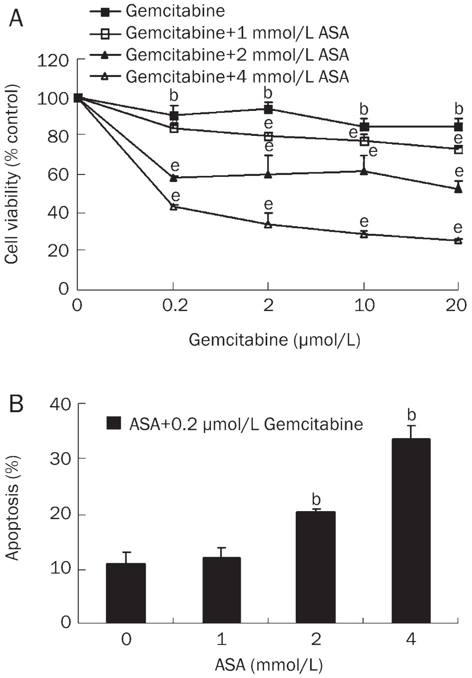

Figure 4. ASA augments the anti-survival and pro-apoptosis effects of gemcitabine on PANC-1 cells. (A) Cells were treated with various concentrations of gemcitabine in the presence/absence of indicated concentrations of ASA for 24 h and cell growth was measured by MTT assay. Data are expressed as percentage of cell growth observed in untreated cultures. Results represent the mean of three different experiments with quintuple wells. $^bP<0.05$ compared with untreated cells; $^eP<0.05$ compared with gemcitabine alone-treated cells at corresponding concentrations. (B) Cells were treated with various concentrations of ASA in combination with 0.2 μmol/L gemctitabine for 24 h. Apoptosis was then determined by Hoechst 33258 assay. $^bP<0.05$ compared with 0.2 μmol/L gemcitabine-treated cells.

ASA inhibits GSK-3β activation in PANC-1 cells

To explore the molecular mechanism underlying the above effect of ASA on PANC-1 cells, we investigated whether the effect of ASA is associated with the inhibition of GSK-3β activation. Using Western blot analysis of total cell proteins, we observed that ASA dose-dependently increased phosphorylated level of GSK-3β at Ser9, which represents the inactive form of GSK-3β kinase, while has no effect on the total level of

GSK-3β (Figure 5A). To exactly verify whether this alteration takes place in the nucleus, we replicated the experiment using nuclear extracts. Interestingly, the change of GSK-3β activation in nuclear fractions followed a similar pattern to that in total extracts (Figure 5B). Thus, we identified that GSK-3β is inactivated by ASA in the nucleus of PANC-1 cells.

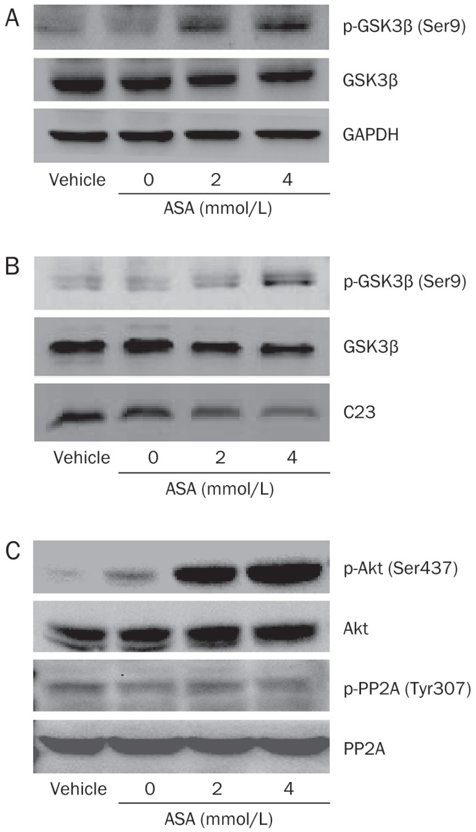

Figure 5. Inactivation of GSK-3β by ASA. Cells were treated with various concentrations of ASA for 24 h. Total extracts (A, C) or nuclear extracts (B) were obtained and subjected to Western blotting analysis. GAPDH and C23 were loaded to normalized total and nuclear protein.

To further elucidate the signaling pathways that inactivate GSK-3β, we examined the effect of ASA on Akt and PP2A, which are both implicated in the regulation of GSK-3β activity[15]. In untreated PANC-1 cells, phosphorylated Akt at Ser437 is marginal. After treatment with ASA for 24 h, a very strong band of the phosphorylated Akt appeared (Figure 5C). Therefore, ASA stimulates Akt activation via protein phosphorylation at Ser437 provided that phosphorylation of the Ser437 residue is required for a maximal Akt activation[16]. On the other hand, ASA causes little change on the inactivated phosphorylation status of PP2A at Tyr307.

ASA downregulates the expression of cyclin D1 and Bcl-2

We then assessed the expression of cyclin D1, which plays important role in tumor cell proliferation and cell cycle progression from G_1 phase to S phase; and Bcl-2, which is involved in tumor survival and chemoresistance in pancreatic cancer cells[17], because both of the genes can be regulated by GSK-3β in pancreatic cancer cells[6]. RT-PCR analysis (Figure 6A) indicates that mRNA level of cylcin D1 and Bcl-2 are significantly suppressed by ASA in a dose-dependent manner in 24 h. Western blotting (Figure 6B) shows that ASA also reduces the protein level of cyclin D1 and Bcl-2.

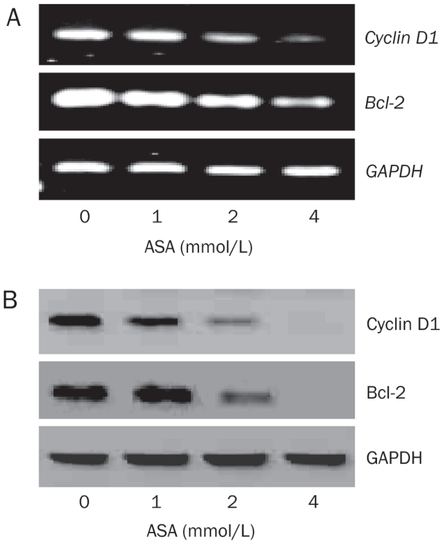

Figure 6. ASA downregulates the expression of cyclin D1 and Bcl-2 in PANC-1 cells. PANC-1 cells were treated with various concentrations of ASA for 24 h and harvested for RT-PCR (A) or Western blotting analysis (B).

ASA inhibits growth, decreases S phase accumulation, augments the effect of gemcitabine and represses GSK-3β activation in Capan-1 cells

To test whether the effects of ASA in PANC-1 cells are cell-specific or not, another human pancreatic cancer cell line Capan-1 cells were used. ASA inhibits cell growth dose- and time-dependently in Capan-1 cells as in PANC-1 cells (Figure 7A). Moreover, 4 mmol/L ASA decreases S phase accumulation time-dependently (Figure 7B). Furthermore, augment of gemcitabine-induced apoptosis by ASA was also seen in Capan-1 cells as in PANC-1 cells (Figure 7C). Mechanically, after treatment with ASA for 24 h, the levels of GSK-3β and Akt phosphorylation displayed the same alteration panel as in PANC-1 cells (Figure 7D). These findings demonstrate that ASA may have a broad therapeutic potential in human pancreatic cancer cells.

Discussion

The aim of this study is to examine the effect of ASA on the growth of pancreatic cancer cells and determine whether ASA, the famous NSAID, can sensitize the cells to gemcitabine. We find that ASA alone inhibits the proliferation of human pancreatic cancer cells by hampering cell cycle progressing, and that ASA enhance the apoptotic effects of gemcitabine; these effects of ASA may be associated with suppression of the

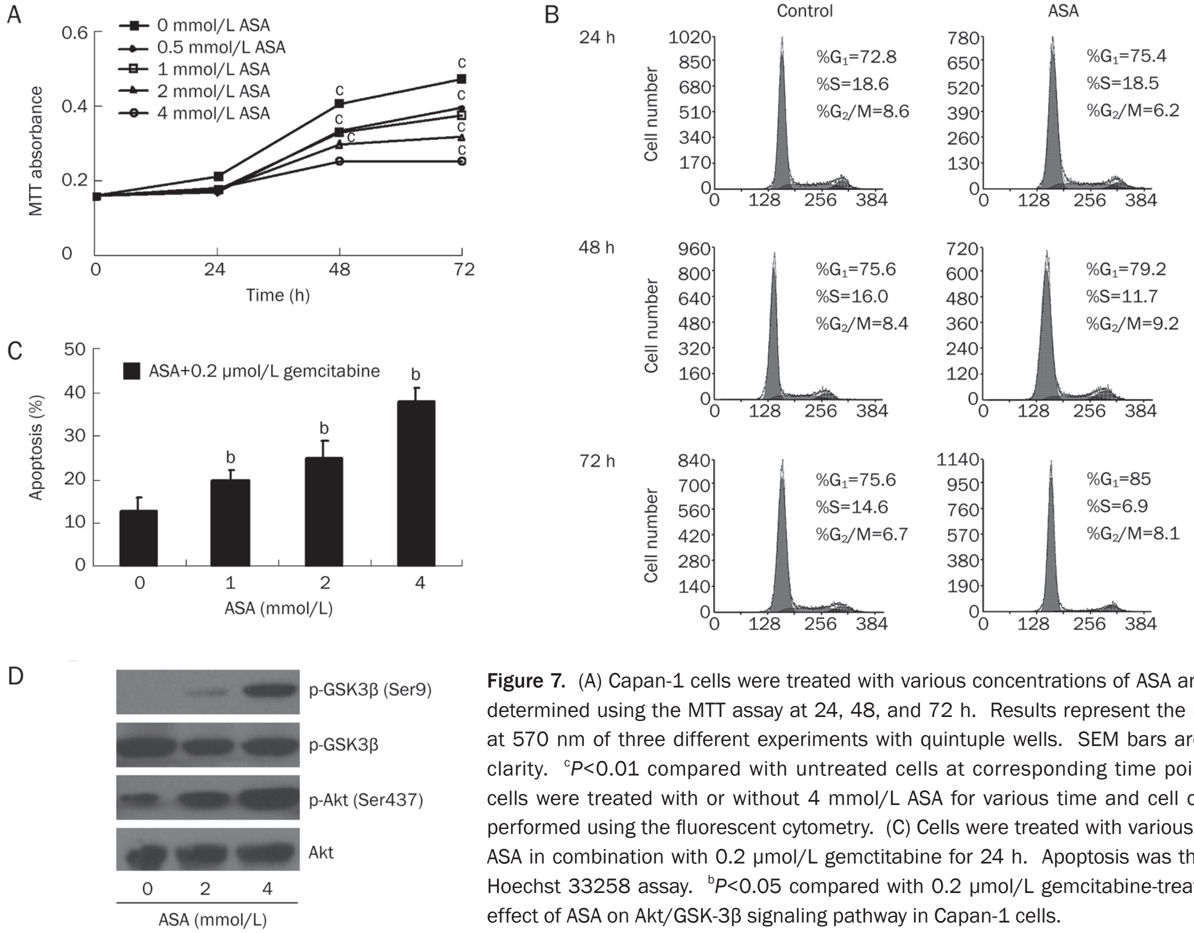

Figure 7. (A) Capan-1 cells were treated with various concentrations of ASA and cell growth was determined using the MTT assay at 24, 48, and 72 h. Results represent the mean absorbance at 570 nm of three different experiments with quintuple wells. SEM bars are not included for clarity. $^cP<0.01$ compared with untreated cells at corresponding time points. (B) Capan-1 cells were treated with or without 4 mmol/L ASA for various time and cell cycle analysis was performed using the fluorescent cytometry. (C) Cells were treated with various concentrations of ASA in combination with 0.2 μmol/L gemctitabine for 24 h. Apoptosis was then determined by Hoechst 33258 assay. $^bP<0.05$ compared with 0.2 μmol/L gemcitabine-treated cells. (D) The effect of ASA on Akt/GSK-3β signaling pathway in Capan-1 cells.

activity of GSK-3β and downregulation of cyclin D1 and Bcl-2. These findings extend our understanding of the function and molecular basis of ASA on the dismal disease.

ASA is a first-line medication in pancreatic cancer pain control, intended to keep patients comfortable without resorting to opioids[18, 19]. Because high concentrations (1–5 mmol/L) of ASA are achievable *in vivo* by oral administration of ASA at 4–10 g/d during treatment of rheumatic disorder and arthritis[20], accumulating literature is evaluating additional, COX-independent, biological activities for these high doses of ASA.

Previous studies suggest that ASA is able to induce apoptosis in pancreatic cancer cells[9]. However, in our work, we demonstrated that ASA, even at its relative high dose (4 mmol/L), hardly causes apoptosis in PANC-1 cells. This was evidenced by the Annexin V and Hoechest 33258 staining and flow cytometry assays. The pronounced inhibition of growth of pancreatic cancer cells by ASA, is mainly due to the reduction of proliferation and retardation of cell cycle progression.

Gemcitabine alone only has a marginal effect on cell growth and apoptosis in PANC-1 cell line, which fits well with previous finding that PANC-1, Capan-1 cells are considered relatively resistant to many chemotherapeutic regimens[2, 10]. However, ASA was shown to significantly enhance the apoptotic effect of gemcitabine in these cells. This finding is not contradictory to the previous report that combination of gemcitabine and celecoxib did not demonstrate significant improvement in patients with advanced pancreatic cancer[21]. Because PANC-1 and Capan-1 cells are cyclooxygenase-2-negative, most bioactivities of ASA on this cell line were thought to be COX-2-independent.

The mechanism by which ASA exerts above bioactivity may involve the suppression of activity of GSK-3β. Ougolkov[22] have reported that GSK-3β aberrantly accumulates in human pancreatic cancer cells and its accumulation in cell nuclear is associated with its kinase activity and tumor differentiation. GSK-3β positively regulates the activity of NF-κB, while NF-κB per se plays a pivotal role in promoting gemcitabine resistance in pancreatic cancer[2], so it is very likely that the inactivation of GSK-3β by ASA can sensitize the cells to gemcitabine. This hypothesis was evidenced by the finding that LiCl, the pharmacological inhibitor of GSK-3β, can significantly sensitize PANC-1 or Capan-1 cells to gemcitabine-induced apoptosis (Supplementary Figure). Additional studies are needed to determine the necessary role of GSK-3β in the effect of ASA on pancreatic cancer cells and provide evidence that this mechanism occurs also *in vivo*. Our results also display that ASA inhibits the expression of GSK-3β downstream genes, *Bcl-2* and *cyclin D1*. Of note, the anti-apoptotic Bcl-2 plays an important role in the development of many chemotherapy resistances in cancer cells. It impairs the mitochondrial apoptotic function by neutralizing the proapoptotic Bcl-2 family members such as Bax and Bak[23]. Thereby, Bcl-2 may be the effecter molecule of ASA to regulate gemcitabine-induced cytotoxicity and apoptosis. Cyclin D1 is overexpressed in human pancreatic cancer tissue and inversely correlated with patient survival[24]. It governs the checkpoint of G_1 to S phase progression[25] and is always responsible for the aberrant cell cycle in tumor cells[26]. In our work, suppression of cylcin D1 expression by ASA seems to contribute to the cell cycle retardation and proliferation reduction in PANC-1 cells.

Admittedly, GSK-3β can also regulate cyclin D1 at the post-translational level by phosphorylating cyclin D1 on T286 and inducing its rapid turnover[25]. In the present work, we display that ASA significantly inactivates GSK-3β and suppresses cyclin D1 at the transcription level in pancreatic cancer cells, which is, to our knowledge, never reported before.

Akt and PP2A pathways are implicated in the activation of GSK-3β. PP2A dephosphorylates and activates GSK-3β[27] while Akt can inactivate GSK-3β by phosphorylating GSK-3β at Ser9[28]. Alternatively, PP2A can act upstream of Akt pathway to indirectly regulate GSK-3β signaling[15]. However, our results demonstrate that only Akt activation is involved in the inactivation of GSK-3β by ASA in PANC-1 cells, which takes place independently of PP2A pathway. Concerns may be aroused that Akt activation renders the resistance of pancreatic carcinoma against anticancer drugs[29, 30]. In fact, Akt does not seem to be involved in gemcitabine resistance of human pancreatic carcinoma cell lines. It is reported that neither did the basal Akt activity correlate with the sensitivity towards gemcitabine treatment, nor did the inhibition of Akt by LY294002 alter gemcitabine-induced apoptosis[2]. Thus ASA is not likely to confer chemoresistance to the current clinical regimen for pancreatic carcinomas.

In conclusion, our results show that ASA inhibits proliferation and potentiates the apoptosis-inducing effect of gemcitabine in pancreatic cancer cells, probably by inhibiting activation of GSK-3β and the expression of its regulated targets. Thus, the traditional agent ASA may prove to be a novel candidate to be used in combination with gemcitabine for the chemotherapy of pancreatic carcinoma.

Acknowledgements

This work was supported by Key program, National Natural Science Foundation of China (No 30830111) and National Natural Science Foundation of China (No 330801408).

Author contribution

Yan-qiu OU and Guang-mei YAN designed research; Yan-qiu OU, Peng-xin QIU, Yi-jun HUANG, Jun XIE, Song-min HE, Xiao-ke ZHENG, Tian-dong LENG, Dong XU performed research; Yan-qiu OU, Wen-bo ZHU, Tian-dong LENG, and Guang-mei YAN analyzed data; Yan-qiu OU, Wen-bo ZHU, Yan-LI wrote the paper.

Supplementary information is available at NPG website.

References

1 Lowenfels AB, Maisonneuve P. Epidemiology and prevention of pancreatic cancer. Jpn J Clin Oncol 2004; 34: 238−44.
2 Arlt A, Gehrz A, Muerkoster S, Vorndamm J, Kruse ML, Folsch UR, *et al*. Role of NF-kappaB and Akt/PI3K in the resistance of pancreatic carcinoma cell lines against gemcitabine-induced cell death. Oncogene 2003; 22: 3243−51.
3 Li L, Aggarwal BB, Shishodia S, Abbruzzese J, Kurzrock R. Nuclear factor-kappaB and IkappaB kinase are constitutively active in human pancreatic cells, and their down-regulation by curcumin (diferuloylmethane) is associated with the suppression of proliferation and the induction of apoptosis. Cancer 2004; 101: 2351−62.
4 Reddy LH, Marque PE, Dubernet C, Mouelhi SL, Desmaele D, Couvreur P. Preclinical toxicology (subacute and acute) and efficacy of a new squalenoyl gemcitabine anticancer nanomedicine. J Pharmacol Exp Ther 2008; 325: 484−90.
5 Ougolkov AV, Bone ND, Fernandez-Zapico ME, Kay NE, Billadeau DD. Inhibition of glycogen synthase kinase-3 activity leads to epigenetic silencing of nuclear factor kappaB target genes and induction of apoptosis in chronic lymphocytic leukemia B cells. Blood 2007; 110: 735−42.
6 Ougolkov AV, Fernandez-Zapico ME, Savoy DN, Urrutia RA, Billadeau DD. Glycogen synthase kinase-3beta participates in nuclear factor kappaB-mediated gene transcription and cell survival in pancreatic cancer cells. Cancer Res 2005; 65: 2076−81.
7 Gilroy DW. The role of aspirin-triggered lipoxins in the mechanism of action of aspirin. Prostaglandins Leukot Essent Fatty Acids 2005; 73: 203−10.
8 Dihlmann S, Klein S, Doeberitz Mv MK. Reduction of beta-catenin/T-cell transcription factor signaling by aspirin and indomethacin is caused by an increased stabilization of phosphorylated beta-catenin. Mol Cancer Ther 2003; 2: 509−16.
9 Sclabas GM, Uwagawa T, Schmidt C, Hess KR, Evans DB, Abbruzzese JL, *et al*. Nuclear factor kappa B activation is a potential target for preventing pancreatic carcinoma by aspirin. Cancer 2005; 103: 2485−90.
10 Rejiba S, Wack S, Aprahamian M, Hajri A. K-ras oncogene silencing strategy reduces tumor growth and enhances gemcitabine chemotherapy efficacy for pancreatic cancer treatment. Cancer Sci 2007; 98: 1128−36.
11 Pan J, Quintas-Cardama A, Kantarjian HM, Akin C, Manshouri T, Lamb P, *et al*. EXEL-0862, a novel tyrosine kinase inhibitor, induces apoptosis *in vitro* and *ex vivo* in human mast cells expressing the KIT D816V mutation. Blood 2007; 109: 315−22.
12 Jenkins JK, Suwannaroj S, Elbourne KB, Ndebele K, McMurray RW. 17-Beta-estradiol alters Jurkat lymphocyte cell cycling and induces apoptosis through suppression of Bcl-2 and cyclin A. Int Immunopharmacol 2001; 1: 1897−911.
13 Chandler NM, Canete JJ, Callery MP. Increased expression of NF-kappa B subunits in human pancreatic cancer cells. J Surg Res 2004; 118: 9−14.
14 Dong YW, Wang XP, Wu K. Suppression of pancreatic carcinoma growth by activating peroxisome proliferator-activated receptor gamma involves angiogenesis inhibition. World J Gastroenterol 2009; 15: 441−8.
15 Lin CF, Chen CL, Chiang CW, Jan MS, Huang WC, Lin YS. GSK-3beta acts downstream of PP2A and the PI3-kinase-Akt pathway, and upstream of caspase-2 in ceramide-induced mitochondrial apoptosis. J Cell Sci 2007; 120: 2935−43.
16 Alessi DR, James SR, Downes CP, Holmes AB, Gaffney PR, Reese CB,

et al. Characterization of a 3-phosphoinositide-dependent protein kinase which phosphorylates and activates protein kinase Balpha. Curr Biol 1997; 7: 261–9.

17 Kunnumakkara AB, Guha S, Krishnan S, Diagaradjane P, Gelovani J, Aggarwal BB. Curcumin potentiates antitumor activity of gemcitabine in an orthotopic model of pancreatic cancer through suppression of proliferation, angiogenesis, and inhibition of nuclear factor-kappaB-regulated gene products. Cancer Res 2007; 67: 3853–61.

18 Moertel CG, Ahmann DL, Taylor WF, Schwartau N. Aspirin and pancreatic cancer pain. Gastroenterology 1971; 60: 552–3.

19 Iconomou G, Kalofonos HP, Koutras AK, Vagenakis AG, Rigas B. Pilot study of nitric oxide-donating aspirin in patients with pancreatic cancer pain. J Support Oncol 2006; 4: 168.

20 Ricchi P, Palma AD, Matola TD, Apicella A, Fortunato R, Zarrilli R, *et al*. Aspirin protects Caco-2 cells from apoptosis after serum deprivation through the activation of a phosphatidylinositol 3-kinase/AKT/p21Cip/WAF1pathway. Mol Pharmacol 2003; 64: 407–14.

21 Dragovich T, Burris H 3rd, Loehrer P, Von Hoff DD, Chow S, Stratton S, *et al*. Gemcitabine plus celecoxib in patients with advanced or metastatic pancreatic adenocarcinoma: results of a phase II trial. Am J Clin Oncol 2008; 31:157–62.

22 Ougolkov AV, Fernandez-Zapico ME, Bilim VN, Smyrk TC, Chari ST, Billadeau DD. Aberrant nuclear accumulation of glycogen synthase kinase-3beta in human pancreatic cancer: association with kinase activity and tumor dedifferentiation. Clin Cancer Res 2006; 12: 5074–81.

23 Ikegaki N, Katsumata M, Minna J, Tsujimoto Y. Expression of bcl-2 in small cell lung carcinoma cells. Cancer Res 1994; 54: 6–8.

24 Kornmann M, Ishiwata T, Itakura J, Tangvoranuntakul P, Beger HG, Korc M. Increased cyclin D1 in human pancreatic cancer is associated with decreased postoperative survival. Oncology 1998; 55: 363–9.

25 Alao JP. The regulation of cyclin D1 degradation: roles in cancer development and the potential for therapeutic invention. Mol Cancer 2007; 6: 24.

26 Vermeulen K, Van Bockstaele DR, Berneman ZN. The cell cycle: a review of regulation, deregulation and therapeutic targets in cancer. Cell Prolif 2003; 36: 131–49.

27 Ivaska J, Nissinen L, Immonen N, Eriksson JE, Kahari VM, Heino J. Integrin alpha 2 beta 1 promotes activation of protein phosphatase 2A and dephosphorylation of Akt and glycogen synthase kinase 3 beta. Mol Cell Biol 2002; 22: 1352–9.

28 Cross DA, Alessi DR, Cohen P, Andjelkovich M, Hemmings BA. Inhibition of glycogen synthase kinase-3 by insulin mediated by protein kinase B. Nature 1995; 378: 785–9.

29 Wendel HG, De Stanchina E, Fridman JS, Malina A, Ray S, Kogan S, *et al*. Survival signalling by Akt and eIF4E in oncogenesis and cancer therapy. Nature 2004; 428: 332–7.

30 di Palma A, Matarese G, Leone V, Di Matola T, Acquaviva F, Acquaviva AM, *et al*. Aspirin reduces the outcome of anticancer therapy in Meth A-bearing mice through activation of AKT-glycogen synthase kinase signaling. Mol Cancer Ther 2006; 5: 1318–24.

Acta Pharmacologica Sinica (2010) 31: 81–92
© 2010 CPS and SIMM All rights reserved 1671-4083/10 $32.00
www.nature.com/aps

Original Article

4'-Chloro-3,5-dihydroxystilbene, a resveratrol derivative, induces lung cancer cell death

Jin-yi WU[1,#], Kun-wei TSAI[2,#], Jia-jen SHEE[3], Yi-zhen LI[1], Ching-hsein CHEN[1], Jing-jing CHUANG[4], Yi-wen LIU[1,*]

[1]Graduate Institute of Biomedical and Biopharmaceutical Sciences, [4]Department of Microbiology and Immunology, College of Life Sciences, National Chiayi University, Chiayi, Taiwan 60004, China; [2]Department of Internal Medicine, Buddhist Tzuchi Dalin General Hospital, Dalin Town, Chiayi, Taiwan 62247, China; [3]Division of Urology, Department of Surgery, Chang Gung Memorial Hospital, Chiayi, Taiwan 61363, China

---

Aim: To examine the antitumor effect of 4′-chloro-3,5-dihydroxystilbene, a resveratrol derivative, on lung adenocarcinoma A549 cells.
Methods: The cytotoxic IC_{50} was determined by direct cell counting. Flow cytometry, monodansylcadaverine (MDC) staining, transfection, Western blot and a proteasome activity assay were used to study the cellular mechanism of 4′-chloro-3,5-dihydroxystilbene. A xenograft nude mouse model was used to analyze the antitumor effect *in vivo*.
Results: 4′-Chloro-3,5-dihydroxystilbene induced a rapid and persistent increase in the intracellular reactive oxygen species in the cells, but the cell death could not be inhibited by two antioxidant agents. The derivative caused sub-G_1 formation, a decrease in the mitochondria membrane potential and poly (ADP-ribose) polymerase degradation, and the caspase inhibitor Z-VAD-FMK could partially prevent cell death. It also induced a significant increase in intracellular acidic vacuoles, LC3-II formation and intracellular GFP-LC3 aggregation. An autophagic inhibitor partially reversed cell death. Additionally, 4′-chloro-3,5-dihydroxystilbene induced the accumulation of ubiquitinated conjugates and inhibited proteasome activity in cells. In an *in vivo* study, 4′-chloro-3,5-dihydroxystilbene retarded tumor growth in nude mice.
Conclusion: These data suggest that the resveratrol derivative 4′-chloro-3,5-dihydroxystilbene could be developed as an anti-tumor compound.

Keywords: 4′-chloro-3,5-dihydroxystilbene; resveratrol derivative; antitumor effects; apoptosis; lung adenocarcinoma A549 cells

---

Acta Pharmacologica Sinica (2010) 31: 81–92; doi: 10.1038/aps.2009.182

Introduction

In the search for new cancer chemopreventive and chemotherapeutic agents over the past several years, the development of novel agents from the fruits and vegetables consumed by humans has been a desirable goal. Resveratrol (3,5,4′-trihydroxy-trans-stilbene) is one of the naturally occurring phytoalexins produced by a wide variety of plants, such as grapes, peanuts, and mulberries, in response to stress, injury, ultraviolet, irradiation or fungal infection[1]. Therefore, the biological function of resveratrol is thought to be protection of the plants from fungal attack and environmental stress. It has been reported that tobacco plants reengineered with stilbene synthase genes are more resistant to infection by *Botrytis cinerea*[2]. In the study of its biological function in animals and humans, resveratrol has been reported to play a role in the prevention of heart disease[3], the reduction of eicosanoid synthesis in macrophages[4] and the inhibition of LDL oxidation[5]. Additionally, resveratrol also exhibits cancer chemopreventive activity in the stages of tumor initiation, promotion and progression[6].

In addition to its chemopreventive effect, resveratrol also has a chemotherapeutic effect. In an *in vitro* study, resveratrol inhibited the growth of several tumor cell lines, including human promyelocytic leukemia cells, human breast cancer cells, human colon cancer cells, and human lung carcinoma cells[7]. In an *in vivo* animal study, resveratrol was also shown to have an anti-tumor effect[8]. In view of resveratrol's anti-tumor potential, it is reasonable to design new chemotherapeutic agents using resveratrol as a prototype. It has been reported that a resveratrol derivative, 3,4,5,4′-tetramethoxystilbene, has stronger anti-proliferative properties in human colon cancer cells[9]. Therefore, we synthesized a series of methoxy group-modified stilbenes and tested their cytotoxicity in human lung

---

[#] The first two authors contributed equally to this work.
[*] To whom correspondence should be addressed.
E-mail ywlss@mail.ncyu.edu.tw
Received 2009-06-22 Accepted 2009-11-19

cancer cells (supplementary information). On the other hand, the addition of a halogen group during the structural modification of resveratrol has seldom been reported. Based on the fact that the water solubility of a halogen is better than that of a methoxyl group, we have also synthesized a series of halogen group-modified stilbenes and found that 4′-chloro-3,5-dihydroxystilbene has better anti-tumor activity (supplementary information).

Lung cancer is the leading cause of cancer-related death in the world and in Taiwan[10, 11]. Therefore, we have studied the cytotoxicity of 4′-chloro-3,5-dihydroxystilbene in human lung adenocarcinoma A549 cells, elucidated the molecular mechanism of cell death and verified its effect *in vivo*.

Materials and methods

Chemicals

F12 Kaighn's medium (F12K), bovine serum and Lipofectamine 2000 were purchased from Invitrogen (Grand Island, NY). 1-[4,5-Dimethylthiazol-2-yl]-3,5-diphenylformazan (MTT), anti-β-actin antibodies, propidium iodide (PI), 2,7-dichlorofluorescin (DCF), *N*-acetyl-*L*-cysteine (NAC), glutathione, monodansylcadaverine (MDC), acridine orange, MG132, 3-methyladenine (3-MA), 4-(2-aminoethyl)benzenesulfonyl fluoride hydrochloride (AEBSF), N-CBZ-PHE-ALA fluoromethyl ketone (Z-FA-FMK), *N*-tosyl-*L*-phenylalanine chloromethyl ketone (TPCK) and N^{α}-tosyl-*L*-lysine chloromethyl ketone hydrochloride (TLCK) were purchased from Sigma-Aldrich (St Louis, MO). [L-3-*trans*-(Propylcarbamoyl)oxirane-2-carbonyl]-*L*-isoleucyl-*L*-proline methyl ester (CA074-Me) was purchased from the Peptide Institute (Osaka, Japan). Antibodies against cyclins, p21, Bcl-2, and Bax were purchased from Lab Vision (Fremont, CA). The antibody against procaspase-3 was purchased from Active Motif (Carlsbad, CA). The antibody against poly(ADP-ribose) polymerase (PARP) was purchased from Cell Signaling Technology (Beverly, MA). The SuperSignal West Pico Chemiluminescent Substrate was obtained from Pierce (Rockford, IL). The PRO-PREP^{TM} Protein Extraction Solution was from iNtRON Biotechnology (Kyungki-Do, Korea). The Bio-Rad protein assay kit was purchased from Bio-Rad (Hercules, CA). Fluorogenic peptide substrates for the proteasome activity assay were purchased from Biomol (Butler Pike, PA).

Cell culture

Human non-small-cell lung adenocarcinoma A549 cells were obtained from the Bioresource Collection and Research Center (Hsinchu, Taiwan), and cultured in F12K supplemented with 10% heat-inactivated fetal bovine serum. Cells were maintained at 37 °C in a humidified atmosphere with 5% CO_2.

Trypan blue dye exclusion method

The cell number was determined by direct cell counting. A549 cells were cultured in 24-well plates at a density of 2×10^4 cells/well for 24 h and then incubated with various concentrations of resveratrol or 4′-chloro-3,5-dihydroxystilbene for 2 days. The cells were then detached by trypsin-EDTA, stained with trypan blue dye and counted with a hemocytometer. The result was expressed as a percentage relative to the solvent-treated control incubations, and the IC_{50} values were calculated.

Measurement of intracellular reactive oxygen species (ROS)

The production of intracellular ROS was detected by flow cytometry using DCFH-DA. A549 cells were cultured in 60-mm tissue culture dishes at a density of 8×10^5 cells/dish for 24 h and then treated with DMSO or 4′-chloro-3,5-dihydroxystilbene for various amounts of time. After treatment, cells were treated with 10 μmol/L DCFH-DA for 30 min in the dark, washed once with PBS, detached by trypsinization, collected by centrifugation, and resuspended in PBS. The intracellular ROS, which are indicated by the fluorescence of dichlorofluorescin (DCF), were measured with a Becton-Dickinson FACScan flow cytometer using CellQuest software.

Measurement of cellular membrane integrity

Cellular membrane integrity was detected by PI staining. A549 cells were cultured in 60-mm tissue culture dishes for 24 h and then incubated with various inhibitors for 60 min. DMSO or 4′-chloro-3,5-dihydroxystilbene was then added to the cells for the indicated times. After treatment, trypsinized cells were resuspended in PBS and stained for 10 min with 5 μg/mL of PI. The stained cells were excited by exposure to an argon laser at 488 nm, and the fluorescence emission was collected at 580 nm. At least 10000 cells were counted with a Becton-Dickinson FACScan flow cytometer using CellQuest software. Living cells prevent the entrance of propidium iodide, indicating complete cellular membrane integrity, and dead cells are stained by propidium iodide, indicating damage to the cellular membranes.

Cell cycle analysis

A549 cells were cultured in 100-mm tissue culture dishes at a density of 1×10^6 cells/dish for 24 h and then treated with 80 μmol/L 4′-chloro-3,5-dihydroxystilbene for various amounts of time. After treatment, cells were collected and washed with PBS, fixed with a PBS-methanol (1:2, volume/volume) solution, and stored at 4 °C for at least 18 h. Following two more PBS washes, the cell pellets were stained with the fluorescent probe solution containing PBS, 40 μg/mL PI, and 40 μg/mL DNase-free RNaseA for 30 min at room temperature in the dark. DNA fluorescence of the PI-stained cells was evaluated by excitation at 488 nm and detected through a 630/22-nm bandpass filter using a Becton-Dickinson FACScan flow cytometer. A minimum of 10000 cells were analyzed per sample, and the DNA histograms were gated and analyzed further using Modfit software to estimate the percentage of cells in various phases of the cell cycle.

Measurement of mitochondria membrane potential

Mitochondria membrane potential (MMP) was detected by flow cytometry using rhodamine123 fluorescent dye (Ex/Em=430 nm/535 nm). A549 cells were cultured in 60-mm tissue culture dishes at a density of 8×10^5 cells/dish for 24 h and then treated with 80 μmol/L 4′-chloro-3,5-dihydroxystilbene for 24 h and 48 h. After treatment, the culture medium was replaced with fresh medium containing 5 μmol/L rhodamine123 and the cells were incubated for 30 min in the dark. After the incubation step, the cells were washed with PBS, detached by trypsinization, collected by centrifugation, and resuspended in PBS. The MMP, as indicated by the fluorescence level of rhodamine123, was measured with a Becton-Dickinson FACScan flow cytometer using CellQuest software.

Measurement of acidic vacuoles by MDC staining and acridine orange staining

A549 cells were cultured in 100-mm tissue culture dishes at a density of 1×10^6 cells/dish for 24 h and then treated with 80 μmol/L 4′-chloro-3,5-dihydroxystilbene for another 24 h. After treatment, the culture medium was replaced with fresh medium containing 50 μmol/L MDC or 1 μg/mL of acridine orange and the cells were incubated for 30 min in the dark. For MDC staining, cells were washed with PBS and photos were taken under a fluorescent microscope. For acridine orange staining, cells were detached by trypsinization, collected by centrifugation, and resuspended in PBS. The fluorescence level of acridine orange was measured with a Becton-Dickinson FACScan flow cytometer using CellQuest software.

Measurement of LC3 localization by immunofluorescence microscopy

The green fluorescent protein-tagged autophagic marker microtubule-associated protein 1 light chain 3 (GFP-LC3) plasmid[12] was transiently transfected into A549 cells using Lipofectamine™ 2000 according to the manufacturer's instruction. Cells were replated 16 h before transfection at a density of 5000 cells per 1 mL of culture medium in a 12-well plastic dish. In transfection, Lipofectamine™ 2000 was incubated with GFP-LC3 (1 μL Lipofectamine™ 2000/0.5 μg DNA/well) in 0.1 mL of OPTI-MEM for 20 min at room temperature. The mixture was added drop by drop to the cells and then incubated for 6 h. The DNA/Lipofectamine™ 2000 medium was replaced by 1 mL of fresh culture medium and the cells were cultured for another 18 h. Then, 80 μmol/L 4′-chloro-3,5-dihydroxystilbene was added to the cells in order to observe GFP-LC3 localization by immunofluorescence microscopy.

Proteasome activity assay

A549 cells were treated with DMSO, 4′-chloro-3,5-dihydroxystilbene or proteasome inhibitor MG132 for 30 to 90 min. Cell lysates were collected and 10 μg of each was incubated for 2 h at 37 °C with 40 μmol/L fluorogenic peptide substrate (Suc-Leu-Leu-Val-Tyr-AMC for chymotrypsin-like, Ac-Gly-Pro-Leu-Asp-AMC and Z-Leu-Leu-Glu-AMC for caspase-like, and Boc-Leu-Arg-Arg-AMC and Ac-Arg-Leu-Arg-AMC for trypsin-like) in 100 μL of assay buffer (20 mmol/L Tris-HCl, pH 8.0). The hydrolyzed AMC was measured by a fluorometer with an excitation filter of 360 nm and an emission filter of 460 nm.

Animal model

Female nude mice aged five weeks were provided by the National Laboratory Animal Center (Taipei, Taiwan), and maintained at our animal care facility for one week prior to use. The mice were kept in a limited access area at a controlled room temperature with food and water provided *ad libitum*. The mice were divided into two groups for two different experiments (vehicle only and 50 mg/kg 4′-chloro-3,5-dihydroxystilbene). All experiments were approved by the Institutional Animal Care and Use Committee of National Chiayi University.

Statistical analysis

Three or more separate experiments were conducted. Statistical analysis was performed with Student's *t*-test. The animal study was analyzed by one-way ANOVA followed by Tukey's test. A $P<0.05$ was considered to indicate a significant difference between the treated and control groups.

Results

Effect of resveratrol and 4'-chloro-3,5-dihydroxystilbene on cell viability

When comparing the cytotoxicity of 4′-chloro-3,5-dihydroxystilbene to that of resveratrol in A549 cells, the IC_{50} of resveratrol (25.5 μmol/L) is about 1.5 times greater than that of 4′-chloro-3,5-dihydroxystilbene (17.4 μmol/L), and the maximum cytotoxic activity reached was 100% with 4′-chloro-3,5-dihydroxystilbene, but only 80% with resveratrol (Figure 1A). In addition to the A549 cells, 4′-chloro-3,5-dihydroxystilbene also showed higher cytotoxicity than resveratrol in two other lung cancer cell lines, NCI-H23 and NCI-H1299 (Figure 1A). A549 cells treated with 100 μmol/L resveratrol displayed a shrunken shape at 24 h and started to detach at 48 h (Figure 1B). With 80 μmol/L 4′-chloro-3,5-dihydroxystilbene, the cells showed vacuolation at 24 h and became almost rounded and detached after 48 h of treatment (Figure 1B). This result suggested that 4′-chloro-3,5-dihydroxystilbene was more potent than resveratrol and that its cytotoxic mechanism might be different from that of resveratrol in human lung carcinoma cells.

4′-Chloro-3,5-dihydroxystilbene induced intracellular ROS elevation that was not the main inducer of cell death. Because ROS have been reported to induce cytotoxicity in cancer cells[13], we analyzed the effect of 4′-chloro-3,5-dihydroxystilbene on the intracellular ROS production by the DCFH-DA staining method. The increase in intracellular ROS occurred after 1 h of treatment with 4′-chloro-3,5-dihydroxystilbene and gradually increased through the 48 h time period. The intracellular ROS were increased approximately 1.6, 2.4, 2.7, 3.2, and 5.6 fold after treatment with 4′-chloro-3,5-dihydroxystilbene for 1 h, 3 h, 6 h, 24 h, and 48 h, respectively (Figure 2A). To further characterize the relationship of ROS and cell death, two antioxidant agents, NAC and glutathione, were used to analyze the protective effect of 4′-chloro-3,5-dihydroxystilbene-treated cells. 4′-Chloro-3,5-dihydroxystilbene-induced ROS production was almost completely inhibited by 10 mmol/L NAC or 10 mmol/L glutathione (Figure 2B); however, these

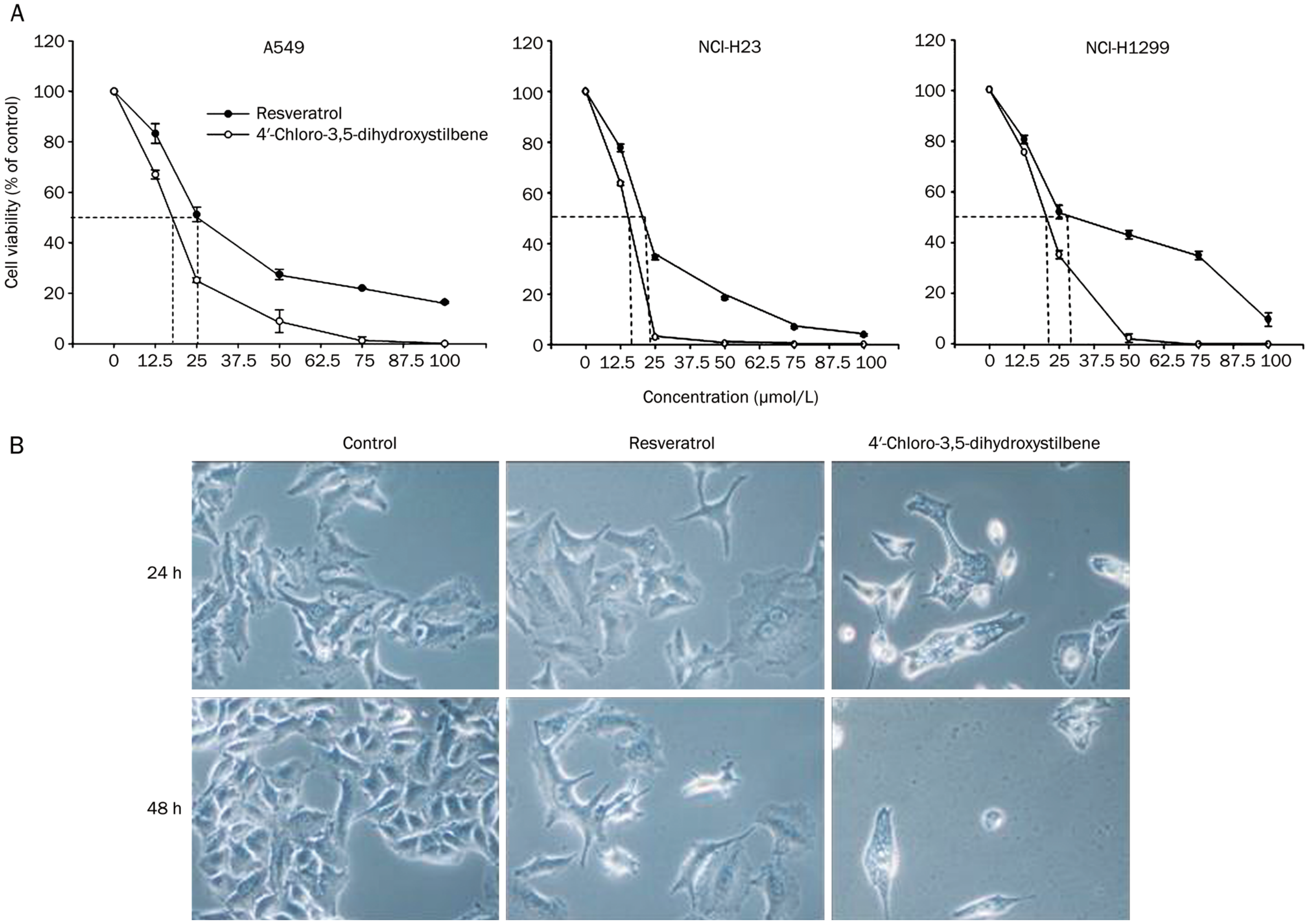

Figure 1. The cytotoxic IC_{50} and morphological changes in resveratrol- and 4′-chloro-3,5-dihydroxystilbene-treated A549 cells. (A) The cytotoxicity IC_{50} of resveratrol and 4′-chloro-3,5-dihydroxystilbene. A549, NCI-H23, and NCI-H1299 cells were treated with various concentrations of resveratrol or 4′-chloro-3,5-dihydroxystilbene for 48 h. Cell numbers were calculated by the trypan blue dye exclusion method using a hemocytometer. The cell number of untreated cells was 100%, and the other data were presented as the mean±SD from three independent experiments. (B) The morphological changes of A549 cells treated with resveratrol or 4′-chloro-3,5-dihydroxystilbene. A549 cells were treated with DMSO, 100 μmol/L resveratrol or 80 μmol/L 4′-chloro-3,5-dihydroxystilbene for 24 h or 48 h. The cells were photographed with an Axio Observer A1 phase-contrast microscope. Magnification ×200.

two antioxidant agents could not prevent cell death (Figure 2C). This result indicated that the ROS elevation induced by 4′-chloro-3,5-dihydroxystilbene was not the main reason for cell death.

Effect of 4′-chloro-3,5-dihydroxystilbene on cell cycle distribution

Because 4′-chloro-3,5-dihydroxystilbene inhibited the growth of A549 cells, we then analyzed the cell-cycle population distribution in A549 cells, with or without 4′-chloro-3,5-dihydroxystilbene. As shown in Figure 3A, the sub-G_1 fraction in cells treated with 80 μmol/L 4′-chloro-3,5-dihydroxystilbene gradually increased to 18% and 43% at 24 h and 48 h, respectively. The data indicated that 4′-chloro-3,5-dihydroxystilbene caused DNA fragmentation in a time-dependent manner. Before the formation of the sub-G_1 fraction, cells were initially accumulated in the G_2/M phase, but those in the G_1 phase did not decrease when they were treated with 4′-chloro-3,5-dihydroxystilbene. When G_2/M phase arrest occurred, the G_1 phase ratio should have decreased if cells in G_1 continued to S without M-returned cells. In our study, the G_1 phase ratio was similar to that of control cells, suggesting that 4′-chloro-3,5-dihydroxystilbene arrested cells in the G_1 and G_2/M phases and that this arrest might result in sub-G_1 formation. Resveratrol induced cell cycle arrest at the G_1 phase, which was different from the results obtained with 4′-chloro-3,5-dihydroxystilbene (Figure 3A). Western blot analysis (Figure 3B) showed that 4′-chloro-3,5-dihydroxystilbene decreased the expression of cyclin D1 and cyclin D3, which might have caused G_1 phase arrest. 4′-Chloro-3,5-dihydroxystilbene also decreased cyclin B1 expression, which might have caused G_2 phase arrest. 4′-Chloro-3,5-dihydroxystilbene decreased p21 expression, which suggested that cell cycle arrest was not mediated by the p53-p21 pathway.

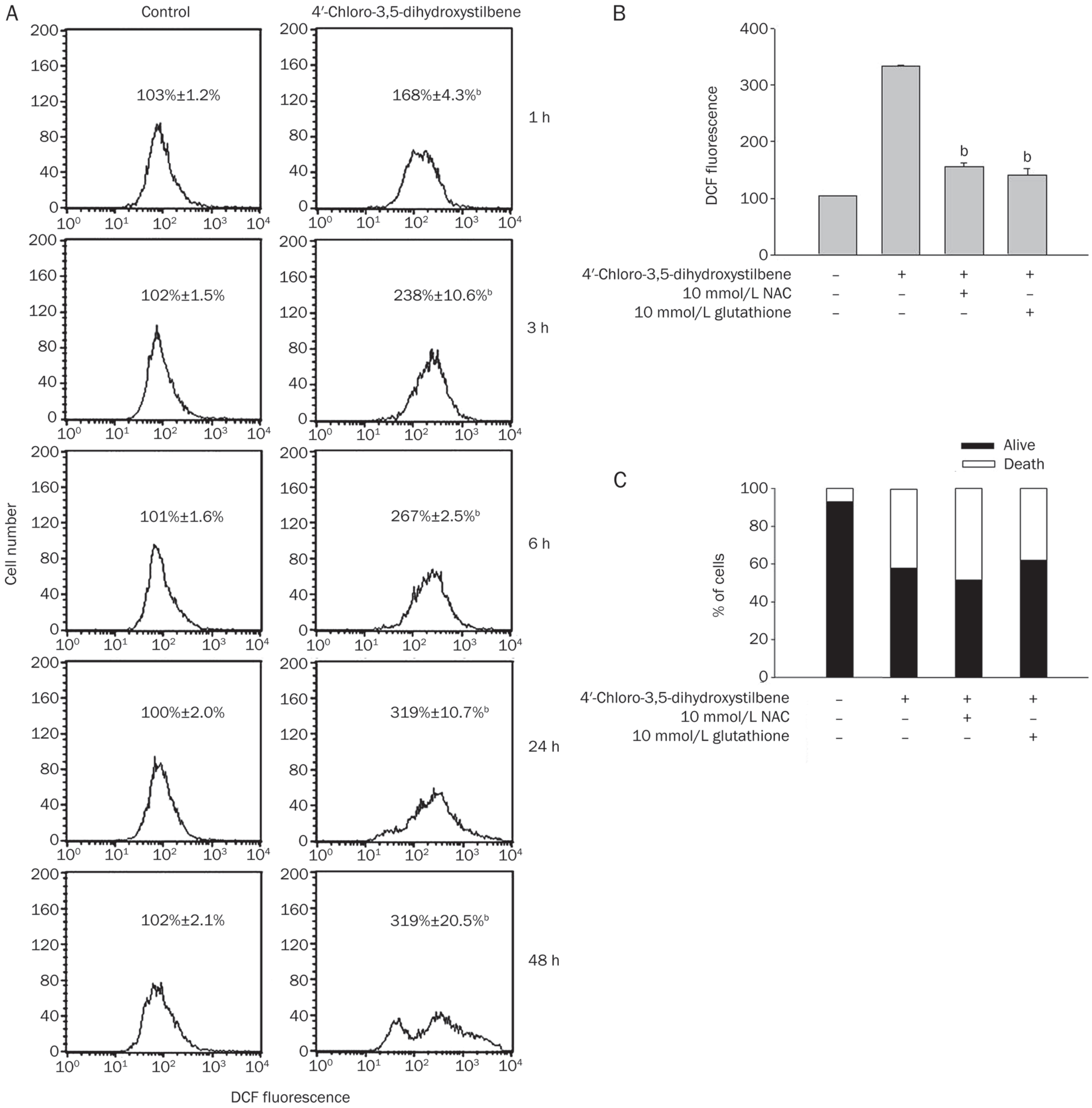

Figure 2. Effect of ROS on 4′-chloro-3,5-dihydroxystilbene-induced A549 cell death. (A) 4′-Chloro-3,5-dihydroxystilbene-induced ROS production. A549 cells were either untreated or treated with 80 μmol/L 4′-chloro-3,5-dihydroxystilbene for 1, 3, 6, 24, and 48 h. Thirty minutes prior to harvesting, cells were incubated with 10 μmol/L DCF-DA. After incubation, the cells were harvested for analysis by FACS. The data in each panel represent the DCF fluorescence intensity within the cells. At each time point, the mean intensity of the control cells was at 100 and the other data were measured in this set condition. The values shown are the mean±SD of three determinations. (B) Effect of antioxidants on 4′-chloro-3,5-dihydroxystilbene-induced ROS. 10 mmol/L NAC or 10 mmol/L glutathione was added 1 h before treatment with 80 μmol/L 4′-chloro-3,5-dihydroxystilbene for 3 h. Cells were harvested for analysis by FACS. The values shown are means±SD of three independent experiments. $^{b}P<0.05$ *vs* the 4′-chloro-3,5-dihydroxystilbene-treated group. (C) Effect of antioxidants on 4′-chloro-3,5-dihydroxystilbene-induced damage of cellular membrane integrity. The cells were exposed to 10 mmol/L NAC or 10 mmol/L glutathione for 1 h before treatment with 80 μmol/L 4′-chloro-3,5-dihydroxystilbene for 36 h. A549 cells were harvested and stained with propidium iodide and analyzed by FACS.

4′-Chloro-3,5-dihydroxystilbene induced apoptosis, which was a minor reason for cell death

Increased mitochondrial permeability is one of the mitochondria-dependent cell death pathways[14]. Therefore, we measured the mitochondrial permeability regulatory proteins Bcl-2 and Bax by Western blot analysis. Treatment of A549 cells with 80 μmol/L 4′-chloro-3,5-dihydroxystilbene caused a significant decrease in the anti-apoptotic protein Bcl-2 in the

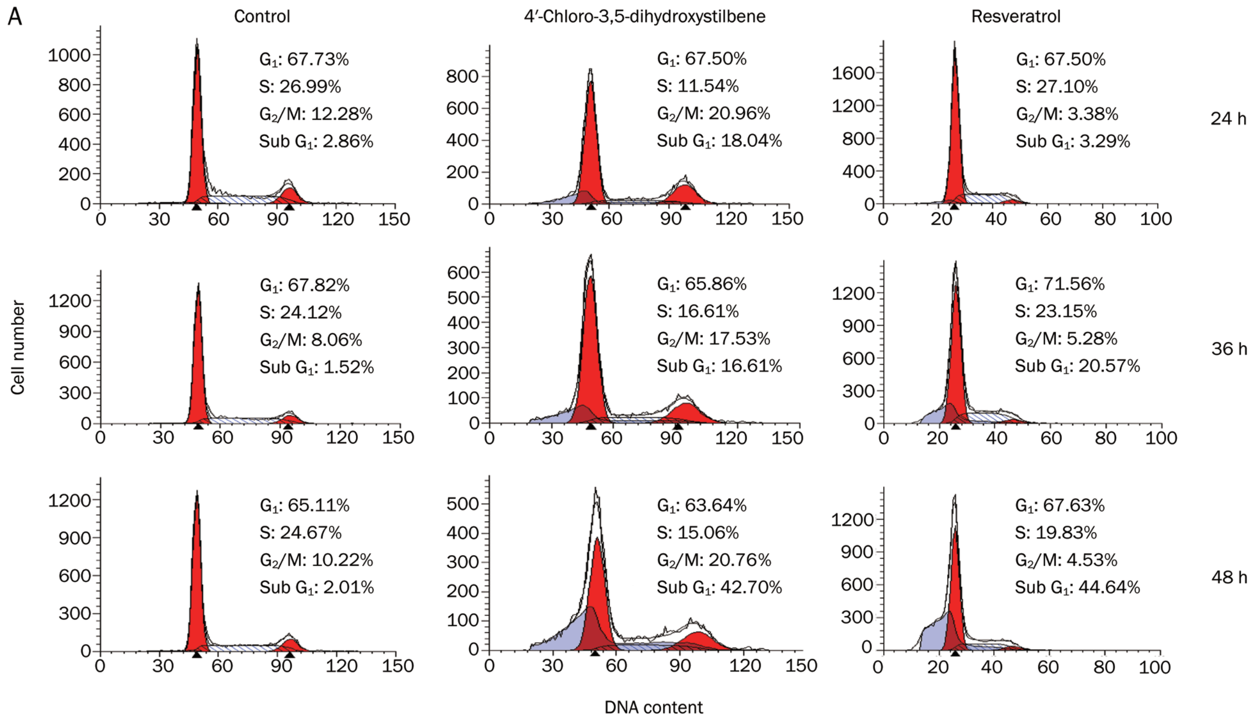

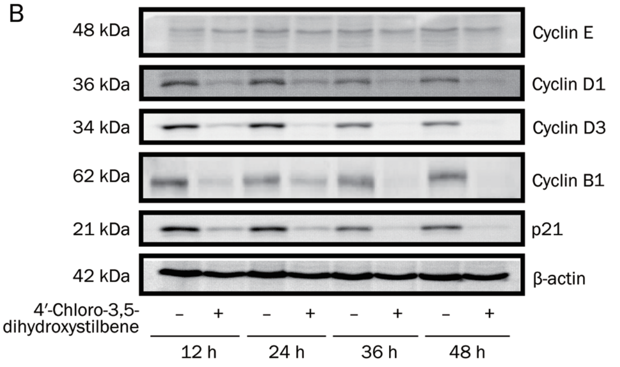

Figure 3. Effect of 4′-chloro-3,5-dihydroxystilbene and resveratrol on cell cycle distribution. (A) The cell cycle distribution is altered by 4′-chloro-3,5-dihydroxystilbene or resveratrol treatment. A549 cells were treated with 80 μmol/L 4′-chloro-3,5-dihydroxystilbene or 100 μmol/L resveratrol for 24, 36, or 48 h. Cells were harvested, fixed with ethanol and stained with PI. The DNA content was analyzed by flow cytometry. A representative FACS scan chart of propidium iodide-stained A549 cells shows the percentages of G_0/G_1, S, G_2/M, and sub-G_1 cell cycle phases in each plot. The values shown are the mean of three determinations. (B) Time course of the 4′-chloro-3,5-dihydroxystilbene-induced degradation of cyclins. A549 cells were treated with or without 80 μmol/L 4′-chloro-3,5-dihydroxystilbene for 12, 24, 36, and 48 h. Cell lysates were harvested and analyzed by Western blotting with antibodies against cyclin E, cyclin D1, cyclin D3, cyclin B1 and p21.

time period from 12 h to 48 h (Figure 4A), as well as a decrease in the pro-apoptotic protein Bax. Therefore, the detection of MMP by rodamine123 was performed, which showed that 4′-chloro-3,5-dihydroxystilbene decreased MMP at 24 h and 48 h (Figure 4B). Because of the formation of the sub-G_1 fraction and the decrease in MMP in 4′-chloro-3,5-dihydroxystilbene-treated cells, we then investigated whether 4′-chloro-3,5-dihydroxystilbene induced the activation of apoptotic effector proteins. The breakdown products of PARP and procaspase-3 were analyzed. Figure 5A shows that 4′-chloro-3,5-dihydroxystilbene induced both the cleavage of PARP and a decrease in procaspase-3. The change in these two proteins started after 24 h of treatment with 4′-chloro-3,5-dihydroxystilbene and persisted to 48 h. A pan caspase inhibitor, Z-VAD-FMK, was then used to identify the relationship of apoptosis and cell death. It was shown that Z-VAD-FMK inhibited 4′-chloro-3,5-dihydroxystilbene-induced sub-G1 formation (Figure 5B) and reversed PARP cleavage in a dose-dependent manner (Figure 5C). ROS are one of the reasons for cell apoptosis; we also analyzed the role of ROS in 4′-chloro-3,5-dihydroxystilbene-induced sub-G_1 formation. The results showed that two antioxidants inhibited the 4′-chloro-3,5-dihydroxystilbene-induced sub-G_1 formation by 30% and the resveratrol-induced sub-G_1 formation by more than 50% (Figure 5D). This result suggests that ROS are one of the reasons for 4′-chloro-3,5-dihydroxystilbene-induced apoptosis. Because these two antioxidants could not reverse 4′-chloro-3,5-dihydroxystilbene-induced cell death (Figure 2C), the reversal effect was further analyzed with Z-VAD-FMK. The results showed that Z-VAD-FMK only slightly reversed cell death (Figure 5E), even though apoptosis was almost completely inhibited by Z-VAD-FMK (Figure 5B, 5C). These data suggested that 4′-chloro-3,5-dihydroxystilbene-induced cell death was mediated by caspase-dependent apoptosis in a minor way. Because Z-VAD-FMK only slightly reversed 4′-chloro-3,5-dihydroxystilbene-induced cell death, ROS-inhibitor-reversible cell death might be too low to be

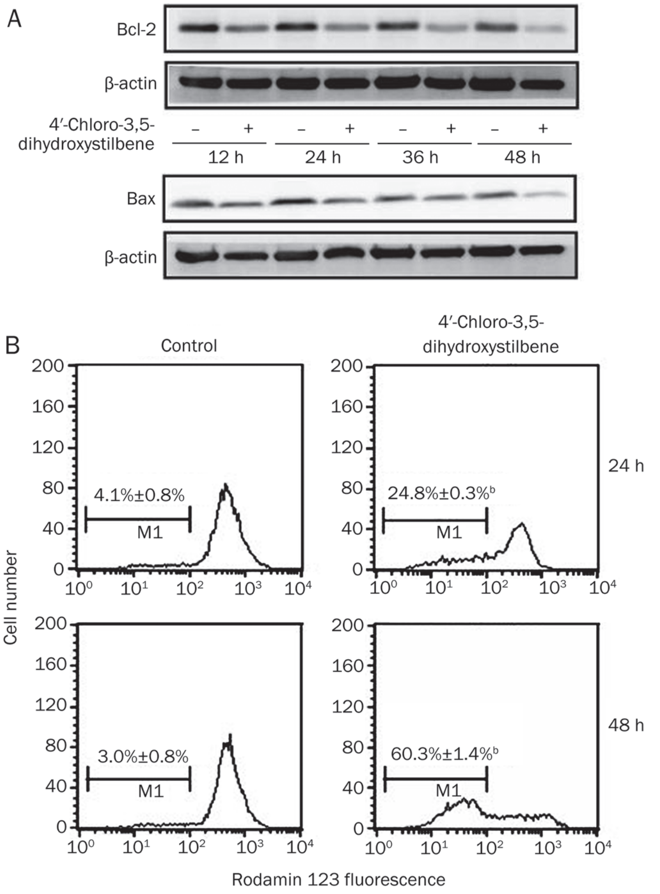

Figure 4. Effect of 4′-chloro-3,5-dihydroxystilbene on mitochondria membrane potential. (A) Time course of the 4′-chloro-3,5-dihydroxystilbene-induced degradation of Bcl-2 and Bax. A549 cells were treated with or without 80 μmol/L 4′-chloro-3,5-dihydroxystilbene for 12, 24, 36, and 48 h. Cell lysates were harvested and analyzed by Western blotting with antibodies against Bcl-2, Bax and β-actin. (B) 4′-Chloro-3,5-dihydroxystilbene decreased the MMP. A549 cells were treated with or without 80 μmol/L 4′-chloro-3,5-dihydroxystilbene for 24 or 48 h. Cells were harvested and analyzed by FACS. A representative FACS scan chart shows the percentages of low MMP in each plot. The values shown are the mean±SD of three determinations.

detected.

Induction of the autophagic early phenomenon by 4′-chloro-3,5-dihydroxystilbene

If 4′-chloro-3,5-dihydroxystilbene-induced cell death was not totally mediated by apoptosis, the death could be caused by a non-apoptotic pathway, such as autophagy, necrosis or another process[15]. Based on the morphological changes induced by 4′-chloro-3,5-dihydroxystilbene, which showed vacuolation in the cells (Figure 1B), an autophagic process is likely[15]. We then attempted to detect the formation of acidic vacuoles in the cells. As shown in Figures 6A and 6B, 4′-chloro-3,5-dihydroxystilbene increased the formation of intracellular acidic vacuoles. Next, we tried to confirm the autophagic phenomenon by more specific methods. First, we showed that 4′-chloro-3,5-dihydroxystilbene induced more obvious LC3-II formation than resveratrol (Figure 6C). Furthermore, the GFP-LC3 produced by transfected cells was used to confirm the process of autophagy[12, 16]. Cytoplasmic LC3 proteins become localized within autophagic vacuoles when a cell begins autophagy[17, 18]. Transient transfection with GFP-LC3 plasmid DNA was performed to express the GFP-LC3 fusion protein in A549 cells. In the GFP-LC3-transfected A549 cells, GFP-LC3 proteins were found diffused through the whole cell (Figure 6D). After 4′-chloro-3,5-dihydroxystilbene treatment, GFP-LC3 became aggregated dots in the cells, suggesting that 4′-chloro-3,5-dihydroxystilbene caused the localization of LC3 and initiated the autophagic early phenomenon. Next, we used a pharmacological inhibitor to identify the relationship between autophagy and cell death. As shown in Figure 6E, 3-MA could partially reverse cell death, which suggested that the 4′-chloro-3,5-dihydroxystilbene-induced cell death was partially mediated by autophagy. Furthermore, we used various protease inhibitors to analyze whether cell death was caused by an acidic lysosomal protease[19, 20]. As shown in Figure 6E, two cathepsin inhibitors (CA074-Me and Z-FA-FMK), two serine protease inhibitors (TLCK and AEBSF) and one proteasome inhibitor (MG132) could not prevent cell death; only one serine protease inhibitor, TPCK, slightly reversed cell death. This result suggested that the 4′-chloro-3,5-dihydroxystilbene-induced cell death was partially mediated by lysosome leakage, but not by proteasome activation. Caspase inhibitor Z-VAD-FMK also partially inhibited resveratrol-induced cell death.

4′-Chloro-3,5-dihydroxystilbene inhibited proteasome activity in A549 cells

While observing the morphological changes of MG132-treated cells, we found vacuole formation similar to that caused by 4′-chloro-3,5-dihydroxystilbene (Figure 7A). Because MG132 is a standard proteasome inhibitor used in anti-cancer studies, we tried to compare the biochemical effect of MG132 and 4′-chloro-3,5-dihydroxystilbene treatment in cells. Figure 7B showed the accumulation of ubiquitinated conjugates induced by 10 μmol/L and 50 μmol/L MG132. 4′-Chloro-3,5-dihydroxystilbene also induced a dose-dependent increase in ubiquitinated conjugates. In an additional study, we analyzed the proteasome activity after 4′-chloro-3,5-dihydroxystilbene or MG132 treatment. This study showed that 4′-chloro-3,5-dihydroxystilbene partially inhibited substrate cleavage by chymotrypsin-like and caspase-like proteasomes (Figure 7C).

4′-Chloro-3,5-dihydroxystilbene retarded tumor growth in nude mice

The anti-tumor effect of 4′-chloro-3,5-dihydroxystilbene was studied in nude mice inoculated with A549 cells. Figure 8 shows that 4′-chloro-3,5-dihydroxystilbene retarded tumor growth *in vivo*, indicating its potential as an anti-tumor drug.

Discussion

Resveratrol has been proposed as a potential chemothera-

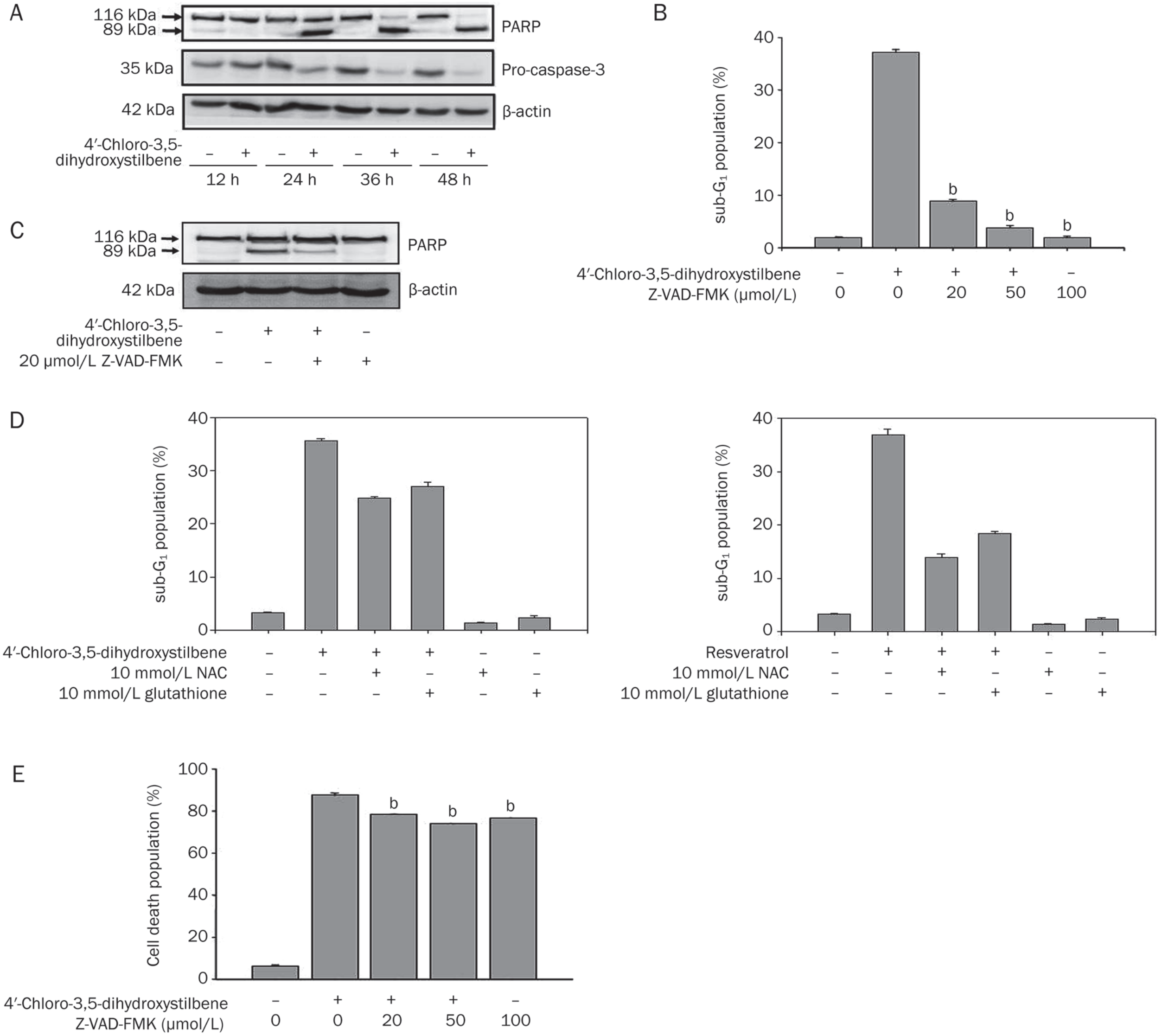

Figure 5. The apoptotic parameters of 4′-chloro-3,5-dihydroxystilbene-treated A549 cells. (A) Time course of the 4′-chloro-3,5-dihydroxystilbene-induced degradation of PARP and procaspase-3. A549 cells were treated with or without 80 μmol/L 4′-chloro-3,5-dihydroxystilbene for 12, 24, 36, and 48 h. Cell lysates were harvested and analyzed by Western blotting with antibodies against two forms of PARP, pre-cleavage caspase-3 and β-actin. (B) Effect of Z-VAD-FMK on 4’-chloro-3,5-dihydroxystilbene-induced sub-G_1 formation. Z-VAD-FMK was added 1 h before treatment with 80 μmol/L 4′-chloro-3,5-dihydroxystilbene for 48 h. Cells were harvested, fixed and stained with propidium iodide and analyzed by FACS. The values shown are the mean±SD of three determinations (C) Effect of Z-VAD-FMK on 4′-chloro-3,5-dihydroxystilbene-induced PARP cleavage. Z-VAD-FMK was added 1 h before treatment with 80 μmol/L 4′-chloro-3,5-dihydroxystilbene for 24 h. Cell lysates were harvested and analyzed by Western blotting with antibodies against two forms of PARP and β-actin. (D) Effect of NAC and glutathione on 4′-chloro-3,5-dihydroxystilbene-induced sub-G_1 formation. NAC or glutathione was added 1 h before treatment with 80 μmol/L 4′-chloro-3,5-dihydroxystilbene or 100 μmol/L resveratrol for 48 h. Cells were harvested, fixed and stained with propidium iodide and analyzed by FACS. The values shown are the mean±SD of three determinations. (E) Effect of Z-VAD-FMK on 4′-chloro-3,5-dihydroxystilbene-induced damage of cellular membrane integrity. Z-VAD-FMK was added 1 h before treatment with 80 μmol/L 4′-chloro-3,5-dihydroxystilbene for 48 h. A549 cells were harvested and stained with propidium iodide and analyzed by FACS. The values shown are the mean±SD of three determinations. $^{b}P<0.05$ *vs* the 4′-chloro-3,5-dihydroxystilbene-treated group.

peutic compound. Therefore, modification of the functional group of resveratrol was studied in this work. In the analysis of the structure-activity relationship, substitution of the hydroxyl group of resveratrol with a methoxy group did not seem to increase its cytotoxic activity (Supplementary information). On the contrary, substitution of the 4′-hydroxyl group of resveratrol with a halogen group potentiated cytotoxic activity (Supplementary information). When comparing the IC_{50} of resveratrol and 4′-chloro-3,5-dihydroxystilbene, the latter showed a higher potency of growth suppression in three lung cancer cell lines (Figure 1A). In the cell cycle analysis, 4′-chloro-3,5-dihydroxystilbene induced cell arrest in the G_1

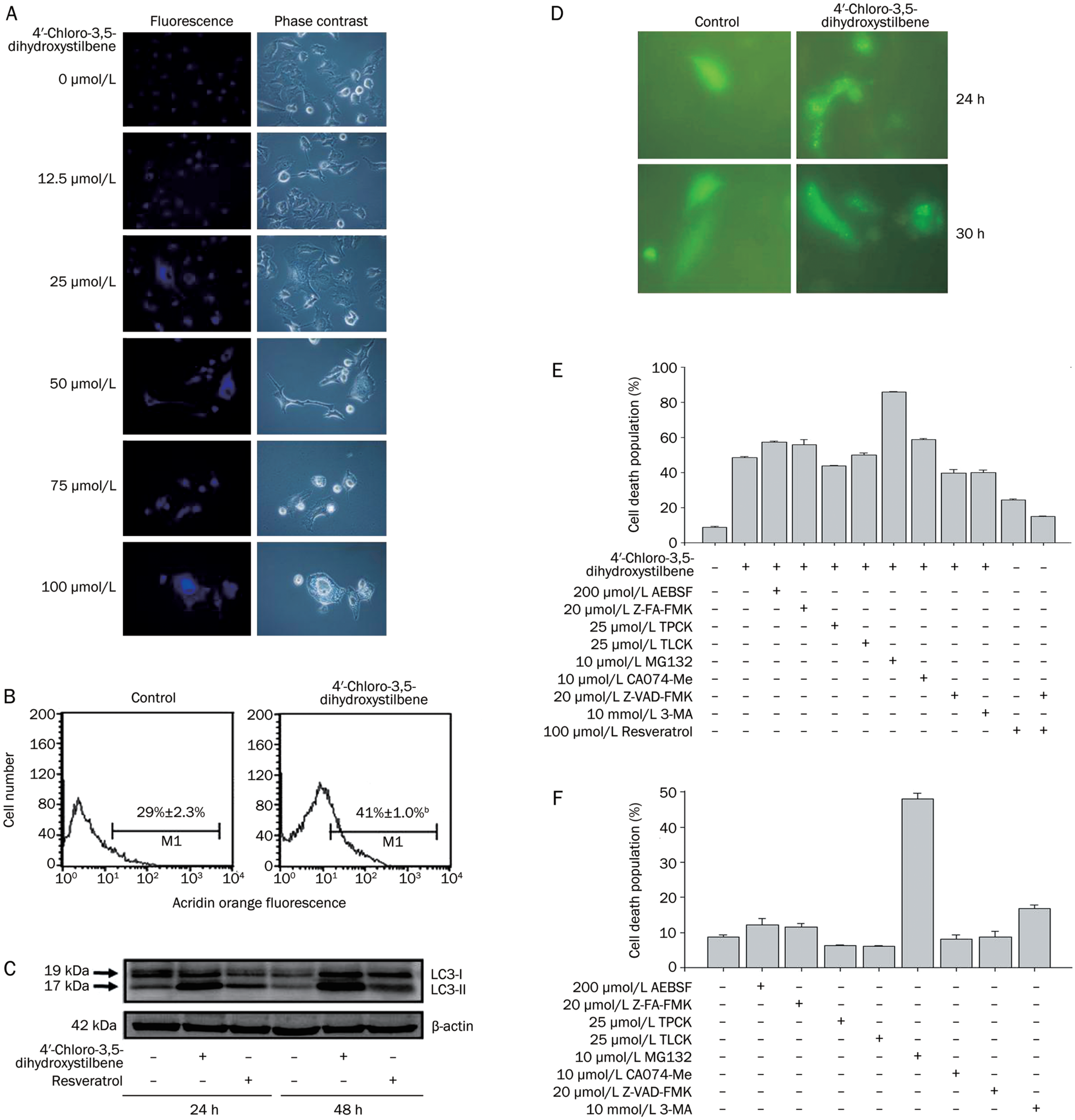

Figure 6. The autophagic parameters of 4′-chloro-3,5-dihydroxystilbene-treated A549 cells. (A) 4′-Chloro-3,5-dihydroxystilbene increased acidic vacuoles as determined by the MDC staining method. A549 cells were treated with or without 80 μmol/L 4′-chloro-3,5-dihydroxystilbene for 24 h. Cells were then stained with MDC for photography. Magnification ×200. (B) 4′-Chloro-3,5-dihydroxystilbene increased acidic vacuoles as determined by the acridine orange staining method. A549 cells were treated with or without 80 μmol/L 4′-chloro-3,5-dihydroxystilbene for 24 h. Cells were then stained with acridine orange for flow cytometry analysis. $^{b}P<0.05$ *vs* control. (C) 4′-Chloro-3,5-dihydroxystilbene induces LC3-II formation. A549 cells were treated with or without 80 μmol/L 4′-chloro-3,5-dihydroxystilbene or 100 μmol/L resveratrol for 24 h and 48 h. Cell lysates were harvested and analyzed by Western blotting with antibodies against LC3 and . (D) Time course of the 4′-chloro-3,5-dihydroxystilbene-induced aggregation of GFP-LC3 in A549 cells. A549 cells were transiently transfected with the GFP-LC3 plasmid. After transfection, the cells were treated with or without 80 μmol/L 4′-chloro-3,5-dihydroxystilbene for 24 h and 30 h. The cells were photographed with an Olympus IX70 fluorescent microscope. Magnification ×200. (E and F) Effect of autophagy inhibitor (3-MA), protease inhibitors (AEBSF, Z-FA-FMK, TPCK, TLCK, CA074-Me), caspase inhibitor (Z-VAD-FMK) and proteasome inhibitor (MG132) on 4′-chloro-3,5-dihydroxystilbene-induced cell death. A549 cells were individually treated with DMSO or various inhibitors for 1 h, then 80 μmol/L 4′-chloro-3,5-dihydroxystilbene or 100 μmol/L resveratrol was added for 36 h. A549 cells were harvested, stained with propidium iodide, and analyzed by FACS. The values shown are the mean±SD of three determinations.

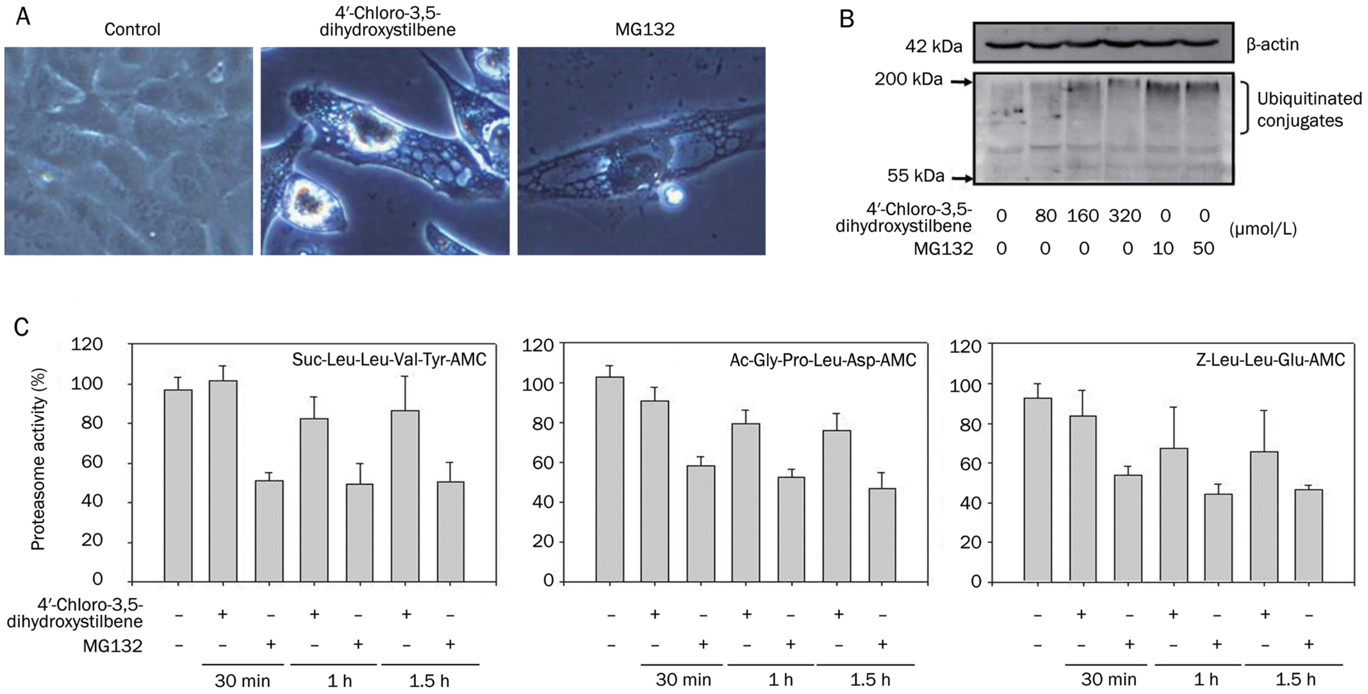

Figure 7. 4′-Chloro-3,5-dihydroxystilbene inhibited proteasome activity in A549 cells. (A) Morphological changes induced by 4′-chloro-3,5-dihydroxystilbene and MG132. A549 cells were treated with 80 μmol/L 4′-chloro-3,5-dihydroxystilbene or 10 μmol/L MG132 for 48 h and the cells were photographed. Magnification ×200. (B) Effect of 4′-chloro-3, 5-dihydroxystilbene on the accumulation of ubiquitinated conjugates. A549 cells were treated with various concentrations of 4′-chloro-3,5-dihydroxystilbene or MG132 for 60 min. Cell lysates were harvested and analyzed by Western blotting with antibodies against ubiquitin and β-actin. (C) Effect of 4′-chloro-3,5-dihydroxystilbene on proteasome activity. A549 cells were treated with 80 μmol/L 4′-chloro-3,5-dihydroxystilbene or 10 μmol/L MG132 for 30 min to 90 min. Cell lysates were harvested and analyzed with proteasome fluorogenic peptide substrates.

and G_2/M phases (Figure 3A and 3B), but resveratrol mainly arrests cells in the G_1 and S phases[21–24]. This result suggests that the simple functional group substitution of a natural compound can change its anti-cancer activity.

ROS are one of the factors for the induction of cell death, which can be prevented by antioxidants[25, 26]. In this study, the production of ROS induced by 4′-chloro-3,5-dihydroxystilbene could be reduced by antioxidants (Figure 2B), but cell death could not be prevented (Figure 2C). Next, we showed that 4′-chloro-3,5-dihydroxystilbene induced apoptosis because it induced a sub-G_1 formation (Figure 3A), a decrease in mitochondria membrane potential (Figure 4B) and the degradation of PARP and procaspase-3 (Figure 5A). The decrease in MMP is one of the reasons for cell death[27], and the Bcl-2 family proteins are one of the groups that regulate MMP[14]. Resveratrol has been reported to induce apoptosis through the Bcl-2-mitochondria pathway[28], but 4′-chloro-3,5-dihydroxystilbene induced a reduction of both the Bcl-2 and the Bax proteins (Figure 4A). Therefore, the MMP was directly analyzed, and we showed that it was decreased by 4′-chloro-3,5-dihydroxystilbene (Figure 4B). PARP, a ubiquitous housekeeping enzyme, signals the presence of DNA damage by catalyzing the addition of ADP-ribose units to DNA, histones and various DNA repair enzymes and facilitates DNA repair[29]. In general, apoptosis is activated by PARP fragmentation, which occurs through activated caspase-3, therefore, we used the pan caspase inhibitor Z-VAD-FMK to block caspase activation. Although Z-VAD-FMK blocked the 4′-chloro-3,5-dihy-

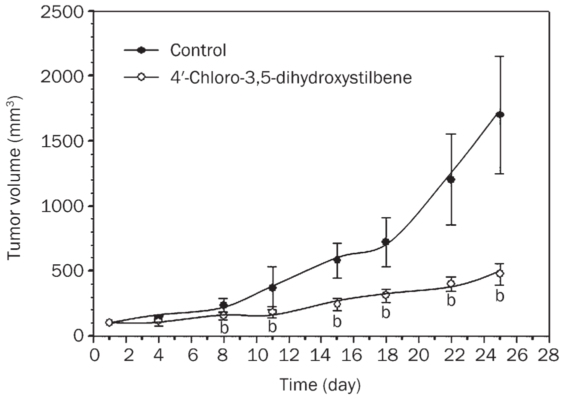

Figure 8. Anti-tumor effect of 4′-chloro-3,5-dihydroxystilbene *in vivo*. Five-week-old female nude mice were injected sc with 1×10^7 A549 cells in 100 μL of Matrigel in one rear flank. When the tumor volume reached 100 mm^3, mice were given vehicle (*n*=7, control) or 50 mg/kg of 4′-chloro-3,5-dihydroxystilbene (*n*=7) ip once daily from day 1 to 4 and day 7 to 10. Tumor volume was calculated by the formula mm^3=(the long axis)×(the short axis)^2/2. $^bP<0.05$ *vs* control.

droxystilbene-induced sub-G_1 formation (Figure 5B), it only slightly reduced the 4′-chloro-3,5-dihydroxystilbene-induced cell death (Figure 5E). This result suggests that there are other mechanisms besides apoptosis that induce cell death by 4′-chloro-3,5-dihydroxystilbene.

Due to the formation of vacuoles in cells after 4′-chloro-3,5-dihydroxystilbene treatment, we thought that autophagocytosis might have been induced. Autophagy is a process during which intracellular autophagosomes form and sequester cellular contents for degradation[18]. Microtubule-associated protein light chain 3 (LC3), the mammalian ortholog of yeast Atg8, is a characteristic protein that aggregates on the membrane of autophagic vesicles[12]. Autophagy can promote cell adaption and survival under stresses such as starvation and pathogen infection, but it can also induce cell death under some conditions. In this study, we showed that 4′-chloro-3,5-dihydroxystilbene induced autophagy in A549 cells because it caused LC3-II formation (Figure 6C) and GFP-LC3 aggregation (Figure 6D). Chemicals such as tamoxifen[30], sodium butyrate[31], rapamycin[32], and resveratrol[33] induce autophagic cell death, and provide a non-apoptotic cell death during cancer treatment. In contrast, autophagy has also been reported to be a protective mechanism in nelfinavir-induced cell death[34]. In this study, we showed that 4′-chloro-3,5-dihydroxystilbene induced the autophagic phenomenon. Like the apoptosis inhibitor, the autophagic inhibitor 3-MA and lysosomal protease inhibitor TPCK could partially reverse cell death (Figure 6E).

Since both 4′-chloro-3,5-dihydroxystilbene and the proteasome inhibitor MG132 cause specific vacuole formation, they may use the same mechanism. The ubiquitin-proteasome system is a new target for cancer therapy[35]. There are three types of peptidase activity in the proteolytic core of the 26S proteasome complex, and they include the chymotrypsin-like, trypsin-like and caspase-like activities[36]. In this study, we found that MG132 and 4′-chloro-3,5-dihydroxystilbene inhibited the chymotrypsin-like and caspase-like proteasome activities (Figure 7C), but they did not inhibit the trypsin-like proteasome activity (data not shown). Proteasome inhibition by 4′-chloro-3,5-dihydroxystilbene provides additional evidence of its cytotoxicity. Finally, we studied the anti-tumor activity *in vivo* and showed that 4′-chloro-3,5-dihydroxystilbene significantly retarded tumor growth in mice (Figure 8). These results suggest that 4′-chloro-3,5-dihydroxystilbene, a resveratrol derivative, has the potential to treat human non-small-cell lung adenocarcinoma through multiple mechanisms.

Acknowledgements

This work was supported by grants from the National Science Council of Taiwan (NSC97-2320-B-415-002) and the Buddhist Tzuchi Dalin General Hospital (DTCRD97(2)-08).

Author contribution

Yi-wen LIU and Kun-wei TSAI designed the research and wrote the paper. Jin-yi WU, Jia-jen SHEE, Yi-zhen LI, Ching-hsein CHEN, and Jing-jing CHUANG performed the research. Jin-yi WU contributed new reagents. Jia-jen SHEE and Yi-wen LIU analyzed the data.

References

1 Burns J, Yokota T, Ashihara H, Lean ME, Crozier A. Plant foods and herbal sources of resveratrol. J Agric Food Chem 2002; 50: 3337−40.

2 Hain R, Reif HJ, Krause E, Langebartels R, Kindl H, Vornam B, *et al*. Disease resistance results from foreign phytoalexin expression in a novel plant. Nature 1993; 361: 153−6.

3 Pace-Asciak CR, Hahn S, Diamandis EP, Soleas G, Goldberg DM. The red wine phenolics *trans*-resveratrol and quercetin block human platelet aggregation and eicosanoid synthesis: implications for protection against coronary heart disease. Clin Chim Acta 1995; 235: 207−19.

4 Djoko B, Chiou RY, Shee JJ, Liu YW. Characterization of immunological activities of peanut stilbenoids, arachidin-1, piceatannol, and resveratrol on lipopolysaccharide-induced inflammation of RAW 264.7 macrophages. J Agric Food Chem 2007; 55: 2376−83.

5 Belguendouz L, Fremont L, Linard A. Resveratrol inhibits metal ion-dependent and independent peroxidation of porcine low-density lipoproteins. Biochem Pharmacol 1997; 53: 1347−55.

6 Jang M, Cai L, Udeani GO, Slowing KV, Thomas CF, Beecher CW, *et al*. Cancer chemopreventive activity of resveratrol, a natural product derived from grapes. Science 1997; 275: 218−20.

7 Aggarwal BB, Bhardwaj A, Aggarwal RS, Seeram NP, Shishodia S, Takada Y. Role of resveratrol in prevention and therapy of cancer: preclinical and clinical studies. Anticancer Res 2004; 24: 2783−840.

8 Kundu JK, Surh YJ. Cancer chemopreventive and therapeutic potential of resveratrol: mechanistic perspectives. Cancer Lett 2008; 269: 243−61.

9 Sale S, Verschoyle RD, Boocock D, Jones DJ, Wilsher N, Ruparelia KC, *et al*. Pharmacokinetics in mice and growth-inhibitory properties of the putative cancer chemopreventive agent resveratrol and the synthetic analogue *trans* 3,4,5,4′-tetramethoxystilbene. Br J Cancer 2004; 90: 736−44.

10 Jemal A, Siegel R, Ward E, Hao Y, Xu J, Murray T, *et al*. Cancer statistics, 2008. CA Cancer J Clin 2008; 58: 71−96.

11 Chen LG, Hung LY, Tsai KW, Pan YS, Tsai YD, Li YZ, *et al*. Wogonin, a bioactive flavonoid in herbal tea, inhibits inflammatory cyclooxygenase-2 gene expression in human lung epithelial cancer cells. Mol Nutr Food Res 2008; 52: 1349−57.

12 Kabeya Y, Mizushima N, Ueno T, Yamamoto A, Kirisako T, Noda T, *et al*. LC3, a mammalian homologue of yeast Apg8p, is localized in autophagosome membranes after processing. Embo J 2000; 19: 5720−8.

13 Alexandre J, Batteux F, Nicco C, Chereau C, Laurent A, Guillevin L, *et al*. Accumulation of hydrogen peroxide is an early and crucial step for paclitaxel-induced cancer cell death both *in vitro* and *in vivo*. Int J Cancer 2006; 119: 41−8.

14 Sharpe JC, Arnoult D, Youle RJ. Control of mitochondrial permeability by Bcl-2 family members. Biochim Biophys Acta 2004; 1644: 107−13.

15 Okada H, Mak TW. Pathways of apoptotic and non-apoptotic death in tumour cells. Nat Rev Cancer 2004; 4: 592−603.

16 Mizushima N, Yamamoto A, Hatano M, Kobayashi Y, Kabeya Y, Suzuki K, *et al*. Dissection of autophagosome formation using Apg5-deficient mouse embryonic stem cells. J Cell Biol 2001; 152: 657−68.

17 Mizushima N, Yamamoto A, Matsui M, Yoshimori T, Ohsumi Y. *In vivo* analysis of autophagy in response to nutrient starvation using transgenic mice expressing a fluorescent autophagosome marker. Mol Biol Cell 2004; 15: 1101−11.

18 Kondo Y, Kanzawa T, Sawaya R, Kondo S. The role of autophagy in cancer development and response to therapy. Nat Rev Cancer 2005; 5: 726−34.

19 Kroemer G, Jaattela M. Lysosomes and autophagy in cell death control. Nat Rev Cancer 2005; 5: 886−97.

20 O'Sullivan MP, O'Leary S, Kelly DM, Keane J. A caspase-independent pathway mediates macrophage cell death in response to *Mycobacterium tuberculosis* infection. Infect Immun 2007; 75: 1984−93.

21 Kim YA, Lee WH, Choi TH, Rhee SH, Park KY, Choi YH. Involvement of p21$^{WAF1/CIP1}$, pRB, Bax and NF-kappaB in induction of growth arrest and apoptosis by resveratrol in human lung carcinoma A549 cells. Int J Oncol 2003; 23: 1143−9.

22 Schneider Y, Vincent F, Duranton B, Badolo L, Gosse F, Bergmann C, *et al*. Anti-proliferative effect of resveratrol, a natural component of grapes and wine, on human colonic cancer cells. Cancer Lett 2000; 158: 85−91.

23 Joe AK, Liu H, Suzui M, Vural ME, Xiao D, Weinstein IB. Resveratrol induces growth inhibition, S-phase arrest, apoptosis, and changes in biomarker expression in several human cancer cell lines. Clin Cancer Res 2002; 8: 893−903.

24 Bernhard D, Tinhofer I, Tonko M, Hubl H, Ausserlechner MJ, Greil R, *et al*. Resveratrol causes arrest in the S-phase prior to Fas-independent apoptosis in CEM-C7H2 acute leukemia cells. Cell Death Differ 2000; 7: 834−42.

25 Pelicano H, Carney D, Huang P. ROS stress in cancer cells and therapeutic implications. Drug Resist Updat 2004; 7: 97−110.

26 Valko M, Rhodes CJ, Moncol J, Izakovic M, Mazur M. Free radicals, metals and antioxidants in oxidative stress-induced cancer. Chem Biol Interact 2006; 160: 1−40.

27 Ly JD, Grubb DR, Lawen A. The mitochondrial membrane potential (deltapsi(m)) in apoptosis; an update. Apoptosis 2003; 8: 115−28.

28 Tinhofer I, Bernhard D, Senfter M, Anether G, Loeffler M, Kroemer G, *et al*. Resveratrol, a tumor-suppressive compound from grapes, induces apoptosis via a novel mitochondrial pathway controlled by Bcl-2. Faseb J 2001; 15: 1613−5.

29 Malanga M, Althaus FR. The role of poly(ADP-ribose) in the DNA damage signaling network. Biochem Cell Biol 2005; 83: 354−64.

30 Bursch W, Ellinger A, Kienzl H, Torok L, Pandey S, Sikorska M, *et al*. Active cell death induced by the anti-estrogens tamoxifen and ICI 164 384 in human mammary carcinoma cells (MCF-7) in culture: the role of autophagy. Carcinogenesis 1996; 17: 1595−607.

31 Shao Y, Gao Z, Marks PA, Jiang X. Apoptotic and autophagic cell death induced by histone deacetylase inhibitors. Proc Natl Acad Sci USA 2004; 101: 18030−5.

32 Takeuchi H, Kondo Y, Fujiwara K, Kanzawa T, Aoki H, Mills GB, *et al*. Synergistic augmentation of rapamycin-induced autophagy in malignant glioma cells by phosphatidylinositol 3-kinase/protein kinase B inhibitors. Cancer Res 2005; 65: 3336−46.

33 Opipari AW Jr, Tan L, Boitano AE, Sorenson DR, Aurora A, Liu JR. Resveratrol-induced autophagocytosis in ovarian cancer cells. Cancer Res 2004; 64: 696−703.

34 Gills JJ, Lopiccolo J, Tsurutani J, Shoemaker RH, Best CJ, Abu-Asab MS, *et al*. Nelfinavir, a lead HIV protease inhibitor, is a broad-spectrum, anticancer agent that induces endoplasmic reticulum stress, autophagy, and apoptosis *in vitro* and *in vivo*. Clin Cancer Res 2007; 13: 5183−94.

35 Bazzaro M, Lee MK, Zoso A, Stirling WL, Santillan A, Shih Ie M, *et al*. Ubiquitin-proteasome system stress sensitizes ovarian cancer to proteasome inhibitor-induced apoptosis. Cancer Res 2006; 66: 3754−63.

36 Kisselev AF, Callard A, Goldberg AL. Importance of the different proteolytic sites of the proteasome and the efficacy of inhibitors varies with the protein substrate. J Biol Chem 2006; 281: 8582−90.

Acta Pharmacologica Sinica (2010) 31: 93–101
© 2010 CPS and SIMM All rights reserved 1671-4083/10 $32.00
www.nature.com/aps

Original Article

Trichostatin A sensitizes cisplatin-resistant A549 cells to apoptosis by up-regulating death-associated protein kinase

Jun WU[1,2], Cheng-ping HU[1,*], Qi-hua GU[1], Ye-peng LI[1], Min SONG[1]

[1]Department of Respiratory Medicine, Xiangya Hospital, Central South University, Changsha 410008, China; [2] Institute of Respiration, Guangdong Medical College, Zhanjiang 524023, China

Aim: To investigate the apoptosis-inducing effect of trichostatin A (TSA) in the human lung adenocarcinoma cisplatin-resistant cell line (A549/CDDP) and to examine whether TSA can enhance sensitivity to cisplatin treatment and the underlying molecular mechanisms of such an enhancement.

Methods: Cell viability was evaluated using the Neutral Red assay. Apoptosis was assessed using Hoechst 33258 staining and flow cytometry analysis. Protein expression was detected by Western blotting. To determine the role of Death-associated protein kinase (DAPK) in TSA-induced apoptosis in the A549/CDDP cell line, cells were transfected with pcDNA3.1(+)-DAPK, which has a higher expression level of DAPK compared to endogenous expression, and DAPK activity was inhibited by both over-expression C-terminal fragment of DAPK which may competitive binding DAPK substrates to inhibit the function of DAPK and RNA interference.

Results: TSA induced apoptosis in both A549 cells and A549/CDDP cells. TSA enhanced the sensitivity of A549/CDDP cells to cisplatin, along with concomitant DAPK up-regulation. When DAPK was over-expressed, A549/CDDP cells became sensitive to cisplatin and the cytotoxicity of TSA could be increased. Moreover, the cytotoxicity of TSA could be alleviated by inhibition of DAPK activity by the expression of a recombinant C-terminal fragment of DAPK or RNA interference.

Conclusion: TSA induced sensitivity to cisplatin treatment in cisplatin-resistant A549 cells. The up-regulation of DAPK is one of the mechanisms mediating sensitization to TSA-induced apoptosis in cisplatin-resistant cells.

Keywords: trichostatin A; cisplatin-resistance; lung cancer; death-associated protein kinase

Acta Pharmacologica Sinica (2010) 31: 93-101; doi: 10.1038/aps.2009.183

Introduction

Lung cancer is one of the most common cancers worldwide. About 80% of lung cancers are non-small cell lung cancer (NSCLC). Although surgery remains the primary treatment at the early stages of cancer development, chemotherapy has been widely used in combination with surgery to treat lung cancer due to a high rate of tumor recurrence[1]. For NSCLC, clinical trial data have demonstrated that cisplatin adjuvant chemotherapy significantly improves patients' survival[1–4]. However, the overall 5-year survival rate remains less than 15%, primarily due to resistance to cisplatin in both the primary and recurrent tumors.

The mechanism of cisplatin-resistance has been associated with multiple factors, including changes in DNA repair and cellular accumulation and detoxification of the drug as well as inhibition of apoptosis[5]. In treating lung cancers, chemosensitivity to cisplatin is affected by changes in gene expression, including genes known to be associated with cell cycle regulation and apoptosis[6, 7].

Epigenetic alterations, such as histone acetylation and methylation of gene promoters, contribute to the changes in gene expression. The dys-regulation in epigenetics can affect the onset and progression of cancer[8, 9]. Histone deacetylase (HDAC) inhibitors have been known to promote transcription of genes required for cell differentiation and apoptosis; therefore, they may also induce differentiation and promote apoptosis in various tumors[10–13].

Trichostatin A (TSA) is one such HDAC inhibitor. It was originally isolated from *Streptomyces hygroscopicus* and identified as a fungistatic antibiotic that inhibits all class I and II HDACs. TSA can alter the expression of 2%–5% of genes[14] and can act as a chemo-sensitizer in cells of ovarian cancer, gastric cancer, and erythroleukemia[15–17]. Although the hyperacetylation of histones following inhibition of HDAC activ-

---

* To whom correspondence should be addressed.
E-mail huchengp28@yahoo.com.cn
Received 2009-06-30 Accepted 2009-11-19

ity could contribute to a general increase in gene expression including cell cycle inhibitor gene p21, p53, DAPK and the von Hippel–Lindau tumor suppressor genes as well as the pro-apoptotic genes Bax and Bad[18–21], the molecular mechanisms of TSA-sensitized cytotoxicity to chemotherapeutic drugs remain largely unknown.

Death-associated protein kinase (DAPK), a modulator of apoptosis, is a cytoskeleton-localized Ca^{2+}/calmodulin (CaM)-regulated serine/threonine kinase that modulates cell death[22]. Recently, it was demonstrated that impaired translation of DAPK mRNA was involved in the acquisition of cisplatin resistance in human cancer cells[23]. However, how it is involved in the development of resistance to chemotherapy in cancer cells is unknown. Based on these observations, we hypothesized that DAPK might play an important role in TSA-induced apoptosis in the cisplatin (CDDP)-resistant A549 lung cancer cell line (A549/CDDP).

In this study, we report that TSA enhances the chemosensitivity of A549/CDDP cells, which correlated with the up-regulation of DAPK.

Materials and methods

Cell culture

Cells from the lung cancer cell line A549 and the CDDP-resistant derivative A549/CDDP were gifts from Cell Center of Cell Culture (Central South University, Changsha, China). They were cultured in Dulbecco's modified Eagle's medium (DMEM, Gibco BRL, Grand Island, NY, USA) containing 100 μg/mL penicillin and 100 μg/mL streptomycin and supplemented with 10% calf blood serum (Sijiqing Laboratories, Hangzhou, China) at 37 °C in a humidified atmosphere with 5% CO_2. Then 2 μmol/L cisplatin (Qilu Pharmaceutical Co, Ltd, Shandong, China) was added to the medium of the A549/CDDP cell line. A549/CDDP cells were cultured in complete DMEM medium without cisplatin for 3 d before being used in experiments.

Plasmids and RNA interference

The pcDNA3.1(+)-DAPK, pcDNA3.1(+)-DCTP, pcDNA3.1(+) and pDsRed1-N1-U6 shRNA vectors were gifts from Dr Haitao ZHANG (Guangdong Medical College, China).

The synthetic sequences (sense, 5′-CGTAACCTATATCCTCCTAAGTTCAAGAGACTTAGGAGGATATAGGTTATTTTTTGGAAG-3′, antisense, 5′-GATCCTTCCAAAAAATAACCTATATCCTCCTAAGTCTCTTGAACTTAGGAGGATATAGGTTACGGTAC-3′) were annealed and cloned into pDsRed1-N1-U6 shRNA vectors.

Cellular transfection

The cells were transfected with different vectors using Lipofectamine 2000 transfection reagent (Invitrogen) according to the manufacturer's guidelines. Stable cell lines were cultured in medium containing 800 μg/mL G418 (Invitrogen). G418 concentration was reduced to 400 μg/mL after three weeks. Cells were treated with TSA or cisplatin and cell viability was determined by cytotoxicity assay using the Neutral Red assay.

Treatment with cisplatin or TSA

Both A549/DDP and A549 cells were cultured in 96-well plates (1.0×10^5 cells/well) and treated with different concentrations of cisplatin or TSA (Sigma, St Louis, MO, USA) at 37 °C in a humidified atmosphere with 5% CO_2 for 24 h.

Combined treatment with cisplatin and TSA

A549/CDDP cells were cultured in 24-well plates (3.0×10^5 cells/well) and treated with different concentrations of cisplatin and TSA at 37 °C in a humidified atmosphere with 5% CO_2 for 24 h. The cells were divided into three groups: the first group was cultured with different concentrations of cisplatin; the second group was cultured with 31.25 nmol/L TSA and cisplatin; and the third group was cultured with 62.5 nmol/L TSA and cisplatin.

Cell viability assays

Following the drug treatments described above, cytotoxicity assays were performed as described previously[24]. Briefly, the drug-containing medium from each well was replaced with 100 μL medium containing 50 mg/L Neutral Red for an additional 5-h incubation. Then, the cells were rinsed with PBS three times. A volume of 200 μL of 1% acetic acid/50% ethanol was added to each well to extract the dye from lysosomes of viable cells. The amount of dye was quantified at 540 nm using a Varioskan Flash Reader spectrophotometer (THERMO, USA). The inhibitory rate of cell growth was calculated as $[1\text{-}A_{\text{test group}}/A_{\text{control group}})]\times100\%$.

Flow cytometry analysis

The cells were collected by centrifugating at 1000 r/min for 5 min after treatment, washed twice in PBS and fixed with ice-cold 70% ethanol overnight. Prior to flow cytometry analysis, the fixed cells were washed once with PBS and incubated with 100 μg/mL propidium iodide (Sigma, USA) plus 200 μg/mL Rnase (Promega,USA) for 10 min. The DNA profile was analyzed by flow cytometry (EPICS XL, Coulter, Fullerton, CA, USA). The percent of apoptosis is calculated as the percentage of the sub-G_1 peak as determined by FACS analysis cell-cycle profile following propidium iodide staining[25].

Hoechst 33258 staining

Apoptosis was evaluated by *in situ* uptake of propidium iodide and Hoechst 33258 as described by McKeague *et al*[26]. In brief, after being treated with TSA, the cells were washed with PBS, and incubated in PBS containing 40 μg/mL propidium iodide and 2.5 μg/mL Hoechst 33258 (Sigma, USA) for 10 min. A volume of 500 μL of methanol:acetic acid (3:1) fixative was then added directly to each well. Cells were viewed under fluorescence microscopy (Nikon Eclipse ET2000-E, Japan). Four replicate wells were analyzed for each treatment by quantitative and qualitative examination of four random fields in each well. The apoptotic index was calculated from the number of apoptotic nuclei *vs* total number of nuclei in each visual field.

Western blot analysis of DAPK expression

The cells were collected, washed twice with PBS and incubated with cell decomposition buffer (pH 8.0) that contained 50 mmol/L Tris-HCl, 150 mmol/L NaCl, 5 mmol/L EDTA, 1% NP40, 0.05% PMSF, 2 μg/mL aprotinin (Sigma, USA), and 2 μg/mL leupeptin (Sigma, USA). The level of proteins was determined by Western blot with a DAPK monoclonal antibody (clone-55, Sigma, USA), anti-DAPK-phosphoserine308 monoclonal antibody (Sigma, USA), and anti-β-actin monoclonal antibody (clone AC-74, Sigma, USA). Primary antibodies were detected with goat anti-mouse or goat anti-rabbit antibodies conjugated to horseradish peroxidase using enhanced chemiluminescence (Beyotime Institute of Biotechnology, Jiangsu, China). Photographs were taken with the FluerChem SP8900 automatic photomicrograph system (ALPHA, USA) and analyzed.

Statistical analysis

Data are presented as mean±SD and were analyzed using the Student's *t*-test and Student-Newman-Keuls (SNK) test. $P<0.05$ was considered to be statistically significant.

Results

Effect of TSA on A549 cells and A549/CDDP cells

Consistent with our previous reports[27], here we showed that the IC_{50} of cisplatin to A549 cells and A549/CDDP cells was 2.36±0.10 μmol/L and 30.27±1.50 μmol/L, respectively (Figure 1A). A549/CDDP cells were 12.8 times more resistant than the parental A549 cells. Western blot analysis showed that A549/CDDP cells had a lower expression of DAPK than the A549 cell line (Figure 1B).

As shown in Figure 2A, morphological evaluation using Hoechst 33258/PI staining with fluorescence microscopy revealed a significant increase in the number of cells showing nuclear condensation and fragmentation after incubation with TSA for 24 h in both A549 and A549/CDDP cells.

A significant decrease in cell viability was detected by the Neutral Red assay after cells had been treated with different concentrations of TSA for 24 h. The assay showed that the IC_{50} of TSA in A549 cells and A549/CDDP cells was 418.66±25.12 nmol/L and 446.59±27.32 nmol/L, respectively ($P>0.05$, Figure 2B). Apoptosis was measured as the percentage of sub-G1 DNA content, as well as DNA condensation with Hoechst 33258 staining. The results showed that TSA induced apoptosis in a dose-dependent manner (Figure 3).

TSA enhances the sensitivity of A549/CDDP cells to cisplatin

Low concentrations of TSA (31.25 nmol/L and 62.5 nmol/L) had little effect on cell viability and apoptosis of A549/CDDP cells. The inhibitory rate of cell growth was 1.08% and 2.33%, respectively (Figure 4). Thus, these two concentrations of TSA were selected to determine whether TSA could sensitize A549/CDDP cells to cisplatin-induced apoptosis.

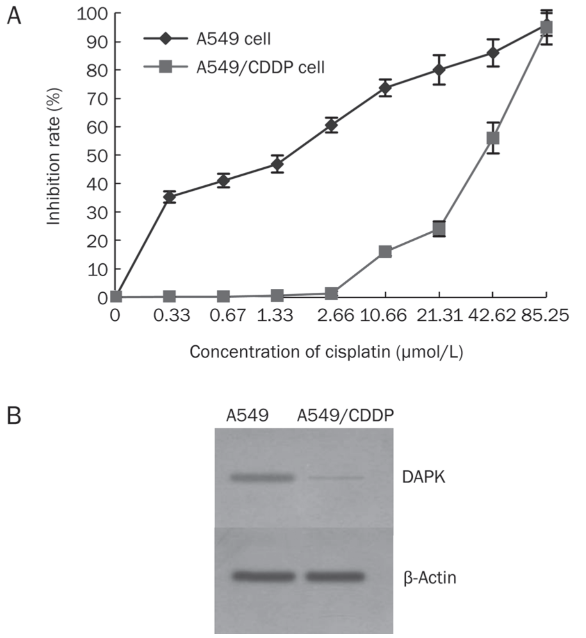

Figure 1. The sensitivity of A549 cells and A549/CDDP cells to cisplatin. (A) The effect of cisplatin on A549 cells and A549/CDDP cells. The plot shows the viability of A549 cells and A549/CDDP cells treated with indicated concentrations of cisplatin. The IC_{50} of cisplatin to A549 cells and A549/CDDP cells is 2.36±0.10 μmol/L and 30.27±1.50 μmol/L, respectively. (B) The expression level of DAPK in A549 cells and A549/CDDP cells.

The results showed that the IC_{50} of cisplatin to A549/CDDP cells was at 31.34±1.23 μmol/L in the absence of TSA, whereas the IC_{50} was 20.61±1.80 μmol/L and 18.48±0.70 μmol/L in the presence of 31.25 nmol/L and 62.5 nmol/L TSA, respectively ($P<0.05$ *vs* control) (Figure 4). The reverse fold was calculated according to the formula (IC_{50} of resisted-drug cell line)/(IC_{50} of combining reversal drug to resistanted-drug cell line).The results showed that the reverse fold was 1.52 and 1.70 in the presence of 31.25 nmol/L and 62.5 nmol/L TSA, respectively. This indicates that TSA treatment increases the sensitivity of A549/CDDP cells to cisplatin.

TSA up-regulates DAPK expression in A549/CDDP cells

The results showed that the expression of DAPK was elevated when A549/CDDP cells were treated with different concentrations of TSA for 24 h (Figure 5A). In addition, DAPK expression was up-regulated in a time-dependent manner (Figure 5C). The phosphorylation of Serine-308 deactivates DAPK and dephosphorylation relieves auto-inhibition and stimulates the pro-apoptotic activities of DAPK[28, 29]. Our results showed that the phosphorylation level of DAPK was unchanged or only slightly increased with TSA treatment (Figure 5A, 5C). However, the relative phosphorylation level actually decreased (Figure 5B, 5D). Furthermore, we confirmed that cisplatin had no effect on DAPK expression in A549/CDDP cells (Figure 6).

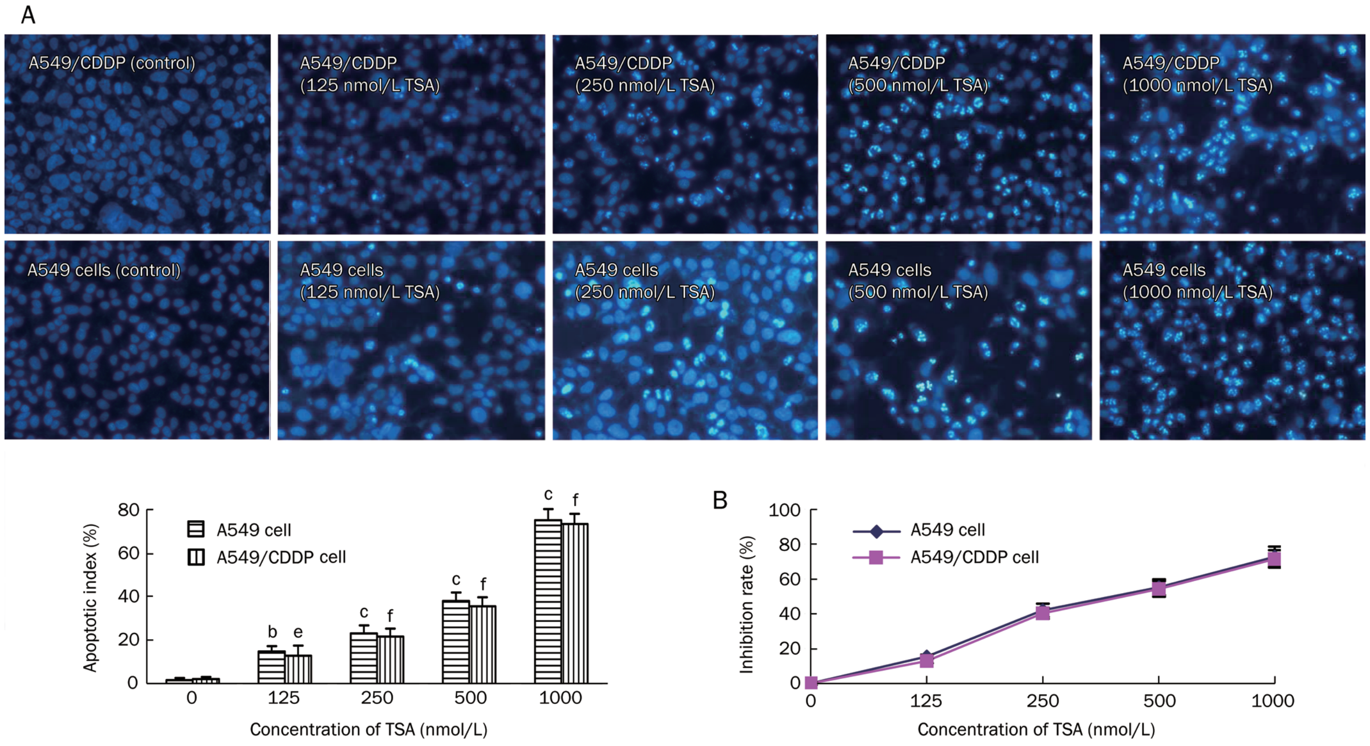

Figure 2. The effect of TSA on A549 cells and A549/CDDP cells. (A) Cells were treated by TSA for 24 h and stained with Hocest 33258/PI to measure apoptosis. Apoptotic cells were stained with light-blue and pictures were taken under a 400×objective. *n*=4. Mean±SD. $^{b}P<0.05$, $^{c}P<0.01$ *vs* A549 control group. $^{e}P<0.05$, $^{f}P<0.01$ *vs* A549/CDDP control group. (B) Cell viability is measured by Neutral Red assay after 24 h TSA treatment at indicated concentrations.

DAPK expression and its activity affect the sensitivity of A549/CDDP cells to cisplatin

Various expression and interference DAPK vectors were transfected into A549/CDDP cells and the effect of DAPK on the sensitivity of A549/CDDP cells to cisplatin was evaluated. DAPK expression increased in cells transfected by pcDNA3.1(+)-DAPK, whereas there was no significant difference in the DAPK level in cells transfected by pcDNA3.1(+)-DCTP or pcDNA3.1(+) as compared to un-transfected cells (Figure 7A). With TSA treatment, DAPK expression increased in cells transfected by pcDNA3.1(+)-DCTP, pcDNA3.1(+), or pcDNA3.1(+)-DAPK (Figure 7B). DCTP, a C-terminal fragment of DAPK, has been reported to mediate inhibition of DAPK activity[30, 31].

The results showed that the IC_{50} of TSA to A549/CDDP cells, transfected by different vectors, was 439.00±21.16 nmol/L (pcDNA3.1(+)), 1122.05±44.88 nmol/L (pcDNA3.1(+)-DCTP) and 220.45±9.927 nmol/L (pcDNA3.1(+)-DAPK), whereas the IC_{50} of TSA to A549/CDDP cells was 418.33±12.78 nmol/L. These data indicate that over-expression of DAPK increases the cytotoxicity of TSA ($P<0.05$ *vs* pcDNA3.1(+) control) (Figure 7C). When DAPK was suppressed by DCTP, the cytotoxicity of TSA was inhibited. Furthermore, our data also showed that the IC_{50} of cisplatin on the transfected A549/CDDP cell was 31.70±0.93 μmol/L (pcDNA3.1(+)), 47.95±1.06 μmol/L (pcDNA3.1(+)-DCTP) ($P<0.05$ *vs* control) and 19.05±0.57 μmol/L (pcDNA3.1(+)-DAPK) ($P<0.05$ *vs* control) (Figure 7D). These data suggest that DAPK could mediate A549/CDDP cell death induced by cisplatin.

In addition, endogenous DAPK expression was decreased by RNA interference to evaluate the role of DAPK in TSA- or cisplatin-induced A549/CDDP cell death (Figure 8A, 8B). These results show that knock-down of DAPK increases the IC_{50} of TSA on A549/CDDP cells to 869.08±34.73 nmol/L, whereas the IC_{50} of TSA on control A549/CDDP cells was 465.99±19.57 nmol/L (non-transfected group) and 485.87±23.16 nmol/L (control vector group) ($P<0.05$ *vs* control) (Figure 8C). Also, the same results were obtained with cisplatin treatment. The results showed that the IC_{50} of cisplatin on the three groups of A549/CDDP cells was 30.90±1.03 μmol/L (non-transfected group), 30.14±0.87 μmol/L (control vector-transfected group) and 40.63±1.00 μmol/L (RNA interference vector-transfected group, $P<0.05$ *vs* control vector-transfected group) (Figure 8D). These results suggest that inhibition of DAPK expression could cause A549/CDDP cell resistance to cisplatin-induced cell death.

Discussion

Apoptosis is usually deregulated in cancer because of increased expression of anti-apoptotic proteins or decreased expression of pro-apoptotic proteins. In human lung cancers, resistance to drug therapy has been often found to be associ-

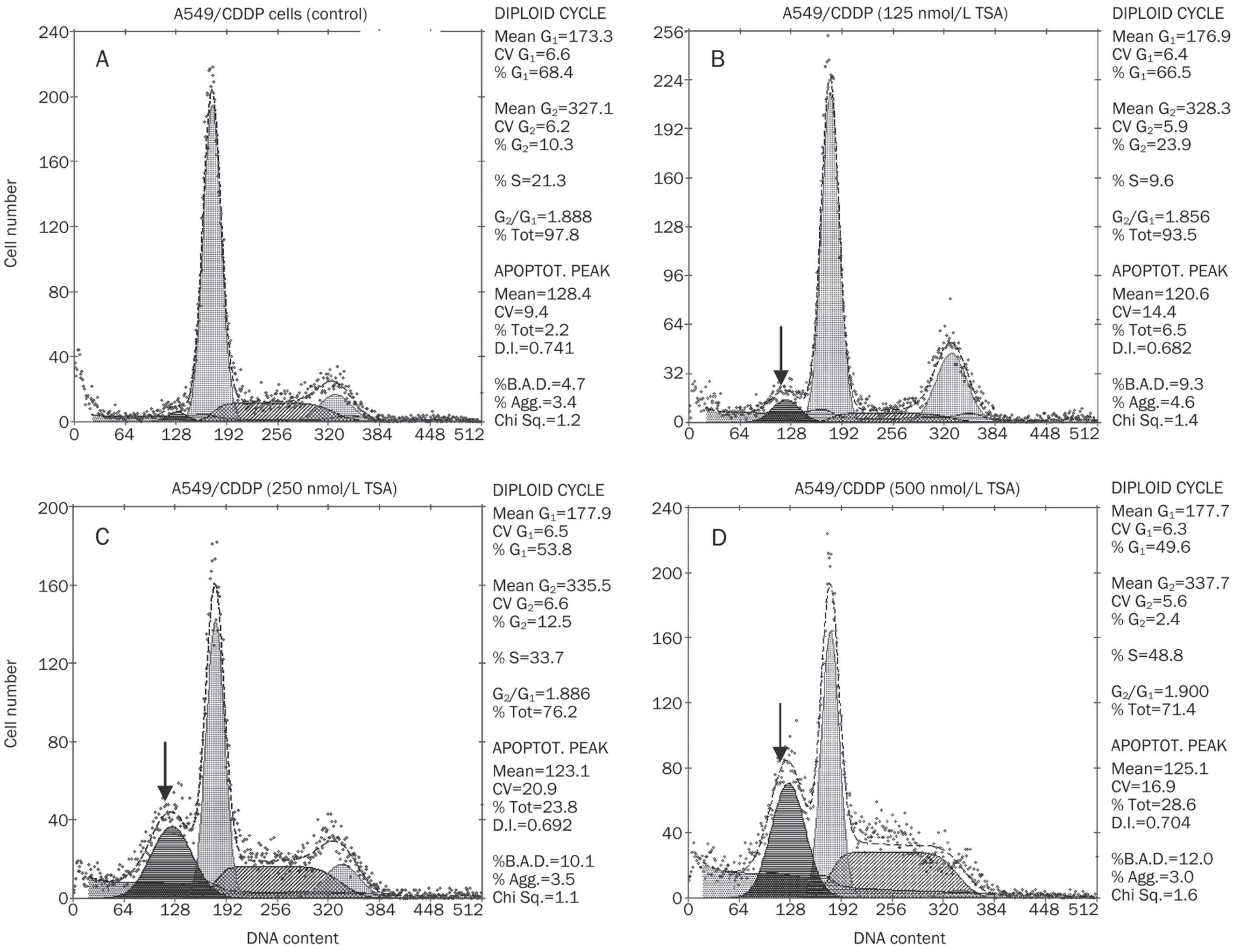

Figure 3. Apoptosis (sub-G_1) analyzed by flow cytometry. DNA profile was analyzed by PI staining with flow cytometry. The percent apoptosis is calculated as the percentage sub-G_1 peak as determined by cell-cycle analysis (arrow indicated sub-G_1 peak).

ated with the silencing of pro-apoptotic proteins including p16INK4a, Bax, and DAPK[32, 33]. Therefore, the up-regulation of apoptosis-inducing factors might be a promising approach to enhance the efficacy of chemotherapy treatment of multi-drug-resistant cancer.

HDAC inhibitors have emerged as a new class of anti-cancer therapeutic agents for both hematologic and solid cancers. More importantly, these inhibitors also display promising anti-tumor activity in clinical trials[34, 35]. A recent report showed that HDAC inhibitors induced apoptosis in cells of cisplatin-resistant ovarian cancer associated with overexpression of Bad[36]. Moreover, Muscolini *et al* also reported that an HDAC inhibitor overcome apoptosis resistance to cisplatin by restoring both p73 and Bax[15]. These results demonstrate that HDAC inhibitors overcome resistance to cisplatin by up-regulating the expression of apoptosis-inducing factors. However, less is known about the role of DAPK in the development of chemotherapy resistance in cancers cells, although DAPK has been reported to play an important role in IFN-γ, tumor necrosis factor (TNF)-α, or Fas-ligand induced apoptosis[37]. Previous studies have shown that DAPK was expressed at a basal level in A549 cells[33], but we found that DAPK was down-regulated in A549/CDDP cells, suggesting its involvement in the cisplatin resistance of A549/CDDP cells.

In this study, we found that TSA induced dose-dependent apoptosis in both A549 cells and cisplatin-resistant A549/CDDP cells. We also provide new evidence that A549 cells and cisplatin-resistant A549/CDDP cells undergo similar level of apoptosis with TSA treatment. However, a low concentration of TSA (31.25 nmol/mL) can sensitize A549/CDDP cells to cisplatin-induced cell death. We found that DAPK was up-regulated with TSA treatment in A549/CDDP cells in a dose- and time-dependent manner. DAPK is known to be negatively regulated by auto-phosphorylation of serine-308. The Serine308 phosphorylated DAPK has lower activity than its non-phosphorylated counterpart. The dephosphorylation of serine-308 on DAPK can activate DAPK and induce apoptosis[28, 29]. Our study demonstrated that the serine-308-

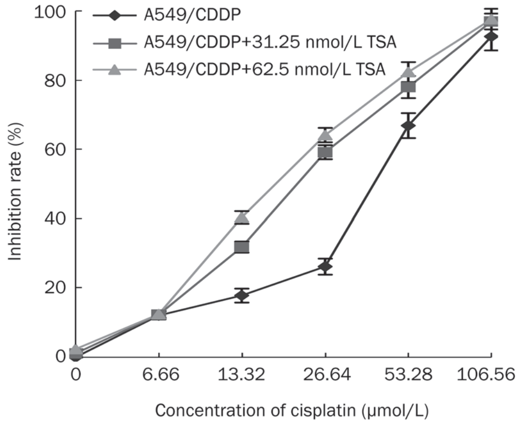

Figure 4. The effect of TSA on the sensitivity of A549/CDDP cells to cisplatin, The IC$_{50}$ of cisplatin to A549/CDDP cells is at 31.34±1.23 μmol/L in absence of TSA, while the IC$_{50}$ values are at 20.61±1.80 μmol/L and 18.48±0.70 μmol/L in presence of 31.25 nmol/L and 62.5 nmol/L TSA, respectively. n=4. Mean±SD.

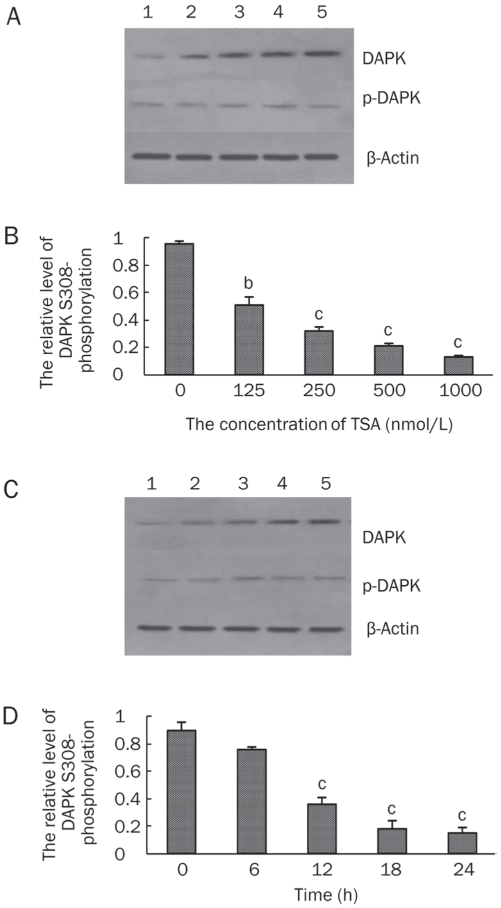

Figure 5. The effect of TSA on DAPK expression and serineS308-phosphorylation level in A549/CDDP cells. (A) Western blot analysis of DAPK expression and serineS308-phosphorylation level induced with indicated concentrations of TSA. 1: control; 2: A549/CDDP cells treated with 125 nmol/L TSA; 3: A549/CDDP cells treated with 250 nmol/L TSA; 4: A549/CDDP cells treated with 500 nmol/L TSA; 5: A549/CDDP cells treated with 1000 nmol/L TSA. (B) The relative level of DAPK serineS308-phosphorylation induced by indicated concentrations TSA was measured by gray scale calculating with AlphaEaseFC software. n=3. Mean±SD. $^{b}P<0.05$, $^{c}P<0.01$ *vs* control group. (C) The changes of DAPK expression and serineS308-phosphorylation level induced with 500 nmol/L TSA for different times were analyzed with Western blot method. 1: control; 2: A549/CDDP cells treated with 500 nmol/L TSA for 6 h; 3: A549/CDDP cells treated with 500 nmol/L TSA for 12 h; 4: A549/CDDP cells treated with 500 nmol/L TSA for 18 h; 5: A549/CDDP cells treated with 500 nmol/L TSA for 24 h. (D) The relative of DAPK serineS308-phosphorylation level induced with 500 nmol/L TSA for indicated time periods was measured by gray scale calculating with AlphaEaseFC software. n=3. Mean±SD. $^{c}P<0.01$ *vs* control group

phosphorylation level of DAPK remained about the same after TSA treatment (Figure 5B, 5D). This observation suggests that the relative ratio of serine308 phosphorylated DAPK to the total DAPK decreased with TSA treatment. Therefore, TSA induces elevation of the active form of DAPK, since the level of Serine308 phosphorylated DAPK remained unchanged as compared to the untreated control. However, DAPK expression did not significantly change in A549/CDDP cells treated with cisplatin.

Cell-transfection experiments reconfirmed that increased DAPK expression increased A549/CDDP cells sensitivity to TSA or cisplatin. We also observed that transient DAPK treatment could promote cell apoptosis. To determine whether DAP kinase contributes to cisplatin resistance, we generated a stable-transfection cell line, A549/CDDP/DAPK, which had a higher expression level of DAPK than A549/CDDP cells. Our data showed that stable expression of DAPK in A549/CDDP could sensitize cells to TSA or cisplatin treatment, which is consistent with previous reports that DAPK is a pro-apoptotic factor and may be involved in the mechanisms increasing the chemosensitivity of anticancer drugs of 5-fluorouracil, paclitaxel and TNF-related apoptosis-inducing ligand[16, 33]. In addition to auto-phosphorylation on Serine-308, the activity of DAPK is also regulated by its C-terminal fragment (DCTP). It has been reported that the expression of DCTP can suppress DAPK activity without affecting the protein level of DAPK. Moreover, DCTP was shown to inhibit PC12 apoptosis induced by DAPK[30]. Our results are consistent with these reports in that DCTP did not affect the protein level of DAPK in A549/DCCP cells. Although Raveh *et al* suggested that the C-terminus of DAPK could block the interaction between DAPK and its substrate and suppress the DAPK activity[31], additional information, such as a structural model, is needed to demonstrate the mechanism. In addition, we also demonstrated that inhibition of DAPK expression causes A549/CDDP resistance to cisplatin-induced cell death. Thus, DAPK expression might contribute to the increased sensitivity of A549/CDDP cells to cisplatin.

In summary, our present results reveal that treatment with TSA induces apoptosis of A549/CDDP cells and enhances the sensitivity of the cells to cisplatin, possibly mediated by the up-regulation of DAPK.

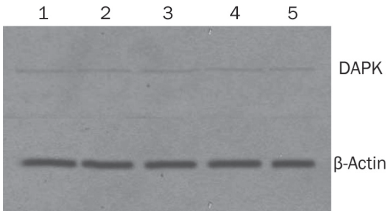

Figure 6. The effect of cisplatin on DAPK expression in A549/CDDP cells. 1: control; 2: A549/CDDP cells treated with 6.66 μmol/L cisplatin; 3: A549/CDDP cells treated with 13.32 μmol/L cisplatin; 4: A549/CDDP cells treated with 26.64 μmol/L cisplatin; 5: A549/CDDP cells treated with 53.28 μmol/L cisplatin.

Acknowledgments

We thank Dr Hai-tao ZHANG for providing us with the DAPK expression vector.

Author contribution

Cheng-ping HU and Jun WU designed research; Jun WU and Min SONG performed research; Qi-hua GU contributed new analytical tools and reagents; Ye-peng LI analyzed data;Cheng-ping HU and Jun WU wrote the paper.

References

1 Pignon JP, Tribodet H, Scagliotti GV, Douillard JY, Shepherd FA, Stephens RJ, *et al*. Lung adjuvant cisplatin evaluation: a pooled analysis by the LACE Collaborative Group. J Clin Oncol 2008; 26: 3552–9.

2 Bria E, Cuppone F, Cecere FL, Milella M, Nisticò C, Cognetti F, *et al.* Adjuvant chemotherapy for non-small cell lung cancer. J Thorac Oncol 2007; 2: S7–11.

3 Winton T, Livingston R, Johnson D, Rigas J, Johnston M, Butts C, *et al*.

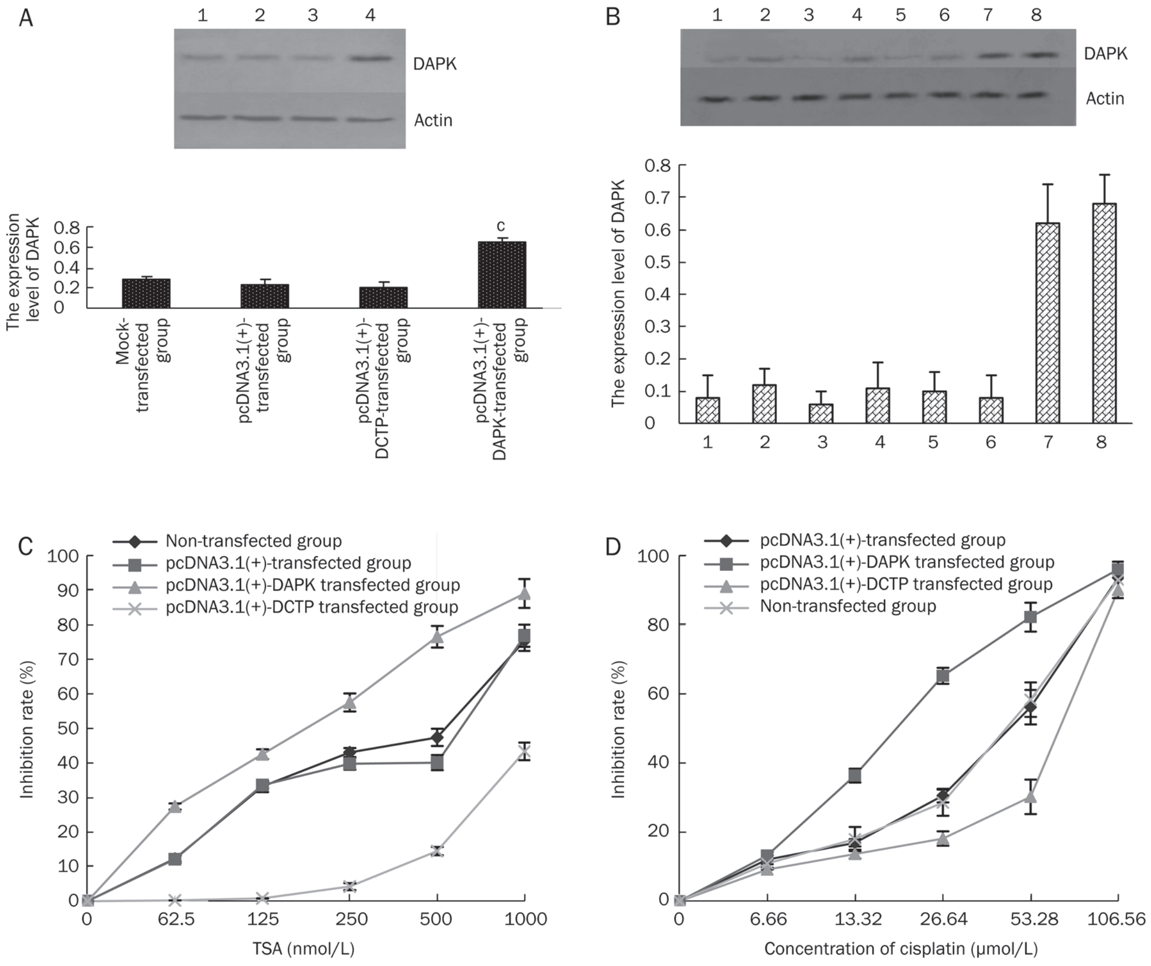

Figure 7. The sensitivity of A549/CDDP cells to TSA and cisplatin is affected by DAPK expression and activity. (A) Western blot analysis of DAPK expression in A549/CDDP cells transfected by various expression vectors. *n*=3. Mean±SD. $^{c}P<0.01$ *vs* control group. 1: non-transfected group; 2: pcDNA3.1(+)-tranfected group; 3: pcDNA3.1(+)-DCTP-tranfected group; 4: pcDNA3.1(+)-DAPK-transfected group. (B) Western blot analysis of DAPK expression in TSA-treated A549/CDDP cells transfected by various expression vectors. 1: non-transfected group in absence of TSA; 2: non-transfected group induced by 500 nmol/L TSA; 3: pcDNA3.1(+)-tranfected group in absence of TSA; 4: pcDNA3.1(+)-tranfected group induced by 500 nmol/L TSA; 5: pcDNA3.1(+)-DCTP-tranfected group in absence of TSA; 6: pcDNA3.1(+)-DCTP-tranfected group induced by 500 nmol/L TSA; 7: pcDNA3.1(+)-DAPK-transfected group in absence of TSA; 8: pcDNA3.1(+)-DAPK-transfected group induced by 500 nmol/L TSA. (C) The sensitivity of A549/CDDP cells to TSA affected by DAPK expression. *n*=4. Mean±SD. (D) The sensitivity of A549/CDDP cells to cisplatin affected by DAPK expression. *n*=4. Mean±SD.

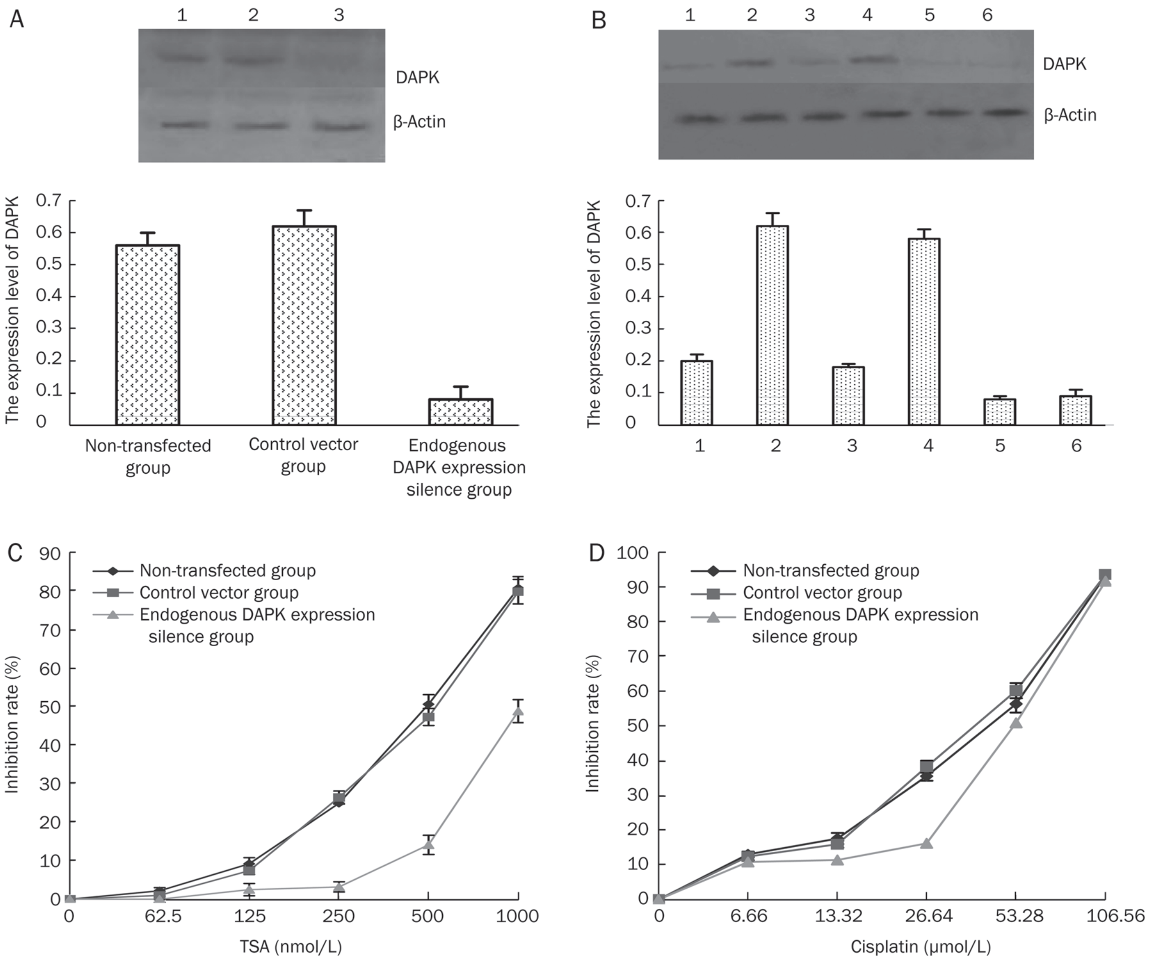

Figure 8. TSA changes the sensitivity of A549/CDDP cells to the cisplatin treatment by affecting DAPK expression. (A) Western blot analysis of DAPK expression in A549/CDDP cells transfected by interference vectors. 1: Non-transfected group 2: control vector group; 3: Endogenous DAPK expression silence group. (B) Western blot analysis of DAPK expression in TSA-treated A549/CDDP cells transfected by interference vectors. 1: non-transfected group in absence of TSA; 2: non-transfected group induced by 500 nmol/L TSA; 3: Control vector group in absence of TSA; 4: Control vector group induced by 500 nmol/L TSA; 5: Endogenous DAPK expression silence group in absence of TSA; 6: Endogenous DAPK expression silence group induced by 500 nmol/L TSA. (C) Effect of endogenous DAPK expression silence on TSA-induced A549/CDDP cells death. *n*=4. Mean±SD. (D) Effect of endogenous DAPK expression silence on cisplatin-induced A549/CDDP cells death. *n*=4. Mean±SD.

Vinorelbine plus cisplatin *vs* observation in resected non-small-cell lung cancer. N Engl J Med 2005; 352: 2589−97.

4 Douillard JY, Rosell R, De Lena M, Carpagnano F, Ramlau R, Gonzáles-Larriba JL, *et al*. Adjuvant vinorelbine plus cisplatin versus observation in patients with completely resected stage IB-IIIA non-small-cell lung cancer (Adjuvant Navelbine International Trialist Association ANITA): a randomised controlled trial. Lancet Oncol 2006; 7: 719−27.

5 Stewart DJ. Mechanisms of resistance to cisplatin and carboplatin. Crit Rev Oncol Hematol 2007; 63: 12−31.

6 Losert D, Pratscher B, Soutschek J, Geick A, Vornlocher HP, Müller M, *et al*. Bcl-2 downregulation sensitizes non small cell lung cancer cells to cisplatin, but not to docetaxel. Anticancer Drugs 2007; 18: 755−61.

7 Yang H, Fu JH, Hu Y, Huang WZ, Zheng B, Wang G, *et al*. Influence of siRNA targeting survivin on chemosensitivity of H460/cDDP lung cancer cells. J Int Med Res 2008; 36: 734−47.

8 Esteller M. Cancer epigenomics: DNA methylomes and histone-modification maps. Nat Rev Genet 2007; 8: 286−98.

9 Jones PA, Baylin SB. The epigenomics of cancer. Cell 2007; 128: 683−92.

10 Mariadason JM. HDACs and HDAC inhibitors in colon cancer. Epigenetics 2008; 3: 28−37.

11 Kumagai T, Wakimoto N, Yin D, Gery S, Kawamata N, Takai N, *et al*. Histone deacetylase inhibitor, suberoylanilide hydroxamic acid (Vorinostat, SAHA) profoundly inhibits the growth of human pancreatic cancer cells. Int J Cancer 2007; 121: 656−65.

12 Roy S, Packman K, Jeffrey R, Tenniswood M. Histone deacetylase inhibitors differentially stabilize acetylated p53 and induce cell cycle arrest or apoptosis in prostate cancer cells. Cell Death Differ 2005; 12: 482−91.

13 Habold C, Poehlmann A, Bajbouj K, Hartig R, Korkmaz KS, Roessner A, *et al*. Trichostatin A causes p53 to switch oxidative-damaged colorectal cancer cells from cell cycle arrest into apoptosis. J Cell Mol Med 2008; 12: 607−21.

14 Van Lint C, Emiliani S, Verdin E. The expression of a small fraction of cellular genes is changed in response to histone hyperacetylation.

Gene Exp 1996; 5: 245–53.

15 Muscolini M, Cianfrocca R, Sajeva A, Mozzetti S, Ferrandina G, Costanzo A, *et al*. Trichostatin A up-regulates p73 and induces Bax-dependent apoptosis in cisplatin-resistant ovarian cancer cells. Mol Cancer Ther 2008; 7: 1410–9.

16 Zhang X, Yashiro M, Ren J, Hirakawa K. Histone deacetylase inhibitor, trichostatin A, increases the chemosensitivity of anticancer drugs in gastric cancer cell lines. Oncol Rep 2006; 16: 563–8.

17 Karagiannis TC, Smith AJ, El' Osta A. Radio- and chemo-sensitization of human erythroleukemic K562 cells by the histone deacetylase inhibitor trichostatin A. Hell J Nucl Med 2004; 7: 184–91.

18 Rosato RR, Almenara JA, Grant S. The histone deacetylase inhibitor MS-275 promotes differentiation or apoptosis in human leukemia cells through a process regulated by generation of reactive oxygen species and induction of p21$^{CIP1/WAF1}$ 1. Cancer Res 2003; 63: 3637–45.

19 Sawa H, Murakami H, Ohshima Y, Sugino T, Nakajyo T, Kisanuki T, *et al*. Histone deacetylase inhibitors such as sodium butyrate and trichostatin A induce apoptosis through an increase of the bcl-2-related protein Bad. Brain Tumor Pathol 2001; 18: 109–14.

20 Kim MS, Kwon HJ, Lee YM, Baek JH, Jang JE, Lee SW, *et al*. Histone deacetylases induce angiogenesis by negative regulation of tumor suppressor genes. Nat Med 2001; 7: 437–43.

21 Zhang HT, Feng ZL, Wu J, Wang YJ, Guo X, Liang NC, *et al.* Sodium butyrate-induced death-associated protein kinase expression promote Raji cell morphological change and apoptosis by reducing FAK protein levels. Acta Pharmacol Sin 2007; 28: 1783–90.

22 Cohen O, Kimchi A. DAP-kinase: from functional gene cloning to establishment of its role in apoptosis and cancer. Cell Death Differ 2001; 8: 6–15.

23 Bai T, Tanaka T, Yukawa K, Umesaki N. A novel mechanism for acquired cisplatin-resistance: suppressed translation of death-associated protein kinase mRNA is insensitive to 5-aza-2′-deoxycitidine and trichostatin in cisplatin-resistant cervical squamous cancer cells. Int J Oncol 2006; 28: 497–508.

24 Grare M, Mourer M, Fontanay S, Regnouf-de-Vains JB, Finance C, Duval RE. *In vitro* activity of para-guanidinoethylcalix4 arene against susceptible and antibiotic-resistant Gram-negative and Gram-positive bacteria. J Antimicrob Chemother 2007; 60: 575–81.

25 Zhang HT, Wu J, Zhang HF, Zhu QF. Efflux of potassium ion is an important reason of HL-60 cells apoptosis induced by *Tachyplesin* J. Acta Pharmacol Sin 2006; 27: 1367–74.

26 McKeague AL, Wilson DJ, Nelson J. Staurosporine-induced apoptosis and hydrogen peroxide-induced necrosis in two human breast cell lines. Br J Cancer 2003; 88: 125–31.

27 Zhang MC, Hu CP, Chen Q. Effect of down-regulation of survivin gene on apoptosis and cisplatin resistance in cisplatin resistant human lung adenocarcinoma A549/CDDP cells. Zhonghua Zhong Liu Za Zhi 2006; 28: 408–12.

28 Shamloo M, Soriano L, Wieloch T, Nikolich K, Urfer R, Oksenberg D. Death-associated protein kinase is activated by dephosphorylation in response to cerebral ischemia. J Biol Chem 2005; 280: 42290–9.

29 Jin Y, Blue EK, Gallagher PJ. Control of death-associated protein kinase (DAPK) activity by phosphorylation and proteasomal degradation. J Biol Chem 2006; 281: 39033–40.

30 Pelled D, Raveh T, Riebeling C, Fridkin M, Berissi H, Futerman AH, *et al*. Death-associated protein (dap) kinase plays a central role in ceramide-induced apoptosis in cultured hippocampal neurons. J Biol Chem 2002; 277: 1957–61.

31 Raveh T, Berissi H, Eisenstein M, Spivak T, Kimchi A. A functional genetic screen identifies regions at the C-terminal tail and death-domain of death-associated protein kinase that are critical for its proapoptotic activity. Proc Natl Acad Sci USA 2000; 97: 1572–7.

32 Gessner C, Liebers U, Kuhn H, Stiehl P, Witt C, Schauer J, *et al*. BAX and p16INK4A are independent positive prognostic markers for advanced tumour stage of non small cell lung cancer. Eur Respir J 2002; 19: 134–40.

33 Tang X, Wu W, Sun SY, Wistuba II, Hong WK, Mao L. Hypermethylation of the death-associated protein kinase promoter attenuates the sensitivity to TRAIL-induced apoptosis in human non-small cell lung cancer cells. Mol Cancer Res 2004; 2: 685–91.

34 Shankar S, Srivastava RK. Histone deacetylase inhibitors: mechanisms and clinical significance in cancer: HDAC inhibitor-induced apoptosis. Adv Exp Med Biol 2008; 615: 261–98.

35 Lee MJ, Kim YS, Kummar S, Giaccone G, Trepel JB. Histone deacetylase inhibitors in cancer therapy. Curr Opin Oncol 2008; 20: 639–49.

36 Strait KA, Warnick CT, Ford CD, Dabbas B, Hammond EH, Ilstrup SJ. Histone deacetylase inhibitors induce G_2-checkpoint arrest and apoptosis in cisplatinum-resistant ovarian cancer cells associated with overexpression of the Bcl-2-related protein Bad. Mol Cancer Ther 2005; 4: 603–11.

37 Cohen O, Inbal B, Kissil JL, Raveh T, Berissi H, Spivak-Kroizaman T, *et al*. DAP-kinase participates in TNF-α- and Fas-induced apoptosis and its function requires the death domain. J Cell Biol 1999; 146: 141–8.

npg
Acta Pharmacologica Sinica (2010) 31: 102–110
© 2010 CPS and SIMM All rights reserved 1671-4083/10 $32.00
www.nature.com/aps

Original Article

HIF-1α links β-adrenoceptor agonists and pancreatic cancer cells under normoxic condition

Heng-tong HU[1], Qing-yong MA[1,*], Dong ZHANG[1], Su-gang SHEN[1], Liang HAN[1], Ya-dong MA[2], Ruo-fei LI[3], Ke-ping XIE[4]

[1]Department of Hepatobiliary Surgery, The First Affiliated Hospital of Medical College, Xi'an Jiaotong University, Xi'an 710061, China;
[2]Department of Urinary Surgery, The Second Affiliated Hospital of Medical College, Xi'an Jiaotong University, Xi'an 710004, China;
[3]Department of Osteological Surgery, The Second Affiliated Hospital of Medical College, Xi'an Jiaotong University, Xi'an 710004, China;
[4]Department of Cancer Biology, University of Texas MD Anderson Cancer Center, 1515 Holcombe Boulevard, Houston, Texas 77030, USA

Aim: To examine whether β-adrenoceptor (β-AR) agonists can induce hypoxia-inducible factor (HIF)-1α accumulation which then up-regulate the expression of its target genes in pancreatic cancer cells at normoxia, and to further elucidate the mechanism involved.
Methods: Pulse-chase assay, RT-PCR, and Western blot were employed to detect the effects of β-AR agonists and antagonists, siRNA as well as several inhibitors of signal transduction pathways on MIA PaCa2 and BxPC-3 pancreatic cancer cells.
Results: Treatment of pancreatic cancer cell lines with β-AR agonists led to accumulation of HIF-1α and then up-regulated expression of its target genes independently of oxygen levels. The induction was partly or completely inhibited not only by β-AR antagonists but also by inhibitors of PKA transduction pathways and by siHIF-1α. Both β1-AR and β2-AR agonists produced the above-mentioned effects, but β2-AR agonist was more potent.
Conclusion: Activation of β-AR receptor transactivates epidermal growth factor receptor (EGFR) and then elicites Akt and ERK1/2 in a PKA-dependent manner, which together up-regulate levels of HIF-1α and downstream target genes independently of oxygen level. Our data suggest a novel mechanism in pancreatic cancer cells that links β-AR and HIF-1α signaling under normoxic conditions, with implications for the control of glucose transport, angiogenesis and metastasis.

Keywords: β-adrenergic receptor; epidermal growth factor receptor; hypoxia-inducible factor-1α; protein kinase A; ERK1/2; Akt; hypothalamic-pituitary-adrenal axis; pancreatic cancer

---

Acta Pharmacologica Sinica (2010) 31: 102–110; doi: 10.1038/aps.2009.181; published online 28 December 2009

Introduction

Stress can alter immune, neurochemical, and endocrine functions, as well as tumor development, but the underlying biological mechanisms are not understood[1]. In response to stressors, activation of the hypothalamic-pituitary-adrenal (HPA) axis leads to release of catecholamines, glucocorticoids and other stress hormones from the adrenal gland as well as from brain and sympathetic nerve terminals. Chronic exposure to these hormones can promote tumor cell growth, migration and invasive capacity, and can stimulate angiogenesis via the induction of pro-angiogenic cytokines.

The effects of catecholamines are primarily mediated by β-adrenergic receptors (β-ARs). These receptors are known to modulate diverse cellular processes including the growth and differentiation of tumor cells. Three β-ARs subtypes have been reported (β1-AR, β2-AR, and β3-AR) though β2-AR appears to be the major mediator of the biological effects of catecholamines[2, 3]. Recent studies in human cancer cell lines and in animal models have shown that adenocarcinoma growth in lung, pancreas and colon is under β-adrenergic control. The β-ARs are widely expressed in adipose tissue, blood, brain, heart, lung, nose, pancreas, skeletal muscle, skin, and vessel. A normal pancreatic duct epithelial cell line and several pancreatic cancer cell lines express β1 and/or β2-ARs as well as epidermal growth factor receptor (EGFR) including Panc-1, BXPC-3, PC-2, PC-3, and HPDE6-c7. Moreover, the EGFR is frequently over-expressed in pancreatic cancer[4–6].

HIF-1 is a heterodimer composed of an inducible HIF-1α subunit and a constitutively-expressed HIF-1β subunit. HIF-1α levels and activity are regulated by cellular oxygen concentration. In human cancer cells, both intratumor hypoxia and genetic alterations affecting signal transduction pathways lead to increased HIF-1 activity, which in turn promotes angiogenesis, metabolic adaptation, and other critical

---

* To whom correspondence should be addressed.
E-mail qyma56@mail.xjtu.edu.cn
Received 2009-06-10 Accepted 2009-11-17

aspects of tumor progression[7]. Moreover, pancreatic cancer is thought to have a poor blood supply and to be able to survive and proliferate under severe hypoxia. This has been ascribed to hypoxia-induced over-expression of HIF-1α in pancreatic cancer[8], indeed malfunction of the HIF-1α signaling network has been associated with several types of cancer.

HIF-1α protein degradation is regulated by O_2-dependent prolyl hydroxylation, which targets the protein for ubiquitylation by E3 ubiquitin-protein ligases. These ligases contain the von Hippel–Lindau tumour-suppressor protein (VHL), which binds specifically to hydroxylated HIF-1α. Ubiquitylated HIF-1α is rapidly degraded by the proteasome at normoxia[9]. However, most pancreatic cancer cell lines (75%) have been shown to weakly accumulate HIF-1α protein under normoxic conditions[10]. It reveals that the existence of HIF-1α protein in the presence of oxygen is not unimaginable.

Agonist binding to the β-AR receptor can transactivate EGFR leading to phosphorylation of Akt and ERK1/2, which are known to promote tumor progression[11, 12]. Coincidently, HIF-1α expression and activity are regulated by major signal transduction pathways including PI3K/Akt/mTOR and Ras/Raf/ERK1/2[7]. We therefore surmised that β-AR activation might lead to HIF-1α accumulation in pancreatic cancer cells via above-mentioned pathways.

To investigate this possibility, we analyzed HIF-1α levels in pancreatic cancer cells exposed to β-AR ligands or hypoxia and elucidate the underlying mechanism involved. As a result, we report that β-AR activation leads to up-regulation of HIF-1α independently of oxygen levels by Akt and ERK1/2. The both pathways are elicited from EGFR, whose transactivation requires PKA. All of above-mentioned pathways further promote the expression of downstream target genes which are responsible for glucose transport, angiogenesis, and metastasis through the heart of this regulatory system-HIF-1α.

Materials and methods

Cell cultures and treatments

The MIA PaCa2 (with K-ras mutation) and BxPC-3 (without K-ras mutation) human pancreatic cancer cell lines (obtained from the American Tissue Type Collection, USA) were maintained in Dulbecco's modified Eagle's medium (DMEM, GIBCO, USA) supplemented with penicillin (100 U/mL), streptomycin (100 μg/mL), 0.1 mmol/L nonessential amino acids, 0.2 mmol/L glutamine, 1 mmol/L pyruvate, and 10% fetal bovine serum (FBS) and incubated in a 95% air/5% CO_2 humidified atmosphere at 37 ºC. Cells were grown to 80% confluence prior to treatment. For exposure to hypoxia experiment, cells were incubated at 37 ºC in a sealed chamber flushed with 3% O_2, 5% CO_2, and 92% N_2. To strengthen the effect, "serum free hypoxic medium" (less than 0.1% O_2) was added to cells during hypoxia. The special medium was achieved using an anaerobic jar equipped with Anaero Pack (O_2 absorbing and CO_2 generating agent, Mitsubishi Gas Chemical, Tokyo, Japan). As normoxic control, serum free medium was added to cells in normoxic condition (21% O_2).

For studies of β-AR agonists, antagonists, other signal transduction pathway inhibitors and hypoxia, media was replaced with basal medium 6 h prior to drug addition and hypoxia treatment. All these drugs were obtained from the Sigma Chemical Co (USA). Inhibitor concentrations employed were LY294002 (10 μmol/L, PI3K inhibitor), PD98059 (10 μmol/L, MAPKK inhibitor), SQ22536 (10 μmol/L, adenyl cyclase inhibitor), H-89 (10 μmol/L, PKA inhibitor), AG1478 (10 μmol/L, selective inhibitor of EGFR-specific tyrosine kinase), metoprolol (10 μmol/L, selective β1-AR antagonist), butaxamine (10 μmol/L, selective β2-AR antagonist) or propranolol (10 μmol/L, nonselective β-AR antagonist). These drugs were dissolved in dimethylsulfoxide (DMSO) and added to the cells 30 min prior to treatment with β-AR agonists xamoterol (1 μmol/L, selective β1-AR agonist), salbutamol (1 μmol/L, selective β2-AR agonist), isoproterenol (1 μmol/L, β-ARs agonist) or with the adenyl cyclase activator forskolin (1 μmol/L). Epidermal Growth Factor (EGF, 100 ng/mL) was a positive control.

Measurements of cyclic AMP levels

MIA PaCa2 and BxPC-3 cells were seeded in complete medium to reach 80% confluence. The media were replaced with basal medium for 6 h; cells were then pre-incubated for 30 min with 1 mmol/L 3-isobutyl-methylxanthine (IBMX) (Sigma). After 3 washes with basal medium, cells were treated with metoprolol (10 μmol/L), butaxamine (10 μmol/L), propranolol (10 μmol/L) or SQ22536 (10 μmol/L). Inhibitors were dissolved in dimethylsulfoxide (DMSO) and added to the cells in fresh basal medium containing 1 mmol/L IBMX 30 min before treatment with xamoterol (1 μmol/L), salbutamol (1 μmol/L) or isoproterenol (1 μmol/L) for 10 min. Forskolin (1 μmol/L) was used as a positive control. After three washes in cold PBS, the concrete operation of cAMP assay was performed following the manufacturer's instructions.

siRNA Assay

MIA PaCa2 and BxPC-3 cells 2×10^6 were transfected with siRNA targeted against HIF-1α (100 nm/L) or control siRNA (Qiagen) using Lipofectamine 2000 (Invitrogen). Cells were recovered overnight before starvation, followed by treatment with xamoterol (1 μmol/L) or salbutamol (1 μmol/L) for 12 h, and then harvested for real-time PCR.

Pulse-chase assay

After starvation, both cells were treated with β1-AR or β2-AR agonist for 12 h, hypoxia (3% oxygen, 12 h) or normoxia (12 h), and then washed and incubated in methionine/cysteine-free DMEM supplemented with 0.5% FBS and 50 μCi/mL of [^{35}S] methionine/cysteine Promix (Amersham Biosciences, Buckinghamshire, UK) for 15 min, chased with cold methionine and cysteine, lysed and immunoprecipitated using antibodies against HIF-1α.

RT-PCR (Reverse transcription-polymerase chain reaction) and Real-time PCR

Total RNA from MIA PaCa2 and BxPC-3 cells was isolated using TRIzol reagent (GIBCO BRL). First-strand cDNA was synthesized from 2 μg of total RNA using the RevertAid Kit (Fermentas MBI, USA). The PCR primers designed for β1-AR (236 bp) were forward 5′-CGCCTCTTCGTCTTCTTCAACTG-3′ and reverse 5′-ACATCGTCGTCGTCGTCGTC-3′; for β2-AR (526 bp) were forward 5′-TGCCAATGAGACCTGCTGTGAC-3′ and reverse 5′-TGTGTTGCCGTTGCTGGAGTAG-3′; for HIF-1α (81 bp) were forward 5′-CGCAAGTCCTCAAAGCACAGTTAC-3′ and reverse 5′-GCAGTGGTAGTGGTGGCATTAGC-3′; for VEGF (140 bp) were forward CTGGGCTGTTCTCGCTTCG-3′ and reverse 5′-CTCTCCTCTTCCTTCTCTTCTTCC-3′; for MMP-9 (111 bp) were forward 5′-TGGTCCTGGTGCTCCTGGTG-3′ and reverse 5′-GCTGCCTGTCGGTGAGATTGG-3′; for GLUT-1 (124 bp) were forward 5′-CCGCTTCCTGCTCATCAACC-3′ and reverse 5′-CATCATCTGCCGACTCTCTTCC-3′; for CXCR-4 (180 bp) were forward 5′-ACGCCACCAACAGTCAGAGG-3′ and reverse 5′-GGAACACAACCACCCACAAGTC-3′; for β-actin (179 bp) were forward 5′-ATCGTGCGTGACATTAAGGAGAAG-3′ and reverse 5′-AGGAAGGAAGGCTGGAAGAGTG-3′. The concrete operation of RT-PCR and real-time PCR assay was performed following the manufacturer's instructions. The housekeeping gene β-actin was used as an internal reference.

Western blotting

For immunodetection, the primary antibody preparations were as following: anti-HIF-1α (120 kDa, 1:1000, CHEMICON, USA); β1-AR (51 kDa, 1:500, ABCAM, UK); β2-AR (60 kDa, 1:500, ABCAM, UK); p-EGFR (Tyr1173, Tyr1608, Tyr992, 175 kDa, 1:1000, CST, USA); EGFR (175 kDa, 1:1000, CST, USA); p-ERK1/2 (Thr202, Tyr204, 42/44 kDa, 1:1000, CST, USA); ERK1/2 (42/44 kDa, 1:1000, CST, USA); p-Akt (Ser473, 60 kDa, 1:1000, CST, USA); Akt (60 kDa, 1:1000, CST, USA); β-actin (43 kDa, 1:1000, SANTA CRUZ, USA); and the secondary antibody preparation was either anti-rabbit or anti-mouse (1:2000, PIERCE, USA). After drug treatments, the concrete operation of Western blot assay was performed following the manufacturer's instructions. And the results were visualized using the ECL Western blotting substrate (Pierce) and photographed by GeneBox (SynGene).

Statistics and graphics

Data from at least 3 independent experiments with duplicate determinations are expressed as means±SEM. One-way ANOVA and Tukey-Kramer multiple comparison tests were applied. Statistical significance was set at $P<0.05$.

Results

β1-AR and β2-AR expression in pancreatic cancer cells

We first addressed whether pancreatic cancer cells express the β-ARs. RT-PCR and Western blot analysis confirmed that β1-AR and β2-AR were expressed in both MIA PaCa2 and BxPC-3 cells. The levels of β2-AR mRNA and protein in both cell lines were significantly higher than of β1-AR, indicating that β2-AR may be the predominant β-adrenergic receptor in these pancreatic cancer cells (Figure 1).

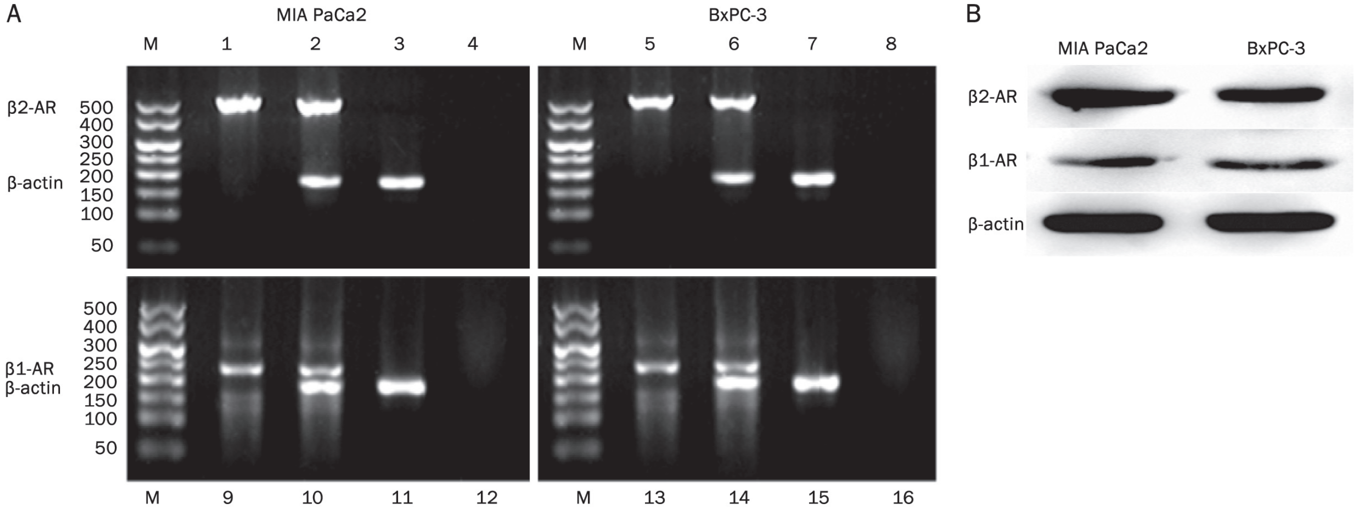

Figure 1. Expression of β1-AR and β2-AR at mRNA and protein levels in MIA PaCa2 and BxPC-3 cells. (A) Expression of mRNA for β1-AR, β2-AR, and β-actin in MIA PaCa2 and BxPC-3 cells. Total RNA was isolated and subjected to RT-PCR. The β1-AR primers amplified a 236 bp fragment, the β2-AR primers amplified a 526 bp fragment and the β-actin amplified a 179 bp fragment. Lane 1 MIA PaCa2, β2-AR primers; Lane 2 MIA PaCa2, β2-AR and β-Actin primers; Lane 3 MIA PaCa2, β-Actin primers; Lane 5 BxPC-3, β-AR2 primers; Lane6 BxPC-3, β2-AR, and β-actin primers; Lane7 BxPC-3, β-actin primers; Lane 9 MIA PaCa2, β1-AR primers; Lane 10 MIA PaCa2, β1-AR and β-actin primers; Lane 11 MIA PaCa2, β-actin primers; Lane 13 BxPC-3, β1-AR primers; Lane 14 BxPC-3, β1-AR, and β-actin primers; Lane15 BxPC-3, β-actin primers; Lane 4, 8, 12, and 16 are negative controls without MMLV reverse transcriptase. (B) Expression of protein for β1-AR, β2-AR and β-actin in MIA PaCa2 and BxPC-3 cells. Total lysate from untreated cells was subjected to Western blot with anti-β1-AR and anti-β2-AR antibody. The house keeping protein β-actin was used as a control to ensure equal loading of the protein.

β-AR agonists and hypoxia lead to HIF-1α protein other than mRNA accumulation in pancreatic cancer cells

Both kinds of cells were treated with xamoterol, salbutamol or isoproterenol for 0, 4, 8, 12, and 24 h. 3% Oxygen was used as a positive control. Some previous studies have reported stimulatory, inhibitory or no effects of hypoxia on HIF-1α mRNA in different cells[13–15]. But in the present study, the mRNA levels of HIF-1α were not significantly affected by either hypoxia or β-AR agonists using real-time PCR assay (Data not shown), indicating that HIF-1α protein accumulation was not due to enhanced mRNA transcription, but rather to later events.

In the absence of β-AR agonists and hypoxia (*t*=0 timepoint) HIF-1α protein was barely detectable in either cell line by means of Western blot. Unlike the mRNA level, exposure (0−24 h) to either β-AR agonists or hypoxia (3% oxygen) led to HIF-1α protein accumulation in both cell lines. After 12 h of exposure to hypoxia and β-AR agonists, HIF-1α levels reached the peak and then decreased. The elevations were statistically significant in all cases ($P<0.05$). And the induction efficiencies were 3% oxygen>isoproterenol>salbutamol>xamoterol in both cell types (Figure 2). Because induction by the selective β2-AR agonist salbutamol was greater than with β1-AR-specific xamoterol, these results confirm that β2-AR activation is the predominant mediator of HIF-1α, although simultaneous activation of both β1-AR and β2-AR produced greater accumulation than either alone.

HIF-1α protein stability was analyzed by pulse-chase assay. Newly synthesized HIF-1α protein declined after 20 min and was hardly detectable after 60 min in the presence of β1-AR or β2-AR agonist and hypoxia. The normoxia control showed HIF-1α protein half-life was merely 5 min. In order to examining the effects of β-AR agonists on HIF-1α protein synthesis, 10 μg/mL cycloheximide (Chx, the protein translation inhibitor) was used. As a result, HIF-1α protein expression was reduced by cycloheximide indicating that HIF-1α accumulation is also dependent on ongoing protein synthesis (Figure 3).

β-AR agonists and hypoxia induce the expression of HIF-1α target genes

To investigate whether β-AR agonists and hypoxia modulate the expression of known HIF-1α target genes, both kinds of cells were treated with drugs either activating or antagonizing β-adrenergic receptors for 12 h and we also explored drugs targeting associated signaling pathways and siRNA targeting HIF-1α. These treatments were applied alone or in combinations. Hypoxia (3% oxygen, 12 h) was as a positive control.

3% Oxygen and the β-AR agonists xamoterol, salbutamol and isoproterenol all increased mRNA levels of VEGF, MMP-9, GLUT-1, and CXCR4 compared to controls ($P<0.05$). The relative efficiencies of inducing effect were isoproterenol> salbutamol>xamoterol, again indicating that β2-AR is the main mediator of effect. Interestingly, β-AR agonists increased

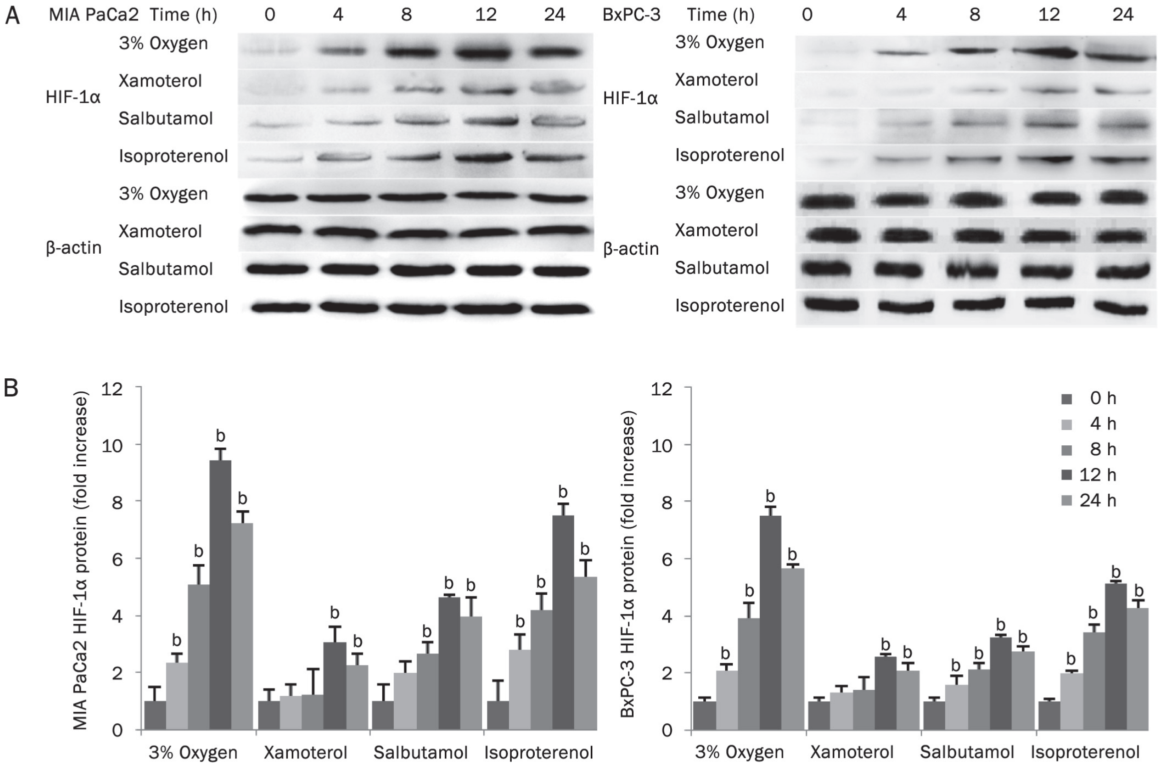

Figure 2. Time course of HIF-1α protein levels following treatment with β-AR agonists. (A) MIA PaCa2 and BxPC-3 cells were treated with xamoterol, salbutamol and isoproterenol; 3% oxygen provided a positive control. Protein levels were determined using Western blotting. (B) Quantitation of Western blotting data. Data from at least 3 independent experiments with duplicate determinations are expressed as means±SEM versus controls. $^{b}P<0.05$ vs control.

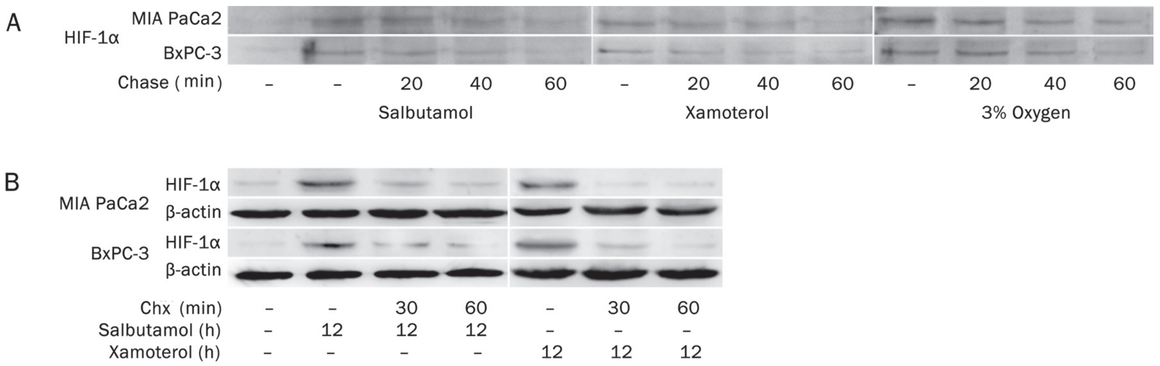

Figure 3. Pulse-chase assay and cycloheximide (Chx) inhibition test. (A) In both cells, newly synthesized HIF-1α protein declined after 20 min and was hardly detectable after 60 min in the presence of β1-AR or β2-AR agonist and hypoxia. (B) HIF-1α protein expression was reduced by cycloheximide indicating that HIF-1α accumulation is also dependent on ongoing protein synthesis.

GLUT-1 mRNA independently of oxygen levels: the encoded enzyme is thought to be a key mediator of glycolysis triggered by HIF-1α at hypoxia[16].

When applied alone, the inhibitors failed to exert detectable effects on HIF-1α target gene expression; nevertheless, they partly or completely blocked the effects of β-AR agonists. These results indicate that the expression of these downstream genes may be under controls of pathways including PKA, PI3K, and ERK1/2. Of all these inhibitors, the blocking effects of PD98059 and LY294002 were weaker than AG1478, indicating that PI3K and ERK1/2 together take part in this process, because the two pathways can be activated by EGFR signaling[17]. To investigate whether the up-regulation of these genes in the presence of hypoxia or β-AR agonists was dependent on HIF-1α transcriptional activity, siRNA targeting HIF-1α was used. For ruling out the off-target effect, two siRNA sequences (Qiagen, No̲ 1 SI00436338 and No̲ 2 SI02778090) were used. Both siRNAs efficiently blocked β-AR-agonists-induced enhancement of HIF-1α protein expression in both kinds of cells, whose inhibition rate ranged similarly from 47% to 61%. The No̲ 2 sequence was selected to carry out the whole study subsequently (Figure 4). siHIF-1α attenuated the effects of β-AR agonists and led to decrease of these genes (Figure 5).

β-AR agonists and forskolin increase cAMP accumulation

To determine whether β-AR agonists modulate cAMP levels in pancreatic cancer cells, both kinds of cells were treated with different drugs alone or in combinations for 10 min. Forskolin provided a positive control. β-AR antagonists were added to the cells 30 min prior to addition of agonists.

Adenyl cyclase activator forskolin or with β-AR agonists (xamoterol, salbutamol or isoproterenol) significantly increased the accumulation of cAMP: levels were increased 16.77, 7.06, 9.97, and 14.90-fold in MIA PaCa2 and 14.85, 6.34, 8.03, and 13.40-fold in BxPC-3 compared to controls ($P<0.05$). The relative efficiencies of inducing cAMP accumulation were forskolin>isoprotereno l>salbutamol>xamoterol. Alone, β-AR antagonists and SQ22536 failed to influence cAMP accumulation but could completely block the effects of β-AR agonists (Figure 6). β2-AR still mainly mediated the effect in this assay.

β-AR agonists and EGF increase EGFR phosphorylation

EGFR transactivation was caused by binding of β-AR agonist to its receptor[5]. Both cells were treated with β-AR ligands alone or in combinations for 10 min. The β-AR antagonists and H-89 were added to the cells for 30 min before the addition of agonists; EGF (100 ng/mL) was as a positive control.

β-AR agonists failed to increase EGFR expression levels. However, increased phosphorylation was recorded at 3 EGFR sites subjected to tyrosine phosphorylation. All of β-AR agonists increased phosphorylation at Tyr1173, Tyr1608 and Tyr992 to varying degrees ($P<0.05$). The relative efficiencies of inducing effect were EGF>isoproterenol>salbutamol>xamoterol, which were completely blocked by β-AR antagonists and H-89 (Figure 7). It indicated that β-ARs agonists elicit transactivation of EGFR reflected by phosphorylation at Tyr1173, Tyr1608, and Tyr992 and this transactivation process requires the key regulatory site-PKA.

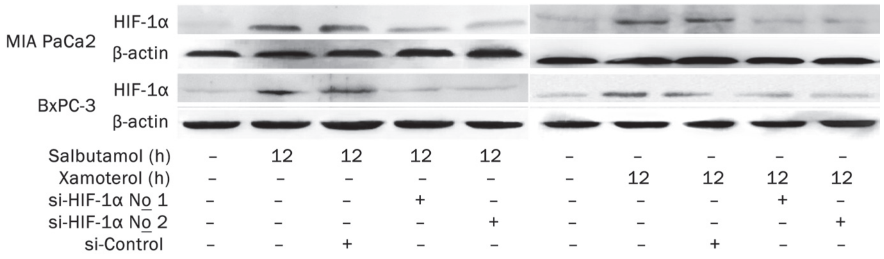

Figure 4. siRNA inhibition assay. Both siRNAs efficiently blocked β-AR-agonists-induced enhancement of HIF-1α protein expression in both kinds of cells, whose inhibition rate ranged similarly from 47% to 61%.

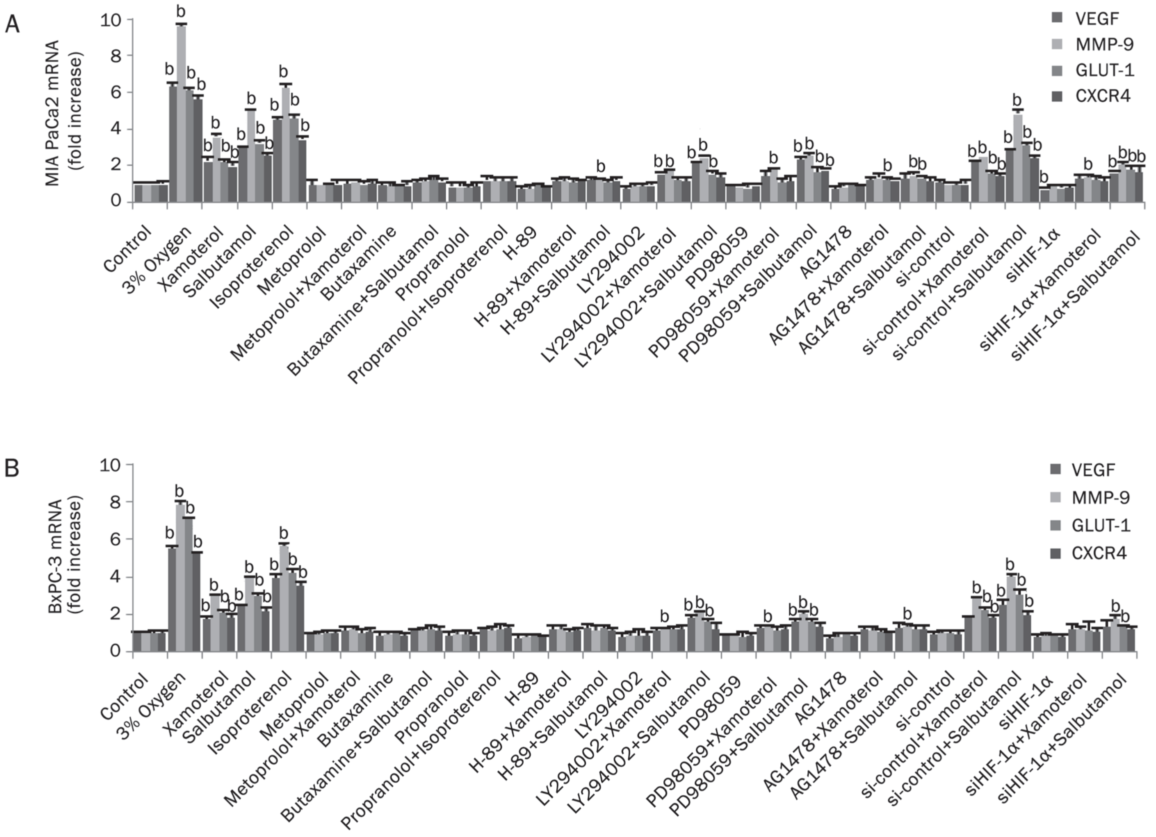

Figure 5. Changes in VEGF, MMP9, GLUT-1, and CXCR4 mRNA levels in (A) MIA PaCa2 and (B) BxPC-3 cells following several treatments as indicated below the panel and 3% oxygen provided a positive control. Cells were treated with the drugs alone or in combinations as indicated below the histogram and mRNA levels were quantified by Real-time PCR. Data from at least 3 independent experiments with duplicate determinations were are expressed as means±SEM *vs* controls. $^{b}P<0.05$ vs control.

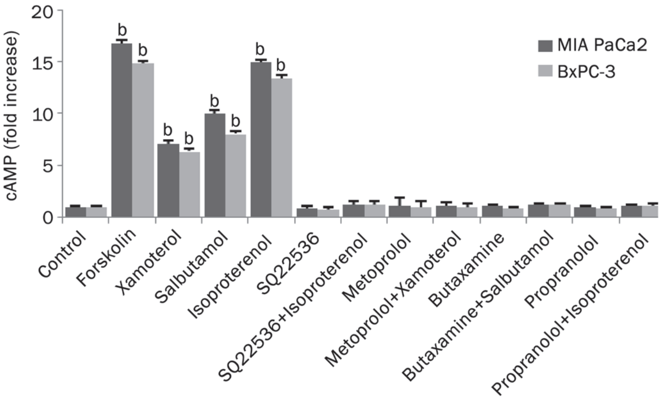

Figure 6. Intracellular cAMP levels following treatment with β-AR agonists and antagonists. MIA PaCa2 and BxPC-3 cells were treated with a range of activators and inhibitors as indicated below the histogram; forskolin provided the positive control. Data from at least 3 independent experiments with duplicate determinations were expressed as means±SEM *vs* controls. $^{b}P<0.05$ *vs* control.

β-AR agonists and hypoxia increase the expression of p-ERK1/2, p-Akt, and HIF-1α

Hypoxia can up-regulate both p-ERK1/2 and p-Akt[18–20]. To investigate whether β-AR agonists also activate ERK and Akt pathways, both kinds of cells were treated with different drugs or their combinations for 10 min and then levels of p-ERK1/2 and p-Akt were measured, whereas levels of HIF-1α were determined at 12 h after treatment. β-AR antagonists and other inhibitors were added to the cells 30 min prior to addition of agonists. Hypoxia (3% oxygen) provided a positive control.

While hypoxia and β-AR agonists failed to increase total ERK1/2 and Akt expression levels, they increased p-ERK1/2, p-Akt and HIF-1α. The increases were statistically significant ($P<0.05$) in all cases. The order of efficiency was 3% oxygen> isoproterenol>salbutamol>xamoterol, again supporting the contention that these effects are mediated principally by β2-AR.

Alone, LY294002 and PD98059 failed to completely block the increases of HIF-1α in response to β-AR agonists ($P<0.05$), indicating that HIF-1α is simultaneously under control of both PI3K and ERK1/2 pathways. As reported by Ratushny *et al* that the two pathways can be activated by EGFR signaling[17], AG1478 showed a complete inhibitory effect on p-ERK1/2, p-Akt and HIF-1α in the presence of β-AR agonists, so did H89 (Figure 8). In addition, we have demonstrated that β-AR

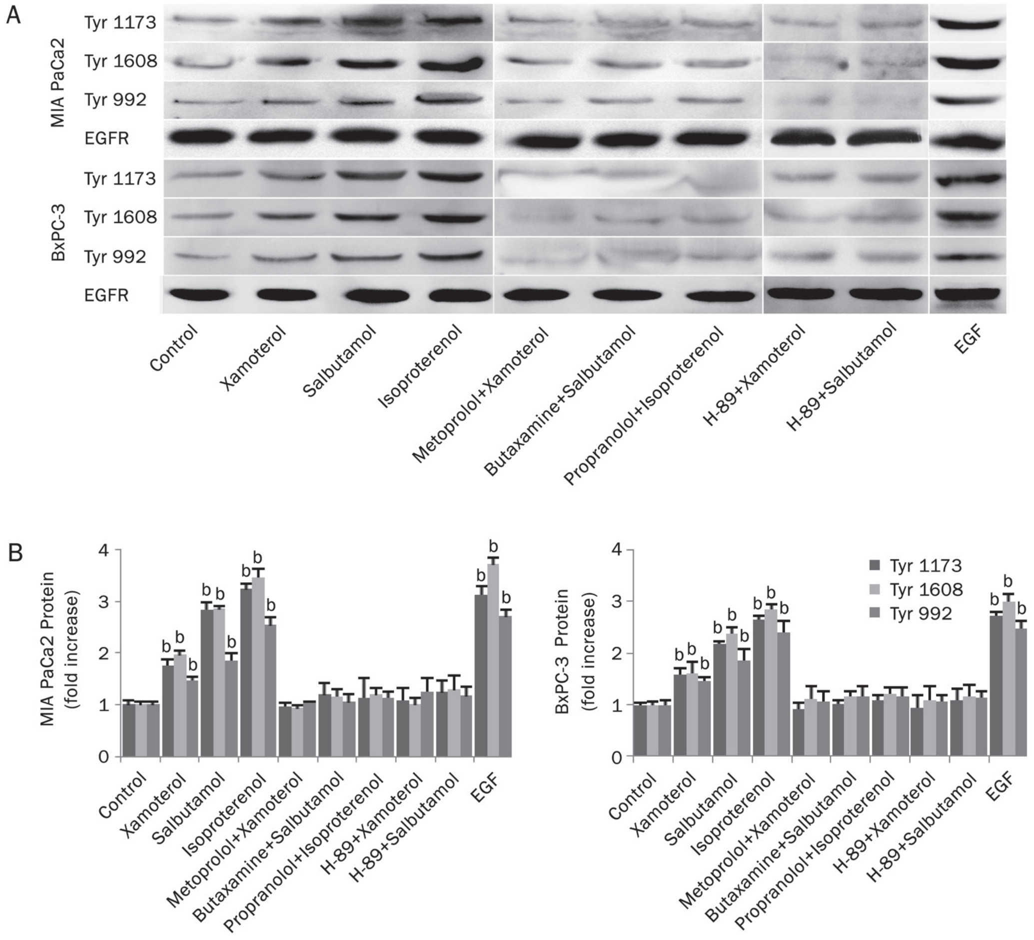

Figure 7. Phosphorylation of EGFR (Tyr 1173, Tyr1608, Tyr992) in response to β-AR agonists and antagonists. (A) MIA PaCa2 and BxPC-3 cells were treated with drugs as indicated below the panel and tyrosine phosphorylation at 3 sites within EGFR was assessed using specific antibodies. EGF provided the positive control. (B) Quantitation of Western blotting. Data from at least 3 independent experiments expressed as means±SEM *vs* controls. $^{b}P<0.05$ *vs* control.

agonists-induced EGFR phosphorylation is dependent on PKA. Altogether, these finding suggest that β-AR agonists can transactivate EGFR and then elicite Akt and ERK1/2 in a PKA-dependent manner, which together up-regulate levels of HIF-1α and downstream target genes independently of oxygen.

Discussion

The transcriptional regulator HIF-1α is crucial for solid tumor growth and survival, and over-expression has been reported in many human tumors. Indeed, HIF-1α over-expression has been linked to poor patient outcome in several kinds of carcinoma[21]. We report here that hypoxia up-regulates the accumulation of HIF-1α in MIA PaCa2 and BxPC-3 pancreatic cancer cells through posttranscriptional mechanisms. Expression of its known target genes was also increased in response to hypoxia, as was the phosphyorylation of ERK1/2 and Akt, indicating that hypoxia may lead to HIF-1α accumulation and then up-regulate its downstream target genes to promote pancreatic cancer progression through the both pathways.

Stress was defined physiologically as the state in which the autonomic nervous system (ANS) and the HPA axis are co-activated[22]. The fight-or-flight stress responses in the ANS or the defeat/withdrawal responses associated with HPA activation result in the secretion of catecholamines (norepinephrine and epinephrine) from sympathetic neurons and the adrenal medulla and of cortisol from the adrenal cortex[23, 24]. Most of the effects of catecholamines are mediated by β-ARs. In addition, it has been suggested that β-ARs play a prominent role in pancreatic cancer, and other studies have implicated β-ARs as important mediators of cancer growth and/or invasiveness in adenocarcinoma of lungs, prostate, colon, stomach, breast, and ovary[25]. In the present study, we showed that β-AR receptor occupancy could up-regulate downstream genes in pancreatic cancer cells, which are responsible for glucose transport, angiogenesis, and metastasis. Of all β-ARs, β2-AR is the main mediator of the effect.

While HIF-1α protein can be weakly detectable in the presence of oxygen and obviously increased at hypoxia condition according to prior report[10], our data demonstrate an interesting phenomenon that β-AR agonists can directly lead to HIF-1α accumulation in MIA PaCa2 and BxPC-3 cells independently of oxygen levels.

Carie and Sebti demonstrated that inhibition of the Raf-1/Mek-1/ERK1/2 pathway by a β-AR agonist can result in growth inhibition of MDA-MB-231 breast cancer cells *in vivo*[26]. Shin *et al* reported that the catecholamines stimulate β2-AR while carcinogens like nicotine can interact with β2-AR to activate the downstream protein kinase C/ERK1/2/cyclooxygenase 2 pathway, leading to the proliferation of gas-

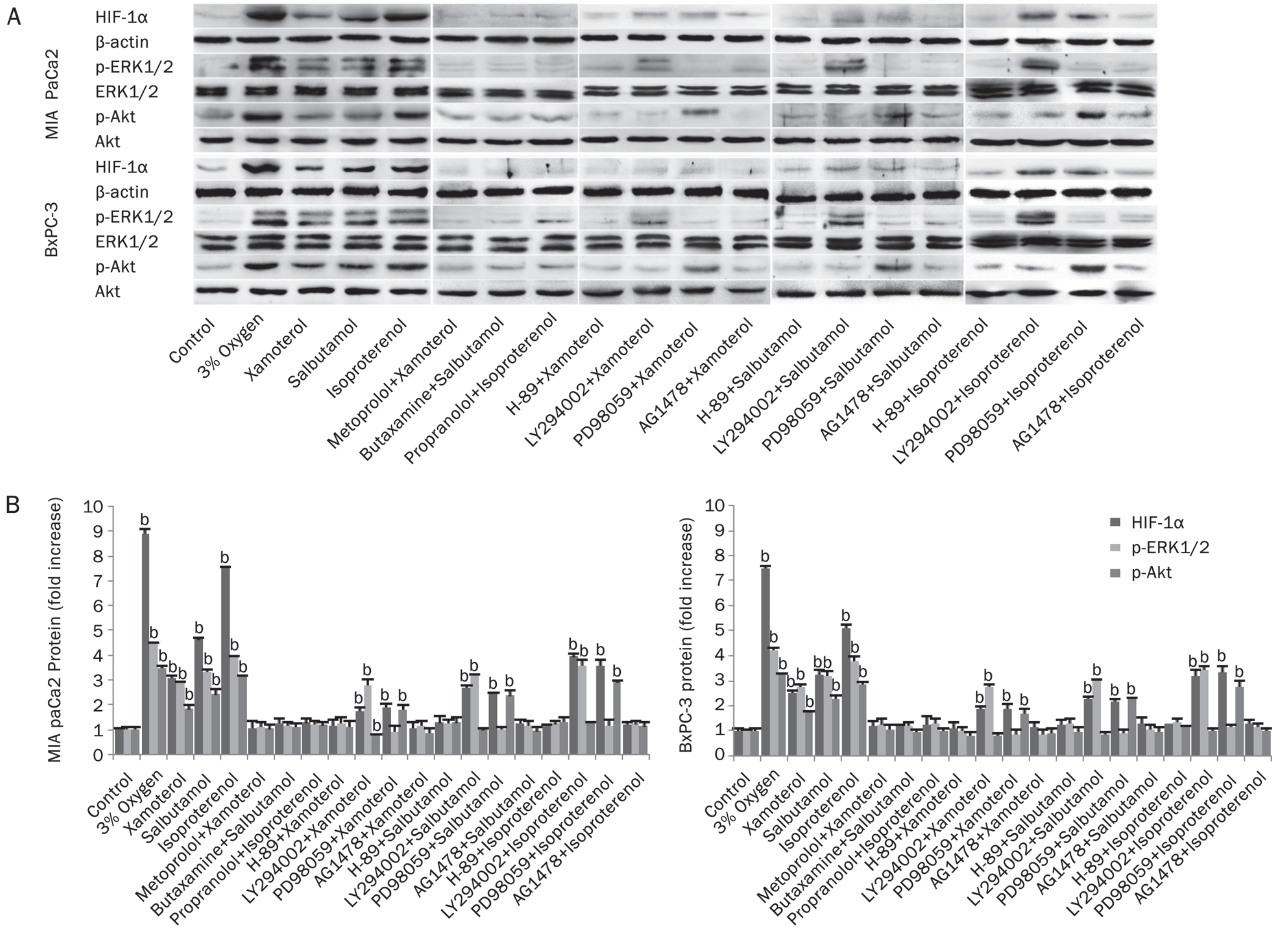

Figure 8. HIF-1α protein accumulation, ERK1/2 phosphorylation (Thr202, Tyr204), and Akt phosphorylation (Ser473) after treatment with β-AR agonists and antagonists. (A) MIA PaCa2 and BxPC-3 cells were treated with drugs as indicated below the panel and protein and phosphoprotein levels were determined using Western blotting. 3% oxygen provided the positive control. (B) Quantitation of Western blotting. Data from at least 3 independent experiments with duplicate determinations were expressed as means±SEM *vs* controls. $^{b}P<0.05$ *vs* control.

tric cancer cells[27]. Agonists binding to β-ARs activate signaling by receptor-coupled GTP binding proteins (G-proteins); downstream effectors include adenylyl cyclase, cyclic AMP, and c-SRC. And c-SRC participates in signal transduction mediated by the epidermal growth factor receptor (EGFR) tyrosine kinase and then leads to activation of the Akt and ERK1/2 pathways[28, 29]. Moreover, HIF-1α expression and activity are regulated by major signal transduction pathways including Akt and ERK1/2[7]. It is also showed in the present study that the increase in HIF-1α levels following treatment with β-AR agonists is dependent on ERK1/2 and Akt by a posttranscriptional mechanism. The both pathways are elicited from EGFR, whose transactivation requires PKA.

Our results suggest that HIF-1α, as a potential target for the prevention and therapy, is an interesting and missing link between β-AR and pancreatic cancer development independently of oxygen level. A cohort study of cardiovascular patients receiving β-AR antagonists found, remarkably, that the cancer risk declined by 49% in these patients compared with control patients who did not receive the drugs; there was a 6% decrease in risk for every additional year of β-AR antagonist use[30]. In accordance with this, our data also indicate that the use of β-AR antagonists significantly attenuate the effects of β-AR agonists on increased expression of HIF-1α and its target genes which are related to glucose transport, angiogenesis and metastasis in pancreatic cancer cells. However, it must be recognized that cancer is a multifactorial disease and management may require multimodal therapy. The potential of β-AR antagonists as anticancer therapeutics may be best realized in combination with other treatment modalities including surgery, chemotherapy and radiotherapy.

Acknowledgements

We thank the staff of the Biology and Genetics Laboratory, Xi'an Jiaotong University for their technical assistance in these studies.

Author contribution

Heng-tong HU, Su-gang SHEN, Qing-yong MA, and Ke-ping XIE designed research; Heng-tong HU, Dong ZHANG, Liang HAN, Ya-dong MA, and Ruo-fei LI performed research; Ya-dong MA and Ruo-fei LI contributed part reagents; Heng-tong HU analyzed data; Heng-tong HU wrote the paper.

Abbreviations

HPA axis, Hypothalamic–pituitary–adrenal axis; β-AR, β-adrenergic receptor; EGFR, Epidermal growth factor receptor; HIF-1, Hypoxia-inducible factor 1; IBMX, 3-isobuty l-methylxanthine; ERK, Extracellular signal-regulated kinase; Akt, Protien kinase B; PI3K, phosphatidylinositol 3-kinase; cAMP: cyclic adenosine monophosphate; PKA, Protein Kinase A; MEK, mitogen activated protein (MAP) kinase; mTOR, mammalian target of rapamycin; Ras, protocogene G protein; Raf, protooncogene serine/threonine kinase;AG1478, 4-(3-Chloroanillino)-6,7-dimethoxyquinazoline; LY294002, 2-(4-Morpholinyl)-8-phenyl-1(4*H*)-benzopyran-4-one hydrochloride; PD98,059, 2-(2-Amino-3-methoxyphenyl)-4*H*-1-benzopyran-4-one; SQ22536, 9-(Tetrahydro-2-furanyl)-9*H*-purin-6-amine, 9-THF-Ade; H-89, N-[2-(p-Bromocinnamylamino)ethyl]-5-isoquinolinesulfonamide·2HCl hydrate

References

1 Thaker PH, Han LY, Kamat AA, Arevalo JM, Takahashi R, Lu CH, *et al*. Chronic stress promotes tumor growth and angiogenesis in a mouse model of ovarian carcinoma. Nat Med 2006; 12: 939–44.
2 Audet M, Bouvier M. Insights into signaling from the β_2-adrenergic receptor structure. Nat Chem Biol 2008; 4: 397–403.
3 Thaker PH, Lutgendorf SK, Sood AK. The neuroendocrine impact of chronic stress on cancer. Cell Cycle 2007; 6: 430–3.
4 Weddle DL, Tithoff P, Williams M, Schuller HM. β-Adrenergic growth regulation of human cancer cell lines derived from pancreatic ductal carcinomas. Carcinogenesis 2001; 22: 473–9.
5 Askari MD, Tsao MS, Schuller HM. The tobacco-specific carcinogen, 4-(methylnitrosamino)-1-(3-pyridyl)-1-butanone stimulates proliferation of immortalized human pancreatic duct epithelia through β-adrenergic transactivation of EGF receptors. J Cancer Res Clin Oncol 2005; 131: 639–48.
6 Shen SG, Zhang D, Hu HT, Li JH, Wang Z, Ma QY. Effects of α-adrenoreceptor antagonists on apoptosis and proliferation of pancreatic cancer cells *in vitro*. World J Gastroenterol 2008; 14: 2358–63.
7 Semenza GL. Signal transduction to hypoxia-inducible factor-1. Biochemical Pharmacol 2002; 64: 993–8.
8 Chang Q, Qin RY, Huang T, Gao J, Feng YP. Effect of antisense hypoxia-inducible factor 1α on progression, metastasis, and chemosensitivity of pancreatic cancer. Pancreas 2006; 32: 297–305.
9 Semenza GL. Targeting HIF-1 for cancer therapy. Nat Rev 2003; 3: 721–32.
10 Akakura N, Kobayashi M, Horiuchi I, Suzuki A, Wang JX, Chen J, *et al*. Constitutive expression of hypoxia-inducible factor-1 renders pancreatic cancer cells resistant to apoptosis induced by hypoxia and nutrient deprivation. Cancer Res 2001; 61: 6548–54.
11 Schuller HM, Cekanova M. NNK-induced hamster lung denocarcinomas over-express β_2-adrenergic and EGFR signaling pathways. Lung Cancer 2005; 49: 35–45.
12 Machida K, Inoue H, Matsumoto K, Tsuda M, Fukuyama S, Koto H, *et al*. Activation of PI3K-Akt pathway mediates antiapoptotic effects of β-adrenergic agonist in airway eosinophils. Am J Physiol Lung Cell Mol Physiol 2005; 288: 860–7.
13 Wang GL, Jiang BH, Rue EA, Semenza GL. Hypoxia-inducible factor 1 is a basic-helix-loop-helix-PAS heterodimer regulated by cellular O_2 tension. Proc Natl Acad Sci USA 1995; 92: 5510–4.
14 Kwon SJ, Lee YJ. Effect of low glutamine/glucose on hypoxia-induced elevation of hypoxia-inducible factor-1alpha in human pancreatic cancer MiaPaCa-2 and human prostatic cancer DU-145 cells. Clin Cancer Res 2005; 11: 4694–700.
15 Li QF, Wang XR, Yang YW, Lin H. Hypoxia upregulates hypoxia inducible factor (HIF)-3α expression in lung epithelial cells: characterization and comparison with HIF-1α. Cell Res 2006; 16: 548–58.
16 Shaw RJ. Glucose metabolism and cancer. Curr Opin Cell Biol 2006; 18: 598–608.
17 Ratushny V, Astsaturov I, Burtness BA, Golemis EA, Silverman JS. Targeting EGFR resistance networks in head and neck cancer. Cell Signal 2009; 21: 1255–68.
18 Zhang SX, Gozal D, Sachleben LR Jr, Rane M, Klein JB, Gozal E. Hypoxia induces an autocrine-paracrine survival pathway via platelet-derived growth factor (PDGF)-B/PDGF-β receptor/ phosphatidylinositol 3-kinase/Akt signaling in RN46A neuronal cells. FASEB J 2003; 17: 1709–11.
19 Minet E, Arnould T, Michel G, Roland I. ERK activation upon hypoxia: involvement in HIF-1 activation. FEBS Lett 2000; 468: 53–8.
20 Sung SM, Jung DS, Kwon CH, Park JY, Kang SK, Kim YK. Hypoxia/reoxygenation stimulates proliferation through PKC-dependent activation of ERK and akt in mouse neural progenitor cells. Neurochem Res 2007; 32: 1932–9.
21 Beasley NJ, Leek R, Alam M, Turley H, Cox GJ, Gatter K, *et al*. Hypoxia-inducible factors hif-1α and hif-2α in head and neck cancer: relationship to tumor biology and treatment outcome in surgically resected patients. Cancer Res 2002; 62: 2493–7.
22 Chrousos GP. The hypothalamic-pituitary-adrenal axis and immune-mediated inflammation. N Engl J Med 1995; 332: 1351–62.
23 Glaser R, Kiecolt-Glaser JK. Stress-induced immune dysfunction: implications for health. Nat Rev Immunol 2005; 5: 243–51.
24 Antoni MH, Lutgendorf SK, Cole SW, Dhabhar FS, Sephton SE, McDonald PG, *et al*. The influence of bio-behavioural factors on tumour biology: pathways and mechanisms. Nat Rev Cancer 2006; 6: 240–8.
25 Schuller HM, Al-Wadei HAN, Majidi M. GABAB receptor is a novel drug target for pancreatic cancer. Am Cancer Soc 2008; 112: 767–77.
26 Carie AE, Sebti SM. A chemical biology approach identifies a beta-2 adrenergic receptor agonist that causes human tumor regression by blocking the Raf-1/Mek-1/Erk1/2 pathway. Oncogene 2007; 26: 3777–88.
27 Shin VY, Wu WK, Chu KM, Koo MW, Wong HP, Lam EK, *et al*. Functional role of beta-adrenergic receptors in mitogenic action of nicotine on gastric cancer cells. Toxicol Sci 2006; 96: 21–9.
28 Schuller HM. Mechanisms of smoking related lung and pancreatic adenocarcinoma development. Nat Rev Cancer 2002; 2: 455–63.
29 Cotton M, Claing A. G protein-coupled receptors stimulation and the control of cell migration. Cell Signal 2009; 21: 1045–53.
30 Algazi M, Plu-Bureau G, Flahault A, Dondon MG, Lê MG. Could treatments with β blockers be associated with a reduction in cancer risk. Rev Epidemiol Sante Publique 2004; 52: 53–65.

Acta Pharmacologica Sinica (2010) 31: 111–117
© 2010 CPS and SIMM All rights reserved 1671-4083/10 $32.00
www.nature.com/aps

Original Article

Application of RT-PCR in formalin-fixed and paraffin-embedded lung cancer tissues

Fan ZHANG[1,2,#], Zhuo-min WANG[1,3,#], Hong-yu LIU[1], Yun BAI[1], Sen WEI[1], Ying LI[1], Min WANG[1], Jun CHEN[1,*], Qing-hua ZHOU[1,2,*]

[1]Tianjin Key Laboratory of Lung Cancer Metastasis and Tumor Microenvironment; Tianjin Lung Cancer Institute, Tianjin Medical University General Hospital, Tianjin 300052, China; [2]The Key Laboratory of Lung Cancer Molecular Biology in Sichuan Province, West China Hospital, Sichuan University, Chengdu 610041, China; [3]The 452 Hospital of PLA, Chengdu 610000, China

---

Aim: To analyze gene expression in formalin-fixed, paraffin-embedded lung cancer tissues using a modified method.
Methods: Total RNA from frozen tissues was extracted using TRIZOL reagent. RNA was extracted from formalin-fixed, paraffin-embedded tissues by digestion with proteinase K before the acid-phenol:chloroform extraction and carrier precipitation. We modified this method by using a higher concentration of proteinase K and a longer digestion time, optimized to 16 hours. RT-PCR and real-time RT-PCR were used to check reproducibility and the concordance between frozen and paraffin-embedded samples.
Results: The results showed that the RNA extracted from the paraffin-embedded lung tissues had high quality with the most fragment length between 28S and 18S bands (about 1000 to 2000 bases). The housekeeping gene GUSB exhibited low variation of expression in frozen and paraffin-embedded lung tissues, whereas PGK1 had the lowest variation in lymphoma tissues. Furthermore, real-time PCR analysis of the expression of known prognostic genes in non-small cell lung carcinoma (NSCLC) demonstrated an extremely high correlation (r>0.880) between the paired frozen and formalin-fixed, paraffin-embedded specimens.
Conclusion: This improved method of RNA extraction is suitable for real-time quantitative RT-PCR, and may be used for global gene expression profiling of paraffin-embedded tissues.

Keywords: lung cancer; formalin-fixed tissues; paraffin-embedded tissues; RNA extraction; RT-PCR

Acta Pharmacologica Sinica (2010) 31: 111–117; doi: 10.1038/aps.2009.178; published online 28 December 2009

Introduction

Lung cancer is the leading cause of cancer death in the world; it accounts for 37% and 26% of the total deaths in men and women, respectively[1]. The overall 5-year survival rate for lung cancer patients is less than 15%. Non-small cell lung carcinoma (NSCLC) accounts for approximately 75% of all lung cancers and represents a heterogeneous group of cancers consisting mainly of squamous cell, adeno- and large cell carcinoma. Despite advances in cancer treatment in the past two decades, the prognosis of patients with lung cancer has been improved only minimally. Less than 50% of the patients that have successfully undergone potentially curative resections survive for 5 years after operation. The TNM staging system is an important but insufficient prognostic parameter; additional prognostic factors still affect the clinical outcomes, independent of stage.

Gene expression profiling by microarray and RT-PCR have been used to identify possible prognostic factors to predict patient outcome[2–4]. Real-time PCR permits quick, robust and quantitative measurement of gene expression, leading to the construction of gene expression-based survival models.

Comprehensive analysis of gene expression using RNA from fresh or frozen tumor specimens is becoming increasingly important to better understand cancer pathogenesis, disease progression and prognosis[5, 6]. However, frozen tumor specimens are not readily available. In contrast, formalin-fixed, paraffin-embedded tissues are widely present and usually have matching clinical data with which to carry out clinical studies.

Recently, several methods to extract RNA from paraffin-embedded tissues have been reported[7, 8]. We have developed an improved method of RNA extraction from paraffin-embedded lymphoid tissues and compared it with two other RNA extrac-

---

[#] These authors equally contribute to this work.
[*] To whom correspondence should be addressed.

E-mail zhouqh1016@yahoo.com.cn (Qing-hua ZHOU);
huntercj2004@yahoo.com (Jun CHEN).

Received 2009-10-12 Accepted 2009-11-13

tion methods[9]. Our method yielded higher amounts of RNA with longer RNA fragments. Furthermore, real-time RT-PCR analysis showed that our method for RNA extraction resulted in significantly better reproducibility and concordance between the paired frozen and paraffin-embedded samples. However, the extent of RNA degradation and modification during the fixation process varied in different tumor tissues. We modified the RNA extraction method and demonstrated its efficiency and reproducibility in obtaining RNA from lung cancer tissues, confirming the purpose of our study. This improved RNA extraction method can likely be used to study gene expression profiling of other paraffin-embedded solid tumor samples.

Materials and methods

Tissue specimens

Formalin-fixed, paraffin-embedded and frozen lung cancer specimens as well as the corresponding normal lung cancer tissues were obtained from 8 patients with adenocarcinoma and squamous cell carcinoma. Fresh surgical specimens were fixed in 10% neutral-buffered formalin at room temperature for 4–6 h before being alcohol dehydrated and embedded in paraffin for 1 year (4 patients), 3 years (2 patients) or 5 years (2 patients) . The study was approved by the Tianjin Medical University Ethical Review Board. All patients consented to the study.

RNA isolation from frozen specimens

Frozen tissues (50−100 mg) were ground into powder in liquid nitrogen, and then suspended in 1 mL TRIZOL Reagent (Invitrogen, USA). Total RNA was extracted using TRIZOL reagent according to the manufacturer's protocol. Briefly, the aqueous phase was used for RNA precipitation with an equal volume of isopropanol. The RNA pellet was washed once with 1 mL 75% ethanol, then air-dried and re-dissolved in an appropriate volume of RNase-free water. RNA was quantified using a spectrophotometer (Beckman, USA), and its quality was checked by agarose gel electrophoresis.

Extraction of total RNA from formalin-fixed, paraffin-embedded specimens

Total RNA was extracted from three 10 μm-thick formalin-fixed, paraffin-embedded sections (corresponding to about 30 mg of tissue). Sections were deparaffinized by two repeated incubations in 1.5 mL xylene at 37 °C for 20 min, followed by two repeated incubations in 1.5 mL 100% ethanol at 37 °C for at least 30 min. Ethanol was aspirated and the pellet was allowed to air-dry for 5 min at room temperature. Then the pellet was resuspended in 600 μL of RNA lysis buffer containing 10 mmol/L Tris/HCl (pH 8.0), 0.1 mmol/L EDTA (pH 8.0), 2% SDS (pH 7.3) supplemented with 50 μL of 60 mg/mL proteinase K (Promega, USA) and incubated at 60 °C for 16–20 h with occasional agitation, until the tissue was completely digested. Next, we purified RNA using two sequential extractions with an equal volume of 70% phenol (pH 4.3):30% chloroform at room temperature, unlike our previously reported method using only one extraction on lymphoid tissue samples[9]. Then, the RNA was precipitated with an equal volume of isopropanol in the presence of 1/10 volume of 3 mol/L sodium acetate (pH 5.2) and 0.5 μL of a 20 mg/mL solution of carrier glycogen (Invitrogen, USA) at -20 °C for at least 1 h. The RNA pellet was washed once in 75% ethanol, dried and redissolved in 20 μL of RNase-free water. All solutions were prepared using DEPC-treated water. RNA was quantified spectrophotometrically, and its quality was assessed by 1.5% agarose gel electrophoresis and staining with ethidium bromide.

To rule out the possibility of DNA contamination, the resolved RNA was incubated with 10 μg/mL RNase-free DNase at 37 °C for 30 min, and then precipitated as stated previously.

Reverse transcription

Two micrograms of total RNA from paraffin-embedded or frozen tissues was reverse transcribed using the M-MLV reverse transcriptase (Promega, USA) according to the manufacturer's protocol, with minor modifications. RNA template and random primers were incubated at 70 °C for 10 min to melt the secondary structure within the template, and cooled on ice for more than 2 min. Then the complete reaction mixture was incubated at 30 °C for 10 min, 42 °C for 60 min and 70 °C for 15 min.

Determination of the length of specific transcripts by PCR

To compare the maximal length of RNA transcripts extracted from paraffin-embedded and frozen tissues, we amplified 13 fragments of the β-actin gene, ranging in size from 99 to 705 bp. The primers for β-actin were used as previously described[9]. To prevent potential amplification of contaminating DNA, most primer pairs were designed to span different exons. PCR was performed in a total volume of 25 μL containing 1 μL of reverse-transcribed cDNA. After an initial incubation at 94 °C for 5 min, the reaction mixtures were subjected to 35 cycles of amplification using the following protocols: 94 °C for 45 s, 55 °C for 45 s and 72 °C for 45 s, followed by a final extension step at 72 °C for 7 min. PCR products were analyzed by 1.2% agarose gel electrophoresis and stained with GoldView nucleic acid dye.

Quantitative real-time RT-PCR

Real-time RT-PCR was performed using ABI PRISM 7500 Sequence Detection System instrument and software (Applied Biosystems, USA). The relative expression level of four housekeeping genes and five target genes was measured using SYBR Green I dye-based method. The sequences of the primers are presented in Table 1.

PCR reactions were prepared in a final volume of 25 μL, with a final concentration of 1×Power SYBR Green PCR Master Mix (Applied Biosystems, USA) and cDNA derived from 25 ng of input RNA, as determined by spectrophotometric measurement using the OD_{260} value. Thermal cycling comprised of an initial UNG incubation at 50 °C for 2 min, AmpliTaq Gold DNA Polymerase activation at 95 °C for 10 min, 40 cycles of denaturation at 95 °C for 15 s and annealing and extension at 60 °C for 1 min. Each measurement was performed in triplicate and the threshold cycle (C_T), the fractional cycle number at which the amount of amplified target reached a fixed threshold, was determined as previously reported[9, 10].

Table 1. Sequences of real-time RT-PCR primers.

Gene	Amplicon size	Primers
GUSB	154 bp	Forward: CTCATTTGGAATTTTGCCGATT Reverse: CCGAGTGAAGATCCCCTTTTTA
PGK-1	75 bp	Forward: GGGAAAAGATGCTTCTGGGAA Reverse: TTGGAAAGTGAAGCTCGGAAA
GAPDH	121 bp	Forward: AGCCGAGCCACATCGCT Reverse: GGCAACAATATCCACTTTACCAGAGT
18S	187 bp	Forward: CGGCTACCACATCCAAGGAA Reverse: GCTGGAATTACCGCGGCT
LCK	62 bp	Forward: CTGCCAACATTCTGGTGTCTG Reverse: GCGTGCTAGGCCAAAGTCT
ERBB3	135 bp	Forward: GAGCCTGTGTACCTCGCTG Reverse: GATCCACCACAAAGTTATGGGG
STAT1	139 bp	Forward: AGGAAAAGCAAGCGTAATCTTCA Reverse: TATTCCCCGACTGAGCCTGAT
MMD	113 bp	Forward: ATGGCCGCTACAAGCCAAC Reverse: GTCATCAGACAGCCGATGGAG
DUSP6	203 bp	Forward: TTCCTCGGACATCGAGTCTGA Reverse: GCAAATTGGGGGTGACGTTC

To compare the expression of endogenous house-keeping genes between the paired paraffin-embedded and frozen specimens, the differences in the average C_T values between these two types of specimens was calculated as follows: Mean C_T =average $C_{t(\text{paraffin–embedded tissue RNA})}$ –average $C_{t(\text{frozen tissue RNA})}$. To compare the RNA expression of target genes among different specimens, normalization based on GUSB gene expression was performed, and the averages of the normalized C_T values (ΔC_T) were calculated as previously reported[10, 11]. Relative mRNA expression of a target gene within a specimen was calculated as $2^{-\Delta CT}$, where $\Delta C_T = C_{T(\text{target gene})} - C_{T(\text{GUSB})}$[7].

Statistical analysis

The degree of variance in the expression of distinct housekeeping genes was calculated using Excel computer software. Correlation of gene expression analysis was done using Pearson linear correlation.

Results

RNA extraction

For comparative purposes, we isolated total RNA from formalin-fixed, paraffin-embedded lung cancer tissues and frozen lung cancer tissues. To obtain a yield of amplifiable RNA, we performed RNA extraction twice with phenol-chloroform in lung tissues, instead of only once as was done in lymphoid tissues previously[9]. Starting from three 10-μm-thick formalin-fixed, paraffin-embedded tissue samples, we obtained an average of 44.9 μg (33.1−55.6 μg) of RNA, with $OD_{260/280}$ ratios ranging from 2.0 to 2.1, indicating good quality purified RNA; this ratio is much better than in our previous method in lymphoid tissues, in which RNA $OD_{260/280}$ ratios were between 1.6 and 1.8. As expected, RNA extracted from the frozen tissues showed distinct 28S and 18S ribosomal RNA (rRNA) bands and $OD_{260/280}$ ratios ranging from 1.9 to 2.1, whereas most of the RNA extracted from formalin-fixed, paraffin-embedded specimens with our method was between the 28S and 18S bands (about 1000 to 2000 bases), and appeared smeary (Figure 1). To rule out the possibility of DNA contamination and to improve RNA quality, we added RNase-free DNase to the resolved RNA and incubated samples at 37 °C for 30 min, then precipitated RNA as stated in the Materials and methods. Compared to the DNase untreated method, we did not find a significant improvement in subsequent experiments, and we found there was less RNA recovered overall (data not shown).

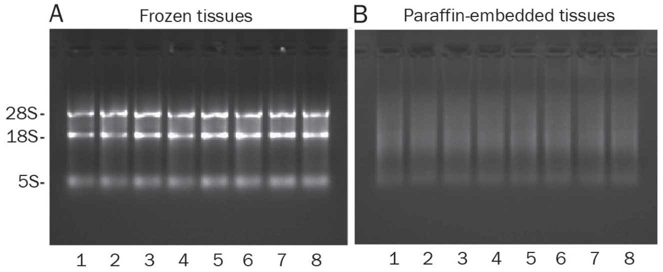

Figure 1. Agarose gel electrophoresis of total RNA extracted from frozen lung cancer tissues (A) and the corresponding paired formalin-fixed, paraffin-embedded lung cancer tissues (B). Lanes 1−4: one-year old samples; Lanes 5−6: 3-year old samples; Lanes 7−8: 5-year old samples.

RT-PCR amplification of different β-actin fragments

To assess the ability of the extracted RNAs to generate longer amplicons by RT-PCR amplification, 13 β-actin amplicons, ranging in size from 99 to 705 bp, were amplified from the RNA extracted from the paraffin-embedded and frozen specimens, as well as from the specimens before and after genomic DNA removal (Figure 2). Compared with frozen lung cancer tissues, the RNA extracted from the formalin-fixed, paraffin-embedded lung cancer tissues yielded β-actin amplicons with similar quality, although at a lower quantity. Using DNase-treated RNA as template did not improve the amplification efficiency and did not result in amplification of longer fragments (data not shown). Amplification of RT products in which reverse transcriptase was omitted did not yield PCR amplicons, thus ruling out the possibility of inadvertent amplification of contaminating DNA (data not shown).

Real-time RT-PCR gene expression analysis

To compare the consistency of quantitative RT-PCR between matched formalin-fixed, paraffin-embedded and frozen lung

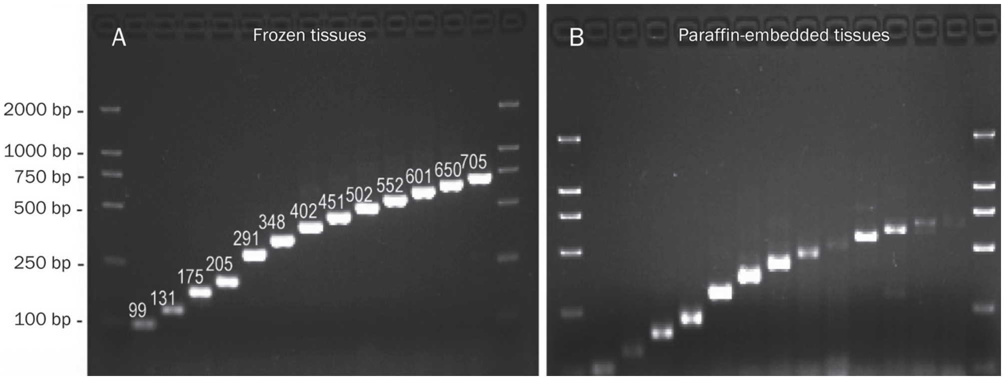

Figure 2. Effects of the method of total RNA extraction from formalin-fixed, paraffin-embedded lung cancer tissues on amplifiable RNA fragment length. Thirteen primer pairs were tested that amplify from 99 to 705 bp of β-actin. The expected product size is given for amplicons amplified from the frozen (A) and formalin-fixed, paraffin-embedded (B) lung cancer specimens.

Table 2. Comparison of average ΔC_t values between formalin-fixed, paraffin-embedded specimens and frozen specimens by target gene.

Target gene	Average ΔC_t values Frozen	Paraffin-embedded	*r* (Pearson correlation)	Sig. (2-tailed)
STAT1	-2.35	-1.38	0.825	0.012
LCK	0.23	0.17	0.806	0.016
MMD	1.76	3.51	0.808	0.015
ERBB3	1.70	4.32	0.838	0.009
DUSP6	-0.42	0.97	0.869	0.005

cancer tissues, and to identify the appropriate endogenous control genes for RNA input normalization in lung cancer tissues, we studied the expression of four commonly used housekeeping genes (GUSB, PGK-1, GAPDH, and 18S), which were selected from among those well-known in the literature as common, constitutively expressed genes across different conditions. The primers amplified amplicons with relatively small sizes (less than 150 bp). As expected, the RNA of the endogenous housekeeping genes extracted from paraffin-embedded specimens was generally lower in quantity (higher C_T) than those extracted from matched frozen specimens (Figure 3). However, different housekeeping genes exhibited different degrees of variation in expression in different specimens. Of the 4 endogenous control genes, expression of GUSB was the least variable both in frozen and in paraffin-embedded specimens, while the expression of 18S was the most variable (Figure 3).

We next examined the expression of several non-housekeeping genes in the matched paraffin-embedded and frozen lung cancer tissues. We selected the following genes: LCK, MMD, STAT1, ERBB3, and DUSP6, which have been linked to the relapse-free and overall survival among patients with NSCLC[6]. The expression of these target genes was normalized to GUSB due to its minimal variation in expression. We were able to obtain similar levels of normalized expression profiles of these target genes in the formalin-fixed, paraffin-embedded specimens and frozen specimens, as shown in Figure 4A. ΔC_T values of the paraffin-embedded tissues and their correlation with that of frozen tissues are shown in Table 2. Although the absolute quantities of specific RNA transcripts amplified from similar amounts of starting RNA were smaller in paraffin-embedded samples compared to the paired frozen specimens, once the data were normalized to endogenous housekeeping gene controls, the resulting relative amounts were very similar. The adjusted Pearson correlation (r) between the formalin-fixed, paraffin-embedded and frozen lung cancer specimens for all tested genes was r=0.885 (Figure 4B).

Measurement of the expression of these five genes using RNA extracted from two 3-year-old and two 5-year-old lung cancer specimens demonstrated a similar correlation between the paired formalin-fixed, paraffin-embedded and frozen specimens, as was observed for the 1-year old-specimens. The age of preservation of the formalin-fixed, paraffin-embedded lung cancer tissue did not have a marked effect on the expression of the housekeeping genes (such as PGK1 and GUSB) and the selected five genes (LCK, MMD, STAT1, ERBB3, and DUSP6), as shown in Figures 3B and 4A (data for other housekeeping genes is not shown). A comparison of 3- or 5-year–old specimens to 1-year-old specimens showed similar C_T differences and ΔC_T values between the matched formalin-fixed, paraffin-embedded and frozen specimens.

Discussion

DNA arrays or real-time RT-PCR are important tools in the diagnosis and treatment of human cancers[12, 13]. However, the requirement for fresh or snap-frozen tissues has limited their clinical application. By contrast, specimens collected and processed for pathological diagnosis are readily available, many with matching clinical data[14]. Recently, progress has been made to extract RNA from formalin-fixed, paraffin-embedded lymphoid tissues and breast cancer tissues[15]. However, these techniques are subjected to the tissue-specific, fixation-associated RNA degradation and modification. Optimization of RNA extraction for each tissue is therefore required. The aim of this study was to investigate whether the method of RNA extraction in formalin-fixed, paraffin-embedded lymphoid tissues we developed can be used on lung cancer specimens. We also wanted to test if the RNAs extracted with our improved method can be used in quantitative real-time RT-PCR. We

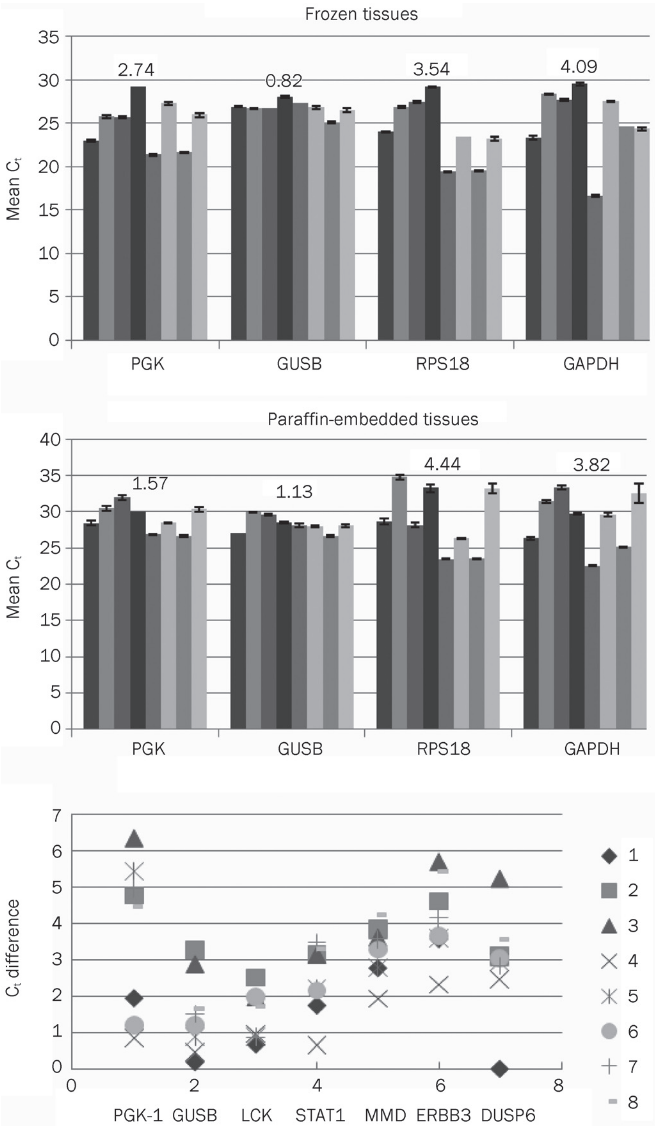

Figure 3. RNA expression of housekeeping genes in paired frozen and formalin-fixed, paraffin-embedded lung cancer tissues. (A) Mean RNA expression (represented by mean C_T) of 4 housekeeping genes (GUSB, PGK-1, GAPDH, and 18S) in 8 frozen and paired formalin-fixed, paraffin-embedded lung cancer tissues. Each bar represents gene expression in an individual specimen. Numbers above the bar represent the variance of expression of particular gene among the specimens. (B) RNA expression of PGK-1, GUSB, LCK, STAT1, MMD ERBB3, and DUSP6 in formalin-fixed, paraffin-embedded lung cancer tissues. The expression of each gene is normalized to its expression in the matched frozen specimens, as represented by C_T difference between the paraffin and frozen specimens. Each symbol represents a distinct paired tissue specimen.

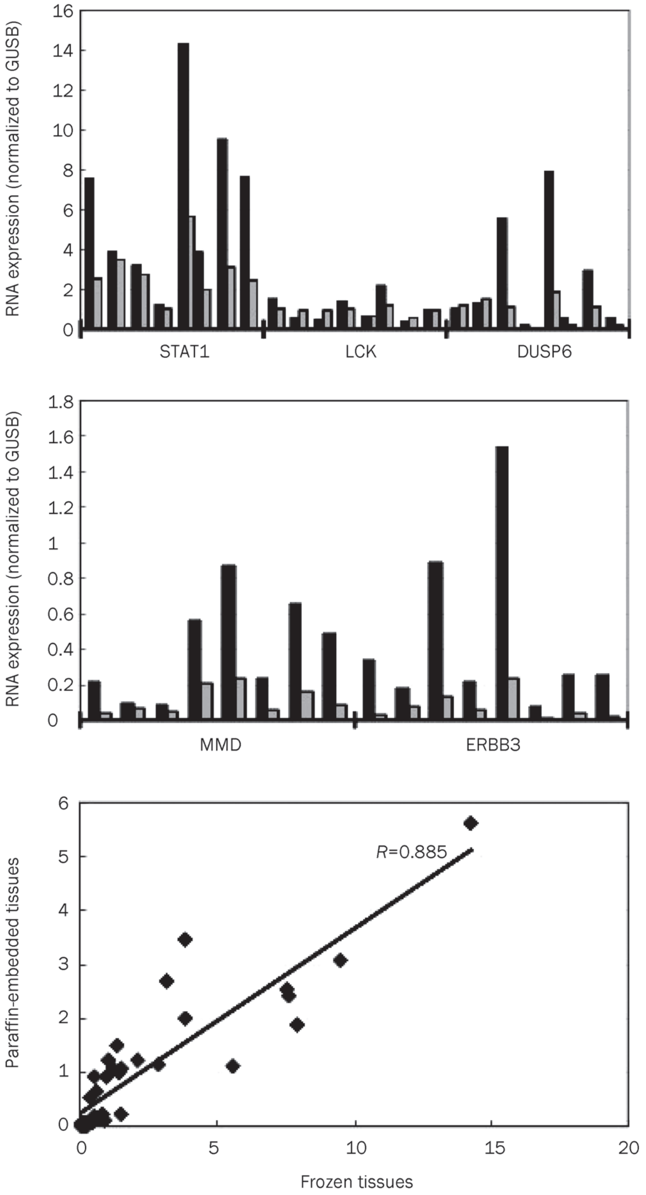

Figure 4. Comparison of RT-PCR expression profiles of 5 genes (LCK, MMD, STAT1, ERBB3, and DUSP6) from paired frozen and formalin-fixed, paraffin-embedded lung cancer tissues. (A) Total RNA was extracted from frozen and paraffin-embedded lung cancer tissues, mRNA levels were determined by real-time SYBR green RT-PCR as described in Material and Methods. Each bar represents the normalized expression relative to GUSB and the mean of three measurements: Grey — formalin-fixed, paraffin-embedded tissues; Black — frozen tissues. (B) Spearman correlation for the 5 gene expression in 8 paired frozen and formalin-fixed, paraffin-embedded lung cancer tissues.

also explored the most appropriate endogenous control genes to use for the normalization of RNA quality and quantity.

The traditional methods of RNA extraction from formalin-fixed, paraffin-embedded tissues often yield RNAs of insufficient quality[10], which are extensively degraded to fragments that are, on average, 200 nucleotides in length[16]. Previous attempts to amplify fragments longer than 200 bp were usually unsuccessful[17]. To date, the most successful method for total RNA extraction from formalin-fixed, paraffin-embedded tissues utilizes digestion with proteinase K before the acid-phenol:chloroform extraction and carrier precipitation[18]. We modified this method by using a higher concentration of proteinase K and a longer digestion time, optimized to 16 h, to obtain higher quality RNA from lymphoid tissues. In this study, we applied the RNA extraction method used in lymphoid tissues to the lung cancer tissues. We were able to obtain high-yield and high-quality RNAs that could be amplified to yield long cDNA fragments (>600 bp). Furthermore, the delta threshold cycle (ΔC_T) values of the formalin-fixed, paraffin-embedded tissues in our experiments had a high correlation to that of frozen lung cancer tissues (r=0.855, P<0.01) for all the test genes. Our results indicated that the formalin-fixed, paraffin-embedded lung cancer tissues may replace frozen tissues in gene expression analysis using real-time RT-PCR when our modified RNA extraction method is utilized.

There are no housekeeping genes whose expression is constant in all tissues during normal or malignant growth[19, 20]. To properly control for the variation in expression of RNAs, endogenous control genes need to be used for each cell type and tumor type in each experimental design[21]. Here, we chose four housekeeping genes with different abundances that have been widely cited in the literature, and exhibit relatively low variation in expression in different lymphoid tissues[9, 21]. Our experiments indicated that the GUSB gene exhibited the lowest variation of expression in formalin-fixed, paraffin-embedded and frozen lung cancer specimens, and should be used as a suitable endogenous gene to control for RNA quality and quantity.

In this study, we were able to obtain similar levels of normalized expression profiles of five target genes (LCK, MMD, STAT1, ERBB3, and DUSP6) in formalin-fixed, paraffin-embedded specimens and frozen specimens. Our observations suggest that real-time RT-PCR measurements of normalized gene expression in paraffin-embedded lung cancer specimens using our method may closely reflect the gene expression in paired frozen specimens and could obviate the need for frozen specimens. Further studies on the applicability of these methods for prediction, for instance, of lung cancer survival using models with five genes or more than five genes, are in progress[6]. Recently, we used this method to analyze BAG-1 expression in human lung cancer specimens that were formalin-fixed and paraffin-embedded between 1999 and 2003 from West China Hospital[22].

In summary, we have modified the method of RNA extraction from formalin-fixed, paraffin-embedded lymphoid tissues and applied it to lung cancer tissues. Our method will enable researchers to use RT-PCR and real-time quantitative RT-PCR to study the pathogenesis, prognosis, and treatment of lung cancer using formalin-fixed, paraffin-embedded archival tissues.

Acknowledgements

This work was supported by grants from the Key project of National Natural Science Foundation of China (No 30430300), the National Natural Science Foundation of China (No 30500221; No 30500496), the grants from 863 project (2006AA02A401), Tianjin Scientific Innovative System (07YFSZSF05300) and from China-Sweden cooperative foundation (No 09ZCZDSF04100). We thank Dr Shou-Ching TANG for his advision.

Author contribution

Jun CHEN, Qing-hua ZHOU designed research; Fan ZHANG, Zhuo-min WANG and Hong-yu LIU performed research; Yun BAI, Sen WEI, and Ying LI contributed new analytical tools and reagents; Min WANG analyzed data; Jun CHEN and Zhuo-min WANG wrote the paper.

References

1 Jemal A, Siegel R, Ward E, Murray T, Xu J, Thun MJ. Cancer statistics, 2007. CA Cancer J Clin 2007; 57: 43−66.

2 Moldvay J, Scheid P, Wild P, Nabil K, Siat J, Borrelly J, *et al.* Predictive survival markers in patients with surgically resected non-small cell lung carcinoma. Clin Cancer Res 2000; 6: 1125−34.

3 Beer DG, Kardia SL, Huang CC, Giordano TJ, Levin AM, Misek DE, *et al.* Gene-expression profiles predict survival of patients with lung adenocarcinoma. Nat Med 2002; 8: 816−24.

4 Ludwig JA, Weinstein JN. Biomarkers in cancer staging, prognosis and treatment selection. Nat Rev Cancer 2005; 5: 845−56.

5 Lossos IS, Czerwinski DK, Alizadeh AA, Wechser MA, Tibshirani R, Botstein D, *et al.* Prediction of survival in diffuse large-B-cell lymphoma based on the expression of six genes. N Engl J Med 2004; 350: 1828−37.

6 Chen HY, Yu SL, Chen CH, Chang GC, Chen CY, Yuan A, *et al.* A five-gene signature and clinical outcome in non-small-cell lung cancer. N Engl J Med 2007; 356: 11−20.

7 Cronin M, Pho M, Dutta D, Stephans JC, Shak S, Kiefer MC, *et al.* Measurement of gene expression in archival paraffin-embedded tissues: development and performance of a 92-gene reverse transcriptase-polymerase chain reaction assay. Am J Pathol 2004; 164: 35−42.

8 Specht K, Richter T, Muller U, Walch A, Werner M, Hofler H. Quantitative gene expression analysis in microdissected archival formalin-fixed and paraffin-embedded tumor tissue. Am J Pathol 2001; 158: 419−29.

9 Chen J, Byrne GE Jr, Lossos IS. Optimization of RNA extraction from formalin-fixed, paraffin-embedded lymphoid tissues. Diagn Mol Pathol 2007; 16: 61−72.

10 Gloghini A, Canal B, Klein U, Dal Maso L, Perin T, Dalla-Favera R, *et al.* RT-PCR analysis of RNA extracted from Bouin-fixed and paraffin-embedded lymphoid tissues. J Mol Diagn 2004; 6: 290−6.

11 Livak KJ, Schmittgen TD. Analysis of relative gene expression data using real-time quantitative PCR and the 2(-Delta Delta C(T)) Method. Methods 2001; 25: 402−8.

12 Davis RE, Staudt LM. Molecular diagnosis of lymphoid malignancies by gene expression profiling. Curr Opin Hematol 2002; 9: 333−8.

13 van de Vijver MJ, He YD, van't Veer LJ, Dai H, Hart AA, Voskuil DW, *et al.* A gene-expression signature as a predictor of survival in breast cancer. N Engl J Med 2002; 347: 1999−2009.

14 Lehmann U, Kreipe H. Real-time PCR analysis of DNA and RNA extracted from formalin-fixed and paraffin-embedded biopsies. Methods 2001; 25: 409−18.

15 Paik S, Shak S, Tang G, Kim C, Baker J, Cronin M, *et al.* A multigene assay to predict recurrence of tamoxifen-treated, node-negative breast cancer. N Engl J Med 2004; 351: 2817−26.

16 Krafft AE, Duncan BW, Bijwaard KE, Taubenberger JK, Lichy JH. Optimization of the isolation and amplification of rna from formalin-fixed, paraffin-embedded tissue: the armed forces institute of pathology experience and literature review. Mol Diagn 1997; 2: 217−30.

17 Lewis F, Maughan NJ, Smith V, Hillan K, Quirke P. Unlocking the

archive--gene expression in paraffin-embedded tissue. J Pathol 2001; 195: 66−71.

18 Masuda N, Ohnishi T, Kawamoto S, Monden M, Okubo K. Analysis of chemical modification of RNA from formalin-fixed samples and optimization of molecular biology applications for such samples. Nucleic Acids Res 1999; 27: 4436−43.

19 Bustin SA. Absolute quantification of mRNA using real-time reverse transcription polymerase chain reaction assays. J Mol Endocrinol 2000; 25: 169−93.

20 Schmittgen TD, Zakrajsek BA. Effect of experimental treatment on housekeeping gene expression: validation by real-time, quantitative RT-PCR. J Biochem Biophys Methods 2000; 46: 69−81.

21 Lossos IS, Czerwinski DK, Wechser MA, Levy R. Optimization of quantitative real-time RT-PCR parameters for the study of lymphoid malignancies. Leukemia 2003; 17: 789−95.

22 Liu HY, Bai Y, Liu BX, Wang ZM, Wang M, Zhou QH, *et al*. The expression of BAG-1 and its clinical significance in human lung cancer. Chin J Lung Cancer 2008; 11: 489−94.

---

npg **Acta Pharmacologica Sinica** (2010) 31: 118–126

www.nature.com/aps

Original Article

Topical delivery of silymarin constituents via the skin route

Chi-feng HUNG[1], Yin-ku LIN[2], Li-wen ZHANG[3], Ching-hsien CHANG[2], Jia-you FANG[3,*]

[1]School of Medicine, Fu Jen Catholic University, Taipei County, Taiwan, China; [2]Department of Traditional Chinese Medicine, Center for Traditional Chinese Medicine, Chang Gung Memorial Hospital, Keelung, Taiwan, China; [3]Pharmaceutics Laboratory, Graduate Institute of Natural Products, Chang Gung University, Kweishan, Taoyuan, Taiwan, China

Aim: Silibinin (SB), silydianin (SD), and silychristin (SC) are components of silymarin. These compounds can be used to protect the skin from oxidative stress induced by ultraviolet (UV) irradiation and treat it. To this end, the absorption of silymarin constituents via the skin was examined in the present report.
Methods: Transport of SB, SD, and SC under the same thermodynamic activity through and into the skin and the effects of pH were studied *in vitro* using a Franz diffusion assembly.
Results: The lipophilicity increased in the order of SC<SD<SB. Increased lipophilicity of a compound resulted in higher skin deposition but had a minor effect on permeation across the skin in the less-ionized form (pH 8). It is apparent that compounds in the less-ionized form showed higher skin uptake compared to the more-ionized form. Hyperproliferative skin produced by UVB exposure showed increased permeation of silymarin constituents in the less-ionized form, but it did not affect deposition within the skin. With *in vivo* topical application for 4 and 8 h, the skin deposition of SB was higher than those of SD and SC by 3.5~4.0- and 30~40-fold, respectively. The skin disruption and erythema test demonstrated that the topical application of these compounds for up to 24 h caused no apparent skin irritation.
Conclusion: The basic profiles of silymarin permeation via skin route were established.

Keywords: silymarin; silibinin; skin; topical delivery; ultraviolet B; permeation; absorption

Acta Pharmacologica Sinica (2010) 31: 118–126; doi: 10.1038/aps.2009.186;

Introduction

Exposure of skin to ultraviolet (UV) radiation results in a variety of biological effects, including inflammation, induction of oxidative stress, formation of sunburned cells, and immunologic alterations[1]. All of these play important roles in the development of non-melanoma skin cancer (NMSC), which is the most frequently diagnosed malignancy in Caucasians around the world[2, 3]. Surgical and medical treatments of NMSC are difficult because of a high recurrence rate, the occurrence of multiple lesions, and location of tumors on the head, neck, and outer arms[4]. These limitations suggest the need for additional approaches to protect skin against UV-caused cellular damage and NMSC[5].

Silymarin, a polyphenolic flavonoid isolated from seeds of the milk thistle [*Silybum marianum* (L) Gaertn], has been used for more than 2000 years as a traditional medicine to treat liver disorders and to protect the liver against poisoning from chemical and environmental toxins[6]. Silymarin is composed primarily of silibinin (SB) together with small amounts of other stereoisomers, such as silydianin (SD) and silychristin (SC) (Figure 1)[7]. The UV light that reaches the earth's surface comprises primarily UVA wavelengths (315–400 nm) and the remainder (approximately 5%) contains the (295–320 nm) UVB radiation. Both UVA and UVB cause wavelength-dependent damage to human skin including skin cancer, whose incidence is dramatically increasing[8]. Recent studies showed that silymarin constituents could strongly protect against photocarcinogenesis and inhibit UVB and chemical tumor promoter-induced skin inflammation and edema[1, 9–11]. Silymarin also attenuates UVA-induced damage to human keratinocytes[12].

A previous study[13] reported that the skin tissue distribution of silibinin is low by oral administration in mice. Hence topical delivery via the skin may be capable of attaining sufficient pharmacological activity by silymarin constituents. Suitable absorption is known to be an essential requirement for the satisfactory application of topical agents. Although silymarin and its components were demonstrated to have significant activity on UV-irradiated skin, there is no information on the

---

* To whom correspondence should be addressed.
E-mail fajy@mail.cgu.edu.tw
Received 2009-09-28 Accepted 2009-11-20

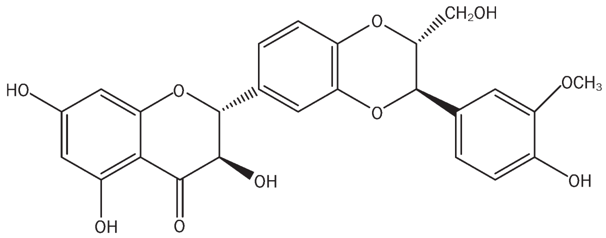

Silibinin (SB)

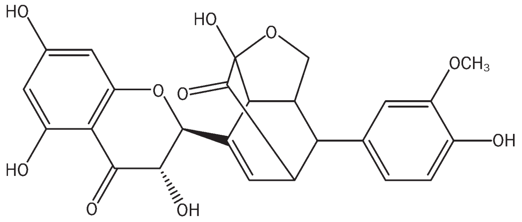

Silydianin (SD)

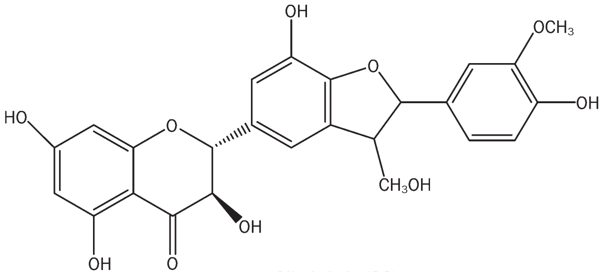

Silychristin (SC)

Figure 1. Chemical structures of silibinin (SB), silydianin (SD), and silychristin (SC).

absorption and permeability parameters of these flavonoids in skin.

The aim of this work was to establish basic profiles of SB, SD, and SC permeation via the skin. Another purpose was to investigate the correlation between skin absorption and physicochemical characteristics of these compounds. Both *in vitro* and *in vivo* skin absorption experiments were performed in this study. Possible pathways of the compounds via the skin were elucidated using skin treated by various strategies as permeation barriers. Moreover, UVB-irradiated skin was used as a skin barrier for permeation in order to mimic the clinical situation.

Materials and methods

Materials

SB (CAS: 22888-70-6) was purchased from ChromaDex (Irvine, CA, USA). SD (CAS: 29782-68-1) was supplied by USP reference standards (Rockville, MD, USA). SC (CAS: 33889-69-9), α-terpineol, and oleic acid were obtained from Sigma-Aldrich (St Louis, MO, USA). All other chemicals and solvents were analytical grade and were used as received.

Preparation of saturated solutions

Saturated solutions of SB, SD, and SC were prepared in Na_2HPO_4-citric acid buffer (McIlvain buffer) with respective pH values of 6, 8, 9.9, and 10.8. An excess amount of each compound was added to 1 mL of the selected buffers, and shaken reciprocally in an incubator at 37 °C for 24 h. The suspension was centrifuged at 10 000 r/min for 10 min, and the concentration of the compound in the supernatant was determined by high-performance liquid chromatography (HPLC) after an appropriate dilution.

HPLC analytical method

The HPLC system for silymarin constituents included an L-2130 pump, an L-2200 sample processor, and an L-2400 UV-visible detector all from Hitachi (Tokyo, Japan). A 25-cm-long, 4-mm inner diameter stainless RP-18 column (Merck, Darmstadt, Germany) was used as the stationary phase. The mobile phase was an acetonitrile-water (35:65) mixture at a flow rate of 1 mL/min. The UV-visible detector was set at 288 nm. The log K' value (capacity factor) of the compounds was determined isocratically using HPLC. The retention time of each compound was measured, and the K' value was calculated from the following equation:

$$\text{Log } K' = \lg[(t_r - t_0)/t_0];$$

where t_r is the retention time of each compound, and t_0 is the retention time of the non-retained solvent peak (methanol).

At the range 0.1−100 μg/mL, the concentration of all silymarin constituents was linearly proportional to their chromatographic peak area. The limit of detection (LOD) of SB, SD, and SC was determined to be 10 ng/mL, 15 ng/mL, and 15 ng/mL, respectively. The intra- and inter-assay precision and accuracy values were evaluated at the concentration range 0.1−100 μg/mL. The overall precision, defined by the relative standard deviation (RSD), ranged from 0.9% to 7.2% on average. Analytical accuracy, expressed as the percentage difference between the mean of measured value and the known concentration, varied from -5.3% to 7.1%.

Preparation of skin membranes

Female nude mice (8 weeks old) were sacrificed, and full-thickness skin was excised from the dorsal region. To obtain delipidized skin, the stratum corneum side was pretreated with chloroform-methanol (2:1) for 1 h. Five percent α-terpineol or oleic acid in a 25% ethanol/water vehicle was used to pretreat skin mounted on a Franz cell for 2 h, followed by the *in vitro* skin absorption experiment.

To obtain UVB-irradiated skin, a Bio-Spectra System Illuminator (Vilber Lourmat, France) was used to emit UVB at a wavelength of 312 nm. This method was modified from Moore *et al*[14]. Briefly, mice were exposed to a single UVB dose of 150 mJ/cm^2 for 7 d and killed after the last exposure. The distance between the UVB lamps and the dorsal skin was about 40 cm. The morphology of the skin was verified by cyclooxygenase (COX)-2 and proliferating cell nuclear antigen (PCNA) staining. Each specimen was dehydrated using ethanol, embedded in paraffin wax, and stained with COX-2 or PCNA. For each skin sample, three different sites were examined and evaluated under light microscopy (Olympus IX70, Tokyo, Japan).

In vitro skin absorption

Skin with or without the various treatments was mounted on the receptor compartment of a Franz cell with the stratum corneum side facing upwards into the donor compartment. Five and a half milliliters of a 3: 7 (*v/v*) ethanol-pH 7.4 buffer was used as the receptor medium to maintain the sink condition of the three compounds. The donor compartment was occluded by parafilm and filled with 0.5 mL of the vehicle containing flavonoids at a dose which ensured saturated solubility. The available diffusion area between the compartments was 0.785 cm^2. The stirring rate and temperature were kept at 600 r/min and 37 °C, respectively. At appropriate intervals, 300-μL aliquots of the receptor medium were withdrawn and immediately replaced with an equal volume of fresh medium.

At the end of the *in vitro* experiment (24 h), the skin was removed from the cell and the skin surface was cleaned with a cotton wool swab immersed in water and methanol three times each. The skin was then weighed, cut with scissors, positioned in a glass homogenizer containing 1 mL of methanol, and homogenized for 10 min at 300 r/min. The resulting solution was centrifuged for 10 min at 10000 r/min and then filtered through a polyvinylidene difluoride (PVDF) membrane with a pore size of 0.45 μm. All samples were analyzed by HPLC.

In vivo skin absorption

For the *in vivo* experiment, an 8-week-old nude mouse was used. A glass cylinder with an available area of 0.785 cm^2 was placed on the dorsal skin with glue (Instant Super Glue®, Kokuyo, Japan). An aliquot of 0.2 mL of vehicle with silymarin constituents was added to the cylinder. The application times of the vehicle were 4 and 8 h. The application region of the skin was excised at the end of the experiment. The procedures for washing and extraction of the compound from the skin were the same as for the *in vitro* experiment.

In vivo skin irritation test

A 0.6-mL aliquot of pH 8 buffer with flavonoids was spread uniformly over a sheet of non-woven polyethylene cloth (1.5 cm×1.5 cm), which was then applied to the back area of a nude mouse. The polyethylene cloth was fixed with Tegaderm® adhesive dressing (3M, USA) and Fixomull® stretch adhesive tape (Beiersdorf AG, Germany). After 24 h, the cloth was removed, and the treated skin area was swabbed clean with a cotton wool swab. After withdrawal of the vehicle for 30 min, transepidermal water loss (TEWL), colorimetric parameters, and the pH of the applied skin were measured. TEWL was recorded using a Tewameter® (TM300, Courage & Khazaka, Köln, Germany). Measurements taken at a stable level were performed 30 s after application of the TEWL probe to the skin. The TEWL was automatically calculated and expressed in g·m^{-2}·h^{-1}. A spectrocolorimeter (CD100, Yokogawa Electrical, Tokyo, Japan) was used to measure the skin erythema (a*). The instrument records color reflectance three-dimensionally (L*, a*, b*) as recommended by the CIE (Commission Internationale de l'Eclairage). When recording the color values, the measuring head was held perpendicular to the dorsal skin of the mouse, and the aperture was fitted with an applicator, to avoid compression of the subcutaneous capillaries. The reading was obtained within a few seconds on the display. The skin surface pH was determined by a Skin-pH-Meter® PH 905 (Courage & Khazaka, Germany). An adjacent untreated site was used as a baseline standard for each determination. The temperature and relative humidity in the laboratory were kept at 26 °C and 55%, respectively. The sample number for each experiment was six (*n*=6).

Data analysis

To calculate the permeation parameters of Fick's law from the plot of the cumulative amount versus time, a graph was plotted as shown in Figure 2. The flux value at the steady-state was determined and expressed per unit of diffusion area in μg·cm^{-2}·h^{-1} by a linear regression calculation from the slope of the linear portion of the cumulative amount-time profiles. The permeability coefficient (K_p, cm/h) was calculated from the flux divided by the saturated compound concentration in the donor compartment. The compound amount in the skin (μg/g) was also calibrated by the saturated solubility (μg/mL) in the donor compartment (calibrated skin deposition) to compare the skin absorption among different silymarin constituents.

A statistical analysis of differences between different treatments was performed using unpaired Student's *t*-test. A 0.05 level of probability was taken as the level of significance. An analysis of variance (ANOVA) test was also used if necessary.

Results

In vitro skin absorption of SB

The effect of the pH of buffers on skin permeation of SB was examined from pH 6 to 10.8. The ionization of these compounds increased following an increase in the pH. The saturated solubilities of SB in pH 6, 8, 9.9, and 10.8 buffers were 4.20±0.41, 31.41±1.86, 190.53±6.63, and 565.10±24.64 μg/mL, respectively. This indicates that the ionic form of SB provided a more-hydrophilic condition of molecules.

In vitro delivery of SB into/across excised skin was investigated for all buffers from pH 6 to 10.8. The permeation characteristics of SB are summarized in Table 1. Figure 2 shows an example of an SB permeation profile to illustrate the permeation kinetics during 48 h. Cumulative amount-time profiles demonstrated the attainment of a steady-state flux of SB across the skin. SB flux was greatest from the saturated solution at pH 10.8 and least from that at pH 6. This trend corresponded to the trend in the concentrations of SB in different saturated solutions. When calibrated by the saturated solubility (K_p), the SB permeability from pH 6 buffer showed the greatest level, followed by pH 10.8, 9.9, and 8. For topical formulations, the drug skin content is considered an important parameter. In the present work, the skin deposition was determined at the end of the *in vitro* experiments as depicted in Table 1. The

Table 1. Permeation data of SB from aqueous solutions with various pH values. *n*=4. Mean±SD.

Vehicle	Flux ($\mu g \cdot cm^{-2} \cdot h^{-1} \times 10^{-3}$)	K_p ($cm/h \times 10^{-3}$)[a]	Calibrated skin deposition ($\times 10^{-1}$)[b]
pH 6 buffer	10.92±4.20	2.60±1.00	9.35±0.91
pH 8 buffer	48.18±13.02	0.74±0.20	8.31±1.09
pH 9.9 buffer	209.58±43.82	1.10±0.23	0.78±0.19
pH 10.8 buffer	858.95±124.32	1.52±0.22	0.17±0.02

[a] K_p, Permeability coefficient=Flux ($\mu g \cdot cm^{-2} \cdot h^{-1}$)/solubility (μg/mL).

[b] Calibrated skin deposition=compound amount retained in skin (μg/g)/solubility (μg/mL).

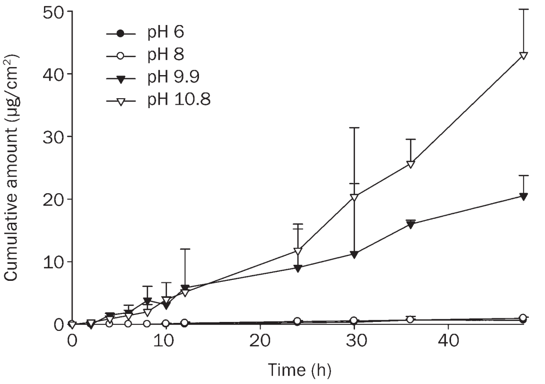

Figure 2. Cumulative amount versus time profiles of *in vitro* topical silibinin (SB) application permeating across nude mouse skin from aqueous buffers with different pH values. *n*=4. Mean±SD.

deposition of SB was noted to have an increasing trend as the pH of the donor compartment decreased. The calibrated skin deposition from pH 6 buffer exhibited a 55-fold increase compared to that from pH 10.8 buffer.

In vitro skin permeation of SB across various skin types

Although the examination of drug permeability across the skin is less advantageous when targeting skin tissue, an understanding of the permeability may be helpful to elucidate the mechanisms involved in the skin absorption of the drugs. Table 2 summarizes the K_p of SB across various skin membranes from pH 8 and 9.9 buffers. The K_p of SB with pH 8 buffer across delipidized skin showed a 2.15-fold ($P<0.05$) increase compared to that of intact skin. On the other hand, the data indicated that the K_p of SB with pH 9.9 buffer across delipidized skin was 11.46-fold higher ($P<0.05$) than that across intact skin. To further explore the permeation mechanisms of SB, α-terpineol and oleic acid were used to pretreat the skin. Ethanol at 25% was used as the pretreatment medium for solubility considerations. Ethanol had no statistically significant effect ($P>0.05$) on SB permeability at pH 8. Similar K_p values ($P>0.05$) were observed for permeation across skin treated with α-terpineol or oleic acid and 25% ethanol. Ethanol at 25% significantly increased ($P<0.05$) the K_p of SB compared to the control by 4.35-fold. The enhancement ratios (ERs) of K_p for α-terpineol and oleic acid were 11.35 and 4.90, respectively. This indicated that pretreatment of the skin with α-terpineol further increased the permeation of SB in a more-ionized form.

Table 2. Permeation data of SB from pH 8 and pH 9.9 aqueous solutions across various skin types. *n*=4. Mean±SD.

pH value	Skin type	K_p ($cm/h \times 10^{-3}$)[a]	Enhancement ratio (ER)[b]
pH 8	Intact skin	0.74±0.20	–
	Delipid skin	1.59±0.15	2.15
	25% ethanol treatment	0.93±0.47	1.26
	α-Terpineol treatment[c]	0.85±0.11	1.15
	Oleic acid treatment[c]	1.06±0.34	1.43
pH 9.9	Intact skin	1.10±0.23	–
	Delipid skin	12.61±0.45	11.46
	25% ethanol treatment	4.78±2.41	4.35
	α-Terpineol treatment[c]	12.49±0.48	11.35
	Oleic acid treatment[c]	5.39±0.91	4.90

[a] K_p, Permeability coefficient=Flux ($\mu g \cdot cm^{-2} \cdot h^{-1}$)/solubility (μg/mL).

[b] Enhancement ratio (ER), K_p across treated skin/K_p across intact skin.

[c] The medium is 25% ethanol.

Comparison of the *in vitro* skin absorption levels of SB, SD, and SC

The aqueous solubility and lipophilicity profiles of SD and SC were established for comparison with those of SB as shown in Table 3. The solubility increased in the order of SB<SD<SC in both pH 8 and 9.9 buffers. The lipophilicity ranking was evaluated by measuring the capacity factor (log K'), which indicates the relative retention of a compound in the HPLC system. The log K' result confirmed the greater lipophilicity of SB compared to SD and SC. Although there are similarities in the structures of silymarin constituents, the K_p and skin deposition of these compounds showed discrepancies as demonstrated in Figure 3. In the less-ionized form (pH 8), SC showed the highest K_p, followed by SB and SD ($P<0.05$). A similar trend was observed in the more-ionized form (pH 9.9) although higher values were detected for pH 9.9 compared to pH 8. The *in vitro* skin uptake of SB at pH 8 was ~4-fold higher than that of SD and SC into intact skin. A correlation

Table 3. Solubility (μg/mL) and capacity factor (log *K*') of SB, SD, and SC in various vehicles. *n*=6. Mean±SD.

Compound	Solubility in pH 8 buffer	Solubility in pH 9.9 buffer	log *K*'[a]
Silibinin (SB)	31.41±1.86	190.53±6.63	0.80
Silydianin (SD)	91.08±22.71	440.83±3.13	0.45
Silychristin (SC)	187.89±12.75	821.68±48.80	0.41

[a] log *K*', logarithm of $(t_r\text{-}t_0)/t_0$, t_r is the retention time of product peak, t_0 is the retention time of solvent peak.

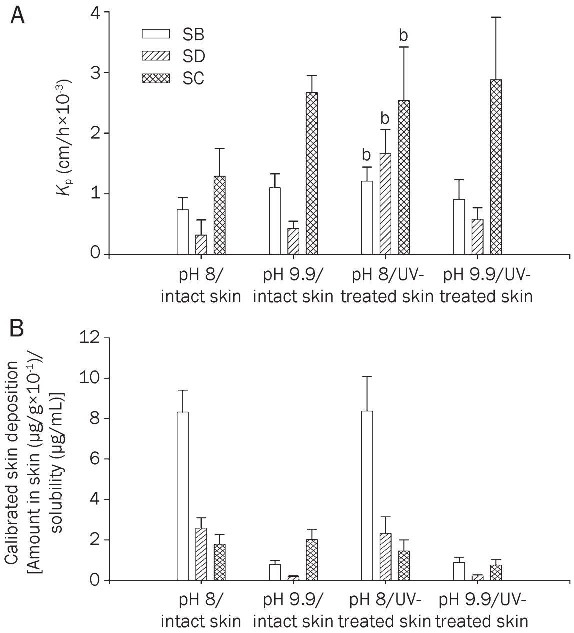

Figure 3. The permeability coefficient (K_p) (A) and in vitro calibrated skin deposition (B) of silibinin (SB), silydianin (SD), and silychristin (SC) from pH 8 and 9 buffers across intact or UVB-irradiated skin. *n*=4. Mean±SD. ^{b}*P*<0.05 *vs* pH 8/intact skin.

was noted between K_p and skin retention of these compounds with pH 9.9 buffer.

In vitro skin absorption across UVB-irradiated skin

The appearance, histological morphology, and compound delivery of UVB-irradiated skin were examined. Figure 4A and 4B depict representative examples of images of the skin surface without and with UVB exposure, respectively. UVB treatment was effective in inducing inflammatory responses including erythema and edema formation. The skin of mice was also desquamated after 7 d of UVB irradiation. As shown in Figure 4C and 4D, COX-2 expression was observed in epidermal cells of the dorsal skin of mice after UVB irradiation. Skin samples isolated from the treated area revealed an epidermal thickening in response to UVB-induced injury in these animals. The UVB irradiation increased the epidermal thickness by ~5-fold. Marked hyperplastic and hyperkeratotic changes with acanthosis were also detected. As shown in Figure 4E and 4F, the expression of PCNA was higher than without UVB irradiation. The PCNA results confirm cellular proliferation, reflecting the intense hyperproliferative process induced by 7 d of UVB exposure.

Figure 3 compares *in vitro* skin absorption of silymarin components *via* normal and hyperproliferative skin. UVB-irradiated skin exhibited higher K_p values compared to normal skin (*P*<0.05) in pH 8 buffer. ER values with UVB treatment were 2.58, 5.19, and 1.97 for SB, SD, and SC, respectively. The more-ionized form (pH 9.9) showed no significant differences (*P*>0.05) between the two skin types. UVB irradiation did not influence the *in vitro* skin uptake of these compounds in either pH 8 or 9.9 buffers (*P*>0.05).

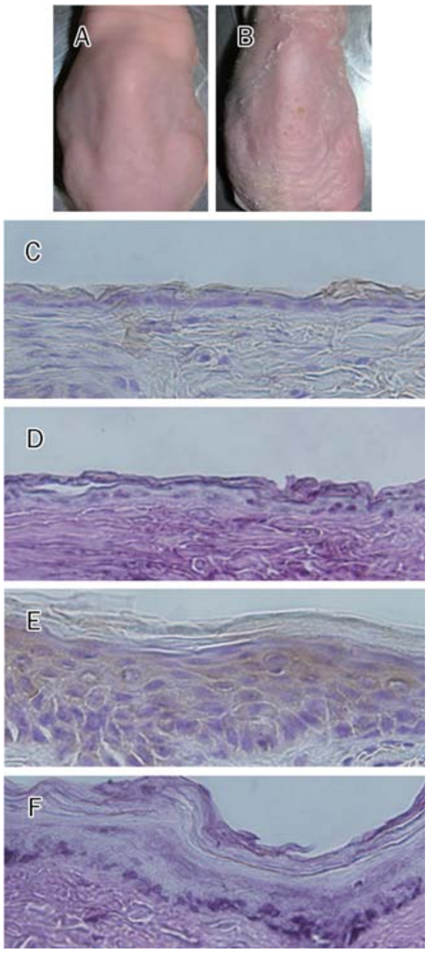

Figure 4. Images of nude mouse skin before and after UVB irradiation for 7 d: (A) clinical observation before UVB irradiation; (B) clinical observation after UVB irradiation; (C) COX-2 expression by immunochemical staining before UVB irradiation, ×400; (D) COX-2 expression by immunochemical staining after UVB irradiation, ×400; (E) PCNA expression by immunochemical staining before UVB irradiation, ×400; (F) PCNA expression by immunochemical staining after UVB irradiation, ×400.

In vivo skin absorption of SB, SD, and SC

Levels of flavonoids in the skin were determined following a single application to the dorsal surface of nude mice. The pH 8 buffer was selected as the vehicle because of the high compound accumulation within the skin in the *in vitro* status. Table 4 shows the *in vivo* skin deposition of SB, SD, and SC after topical delivery for 4 and 8 h. Similar to the *in vitro* results, the *in vivo* uptake of SB was greater than those of SD and SC. There was no significant difference (*P*>0.05) between the intradermal concentrations of any compound at 4 and 8 h.

Bioengineering methods such as TEWL, colorimetry, and pH for evaluating the safety of silymarin constituents on skin were conducted *in vivo*. The Δ value (the value of the treated site minus the value of an adjacent untreated site) of TEWL, skin redness (a*), and pH were determined after a 24-h admin-

Table 4. *In vivo* skin deposition of SB, SD, and SC from pH 8 aqueous solution. *n*=6. Mean±SD.

Compound	Calibrated skin deposition at 4 h (×10^{-1})^a	Calibrated skin deposition at 8 h (×10^{-1})^a
Silibinin (SB)	8.07±1.93	7.25±1.94
Silydianin (SD)	2.11±0.25	2.03±0.42
Silychristin (SC)	0.20±0.04	0.25±0.07

^{a} Calibrated skin deposition=compound amount retained in skin (μg/g)/solubility (μg/mL).

istration as shown in Figure 5. No significant skin irritation was determined when the bar of the standard deviation (SD) passes across the zero line in Figure 5. Silymarin constituents produced negligible changes in TEWL, suggesting a tolerance of the skin to topically applied formulations. Colorimetry measurements of a* in nude mice did not change during the full treatment, indicating that erythema formation was not induced. Only a slight increment (P<0.05) in the skin pH was observed in the case of SC.

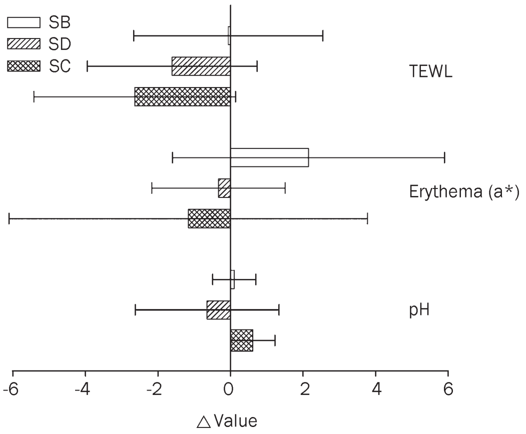

Figure 5. *In vivo* skin irritation examination determined by transepidermal water loss (TEWL), erythema (a*), and the pH value after a 24-h application of topically applied silibinin (SB), silydianin (SD), and silychristin (SC) from pH 8 buffer. The Δ value indicates the value of the treated site minus the value of an adjacent untreated site. *n*=6. Mean±SD.

Discussion

Studies focusing on the development of silymarin constituents with protective activity against UV-induced skin damage are intensively being carried out. Despite various reports linking the beneficial properties of silymarin to dermal use, no comprehensive study has been conducted investigating the skin absorption ability of these compounds. The purpose of this study was to identify formulation variables including pH and compounds that influence silymarin absorption via skin. We found that the structures of silymarin constituents largely affected their skin absorption. The results showed that SB exhibited considerable absorption into the skin, especially in the non-ionized form. Negligible skin irritation was also detected.

SB was first selected to evaluate its skin absorption because SB is the most active and abundant constituent present in silymarin[7]. In the skin absorption studies, the selection of a skin model is an important prerequisite. The most reliable skin absorption data are collected from human studies. However, such studies are generally not feasible during the initial development of a novel dosage form or system. The availability of such systems is also limited. The skin of rodents is most commonly used for *in vitro* and *in vivo* skin permeation studies. There are a number of hairless species (*eg*, nude mice and hairless rats) in which the absence of a hairy coat mimics the human skin better than hairy skin[15]. Hence nude mice were used as an animal model in this study. Although nude mouse skin is more permeable than human skin[16, 17], it is still a good model for examining the skin transport of permeants because of the limited variability among individuals and similar hair follicle density to human skin[18].

Saturated solutions were used for the skin absorption experiment to ensure that there was uniform thermodynamic activity and thus common activity by the compounds in each formulation[19, 20]. The pH of the aqueous vehicle was shown to be one of the major variables that can influence the diffusivity of drugs[21, 22]. The structures of silymarin constituents have multiple protonation sites. For example, the acidic-dissociation constants of SB at 37 °C were determined to be pK_{a1}=6.86, pK_{a2}=8.77, pK_{a3}=9.62, and pK_{a4}=11.38[23]. SB is predominantly in a non-ionic form in pH 6 buffer, which is beneficial due to its lipophilicity. The neutral form of a compound always shows higher skin partitioning compared to the ionic form because of the lipophilic characteristics of the stratum corneum. The ionized degree of SB increased following an increase in the donor pH value. The results showed that the skin deposition of SB from an aqueous solution was directly related to its lipophilicity.

The higher skin reservoir of non-ionic SB may result in a high release into the receptor compartment because of the fast diffusion due to the concentration gradient. However, the trend of K_p values from pH 8 to pH 10.8 somewhat differed from that of calibrated skin deposition although there was no significant difference (P>0.05) among K_p values from these three solutions. Increased pH can ionize a greater part of the intercellular fatty acids of the stratum corneum, changing the phase behavior and packing of the barrier lipid mixture[24]. A long-term application of an alkaline formulation on the skin surface might not be suitable for clinical use.

The predominant route for most permeant transport into or across the skin is the intercellular region of the stratum corneum. The delipidation process can remove intercellular lipids in the stratum corneum[20]. The stratum corneum is principally lipophilic in nature and far more resistant to polar than non-polar compounds. This speculation is consistent with the permeation profiles of SB with lipid removal which largely increased the permeation of the more-ionized form (pH 9.9) but not the less-ionized form (pH 8). SB in pH 9.9 buffer showed the highest enhancement of skin permeation across delipidized skin, suggesting that permeation through the stratum corneum layer was the rate-limiting process. The permeation of SB in pH 8 buffer was not greatly enhanced by the extraction of lipid bilayers, or the main barrier to permeation could lie in the lower viable skin layer. Thus, it appears that the stratum corneum was not the sole significant contributor to resistance to the less-ionized form of SB. However, it cannot be neglected that this superficial layer still constitutes an important barrier for SB in pH 8 buffer.

α-Terpineol and oleic acid are used as permeation enhancers for topical/transdermal drug delivery. Terpenes are known to act at the lipid polar heads of ceramides, while fatty acids act at the lipid tail portion of intercellular lipid bilayers[25, 26]. Neither enhancer in 25% ethanol was able to express any enhancing activity on the permeation of SB in the less-ionized form after disruption of the lipid bilayers. This suggests that SB in pH 8 buffer is easily partitioned into the bilayers. It also demonstrates that the intracellular route might not be important for lipophilic SB since oleic acid can affect corneocytes[27].

Ethanol at 25% increased SB permeation in pH 9.9 buffer by 4.35-fold. The ER by enhancers should be normalized to the value of 25% ethanol to neglect the vehicle influence. After calculation, it is found that α-terpineol but not oleic acid increased the permeation of the more-ionized form of SB. This result confirms that the lipid bilayers are the main barrier blocking the transit of ionic SB. Terpenes cause loosening of the lipid bilayers due to breaking of H-bonds between ceramides as they have the potential to accept or donate H-bonds[26]. The higher enhancement by α-terpineol than by oleic acid indicates that the diffusion of ionic SB along the lipid portion was more significant than that along the H-bonds between ceramides.

Skin absorption of a drug is determined by its physicochemical properties, in particular, the molecular weight and lipophilicity which play major roles in the process[20, 28]. SB, SD, and SC possess the same molecular weight of 482.4 Da. Therefore, any difference in skin absorption must have been attributable to another factor. There was a correlation between the skin deposition and lipophilicity of the three compounds in pH 8 buffer. The highest lipophilicity of SB increased partitioning into the stratum corneum, forming a reservoir. On the other hand, SC has an additional hydroxyl group in its structure compared to SB and SD. The extra moiety contributes to the lower lipophilicity of SC. The amount of SC retained in the skin was also less because of its more-hydrophilic properties compared to the other compounds. However, lipophilicity is not a common rule for explaining the absorption trend of these flavonoids. SD generally showed the lowest values of K_p and deposition among the three compounds. A cyclic ketone moiety forming a steric bridge is seen in SD's structure (Figure 1). Both SB and SC show a planar structure. Although the molecular weights of these compounds are the same, SD may present a larger molecular volume compared to SB and SC. This suggests evidence of the selective absorption of SD over SB and SC. In order to confirm this hypothesis, molecular modeling software (Discovery Studio® version 2.0, Accelrys Inc, San Diego, USA) was used to draw the stereo structure of the three flavonoids as shown in Figure 6. It is clearly seen that the three-dimensional structure of SD may hinder its penetration into skin. Further study is needed to explore the mechanisms involved in the relationship between the structure and skin absorption.

Figure 6. The stereo structure of silibinin (SB), silydianin (SD), and silychristin (SC) pictured by a molecular modeling software (Discovery Studio® version 2.0, Accelrys Inc, San Diego, USA).

It was expected that permeation through the skin would be reduced as the permeant is largely retained within the skin reservoir[29]. This theory can explain the contrary trend between K_p and skin deposition for the three flavonoids in the less-ionized form (pH 8). This phenomenon was not observed in pH 9.9 buffer since a direct correlation between K_p and skin deposition was achieved for the more-ionized form. The concentration gradient between the skin and receptor may have contributed to this result. This suggests that the degree of ionization can influence the delivery behavior via the skin route.

UVB exposure can trigger oxidative damage and inflammation of the skin, subsequently inducing prominent epidermal thickening. Inflammation and DNA damage occur with UVB irradiation which lead to COX-2 and PCNA expressions[30, 31]. PCNA expression is a marker of DNA repair and indirectly an indicator of UVB-induced damage[14]. These effects were confirmed by the histopathlogic profiles of skin tissue in the present study. When epidermal hyperplasia was well developed by UVB, K_p values of the flavonoids significantly increased in pH 8 buffer. The increment in thickness of the epidermis may have created a longer pathway through which the permeant had to pass. This was not the case in the present study. The inflammation produced disruption of the epidermal structure. As indicated in the previous section, viable epidermis/dermis is an important barrier for neutral SB permeation. This disruption may attenuate the barrier function of viable skin, leading to increased K_p values. This result was not observed for ionized SB, indicating a limited alteration of lipid bilayers of the stratum corneum after UVB irradiation. Although permeability across the skin could be enhanced after exposure, retention within the skin reservoir remained unchanged. This result indicates that the dermal use of silymarin constituents for topical aims can minimize absorption differentiation between normal and disordered skin. Most research papers have utilized healthy skin to examine drug absorption, and results from such studies might not be appropriately applied to predict the skin targeting ability of a drug on disordered skin. The skin model used in this work may be useful for resolving this problem.

The *in vivo* topical application data show that silymarin constituents were efficiently absorbed into intact skin. A good *in vitro-in vivo* correlation was observed for the skin absorption trends from various formulations. This suggests that the amount of flavonoids retained in the skin in the *in vitro* status can predict the *in vivo* compound accumulation within the skin. According to a previous study by Lu *et al*[32], the original contents of SB, SD, and SC in silymarin determined by HPLC were 33.40%, 3.51%, and 12.91%, respectively. It is beneficial for topical silymarin administration since SB, the compound with the highest percentage, showed greater skin absorption.

Besides the efficiency of diffusion into the skin, the skin tolerance is another concern for topical delivery systems. Many cutaneous reactions to herbal preparations and natural products have been reported[33, 34]. The most common cutaneous adverse effect is allergic contact dermatitis. By evaluating established endpoints of skin irritation (TEWL, skin redness, and pH), the present study demonstrates that the topical application of SB, SD, and SC for up to 24 h did not cause skin irritation. Oral administration and cell incubation of silymarin and the components have shown that they are well tolerated and do not cause any significant adverse health effects[6, 12, 35]. The same phenomenon was also observed in skin tissue.

Conclusions

The incidence of NMSC is directly associated with exposure to solar UV radiation. Chemoprevention of skin cancer using natural agents is suggested as a promising approach and has generated enormous research efforts in recent years. As demonstrated in this study, the compounds of silymarin were readily absorbed by the skin in both *in vitro* and *in vivo* experiments. SB showed higher skin absorption than SD and SC. The skin deposition of the non-ionic form was superior to that of ionic molecules. The viable epidermis/dermis represents an important barrier for non-ionic SB permeation via the skin. On the other hand, the stratum corneum is still the predominant permeation barrier for ionic SB. The uptake of silymarin constituents into the skin remained the same after UVB exposure. However, permeation across the skin significantly increased in pH 8 buffer by this irradiation. The preliminary safety examination of the skin showed an acceptable skin tolerance to SB, SD, and SC. This present work indicates the promise of further *in vivo* and clinical applications of silymarin delivery via the skin. Further study is needed to explore the the delivery vehicles with more-efficient absorption.

Acknowledgements

We thank the financial support from Chang Gung Memorial Hospital at Keelung (No CMRPG260212).

Author contribution

Jia-you FANG designed research; Chi-feng HUNG, Yin-ku LIN, and Li-wen ZHANG performed research; Ching-hsien CHANG contributed new analytical tools and reagents; Chi-feng HUNG analyzed data; Jia-you FANG wrote the paper.

References

1 Meeran SM, Katiyar S, Elmets CA, Katiyar SK. Silymarin inhibits UV radiation-induced immunosuppression through augmentation of interleukin-12 in mice. Mol Cancer Ther 2006; 5: 1660–8.

2 Dhanalakshmi S, Mallikarjuna GU, Singh RP, Agarwal R. Dual efficacy of silibinin in protecting or enhancing ultraviolet B radiation-caused apoptosis in HaCaT human immortalized keratinocytes. Carcinogenesis 2004; 25: 99–106.

3 Leiter U, Garbe C. Epidemiology of melanoma and nonmelanoma skin cancer — the role of sunlight. Adv Exp Med Biol 2008; 624: 89–103.

4 Ramos J, Villa J, Ruiz A, Armstrong R, Matta J. UV dose determines key characteristics of nonmelanoma skin cancer. Cancer Epidemiol Biomarkers Prev 2004; 13: 2006–11.

5 Afaq F, Adhami VM, Mukhtar H. Photochemoprevention of ultraviolet B signaling and photocarcinogenesis. Mutat Res 2005; 571: 153–73.

6 Gažák R, Walterová D, Křen V. Silybin and silymarin — new and emerging applications in medicine. Curr Med Chem 2007; 14: 315–38.

7 Singh RP, Agarwal R. Flavonoid antioxidant silymarin and skin cancer. Antioxid Redox Signal 2002; 4: 655–63.

8 Pinnel SR. Cutaneous photodamage, oxidative stress, and topical antioxidant protection. J Am Acad Dermatol 2003; 48: 1–22.

9 Yang B, Kotani A, Arai K, Kusu F. Estimation of the antioxidant activities of flavonoids from their oxidation potentials. Anal Sci 2001; 17: 599–604.

10 Zielińska-Przyjemska M, Wiktorowicz K. An *in vitro* study of the protective effect of the flavonoid silydianin against reactive oxygen species. Phytother Res 2006; 20: 115–9.

11 Gu M, Singh RP, Dhanalakshmi S, Agarwal C, Agarwal R. Silibinin inhibits inflammatory and angiogenic attributes in photocarcinogenesis in SKH-1 hairless mice. Cancer Res 2007; 67: 3483–91.

12 Svobodová A, Zdařilová A, Mališková J, Mikulková H, Walterová D, Vostalová J. Attenuation of UVA-induced damage to human keratinocytes by silymarin. J Dermatol Sci 2007; 46: 21–30.

13 Zhao J, Agarwal R. Tissue distribution of silibinin, the major active constituent of silymarin, in mice and its association with enhancement of phase II enzymes: implications in cancer chemoprevention. Carcinogenesis 1999; 20: 2101–8.

14 Moore JO, Palep SR, Saladi RN, Gao D, Wang Y, Phelps RG, *et al*. Effects of ultraviolet B exposure on the expression of proliferating cell nuclear antigen in murine skin. Photochem Photobiol 2004; 80: 587–95.

15 Godin B, Touitou E. Transdermal skin delivery: predictions for humans from *in vivo*, *ex vivo* and animal models. Adv Drug Deliv Rev 2007; 59: 1152–61.

16 Catz P, Friend D. Transdermal delivery of levonorgestrel: VIII. Effect of enhancers on rat skin, hairless mouse skin, hairless guinea pig skin, and human skin. Int J Pharm 1990; 58: 93–102.

17 Fang JY, Fang CL, Sung KC, Chen HY. Effect of low frequency ultrasound on the *in vitro* percutaneous absorption of clobetasol 17-propionate. Int J Pharm 1999; 191: 33–42.

18 Sloan KB, Wasdo S. Designing for topical delivery: prodrugs can make the difference. Med Res Rev 2003; 23: 763–93.

19 Cole L, Heard C. Skin permeation enhancement potential of *aloe vera*

and a proposed mechanism of action based upon size exclusion and pull effect. Int J Pharm 2006; 333: 10–6.

20 Huang ZR, Hung CF, Lin YK, Fang JY. *In vitro* and *in vivo* evaluation of topical delivery and potential dermal use of soy isoflavones genistein and daidzein. Int J Pharm 2008; 364: 36–44.

21 Shin SC, Kim HJ, Oh IJ, Cho CW, Yang KH. Development of tretinoin gels for enhanced transdermal delivery. Eur J Pharm Biopharm 2005; 60: 67–71.

22 Hung CF, Lin YK, Huang ZR, Fang JY. Delivery of resveratrol, a red wine polyphenol, from solutions and hydrogels *via* the skin. Biol Pharm Bull 2008; 31: 955–62.

23 Meloun M, Burkoňová D, Syrový T, Vrána A. Thermodynamic dissociation constants of silychristin, silybin, silydianin and mycophenolate by the regression analysis of spectrophotometric data. Anal Chim Acta 2003; 486: 125–41.

24 Vávrová K, Lorencová K, Klimentová J, Novotný J, Holý A, Hrabálek A. Transdermal and dermal delivery of adefovir: effects of pH and permeation enhancers. Eur J Pharm Biopharm 2008; 69: 597–604.

25 Jain AK, Thomas NS, Panchagnula R. Transdermal drug delivery of imipramine hydrochloride. I. Effect of terpenes. J Control Release 2002; 79: 93–101.

26 Panchagnula R, Desu H, Jain A, Kriandarilli S. Effect of lipid bilayer alteration on transdermal delivery of a high-molecular-weight and lipophilic drug: studies with paclitaxel. J Pharm Sci 2004; 93: 2177–83.

27 Touitou E, Godin B, Karl Y, Bujanover S, Becker Y. Oleic acid, a skin penetration enhancer, affects Langerhans cells and corneocytes. J Control Release 2002; 80: 1–7.

28 Marti-Mestres G, Mestres JP, Bres J, Martin S, Ramos J, Vian L. The "*in vitro*" percutaneous penetration of three antioxidant compounds. Int J Pharm 2007; 331: 139–44.

29 Batchelder RJ, Calder RJ, Thomas CP, Heard CM. *In vitro* transdermal delivery of the major catechins and caffeine from extract of *Camellia sinensis*. Int J Pharm 2004; 283: 45–51.

30 Chang HW, Lai YC, Cheng CY, Ho JL, Ding ST, Liu YC. UV inducibility of rat proliferating cell nuclear antigen gene promoter. J Cell Biochem 1999; 73: 423–32.

31 Athar M, An KP, Morel KD, Kim AL, Aszterbaum M, Longley J, *et al*. Ultraviolet B (UVB)-induced COX-2 expression in murine skin: an immunohistochemical study. Biochem Biophys Res Commun 2001; 280: 1042–7.

32 Lu C, Lu Y, Chen J, Zhang W, Wu W. Synchronized and sustained release of multiple components in silymarin from erodible glyceryl monostearate matrix system. Eur J Pharm Biopharm 2007; 66: 210–9.

33 Stratton SP, Bangert JL, Alberts DS, Dorr RT. Dermal toxicity of topical (−)epigallocatechin-3-gallate in BALB/c and SKH1 mice. Cancer Lett 2000; 158: 47–52.

34 Bedi MK, Shenefelt PD. Herbal therapy in dermatology. Arch Dermatol 2002; 138: 232–42.

35 Gu M, Dhanalakshmi S, Mohan S, Singh RP, Agarwal R. Silibinin inhibits ultraviolet B radiation-induced mitogenic and survival signaling, and associated biological responses in SKH-1 mouse skin. Carcinogenesis 2005; 26: 1404–13.

Acta Pharmacologica Sinica (2010) 31: 127–136
© 2010 CPS and SIMM All rights reserved 1671-4083/10 $32.00
www.nature.com/aps

Original Article

Preparation, characterization and *in vivo* evaluation of bergenin-phospholipid complex

Xuan QIN[1], Yang YANG[1], Ting-ting FAN[1], Tao GONG[1], Xiao-ning ZHANG[2], Yuan HUANG[1,*]

[1]*Key Laboratory of Drug Targeting and Drug Delivery System, Ministry of Education, West China School of Pharmacy, Sichuan University, Chengdu 610041, China;* [2]*School of Medicine, Tsinghua University, Beijing 100084, China*

Aim: To prepare a bergenin-phospholipid complex (BPC) to increase oral bioavailability of the drug.
Methods: In order to obtain the acceptable BPC, a spherical symmetric design-response surface methodology was used for process optimization. The influence of reaction medium, temperature, drug concentration and drug-to-phospholipid ratio on the combination percentage and content of bergenin in BPC were evaluated. BPC was then characterized by thin-layer chromatography (TLC), high-performance liquid chromatography (HPLC), ultra-violet (UV) spectroscopy, fourier transform infrared spectroscopy (FT-IR), differential scanning calorimetry (DSC) and X-ray powder diffraction. The physicochemical properties such as microscopic shape, particle size, zeta-potential, solubility, crystalline form, and hygroscopicity were tested. The pharmacokinetic characteristics and bioavailability of BPC were investigated after oral administration in rats in comparison to bergenin and the physical mixture (bergenin and phospholipids).
Results: BPC was successfully prepared under the optimum conditions [temperature=60 °C, drug concentration=80 g/L and drug-to-phospholipids ratio=0.9 (*w/w*)]. The combination percentage was 100.00%±0.20%, and the content of bergenin in the complex was 45.98%±1.12%. Scanning electron microscopy and transmission electron microscopy of BPC showed spherical particles. The average particle size was 169.2±20.11 nm and the zeta-potential was –21.6±2.4 mV. The solubility of BPC in water and in *n*-octanol was effectively enhanced. The $C_{\max}$ and $AUC_{0\rightarrow\infty}$ of BPC were increased, and the relative bioavailability was significantly increased to 439% of bergenin.
Conclusion: The BPC is a valuable delivery system to enhance the oral absorption of bergenin.

Keywords: bergenin; phospholipid complex; spherical symmetric design-response surface methodology; physicochemical properties; bioavailability

---

Acta Pharmacologica Sinica (2010) 31: 127–136; doi: 10.1038/aps.2009.171;

Introduction

Bergenin (3,4,8,10-tetrahydroxy-2-hydroxymethyl-9-methoxy-2,3,4,4a-tetrahydropyrano[3,2-c]isochromen-6-one) is a major component of traditional Chinese medicine *Bergenia crassiflora*[1, 2]. Bergenin has been widely used for the treatment of chronic bronchitis and has other effects such as antitussive, hepatoprotective, anti-inflammatory, neuroprotective and weak anti-HIV activities[3–6]. Although bergenin has been used for more than 30 years, its poor oral bioavailability is still an obstacle to its further application[7]. The Biopharmaceutics Classification System (BCS) classifies drugs into four categories depending on their solubility and permeability characteristics[8]. According to this scheme, as a class IV compound, bergenin has neither sufficient solubility nor permeability for complete absorption[9]. Furthermore, conventional tablet is the formulation of bergenin on the market, but a high dose (375 mg/d) has to be used in order to exert therapeutic effects. Many efforts have been made to enhance its bioavailability, such as structure modification, prodrugging and new dosage forms such as dripping pills, soft capsules and β-cyclodextrin inclusion complexes[10–14]. However, no data has been published in relation to the improved bioavailability after oral administration.

In this study, a phospholipid complex was adopted to increase both the water solubility and liposolubility of bergenin to enhance its oral bioavailability. The preparation of the bergenin-phospholipid complex (BPC) was optimized by a spherical symmetric design-response surface methodology. Furthermore, the physicochemical properties and oral bioavailability of BPC was explored in comparison to bergenin

---

* To whom correspondence should be addressed.
E-mail huangyuan0@yahoo.com.cn
Received 2009-07-20 Accepted 2009-10-29

and the physical mixture (bergenin and phospholipids).

Materials and methods

Materials

Bergenin was kindly supplied by Sichuan Dihon Medical Development Co, Ltd (Chengdu, China). Phospholipid was purchased from Shanghai Toshisun Enterprise Co, Ltd (Shanghai, China), and the phosphatidyl content was approximately 80% (*w/w*). Methanol and water were of HPLC grade. All the other reagents and solvents were of the highest purity commercially available.

Chromatography

A sensitive HPLC assay was developed to analyze the content of bergenin. The HPLC instrument employed was an Alltech™ (manufactured by Alltech Technologies, USA) LC system with a model 426 pump and model UVIS-201 absorbance detector. The output signal was monitored and processed using the AllChrom™ Plus Chromatograph Data System (designed by Multilink Services Co Ltd). The columns were Dikma Diamonsil® C_{18} (150×4.6 mm, 5 μm) and Dikma EasyGuard 6101 C_{18} kit guard column. The mobile phase was a mixture of methanol-water (20:80, *v/v*, pH 2.50) at a flow rate of 1 mL/min. The wavelength was set at 275 nm. All analyses were performed at 30 °C.

Preparation of BPC

A weighed amount of bergenin and phospholipids were charged in a round bottom flask and dissolved in anhydrous ethanol. The mixture was refluxed at a controlled temperature for about 2 h. The resultant clear solution was evaporated and dried under vacuum (40 °C). The residues were then gathered and placed in desiccators.

Preliminary investigations of the process parameters revealed that reaction temperature (X_1), drug concentration (X_2) and the drug to phospholipid ratio (X_3) highly influenced both the combination percentage (Y_1) and content of bergenin (Y_2). A statistical model incorporating interactive and polynomial terms was used to evaluate the response employing the equation:

$$Y=b_0+b_1X_1+b_2X_2+b_3X_3+b_4X_1^2+b_5X_2^2+b_6X_3^2+b_7X_1X_2+b_8X_1X_3+b_9X_2X_3$$

where Y was the dependent variable, b_0 was the intercept representing the arithmetic average of the 15 runs, and b_1 to b_9 were the estimated coefficients for the factors (X_i, i=1, 2, 3). X_1, X_2, and X_3 were the coded levels of the independent variable(s). The interaction terms X_1X_2, X_1X_3, and X_2X_3 showed how the response changed when two factors were changed simultaneously. The polynomial terms (X_i^2) were included to investigate nonlinearity. The level values of three factors and the composition of central composite design batches 1 to 15 are shown in Tables 1 and 2.

The combination percentage of bergenin was calculated using the following equation: Combination percentage (%)=(A–B)/A*100%, where A was the weighed amount of bergenin for preparing the complex and B was the content not forming a complex. The content of bergenin in the complex was estimated by HPLC. It was calculated as: content (*w/w*, %)=C/D*100%, where C was the amount of bergenin that formed a complex and D was the weight of the BPC.

Table 1. Independent variables and their correspondent values for optimization of BPC preparation using the spherical symmetric design-response surface methodology.

Variables	Levels				
	-1.732	-1	0	1	1.732
X_1	30	38.45	50	61.55	70
X_2	20	36.91	60	83.09	100
X_3	0.4	0.57	0.8	1.03	1.2

Table 2. Response values of different variables for the optimization of BPC preparation using the spherical symmetric design-response surface methodology.

Formulation	Factors			Responses	
	X_1	X_2	X_3	Y_1	Y_2
1	-1	-1	-1	100.00	34.70
2	-1	-1	1	98.82	47.02
3	-1	1	-1	67.19	26.76
4	-1	1	1	76.19	43.06
5	1	-1	-1	97.82	37.22
6	1	-1	1	90.25	46.13
7	1	1	-1	98.44	35.91
8	1	1	1	96.85	47.07
9	-1.732	0	0	65.27	32.97
10	1.732	0	0	99.12	43.50
11	0	-1.732	0	100.00	45.78
12	0	1.732	0	90.11	45.36
13	0	0	-1.732	100.00	26.94
14	0	0	1.732	90.74	49.85
15	0	0	0	100.00	41.41

Thin-layer chromatography (TLC)

Sample solutions were prepared by dissolving bergenin, phospholipids, the physical mixture and BPC in methanol. TLC plates were precoated with silica gel at a 0.15−0.2 mm thickness. The plates were saturated with a solvent system of acetic ether:methanol (5:1, *v/v*), developed to a distance of about 4.5 cm and removed from the chamber to dry in air. Phospholipids were visualized by ninhydrin, and the spot of bergenin was observed with a ZF-I ultraviolet analysis instrument (Shanghai Gucun Optic Instrument Factory, China).

Ultraviolet (UV) spectra, HPLC, and Fourier Transform Infrared spectra (FT-IR)

Tested samples were dissolved in water and then scanned with a UV spectrometer (Varian Cary 100, America) over the wavenumber range of 200−600 nm. For HPLC, a 10 μL aliquot sample solution was injected into the HPLC. The FT-IR spectra were recorded on an FT-IR spectrometer (VECTOR 22, Bruker, Germany) after the samples were compressed into a KBr pellet.

Differential scanning calorimetry (DSC)

The samples were sealed in an aluminum crimp cell and heated at 5 °C/min from 0 to 300 °C in a nitrogen atmosphere at a flow rate of 50 mL/min. The peak transition onset temperature of bergenin, phospholipids, BPC and the physical mixture were determined and compared with the help of a differential scanning calorimeter (EXSTAR6000 DSC, Japan).

X-ray powder diffraction

The X-ray diffraction was recorded on an X-ray diffractometer (PHILIPS X'Pert Pro MPD DY1291, Japan). Samples of certain weight were added into the slide for packing prior to X-ray scanning. Spectra of graphs were plotted from 3.00° to 65.00° of 2 θ with a step width of 0.03° and step time of 0.2 s at room temperature.

Morphological characteristics

The samples were coated with platinum in a sputter coater, and their surface morphology was viewed and photographed with a scanning electron microscope (SEM). A transmission electron microscope (TEM, H-600IV, Hitachi, Japan) was used for microscopic characterization of the complex. The complex was suspended in distilled water, and a drop was placed on a carbon-coated copper grid. The films on the grid were negatively stained by immediately adding a drop of 2% (*w/w*) ammonium molybdate in 2% (*w/v*) ammonium acetate buffer (pH 6.8), removing the excess staining solution with a filter paper and air-drying.

Particle size and zeta-potential

The particle size and zeta-potential of BPC were determined at 25 °C using photon correlation spectroscopy (Malvern ZetaSize Nano ZS90, UK). A proper dilution of the suspension was prepared with double-distilled water before each analysis.

Solubility studies

Solubility determination was carried out by adding an excess of sample to 5 mL of water or *n*-octanol in sealed glass containers at 25 °C. Each experiment was performed in triplicate. The liquids were agitated for 24 h and then centrifuged to remove solid substances (12000×*g*, 5 min). The supernatant was filtered through a 0.45 μm membrane. Then, 1 mL of filtrate was mixed with 9 mL of solvent, and a 10 μL aliquot of the resulting solution was injected into an HPLC.

Hygroscopicity

Solid samples were stored under controlled temperature and humidity conditions to investigate the ability of bergenin and BPC to take up water from the environment. The relative humidity (RH) at 25 °C was prepared using saturated solutions with known RH values (22.45%, 42.76%, 57.7%, 75.28%, 84.26%, 92.50%, and 98.00%) in desiccators[15]. Certain amounts of samples were weighed and put into open clear glass bottles that were exposed to the desired RH. The gain in weight of the samples was determined up to saturation humidity. At each investigated RH, samples were prepared in triplicate.

Pharmacokinetic study in rats

Experiment design

Male Wistar rats (250±20 g) were obtained from the Laboratory Animal Center of Sichuan University. All experiments were approved by the Institutional Animal Care and Use Committee of Sichuan University. Animals were divided randomly into three groups (*n*=5). Each group of rats was given a single oral dose of free bergenin, the physical mixture or BPC (equivalent to 300 mg of bergenin). Blood samples were obtained at appropriate time points; 0.2 mL of plasma was separated by centrifugation (12000×*g*) for 5 min and then stored at -20 °C until analysis.

Plasma sample preparation

The preparation method of the plasma samples was developed in our laboratory to quantify the bergenin concentration in biosamples[16]. When the plasma sample was thawed, 20 μL of the IS solution was added and agitated for 20 s. Then 600 μL of ethyl acetate was added and shaken for 2 min, and sonic oscillation was performed to obtain complete extraction. The extracts were then centrifuged at 3000×*g* to achieve better phase separation. This procedure was repeated three times, and all of the supernatant was mixed and dried under vacuum. The residues were reconstituted with 100 μL of mobile phase and then centrifuged at 12000×*g* for 2 min. A 20 μL aliquot of the supernatant was then injected into the HPLC system.

Pharmacokinetic parameters

The pharmacokinetic parameters for bergenin in plasma were estimated by appropriate compartmental methods. All parameters were determined from the sample collection times and the assayed concentrations at these time points. Plasma concentrations were plotted against time, and the pharmacokinetic calculations were performed using the standard software program DAS 2.0 (Drug and Statistics, Anhui, China). The following parameters were estimated: absorption half-life ($t_{1/2\alpha}$), elimination half-life ($t_{1/2\beta}$), maximal plasma concentration (C_{max}), area under the plasma concentration time curve (AUC), and mean residence time (MRT). Free bergenin was taken as the control group to calculate the relative BA values.

Results

Preparation of BPC

The experimental results concerning the tested variables on the combination or content of bergenin in the complex are shown in Table 2. A mathematical relationship between factors and parameters was generated by response surface regres-

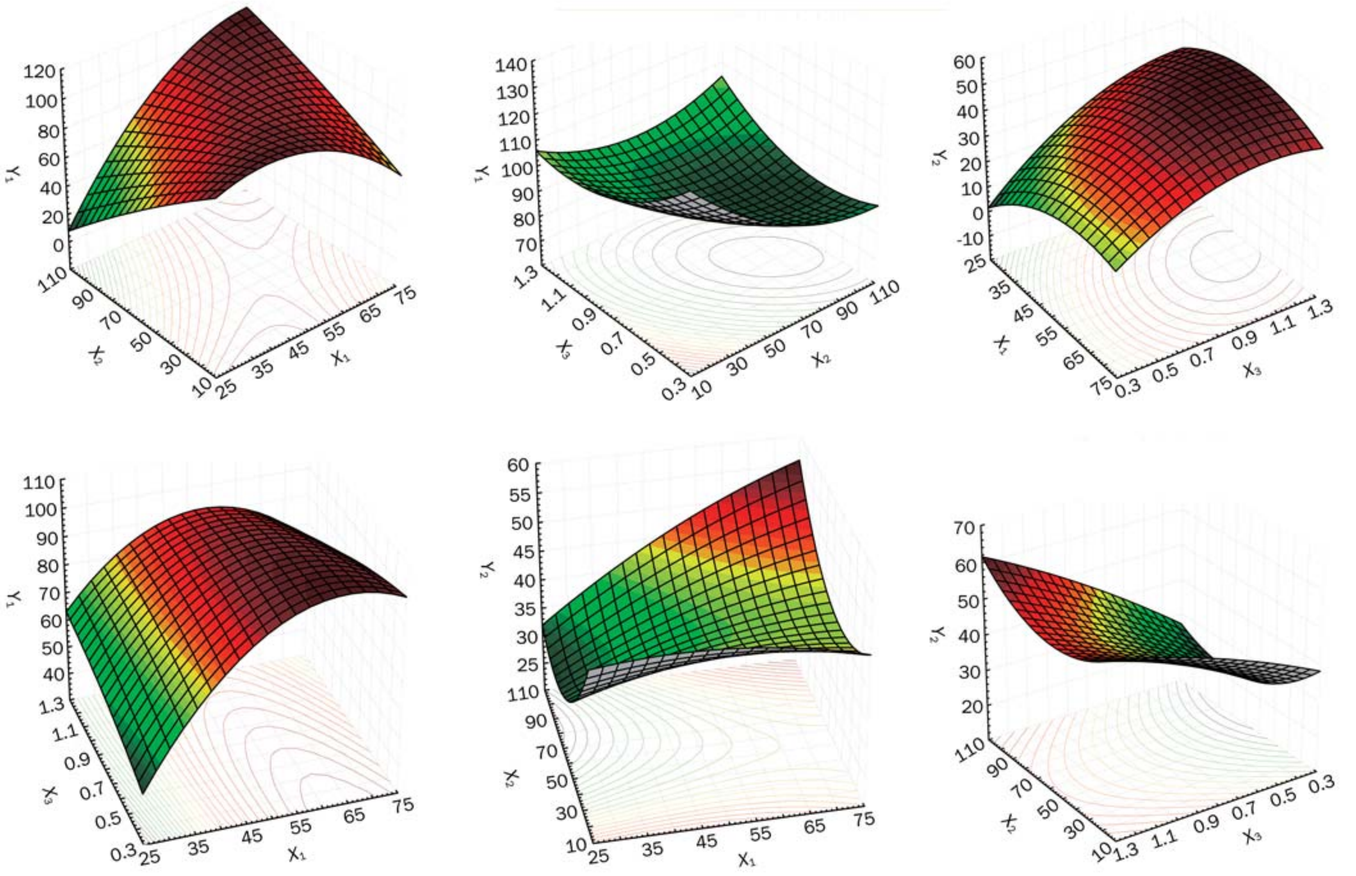

Figure 1. Response surface plot showing the influence of reaction temperature (X_1), drug concentration (X_2), drug to phospholipids ratio (X_3) on combination percentage (Y_1) and content of bergenin (Y_2).

sion analysis in the software STATISTICA 6.0. The three-dimensional response surface plots for the most statistically significant variables on the evaluated responses are shown in Figure 1. The equations represented the quantitative effect of process variables (X_1, X_2, and X_3), and their interactions on their responses Y_1 and Y_2 are listed as follows:

$$Y_1=17.8292+3.9683X_1-1.5953X_2+59.0044X_3-0.0448X_1^2-0.0032X_2^2 -29.5646X_3^2+0.0294X_1X_2-0.7960X_1X_3+0.3788X_2X_3$$

$$Y_2=-10.7459+1.1372X_1-0.6964X_2+74.4763X_3-0.0094X_1^2+0.0022X_2^2 -22.4228X_3^2+0.0054X_1X_2-0.4008X_1X_3+0.1462X_2X_3$$

The polynomial models for Y_1 and Y_2 were found to be significant, with F values of 482.45 and 760.97, respectively ($P<0.05$). The values of correlation coefficients (R) were found to be 0.9670 and 0.9892, respectively, indicating a good fit to the quadratic model.

The response surface and contour plots (Figure 1) clearly indicated that X_1, X_2, and X_3 strongly influenced the combination percentage (Y_1) and content of bergenin (Y_2). The combination (%) for the 15 batches showed a wide variation of 65.27% to 100.00%, and the content was in the range of 26.94% to 49.85% (Table 2). It was found that an increase in reaction temperature led to an increase of combination percentage and drug content. The drug-to-phospholipids ratio was an important factor affecting the drug content.

In order to evaluate the optimization capability of the models generated according to the results of the spherical symmetric design-response surface methodology, the BPC was prepared using the optimal process variable settings, where X_1, X_2, and X_3 were equal to 60 °C, 80 g/L and 0.9, respectively (Table 3). The combination percentage was 100.00%, and the content of bergenin in the complex was 45.98%±1.12%. The results illustrated a good relationship between the experimental and predicted values, which confirmed the practicability and validity of the model. The predicted error for all the response variables was below 3%, indicating that the optimization technique was appropriate for optimizing BPC.

Table 3. Comparison of the observed and predicted values in BPC prepared under predicted optimum conditions.

Response variable	Predicted value	Observed value	Bias (%)
Combination (%)	100.00	100.00±0.20	0
Content (%)	47.37	45.98±1.12	-2.93

Thin-layer chromatography (TLC)

The chromatogram of BPC was the same as the physical mixture. Two spots were observed (Figure 2): one was similar to the phospholipids (on the starting line), and the other had the same R_f as bergenin (R_f=0.58). No new spot was found.

UV, HPLC, and FT-IR spectrum

The UV spectra are shown in Figure 3. The phospholipids showed only end absorptions close to 200 nm. The absorption curves of bergenin, the physical mixture and BPC were nearly the same. Two characteristic absorption bands of bergenin were observed at 220 and 275 nm, which was in accordance with the Pharmacopoeia of PRC[17]. The retention time of BPC was the same as bergenin, and no new peak was present in the HPLC chromatogram (Figure 4). As shown in Figure 5,

Figure 2. TLC of phospholipids (a), bergenin (b), physical mixture (c), and BPC (d).

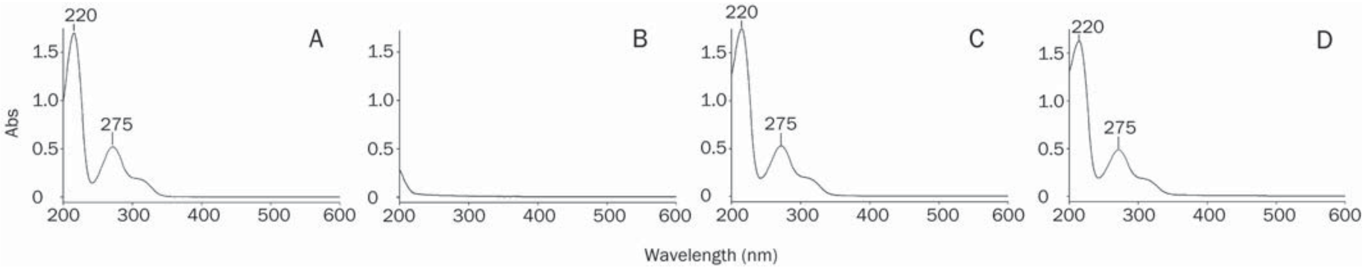

Figure 3. UV spectra of bergenin (A), phospholipids (B), physical mixture (C), and BPC (D).

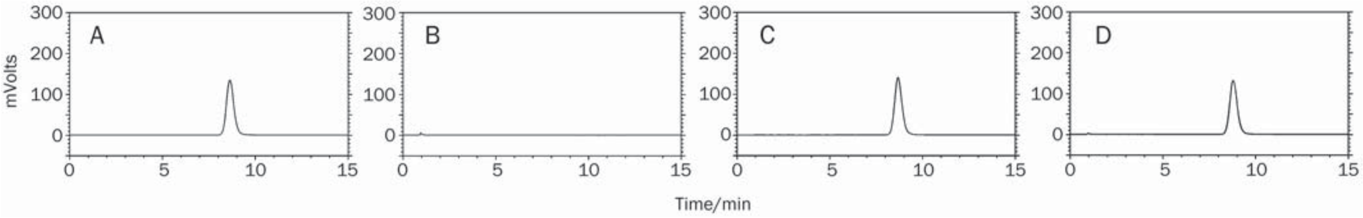

Figure 4. HPLC of bergenin (A), phospholipids (B), physical mixture (C), and BPC (D). The mobile phase was consisted of methanol-water (20:80, *v/v*), pH 2.50.

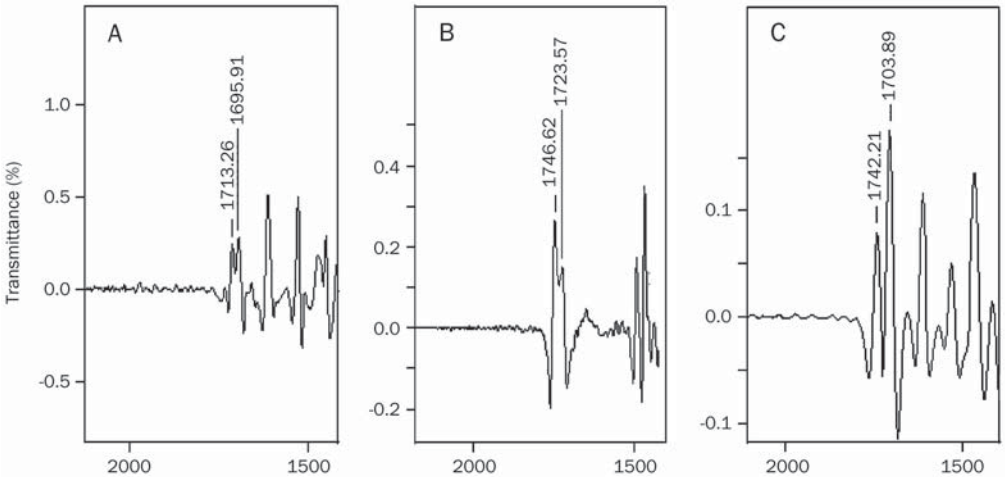

Figure 5. FT-IR spectra of bergenin (A), phospholipids (B), and BPC (C).

the carbonyl absorptions (C=O) of bergenin and the phospholipids were at 1713 cm^{-1} and 1746 cm^{-1}, respectively. Bergenin contains phenolic hydroxyl groups, and hydrogen bonding interactions between molecules was observed (1695 cm^{-1}). The hydrogen bonds between molecules of phospholipids were present at 1723 cm^{-1}. The hydrogen bonds in BPC (1703 cm^{-1}) were different from the bonds in either bergenin or the phospholipids.

Differential scanning calorimetry (DSC)

DSC thermograms of bergenin (a), phospholipids (b), the physical mixture (c) and BPC (d) are shown in Figure 6. The thermogram of bergenin exhibited peaks at 143.0, 153.5, and 240.7 °C. The peak at 240.7 °C was very sharp and appeared to be due to a phase transition from solid to liquid, which is in accordance with a report that 232−240 °C is the melting point of bergenin[17]. DSC of BPC showed that the endothermal peaks of bergenin and phospholipids disappeared.

X-ray powder diffraction

The powder of X-ray diffraction patterns of bergenin, the physical mixture and BPC are shown in Figure 7. Bergenin displayed partial sharp crystalline peaks, which is characteristic of a molecule with some crystallinity. The physical mixture exhibited both crystalline peaks and a wide peak due to the phospholipids. Compared with the above two, the crystalline peaks disappeared in the complex.

Morphological characteristics of BPC

The SEM and TEM photographs are shown in Figures 8 and 9. Bergenin exhibited a distinctive external crystal shape. BPC did not exist on the appearance of drug but appeared to be spherical with a smooth surface.

Particle size and zeta-potential

The particle size of BPC was distributed in a narrow range of 169.2±20.11 nm, and the PDI was 0.212±0.032. The zeta-potential is a key factor that could influence some properties of the particles, such as the stability in solution and interaction with other materials. However, no studies have been published to date in relation to this aspect of phospholipid complexes. The zeta-potential of BPC prepared in our experiment was -21.6±2.4 mV, which might be related to the type and composition of the phospholipids.

Solubility studies

The data showed that the solubility of BPC in *n*-octanol or water was increased 177.32- and 6.03-times higher than bergenin, respectively (Table 4, 5). The results also indicated that, for the physical mixture, the phospholipids enhanced the solubility of the drug, but this effect was weaker.

Table 4. Apparent solubility of bergenin and BPC in water at 25 °C. *n*=3.

Sample	Apparent solubility (mg/mL) 1	2	3	Mean±SD
Bergenin	1.35	1.39	1.36	1.37±0.02
Physical mixture	1.55	1.46	1.36	1.46±0.08
BPC	10.38	8.96	9.55	9.63±0.58

Table 5. Apparent solubility of bergenin and BPC in *n*-octanol at 25 °C. *n*=3.

Sample	Apparent solubility (mg/mL) 1	2	3	Mean±SD
Bergenin	0.71	0.70	0.74	0.72±0.02
Physical mixture	1.15	1.17	1.13	1.15±0.02
BPC	135.40	116.06	133.73	128.39±8.75

Hygroscopicity studies

In our experiments, we found that BPC could absorb moisture in the air and become viscous. Little information was available about this aspect, so the critical relative humidity (CRH) was investigated. The weight increases of bergenin stored at 22.45%−98.00% RH (25 °C) are shown in Figure 10. It was demonstrated that the bulk drug gained weight very slightly (-0.03%−0.19% *w/w*), which suggested a good stability of bergenin in response to moisture during formulation and storage. When the drug was formed into the complex, the hygroscopicity was stronger. The CRH was about 80% at 25 °C, suggesting that BPC should be stored under relatively dry conditions (RH<80%).

Pharmacokinetic study in rats

After administration of a single dose (300.0 mg/kg) of ber-

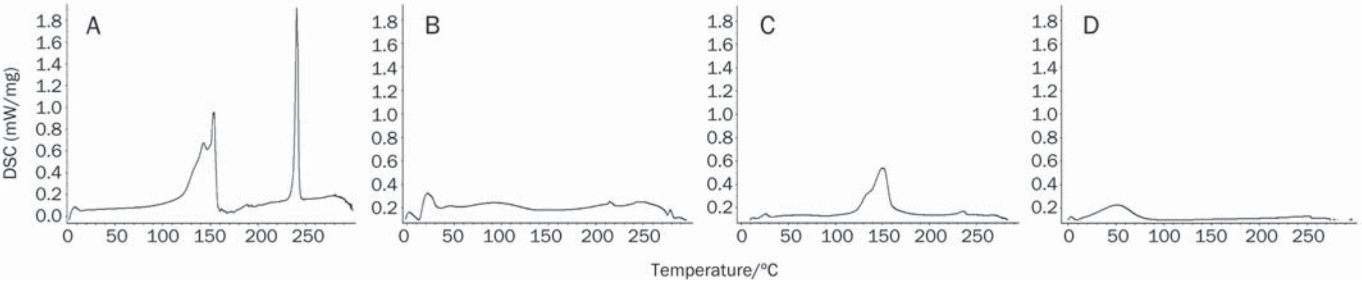

Figure 6. DSC thermograms of bergenin (A), phospholipids (B), physical mixture (C), and BPC (D).

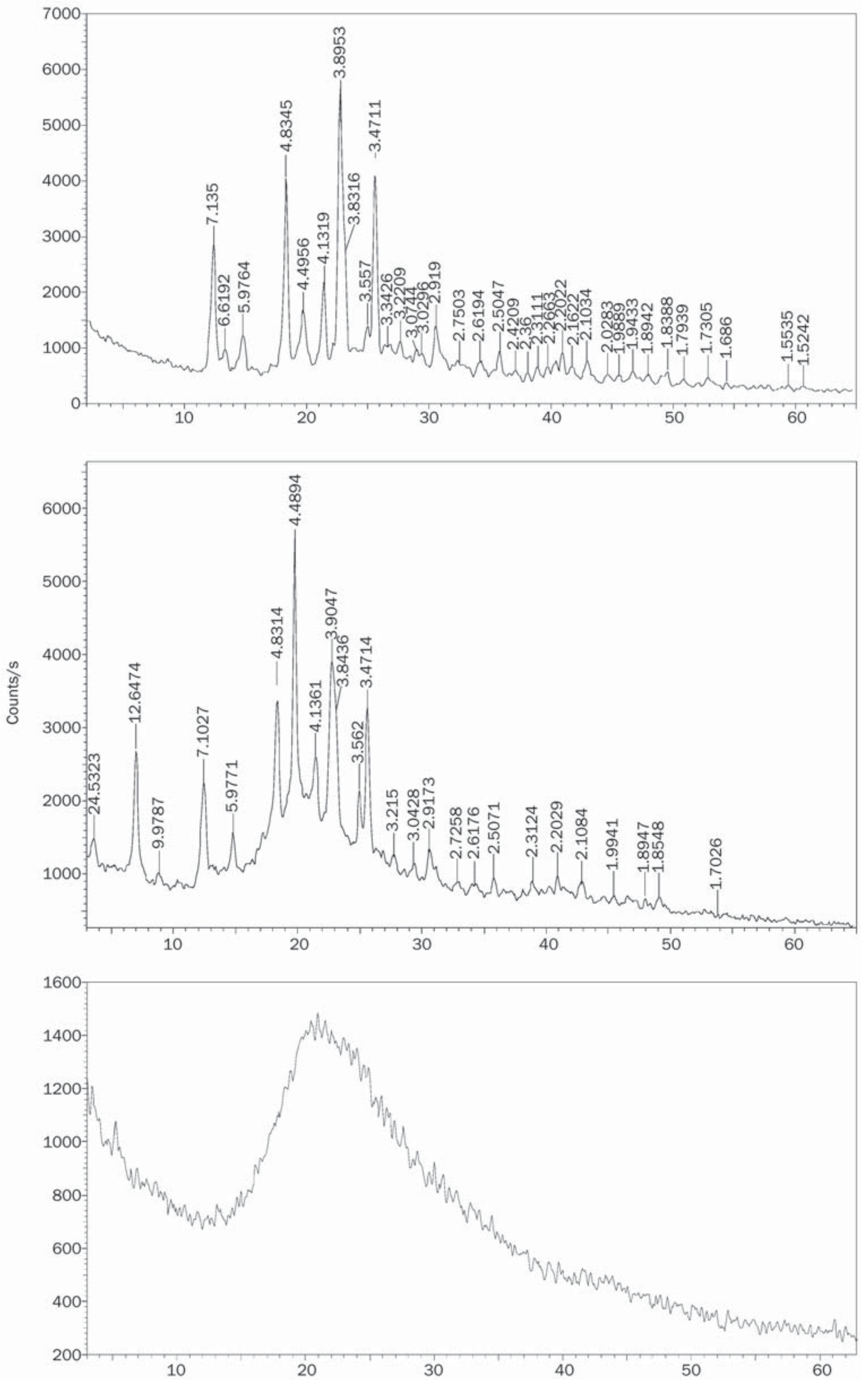

Figure 7. X-ray diffraction patterns of bergenin (A), physical mixture (B), and BPC (C).

genin, the physical mixture and BPC to rats, the plasma bergenin levels were analyzed over a 60 h period. The mean plasma concentration-time profiles are shown in Figure 11, and the pharmacokinetic parameters calculated from the data are summarized in Table 6. The concentration–time profiles were best described as a two-compartment open model and a biphasic phenomenon, with a rapid absorption followed by a slower elimination phase. As seen in the plasma curves, both the physical mixture and BPC showed higher plasma levels than free bergenin. For BPC, the $AUC_{0\rightarrow\infty}$ value

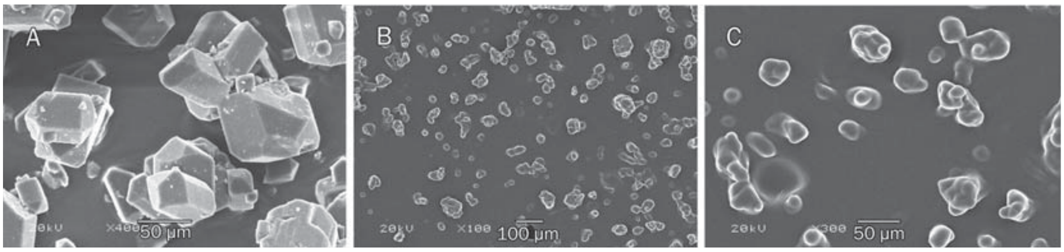

Figure 8. Scanning electron micrographs of bergenin at ×400 (A) and BPC at ×100 (B), and ×300 (C) magnification.

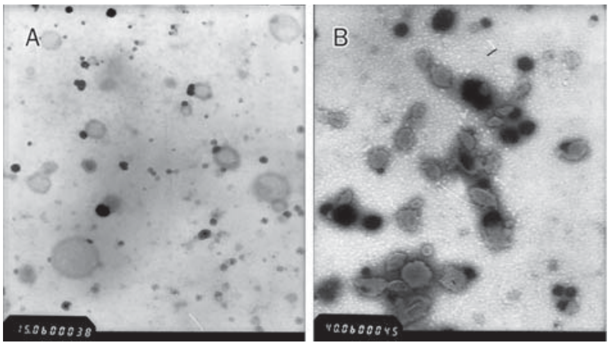

Figure 9. Transmission electron micrographs of BPC after slightly shaking in distilled water at ×1500 magnification (A) and at ×4000 magnification (B), respectively.

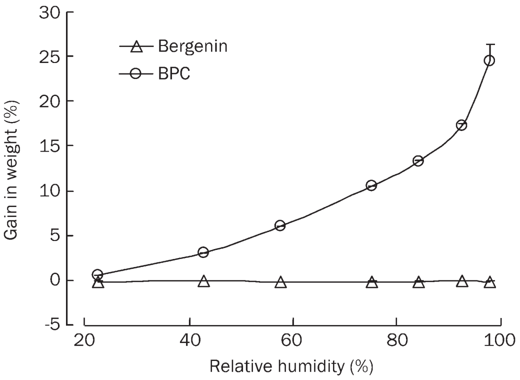

Figure 10. Moisture adsorption curve of bergenin and BPC.

Table 6. Main pharmacokinetic parameters of free bergenin (300.0 mg/kg), physical mixture and BPC (equivalent to 300.0 mg/kg of free bergenin) in rats after oral administration. *n*=5. Mean±SD.

Parameter	Bergenin	Physical mixture	BPC
$t_{1/2\alpha}$ (h)	9.16±3.66	7.98±3.16	1.12±0.16
$t_{1/2\beta}$ (h)	40.78±19.63	20.74±10.84	51.73±8.61
$MRT_{0\to t}$ (h)	21.31±1.70	21.83±2.66	30.30±4.95
C_{max} (μg/mL)	0.44±0.06	0.73±0.12	2.87±1.29
$AUC_{0\to\infty}$ (μg·h/mL)	12.11±3.51	18.91±8.20	53.17±11.81

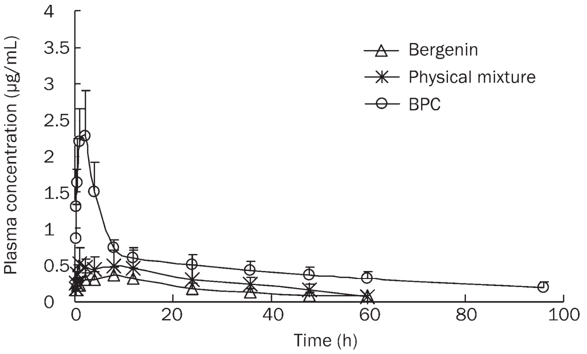

Figure 11. Plasma concentration profiles of bergenin in rat after oral administration of bergenin alone, physical mixture and BPC (equivalent to 300.0 mg/kg of bergenin). *n*=5. Mean±SD.

was 53.17±11.81 μg·h/mL, and the relative bioavailability increased significantly to 439% of the control group. The C_{max} value (2.87±1.29 μg/mL) was almost 6.52 times that of bergenin (0.44±0.06 μg·h/mL). When the physical mixture was administered, a 1.56-fold higher $AUC_{0\to\infty}$ (18.91±8.20 μg·h/mL) and 1.66-fold higher C_{max} (0.73±0.12 μg/mL) were observed compared to the control group.

Discussion

In recent years, it has been reported that some poorly soluble drugs combined with phospholipids could result in an increase of oral bioavailability and/or improvement of the biological effects, such as silybin, curcumin and puerarin[18–20]. However, detailed information about the preparation of these complexes is limited. Peng *et al* used a central composite design approach for the optimization of ursodeoxycholic acid-phospholipid complex (UDCA). The yield (%) of UDCA present as a complex was the unique evaluation index for the preparation[21]. However, the content of drug in the complex that determines the pharmacologic action is another key factor and should not be neglected. In our experiment, both the combination percentage and content of the drug were taken into consideration. The spherical symmetric design-response surface methodology constitutes an alternative approach because it offers the possibility of investigating a high number of variables at different levels, while performing only a limited number of experiments[22]. In the experimental design of the spherical symmetric design-response surface methodology, the preliminary studies were investigated in detail. Organic solvents like chloroform, diethyl ether, acetone, methylenechloride, tetrahydrofuran, acetic ether, methanol and ethanol were investigated. A high combination percentage was achieved when methanol and ethanol were used. Considering that ethanol could be removed easily and is less harmful to the environment and human body compared with other solvents, it was used as the reaction medium. When the drug-to-phospholipids ratio was lower than 0.4, the resultant materials appeared viscous. When the ratio was more than 1.2, crystals of bergenin could be observed in SEM photographs, and the combination percentage was low (these results were not shown).

In the literature, researchers have demonstrated that phospholipid complexes are not new chemical compounds or simple physical mixtures. Drugs and phospholipids should have some interactions, such as hydrogen bonding or van der Waals interactions, when they form complexes[18, 23, 24]. We performed some experiments to prove this point. In the structure of bergenin and the phospholipids, there were no chemical groups that could react with each other under our preparation conditions. Thus, it is hard for them to form a new substance. TLC was performed in order to determine whether a new substance was formed. In the chromatogram, no new spot was found. The result was further proven by UV and HPLC analyses. The chromatographic behavior of BPC was the same as bergenin, and no new peaks were found. This indicated that no new substance was formed in the preparation. However, the BPC showed different physical properties from bergenin and the physical mixture, such as increased solubility, different morphological characteristics and stronger hygroscopicity. Some interactions might exist between bergenin and phospholipids. In order to clarify the interactions, Fourier transform infrared spectral (FT-IR) analysis was performed. From the FT-IR spectra, the hydrogen bonds in BPC were different from the hydrogen bonds in either bergenin or the phospholipids. There are carbonyl groups belonging to phospholipids that allow the formation of hydrogen bonds with the phenolic hydroxyl groups of bergenin. This means that, when BPC was prepared, intermolecular coupling interactions changed and absorption bands attributed to the vibration of hydrogen-bonded carbonyl groups were observed in the FT-IR spectra. With the hydrogen bonds between the molecules gone, the crystal shape of bergenin disappeared (from SEM photographs), and the sharp melting peak of bergenin was absent in DSC thermograms. The results of the X-ray diffraction studies also confirmed that in the phospholipids complex, bergenin was either molecularly dispersed or present as an amorphous form.

Phospholipids are an important component of cell membranes, having low toxicity and good biocompatibility. Due to their surface-active properties, phospholipids are commonly used as solubilizers or absorption enhancers to increase the permeability of some drugs. In the present study, the relative bioavailability of bergenin was significantly enhanced when it was administered as a phospholipid complex. In order to explore whether the enhanced absorption was the effect of phospholipids, a physical mixture of the drug and phospholipids was investigated and compared with the complex. The results showed that phospholipids could enhance both the C_{max} and relative bioavailability of bergenin, but the effect was weaker than in BPC ($P<0.05$). It indicated that BPC could markedly improve the oral absorption of bergenin, and not just through the action of phospholipids. Small particle size, good solubility and permeability may be the main reasons for the improved absorption.

In conclusion, the preparation of BPC was optimized using the spherical symmetric design-response surface methodology by fitting a quadratic model to the response data. The experimental values of the BPC prepared under the optimum conditions were close to the predicted values and had a low percentage bias. The physicochemical properties and pharmacokinetic characteristics of BPC in rats were explored. Our results indicate that BPC has greatly enhanced solubility and improved oral bioavailability compared to bergenin and is more suitable for oral administration. However, the detailed mechanism of BPC oral absorption needs further investigation.

Acknowledgements

The research described above was supported by the National Basic Research Program of China (973 program, No 2009CB903301).

Author contribution

Xuan QIN, Yuan HUANG designed the research; Xuan QIN, Yang YANG, Ting-ting FAN and Tao GONG carried out laboratory experiments; and Xuan QIN, Yuan HUANG and Xiaoning ZHANG analyzed data and wrote the paper.

References

1 Nazir N, Koul S, Qurishi MA, Taneja SC, Ahmad SF, Bani S. Immunomodulatory effect of bergenin and norbergenin against adjuvant-induced arthritis–a flow cytometric study. J Ethnopharmacol 2007; 112: 401–5.

2 Ye YP, Sun HX, Pan YJ. Bergenin monohydrate from the rhizomae of *Astilbe chinensis*. Acta Crystallogr C 2004; 60: 397–8.

3 Wang G, Ma BJ. Overview of recent progress on bergenin. Anhui Zhong Yi Xue Yuan Xue Bao 2002; 21: 59–62.

4 Lim HK, Kim HS, Choi HS, Choi J, Kim SH, Chang MJ. Effects of bergenin, the major constituent of *Mallotus japonicus* against *D*-galactosamine-induced hepatotoxicity in rats. Pharmacology 2001; 63: 71–5.

5 Piacente S, Pizza C, Tommasi N, Mahmood N. Constituents of *Ardisia japonica* and their *in vitro* anti-HIV activity. J Nat Prod 1996; 59: 565–9.

6 Takahashi H, Kosaka M, Watanabe Y, Nakade K, Fukuyama Y. Synthesis and neuroprotective activity of bergenin derivatives with antioxidant activity. Bioorg Med Chem 2003; 11: 1781–8.

7 Jiangsu New Medical College. Traditional Medicine. Shanghai, China: Shanghai People's Publishing House 1999; p 2359.

8 Lipkaa E, Amidonb GL. Setting bioequivalence requirements for drug development based on preclinical data: optimizing oral drug delivery

systems. J Control Rel 1999; 62: 41–9.

9 Dan Z, Xuan Q, Zhi RZ, Yuan H. Physicochemical properties of bergenin. Pharmazie 2008; 63: 366–71.

10 Cyril R, Olivier RM. Synthesis of bergenin-related natural products by way of an intramolecular C-glycosylation reaction. Tetrahedron-Asymmetr 2000; 11: 409–12.

11 Wang G, Liu JK, Ma BJ. The acetylate of bergenin and its application. PR China Patent 2006; 200510010970.0.

12 Li XD, Lu SL, He B. The preparation of bergenin compositae pills. PR China Patent 2005; 200410040660.9.

13 Li J. The preparation of bergenin compositae soft capsules. PR China Patent 2005; 200410078846.3.

14 Guan JY, Sun DJ, Wu GL. The study of bergenin's inclusion complex. Zhong Cheng Yao 1991; 13: 4–5.

15 Stokes RH. Standard solutions for humidity control at 25 °C. Ind Eng Chem 1949; 41: 2013.

16 Xuan Q, Dan Z, Zhi RZ, Yuan H. Determination of bergenin in rat plasma by high-performance liquid chromatography. Pharmazie 2007; 62: 323–6.

17 Chinese Pharmacopoeia Commission. The Pharmacopoeia of the People's Republic of China 2005; part I: 278.

18 Xiao YY, Song YM, Chen ZP, Ping QN. The preparation of silybin–phospholipid complex and the study on its pharmacokinetics in rats. Int J Pharm 2006; 307: 77–82.

19 Kuntal M, Kakali M, Arunava G, Bishnu, PS, Pulok KM. Curcumin–phospholipid complex: Preparation, therapeutic evaluation and pharmacokinetic study in rats. Int J Pharm 2007; 330: 155–63.

20 Li Y, Pan WS, Chen SL, Xu HX, Yang DJ, Chan ASC. Pharmacokinetic, tissue distribution, and excretion of puerarin and puerarin-phospholipid complex in rats. Drug Dev Ind Pharm 2006; 32: 413–22.

21 Peng FY, Zhang WJ, Yuan HL, Yang M, Zhu WF, Cai PL, *et al*. Process optimization, characterization and pharmacokinetic evaluation in rats of ursodeoxycholic acid–phospholipid complex. AAPS PharmSciTech 2008; 9: 322–9.

22 Wu W, Cui GH. Central composite design-response surface methodology and its application in pharmaceutics. Foreign Med Sci Sect Pharm 2000; 27: 292–8.

23 Venema FR, Weringa WD. The interactions of phospholipid vesicles with some anti-inflammatory agents. J Colloid Interface Sci 1988; 125: 484–500.

24 Peng FY, Hai LY, Huan X, Xiao HX, Ming Y, *et al*. Preparation, characterization, and bioavailability of ursodeoxycholic acid-phospholipid complex *in vivo*. Drug Dev Ind Pharm 2008; 34: 708–18.